A multi-scale approach towards reusable steel-concrete composite floor systems

Martin Paul Nijgh

A MULTI-SCALE APPROACH TOWARDS REUSABLE STEEL-CONCRETE COMPOSITE FLOOR SYSTEMS

A MULTI-SCALE APPROACH TOWARDS REUSABLE STEEL-CONCRETE COMPOSITE FLOOR SYSTEMS

Proefschrift

ter verkrijging van de graad van doctor
aan de Technische Universiteit Delft,
op gezag van de Rector Magnificus prof. dr. ir. T.H.J.J. van der Hagen,
voorzitter van het College voor Promoties,
in het openbaar te verdedigen op woensdag 31 maart 2021 om 15:00 uur

door

Martin Paul NIJGH

civiel ingenieur,
geboren te Vlaardingen, Nederland

Dit proefschrift is goedgekeurd door de promotoren.

Samenstelling promotiecommissie:

Rector Magnificus	voorzitter
Prof. dr. M. Veljkovic	Technische Universiteit Delft, promotor
Prof. dr. ir. L.J. Sluijs	Technische Universiteit Delft, promotor
Dr. M. Pavlovic	Technische Universiteit Delft, copromotor

Onafhankelijke leden / Independent members:

Prof. dr. ir. J.F. Demonceau	Université de Liège
Prof. dr. M. Knobloch	Ruhr-Universität Bochum
Prof. dr. ing. U. Kuhlmann	Universität Stuttgart
Prof. dr. ir. E. Schlangen	Technische Universiteit Delft
Prof. dr. ir. A. Metrikine	Technische Universiteit Delft, reservelid

Keywords:	Demountable shear connector; design for reuse; steel-concrete composite floor system; injected bolted connection; (steel-reinforced) epoxy resin system; multi-scale approach.
Cover:	Designed by Eline Siepel

Een digitale versie van dit proefschrift is beschikbaar via
`http://repository.tudelft.nl/`.

I often say that when you can measure what you are speaking about, and express it in numbers, you know something about it; but when you cannot measure it, when you cannot express it in numbers, your knowledge is of a meagre and unsatisfactory kind; it may be the beginning of knowledge, but you have scarcely, in your thoughts, advanced to the stage of science, whatever the matter may be.

Lord Kelvin, 1883

CONTENTS

LIST OF SYMBOLS AND ABBREVIATIONS

The list of symbols contains a number of variables with two or more definitions: in such a case the meaning of the symbol follows from its context.

a	Creep slip rate coefficient
b	Width (general)
$b_{f,b}$	Width of bottom (tensile) flange
$b_{f,t}$	Width of top (compression) flange
$\mathbf{c}$	Vector containing unknown constants
c	Cohesion in Mohr-Coloumb model
c_0	Nominal bolt-to-formwork clearance
$c_{f,t}$	Width of outstand compression flange
c_{sc}	Shear connector spacing
c_w	Width of internal compression element
$c_{\varphi,m}$	Weighing factor for rotation mode m
$c_{v,m}$	Weighing factor for lateral deflection mode m
dx	Length of infinitesimal segment
d	Bolt diameter
d	Cohesion (Drucker-Prager)
d	Material specimen diameter
d_0	Hole diameter
$d_0 - d$	Nominal hole clearance
e	Distance between the neutral axes of the steel beam and the prefabricated concrete floor element
e	Edge distance of shear connector
f	Frequency (general)
f_n	The n-th eigenfrequency ($n = 1, 2, 3, \ldots$)
$f_{1,\infty}$	Fundamental frequency of the floor system under assumption of rigid shear interaction
$f_{1,K}$	Fundamental frequency of the floor system for the actual shear connector stiffness and arrangement
$f_{b,resin}$	Nominal bearing strength of epoxy resin injectant
f_{cd}	Design value of the concrete compressive strength
f_{ck}	Characteristic concrete compressive strength
$f_{cm,cube}$	Mean concrete cube compressive strength
f_{cm}	Mean concrete compressive strength
f_{ctm}	Mean concrete tensile strength
f_{ub}	Bolt tensile strength
f_u	Ultimate strength
$f_{y,c}$	Yield strength in compression
$f_{y,t}$	Yield strength in tension

f_{yb}	Bolt yield strength
f_y	Yield strength (general)
h	Cross-section height
$h_r(x_i, y_j)$	Total height of resin matrix of the element at (x_i, y_j)
$h_{s,p}(x_i, y_j)$	Height of steel particle p of the element at (x_i, y_j)
$h_s(x_i, y_j)$	Total height of steel particles of the element at (x_i, y_j)
k	Yield stress in pure shear
$k_{b,eff}$	Effective bending stiffness
$k_{eq}(x_i, y_j)$	Equivalent spring stiffness of the element at (x_i, y_j)
k_n	Normal interface stiffness
k_n	Statistical parameter to account for number of test results
k_{red}	Reduction factor to account for the effects of web distortion
$k_{s,eff}$	Effective shear stiffness
k_{sc}	Secant shear connector stiffness
k_s	Adjustment factor for the nominal bearing strength depending on the nominal hole clearance
k_s, k_t	Shear interface stiffness
$k_s(x_i, y_j)$	Spring stiffness of the resin matrix of the element at (x_i, y_j)
$k_s(x_i, y_j)$	Spring stiffness of the steel particles of the element at (x_i, y_j)
k_t	Limit state constant for resin-injected bolted connections
k_y, k_z	Spring stiffness in y and z direction
m	Mass or mass per unit length (general)
n	Number of Rayleigh-Ritz modes
n	Number of standard deviations
p	Hydrostatic pressure
n	Number of discrete elements in unit cell along one axis
q	Number of spherical particles in unit cell
q	Von Mises stress
q_z	Uniformly distributed load in z direction
q_z	Uniformly distributed load in z-direction
$q_{G,d}$	Design value of uniformly distributed load due to self-weight
q_G	Uniformly distributed load due to self-weight
q_Q	Uniformly distributed variable load
$q_{z,cr}$	Critical uniformly distributed load in z-direction
r	Radius of spherical particle
r	Distance between the actual centre of the bolt hole and the actual centre of the demountable shear connector
s	Slip (longitudinal relative displacement between two components)
s_0	Slip amplitude due to self-weight
$\Delta s_{cr,DLSC,SRR}$	Creep slip increment of double-lap shear connection due to creep of the steel-reinforced resin
$\Delta s_{cr,POT,concrete}$	Creep slip increment of push-out specimen due to concrete creep
$\Delta s_{cr,POT}$	Creep slip increment of push-out specimen
t	Traction vector (general)
t	Measure of stress condition in linear Drucker-Prager model
t	Thickness (general)
t	Time (general)
t_0	Time of first load application
t_1	Thickness of centre plate of double-lap shear connection
t_2	Thickness of cover plate of double-lap shear connection
$t_{b,resin}$	Effective bearing length of injection bolt

$t_{\text{f,b}}$	Thickness of bottom (tensile) flange
$t_{\text{f,t}}$	Thickness of top (compression) flange
t_{n}	Normal traction
t_{n}^0	Normal interface strength
t_{s}, t_{t}	Shear traction
t_{s}^0, t_{t}^0	Shear interface strength
t_{w}	Web thickness
Δt	Time increment (general)
u_0	Imposed axial deformation to each element in unit cell
$u_{\text{r}}(x_i, y_j)$	Axial deformation of resin matrix of the element at (x_i, y_j)
Δu_{max}	Convergence tolerance for axial deformation
$\overline{u}_{\text{f,s,bolt}}^{\text{pl}}$	Equivalent plastic shear displacement at failure
$\overline{u}_{\text{f}}^{\text{pl}}$	Equivalent plastic displacement accumulated during the necking stage
$\overline{u}_i^{\text{pl}}$	Equivalent plastic displacement
v	Out-of-plane deflection
w	In-plane deflection
$w_{\text{m},\infty}$	Deflection at midspan of the floor system for rigid composite interaction
$w_{\text{m},K}$	Deflection at midspan of the floor system for the actual shear connector stiffness and arrangement
Δw	Deflection increment
$\widetilde{w}$	Deflection function used in separation of variables
x, y, z	Right-handed coordinate system
Δx_{beam}	Total longitudinal deviation from nominal position of the centre of the bolt hole in the steel beam
$\Delta x_{\text{c,L}}$	Longitudinal offset of left beam from intended position
$\Delta x_{\text{c,R}}$	Longitudinal offset of right beam from intended position
Δx_{floor}	Total longitudinal deviation from nominal position of the centre of the shear connector in the floor element
Δx_{hole}	Longitudinal deviation of bolt hole position
Δx_{sc}	Longitudinal deviation of shear connector position in concrete element
Δx_{sc}	Tranversal deviation of shear connector position in concrete element
Δx_{slip}	Longitudinal translation of the prefabricated floor element due to self-weight
Δy_{beam}	Total transveral deviation from nominal position of the centre of the bolt hole in the steel beam
$\Delta y_{\text{c,1,L}}$	Tranversal deviation of the left beam at the first support
$\Delta y_{\text{c,1,R}}$	Tranversal deviation of the right beam at the first support
$\Delta y_{\text{c,2,L}}$	Tranversal deviation of the left beam at the second support
$\Delta y_{\text{c,2,R}}$	Tranversal deviation of the right beam at the second support
$\Delta y_{\text{c,L}}$	Transversal deviation of the left beam along the span
$\Delta y_{\text{c,R}}$	Transversal deviation of the right beam along the span
Δy_{floor}	Total transversal deviation from nominal position of the centre of the shear connector in the floor element
Δy_{hole}	Transversal deviation of bolt hole position
$\Delta y_{\text{str,b}}$	Transversal deviation of braced beam due to out-of-straightness
$\Delta y_{\text{str,u}}$	Transversal deviation of unbraced beam due to out-of-straightness
z_P	Ordinate with respect to centroid where P_z is applied
z_q	Ordinate with respect to centroid where q_z is applied
$\overline{z}_{\text{c}}$	Distance from outer compressive fibre to elastic neutral axis
$\overline{z}_{\text{s}}$	Distance from outer compressive fibre to the shear centre

LATIN ALPHABET, UPPER CASE

$\mathbf{A}$	Coefficient matrix
A_0	Initial cross-sectional area
$A_{0,b}$	Out-of-straightness amplitude of braced beam
$A_{0,u}$	Out-of-straightness amplitude of unbraced beam
A_s	Bolt shear area
C_i	Integration or model constant ($i = 1, 2, \dots$)
$C_{i,j}$	Integration constant i for beam segment j
D	Compliance (general)
D	Damage variable (general)
D_c	Compressive damage variable
D_t	Tensile damage variable
E	Young's Modulus (general)
$E_{c,eff}$	Effective concrete Young's Modulus
$E_{c,lower}$	Lower bound for Young's Modulus of composite material
$E_{c,upper}$	Upper bound for Young's Modulus of composite material
E_{cm}	Mean concrete Young's Modulus
E_r	Young's Modulus of epoxy resin system
E_{srr}	Young's Modulus of steel-reinforced epoxy reisn system
EA	Axial stiffness
EI	Bending stiffness (general)
EI_0	Bending stiffness without composite interaction
EI_∞	Bending stiffness with rigid composite interaction
EI_z	Bending stiffness of the steel beam around the weaker z-axis
G_r	Shear modulus of epoxy resin system
$\overline{E}_r$	Apparent Young's Modulus of epoxy resin system
$\overline{E}_{srr}$	Apparent Young's Modulus of steel-reinforced epoxy resin system
F	Concentrated force, actuator force
$F_{b,Rd,resin}$	Design slip resistance of injected bolted connection
F_{Ed}	Design value of external force
ΔF	Actuator force increment
G	Flow potential
G	Self-weight (general)
G	Shear modulus (general)
G^C	Mixed-mode fracture energy
G_{cr}	Creep flow rule
G_n	Normal fracture energy
G_n^C	Critical normal fracture energy
G_s, G_t	Shear fracture energy
G_s^C, G_t^C	Critical shear fracture energy
GJ	Torsional rigidity
GJ_{eff}	Effective torsional rigidity
I_1	First invariant of the stress tensor
I_ω	Warping rigidity
I_i	Second moment of area around i-axis ($i = x, y, z$)
$I_{z,b}$	Area moment of inertia around the z-axis of the bottom flange
$I_{z,t}$	Area moment of inertia around the z-axis of the top flange
J	Number of segments in which the beam is subdivided
J	Torsional constant for cross-section
J_2	Second invariant of the deviatoric stress tensor
K	Ratio of yields stress in trixial tension over yield stress in triaxial compression

K	Shear connection parameter
K_n	Constant for the n-th eigenfrequency for given boundary conditions
L	Length, span
L_0	Initial specimen length
$L_{c,i}$	Reduced gauge length at strain state i
L_c	Coupon specimen gauge length
L_E	Finite element size
L_{loc}	Strain localisation length
ΔL_i	Elongation of specimen at strain state i
ΔL_n	Elongation at the onset of necking
ΔL_r	Elongation at rupture
M	Bending moment (general)
M_{cr}	Critical bending moment
$M_{pl,R}$	Plastic bending moment resistance
N	Normal force (general)
N	Number of Monte-Carlo simulations
N	Number of elements used in hybrid homogenisation method
N_i	Normal force in element i ($i = 1, 2$)
P	Arc length
$P(A)$	Probability of A
$P(A \cap B)$	Probability of A and B
P_z	Concentrated force in z-direction
P_{Rd}	Design value of shear connector resistance
P_{Rk}	Characteristic value of shear connector resistance
P_u	Ultimate shear connector resistance
$P_{z,cr}$	Critical concentrated force in z-direction
Q	Variable load (general)
R	Offset of hole from intended position
R^2	Coefficient of determination
$\mathbf{S}$	Deviatoric stress tensor
T_g	Glass transition temperature
U	Strain energy (general)
$U_{bending,z}$	Strain energy due to out-of-plane bending
$U_{uniform\ torsion}$	Strain energy due to uniform torsion
$U_{warping\ torsion}$	Strain energy due to warping torsion
V	Vertical shear force (general)
V	Virtual work done by the loads
V_f	Volume fraction (general)
V_s	Longitudinal shear force flow between steel and concrete elements
$\Delta X_{c,L}$	Random variable controlling offset of left beam from intended position
$\Delta X_{c,R}$	Random variable controlling offset of right beam from intended position
$\Delta Y_{c,1}$	Random variable controlling the deviation of the distance between adjacent erected beams measured at the first support
$\Delta Y_{c,2}$	Random variable controlling the deviation of the distance between adjacent erected beams measured at the second support

GREEK ALPHABET

α	Auxiliary cross-section parameter to determine k_{red}
α	Exponential shear damage law parameter
$\alpha, \alpha_{tD}, \alpha_{tE}$	Parameters for concrete damage model
α, β	Model parameters
α^2	Shear connection parameter

α_L	Localisation rate factor
$\alpha_{\mathrm{cr,op}}$	Ratio of the critical bending moment over the design bending moment
α_{D}	Damage eccentricity factor
α_{LT}	Imperfection factor for lateral-torsional buckling
$\alpha_{\mathrm{ult,k}}$	Minimum load amplifier of the design loads to attain the characteristic in-plane resistance of the cross section
α_{w}	Slope of beam web
β	Adjustment factor based on thickness ratio t_1/t_2 for double-lap shear connections
β	Auxiliary model parameter in concrete material model
β	Friction angle in Drucker-Prager model
β^2	EI_∞/EI_0
β_y	Wagner torsional rigidity
$f_{\mathrm{u,t}}$	Ultimate strength in tension
$f_{\mathrm{y,c}}$	Yield strength in compression
$f_{\mathrm{y,t}}$	Yield strength in tension
γ	Partial safety factor
δ	Change in length
δ_{n}	Normal separation
$\delta_{\mathrm{s}}, \delta_{\mathrm{t}}$	Shear separation
δ_{u}	Shear connector deformation capacity
ε	Strain (general)
ε_i	Concrete compressive strain at state i ($i = \mathrm{A, B, C, D, E}$)
$\varepsilon_{\mathrm{cr,r}}$	Uniaxial creep strain of resin
$\varepsilon_{\mathrm{cr,srr}}$	Uniaxial creep strain of steel-reinforced resin
$\varepsilon_{\mathrm{cr}}$	Uniaxial creep strain (general)
$\varepsilon_{\mathrm{cr}}$	Uniaxial creep strain
ε_{c}	Uniaxial concrete compressive strain
$\varepsilon_{\mathrm{f}}^{\mathrm{pl}}$	Uniaxial plastic strain at fracture
$\varepsilon_{\mathrm{n}}^{\mathrm{pl}}$	Uniaxial plastic strain at the onset of necking
ε_{r}	Uniaxial strain at rupture
ε_{t}	Uniaxial concrete tensile strain
ε_{ij}	Strain components
ε'	True strain (general)
$d\varepsilon^{\mathrm{pl}}$	Plastic strain increment
$\bar{\varepsilon}_0^{\mathrm{pl}}$	Equivalent plastic strain at the onset of damage
$\bar{\varepsilon}_{\mathrm{cr}}$	Equivalent creep strain
$\bar{\varepsilon}_{\mathrm{f}}^{\mathrm{pl}}$	Equivalent plastic strain at fracture
$\bar{\varepsilon}_{\mathrm{s,bolt}}^{\mathrm{pl}}$	Equivalent plastic shear strain of bolt
$\Delta\bar{\varepsilon}_{\mathrm{cr}}$	Equivalent creep strain increment
$\Delta\boldsymbol{\varepsilon}_{\mathrm{cr}}$	Creep strain tensor increment
ζ^4	Auxiliary parameter for determination of fundamental frequency
η	Degree of shear connection according to Eurocode 4
η	Model parameter in the Benzeggagh-Kenane fracture criterion
η	Parameter describing strain state of concrete
η	Random variable on the interval $[0,1]$
Θ	Domain of representative volume element or unit cell
θ	Random variable on interval $[0,2\pi]$ controlling angle of bolt hole offset
θ	Stress triaxiality
$\lambda_{\mathrm{S}}, \lambda_{\mathrm{E}}$	Finite element size and finite element type factors
$\bar{\lambda}_{\mathrm{op}}$	Global non-dimensional slenderness

μ	Mean (general)
μ	Relative coordinate
ξ	Correction factor for torsional constant
Π	Potential energy
π	Mathematical constant
ρ_s	Mass per unit volume of steel
ρ_c	Mass per unit volume of concrete
ρ_r	Mass per unit volume of epoxy resin system
ρ_{srr}	Mass per unit volume of steel-reinforced epoxy resin system
ρ_s	Mass per unit volume of steel
σ	Standard deviation (general)
σ	Stress (general)
σ_i	Concrete compressive stress at state i ($i = A, B, C, D, E$)
σ_i	Principal stresses ($i = 1, 2, 3$)
$\sigma_{b,resin}$	Actual bearing stress in epoxy resin injectant
σ_c	Uniaxial concrete compressive stress
σ_t	Uniaxial concrete tensile stress
σ_y	Yield stress
σ_{ij}	Cauchy stress components
σ'	True stress (general)
$\overline{\sigma}$	Equivalent stress
$\overline{\sigma}_{cr}$	Equivalent creep stress
τ	Shear stress
ν	Poisson ratio (general)
ν_r	Poisson ratio of epoxy resin system
ν_{srr}	Poisson ratio of steel-reinforced epoxy resin system
ν_s	Poisson ratio of steel
ϕ	Angle of internal friction in Mohr-Coloumb model
Φ_{op}	Auxiliary parameter to determine χ_{op}
φ	Cross-sectional rotation around x-axis
φ_i	Estimated service life factors ($i = A \dots G$)
χ_{op}	Reduction factor for lateral-torsional buckling resistance
ψ	Dilatation angle in Concrete Damage Plasticity and/or Drucker Prager model
ψ	Random variable on interval $[0, 2\pi]$ controlling angle of shear connector offset
$\omega_{1,\infty}$	Fundamental angular frequency of the floor system under assumption of rigid shear interaction

ABBREVIATIONS

BK	Benzeggagh-Kenane
ECI	Environmental cost indicator
ESL	Estimated service life
FBSC	Friction-based shear connector
FE	Finite element
FEA	Finite element analysis
GDP	Gross domestic product
IBC	Injected bolted connection
LCA	Life cycle assessment
LNSC	Locking nut shear connector
RSL	Reference service life
RVE	Representative volume element
SRR	Steel-reinforced (epoxy) resin
WOCD	World commission on environment and development

SUMMARY

Traditionally welded headed studs have been used to generate composite interaction between a steel beam and a (cast in-situ) concrete floor. This permanent connection impairs the demountability of the structural components and therefore demolition of the composite floor system is inevitable at the end of the functional service life. The demolition of functionally obsolete but technically sound building components is in contradiction with the globally prevailing ambition of more sustainable development of the built environment through reduced demand for primary resources and reduced emissions of harmful substances.

This dissertation aims to overcome the need for demolition of composite floor systems by developing methods, tools and recommendations to enable easy demountability of the structural components. The recommendations are both based on practical experience obtained by full-scale laboratory experiments on a demountable composite floor system consisting of large prefabricated concrete floor elements (2.6 × 7.2 m), and on the (analytical) methods and tools developed to predict the response of the floor system during execution (e.g. instability) and service life (e.g. deflection and stresses).

The first task in this dissertation is the development of a demountable shear connector (as an alternative to the welded headed stud) that addresses all desirable characteristics in the context of the final application. For example, geometrical and dimensional deviations of the large prefabricated structural components are accounted for by using oversized holes in the beam flange to reduce the (dis)assembly time of the floor system. The remaining bolt-hole clearance is subsequently injected with a (steel-reinforced) epoxy resin system, which results in a stiff and load-bearing connection that contributes to composite interaction of the floor system during the service live. The developed demountable shear connector consists of (i) a bolt and coupler embedded in the floor element, (ii) an external bolt through the beam flange and (iii) an injectant in the bolt-hole clearance. The aforementioned design and characteristics of the floor system identified the need for research on three levels of scale: on material level (the injectant), on connector level (component behaviour), and on the level of the composite floor system (effect of the connectors on the global response). This dissertation provides new knowledge by experimental and numerical research at all three levels of scale and hereby provides an integral contribution to the development of demountable and reusable steel-concrete composite floor systems. The practical applicability of the work presented in this dissertation is highlighted in Chapter 10, where the developed design philosophy and prediction models are used to design and optimise a case study composite floor system.

On the injectant level, experiments revealed the short- and long-term response of (steel-reinforced) epoxy resin systems RenGel SW 404 + HY 2404/5159 subject to uniaxial compression. It was found that the steel-reinforced variant, consisting of 60% steel spherical particles in volume, had a Young's Modulus 2.8 times that of the standard epoxy resin system. The benefits in terms of the uniaxial creep sensitivity varied significantly depending on the stress level. Material models for the injectants were derived based on experimental

findings for uniaxial (non-confined) compression and based on the behaviour in tension obtained by (computational) homogenisation methods.

On the level of the demountable shear connector, experimental and numerical *push-out* tests were performed to study the load-slip response of the proposed demountable shear connector. In addition, long-term double-lap shear connection experiments revealed the time-dependent slip caused by the injectants. It was found that the long-term material models of the injectants did not accurately describe the long-term response of the connections, which was attributed to a pressure-dependent creep mechanism not considered in the uniaxial material experiments. The short-term material model for the (steel)-reinforced resin provided accurate predictions for the instantaneous slip, although for resin-injected specimens this was only the case for relatively low nominal bearing stresses (up to 125 MPa). The discrepancy for higher nominal bearing stresses was hypothesised to originate from viscoelastic or -plastic effects. A parametric study base on the calibrated finite element model of the short-term *push-out* tests revealed design recommendations to further increase the shear connector stiffness and resistance to maximise impact on the structural response of composite floor systems.

On the level of the composite floor system, this dissertation presents the first ever experimental work on a non-prismatic demountable composite floor system with non-uniform shear connection. The experimental work highlighted the previously hypothesised need for oversized holes to successfully install the large prefabricated concrete floor elements. A statistics-based prediction model to quantify the required magnitude of the oversized hole for a given probability of successful installation of the prefabricated floor elements was derived based on relevant geometrical and dimensional deviations reported in the literature. Prediction models for the elastic in-plane response, the fundamental eigenfrequency, and for the critical bending moment (related to out-of-plane instability of the steel beams) for non-prismatic demountable composite floor systems were derived and validated against the experimental results or against results available in the literature. In line with previous research, it was found that discrepancy between shear connector stiffness obtained in push-out and beam tests exists, and that the magnitude of the slip could not be accurately predicted. The implications of the in-plane and out-of-plane prediction models were used to derive design optimisation strategies to minimise material use and to increase the speed of (disassembly) by limiting the need for bracing systems that ensure stability during execution. A design example for a steel-concrete composite floor system is presented in Chapter 10 to highlight the practical applicability of the work presented in this dissertation.

SAMENVATTING

Tot op heden worden gelaste deuvels toegepast om composietwerking tussen een stalen ligger en een (in het werk gestorte) betonnen vloer te genereren. Deze permanente verbinding verhindert de demonteerbaarheid van de constructieve elementen, en daarom is sloop van het vloersysteem onvermijdelijk aan het eind van de functionele levensduur. Het slopen van functioneel obsolete maar constructief gezien betrouwbare constructieve elementen is in tegenspraak met de heersende mondiale ambitie om de gebouwde leefomgeving op een duurzamere manier te ontwikkelen door het gebruik van minder primaire materialen en door de gereduceerde emissies van schadelijke stoffen.

Dit proefschrift tracht om de sloop van staal-beton composiete vloersystemen te voorkomen door methoden en aanbevelingen te ontwikkelen die een eenvoudige demontage van de constructieve elementen mogelijk maken. De aanbevelingen zijn zowel gebaseerd op praktische ervaringen verkregen door laboratoriumexperimenten (op ware grootte) op een demontabel staal-beton composiet vloersysteem, als op (analytische) modellen om het gedrag van vloersystemen tijdens de uitvoering (bijv. instabiliteit) en de levensduur (bijv. doorbuiging en spanningen) te voorspellen.

De eerste opgave in dit proefschrift is het ontwikkelen van een innovatief demontabel afschuifverbindingsmiddel (als alternatief voor de gelaste deuvel) dat alle gewenste eigenschappen bezit voor een toepassing in een losmaakbaar vloersysteem. Zo worden bijvoorbeeld afwijkingen in de geometrie en maatvoering van de constructieve elementen opgevangen in de verbinding door het gebruik van overmaatse gaten. De gatspeling tussen boutsteel en boutgat wordt vervolgens geïnjecteerd met een (staal-versterkte) epoxy kunsthars: dit resulteert in een stijve en krachtsoverdragende verbinding die bijdraagt aan de composietwerking gedurende de functionele levensduur van het vloersysteem. Het bovengenoemde ontwerp van het ontwikkelde demontabel afschuifverbindingsmiddel leidt tot de noodzaak van onderzoek op drie schaalniveaus: op materiaalniveau (het injectiemiddel), het verbindingsniveau, en op het niveau van het vloersysteem. Dit proefschrift levert nieuwe kennis door middel van experimenteel en numeriek onderzoek en draagt hiermee integraal bij aan de ontwikkeling van een demontabel en herbruikbaar staal-beton composiet vloersysteem. De bijdrage van dit proefschrift aan de dagelijkse praktijk wordt uitgelicht in Hoofdstuk 10, waar de ontwikkelde ontwerpfilosofie en voorspellingsmethoden worden gebruikt om een staal-beton composiet vloersysteem te ontwerpen en te optimaliseren als casestudy.

Op materiaalniveau leidden experimenten tot inzicht in het korte- en langeduurgedrag van de (staal-versterkte) epoxy kunstharsen RenGel SW 404 + HY 2404/5159 belast op eenassige druk. De resultaten lieten zien dat de staal-versterkte variant, bestaand uit 60 volumeprocent stalen kogelvormige deeltjes, een elasticiteitsmodulus heeft die 2.8 maal de waarde heeft van de standaard epoxy kunsthars. Het voordeel van de staal-versterkte variant in eenassige kruipproeven hing sterk af van het spanningsniveau. Op basis van de experimentele bevindingen voor uniaxiale druk en op basis van (numerieke) homogenisatietechieken

om het gedrag op trek in kaart te brengen, zijn materiaalmodellen voor de injectiemiddelen ontwikkeld.

Op het niveau van het afschuifverbindingsmiddel zijn experimentele en numerieke *push-out* proeven uitgevoerd om de relatie tussen kracht en vervorming van het ontwikkelde demontabele afschuifverbindingsmiddel te bestuderen. Daarnaast zijn langeduurproeven uitgevoerd op dubbelsnedige verbindingen om de tijdsafhankelijke vervorming ten gevolge van de injectiemiddelen in kaart te brengen. De materiaalmodellen konden de tijdsafhankelijke vervorming niet nauwkeurig voorspellen: deze afwijking werd toegeschreven aan een drukafhankelijk kruipmechanisme dat niet tot uiting kwam in de eenassige materiaalproeven. Op de korte termijn konden de materiaalproeven het gedrag van de verbindingen goed voorspellen, hoewel dit voor verbindingen geïnjecteerd met niet-versterkte epoxy kunsthars alleen het geval was voor geringe nominale stuikspanningen (tot 125 MPa). Er wordt verwacht dat de afwijkingen voor hogere nominale stuikspanningen het gevolg zijn van viscoelastische of -plastische effecten. Op basis van het gecalibreerde eindige-elementenmodel van de korteduur push-out tests is een parameterstudie uitgevoerd om ontwerpaanbevelingen te maken die leiden tot een hogere stijfheid en weerstand van het verbindingsmiddel, om zo de gunstige effecten van composietwerking in vloersystemen te maximaliseren.

Op het niveau van het vloersysteem presenteert dit proefschrift de eerste proevenserie ooit op een niet-prismatisch demontabel staal-beton composiet vloersysteem met niet-uniform verdeelde afschuifverbindingsmiddelen. De assemblage van dit vloersysteem benadrukte de veronderstelde noodzaak van overmaatse gaten om de afschuifverbindingsmiddelen te kunnen installeren. Een model dat voorspelt wat de diameter van het overmaatse boutgat moet zijn om de verbinding tussen ligger en vloerelement met een bepaalde kans tot stand te kunnen brengen werd ontwikkeld, en is gebaseerd op relevante afwijkingen in de geometrie of maatvoering van de constructieve elementen. Voorspellingsmodellen voor het elastische gedrag in het vlak van de belasting, de eerste eigenfrequentie, en voor het kritieke buigend moment (uit-het-vlak instabiliteit van de stalen liggers) werden ontwikkeld voor niet-prismatische demontabele vloersystemen en werden gevalideerd tegen experimentele resultaten of resultaten uit de literatuur. In lijn met eerder onderzoek werd gevonden dat er verschil zit tussen de stijfheid van het verbindingsmiddel in push-out proeven en in proeven op vloersystemen, en dat de grootte van de slip voor het vloersysteem niet accuraat voorspeld kon worden. De voorspellingsmodellen voor het in- en uit-het-vlak gedrag werden gebruikt om ontwerpaanbevelingen te maken om het materiaalgebruik te minimaliseren en om de (de)montagesnelheid van het vloersysteem te verhogen door het aantal kipsteunen te beperken. In Hoofdstuk 10 wordt de praktische toepasbaarheid van het werk uit dit proefschrift uitgelicht aan de hand van een voorbeeldontwerp van een staal-beton composiet vloersysteem.

1

INTRODUCTION

The goods of today are the resources of tomorrow at yesterday's resource prices.

Walter Stahel

1.1. BACKGROUND

The production of construction materials contributes to the exhaustion of natural resources and causes negative environmental impact. The economic development of emergent nations and the growing world population are projected to double the global demand for primary materials by 2060 [1]. Decoupling the economic activity from resource use and environmental impact is a key strategy for global sustainable development, which "*...meets the needs of the present without compromising the ability of future generations to meet their own needs*" [2]. Resource and impact decoupling can be accomplished by maintaining the highest possible resource value, for example by adapting obsolete but technically sound building structures to new functional needs.

One of the main limitations of traditional steel-concrete floor systems for future reuse is that they are not adaptable with respect to function or location: the major barrier is the permanent connection between the steel beam and concrete floor, see Figure 1.1a. The development of demountable and reusable composite floor systems (see Figure 1.1b) is thus a logical one in the transition to sustainable development of the built environment.

1.2. OBJECTIVES

The overarching objective of this dissertation is to provide a (scientific) research background for a technical solution to enable the demountability and subsequent reusability of steel-concrete composite floor systems. The dissertation is undertaken in the global framework of the transition from a linear to a circular construction sector, where priority is given to prevention of material use. This calls for a technically integrated solution that enables the easy reusability of the composite floor system whilst optimising the material efficiency of the structural components. To this extent, prediction models for the mechanical behaviour of generic demountable steel-concrete composite floor systems during their execution and
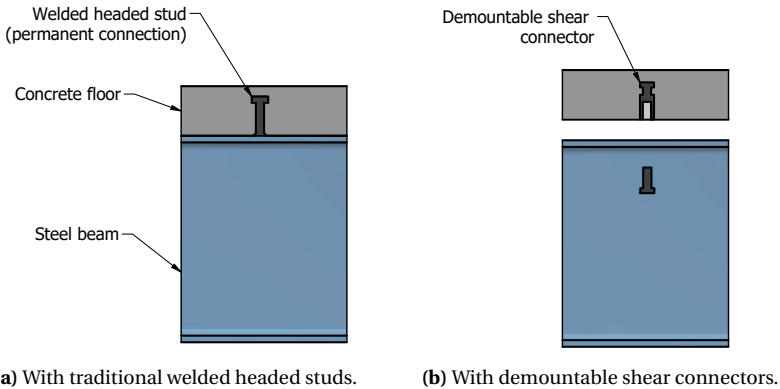
1

(a) With traditional welded headed studs. **(b)** With demountable shear connectors.

Figure 1.1 | Composite floor systems: the solution with demountable shear connectors enables the reuse of the structural components and hereby contributes to more sustainable development of the built environment.

service life will be developed. The macroscale prediction models of the structural response rely on the upscaling of component and material characteristics: establishing the link between these three levels of scale is the main theme of this dissertation. An overview of the relations between the three levels of scale considered in this dissertation is illustrated in Figure 1.2. The multi-scale approach enables the evaluation of the behaviour or response for every level of scale. The main advantage is that only key characteristics obtained at a given level of scale (e.g. short- and long-term material models, shear connector stiffness) are necessary to predict the behaviour at a larger scale. This approach therefore simplifies the design at the level of the intended application (composite floor system) without compromising on accuracy.

The first objective of this thesis is to develop a demountable shear connector by combining existing commercially available products, hereby facilitating the rapid and easy (dis)assembly of the composite floor system consisting of prefabricated elements. In essence the final product solves the shortcomings of welded headed studs traditionally used in composite floor systems.

The second objective is to experimentally establish the material behaviour of the demountable shear connectors constituents. The research mainly focuses on the behaviour of load-bearing (steel-reinforced[1]) epoxy resin injectants which facilitate the use of larger nominal hole clearances and enable instantaneous composite interaction despite these clearances. The goal is to derive short-term and long-term material characteristics of the injectants that enable implementation in commercial finite element software packages to predict the mechanical behaviour of injected bolted connections.

Thirdly, the objective is to obtain the short-term and long-term relation between applied load and deformation (slip) of the proposed demountable shear connector. The objective is complemented by the aim to predict the short-term behaviour of the proposed shear connector system based on the established material characteristics. In addition the prediction of the long-term behaviour of injected bolted steel-to-steel connections is made. The nu-

---

[1]Steel-reinforced resin is a two-phase composite, consisting of 60% (volume) spherical steel particles in an epoxy resin matrix. The material is further introduced in Chapter 2, p. 30.
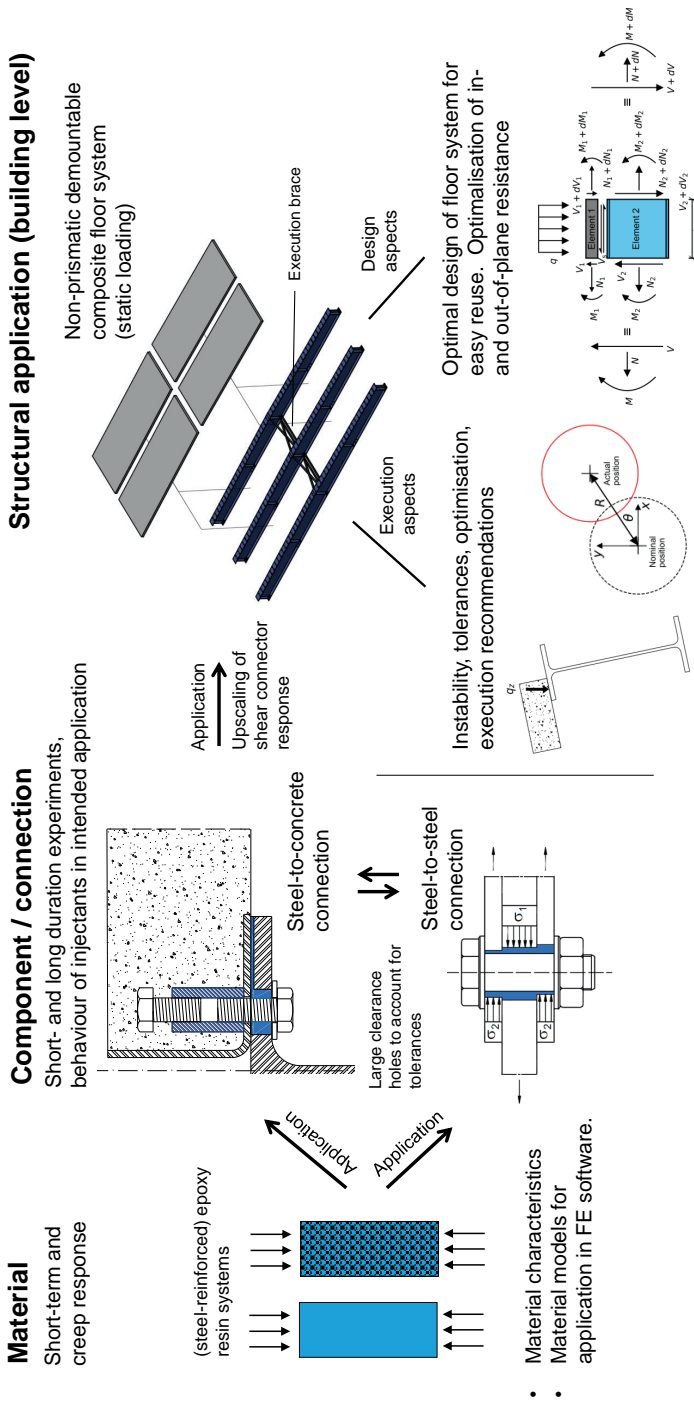
Figure 1.2 | Visualisation of the dissertation, showing the relations between the three levels of scale and the outcomes.

1

merical models for the connection behaviour are validated against experimental *push-out* and double-lap (steel-to-steel) shear connection tests, followed by an extensive parameter study to derive design recommendations for the demountable shear connector for its short-term response. The overall goal of the objective is to provide structural shear connector characteristics that can be used to predict the mechanical behaviour of demountable and reusable composite floor systems.

A fourth and final objective is to investigate the feasibility of construction and the structural response of a demountable composite floor system. The research distinguishes itself through the focus on non-prismatic steel beams and a non-uniform distribution of shear connectors to optimise the elastic structural response. The feasibility of construction is addressed experimentally by full-scale experiments and analytically by proposing a prediction methodology to quantify the minimum nominal hole clearances required for successful assembly and disassembly. The experimental results are used to validate analytical prediction models for the load-deflection and load-slip response for a composite floor systems with web-tapered steel beams and optimised shear connector arrangements. Further models are developed to analyse instability during execution and the first (fundamental) eigenfrequency during the use-phase. The overall goal of the objective is to enable implementation of demountable and reusable composite floor systems in engineering and construction practice. To this extent a design example for a case study building will be presented based on the proposed design strategies and prediction models.

1.3. RESEARCH QUESTIONS

Based on the research objectives, the following research questions were defined:

- What are the desired characteristics of a demountable shear connector? And how can these be reflected in the design, for example by implementing a novel composite material, *steel-reinforced* epoxy resin?

- What are the mechanical properties of the (*steel-reinforced*) epoxy resin in confined and unconfined compression when subject to short- and long-term loads and how can they be modelled?

- What are the mechanical properties of the proposed demountable shear connector when subject to short- and long-term loads? Can the derived material models for the injectants be used for upscaling to predict the behaviour of the demountable shear connector?

- What is the practical feasibility of demountable steel-concrete composite floor systems with the proposed shear connector during execution and (dis)assembly? How do dimensional and geometrical deviations of the structural components affect the swift assembly and disassembly of demountable composite floor systems? How can the magnitude of the required execution tolerances be predicted? How can potential instability of the steel beam during execution be mitigated?

- What is the structural response of demountable steel-concrete composite floor systems with non-prismatic steel beams and a non-uniform distribution of the proposed

demountable shear connectors? What type of prediction method can be used to determine the load-deflection and load-slip response for generic floor system designs? How can demands related to vibrations and structural resistance be verified?

1.4. STRUCTURE

This dissertation is divided into four Parts and eleven Chapters. The structure of each Part and Chapter is summarised below in the order of appearance in the Table of Contents.

Chapter 2 presents the literature review in the field of demountable composite floor systems and their relation to the circular economy. Technical requirements and perceived barriers for reusable structures are identified based on literature research. A new demountable shear connector is synthesised based on prior work and based on the need for large nominal hole clearances to enable swift execution. A mitigating measure for the large hole clearances in the form of injection bolts is presented, followed by an overview of the material behaviour of (steel-reinforced) epoxy resin injectants. The current regulations for composite floor systems according to EN 1994 [3] are addressed, and the available modelling techniques to address the short-term and long-term deflection and internal actions are presented.

Part I addresses the short-term and long-term mechanical properties of the (steel-reinforced) epoxy resin injectant RenGel SW 404 + HY 2404/5159. Chapter 3 focuses on the short-term behaviour of both types of injectants: a combination of analytical and finite element models are derived to predict the material behaviour, and the predicted material response is compared to and validated against experimental results. Chapter 4 aims at establishing long-term uniaxial compressive material properties of the injectants based on experimental results. In both chapters the materials' response is converted to material models that are suitable for implementation in commercial finite element software, with the objective to predict the upscale behaviour at the connection level.

Part II focuses on the short-term and long-term response of the proposed (steel-reinforced) resin-injected demountable shear connector. In Chapter 5, experimental push-out tests are carried out and finite element models are validated against experimental results. A finite element parameter study is performed to indicate the sensitivity of the mechanical response to changes in geometry and strength class and to derive design recommendations. In Chapter 6 push-out specimens and injected bolted double-lap shear connections are exposed to sustained loads to determine the creep sensitivity of the demountable shear connector, and to distinguish between the deformations of the concrete and the injectant over time. In both Chapters the short- and long-term material models developed in Part I are implemented.

Part III addresses the technical feasibility and structural response of full-scale composite floor systems. Chapter 7 presents the experimental work on a web-tapered demountable composite floor system, which confirms the hypothesised need for comparatively large nominal hole clearances to enable its successful execution. Structural testing based on four-point bending experiments are conducted for multiple shear connector arrangements to optimise the distribution and amount of demountable shear connectors. Chapter 8 focuses on the derivation of a methodology aimed at predicting the required nominal hole clearance for generic composite floor system designs. The magnitude of the nominal hole clearance is quantified using Monte Carlo simulations based on geometrical and dimensional deviations obtained from literature. Chapter 9 presents prediction models for the mechanical response of non-prismatic composite floor systems with non-uniform shear connection.

1

1

Prediction models are derived for the deflection and elastic in-plane resistance, the fundamental frequency, and the resistance of the steel beam to lateral-torsional buckling during execution. Particularly in Chapter 9 the findings of Part II at the level of the demountable shear connector are introduced at the level of the composite floor system. Opportunities for design optimisation of the cross-section of the steel beam are identified. Part III concludes with Chapter 10, where all prediction models developed in the context of this dissertation are combined to design a demountable composite floor system for a case study building.

Part IV consists only of Chapter 11. This chapter closes this dissertation by providing the conclusions of the work conducted in Parts I-III, by highlighting the relation between the findings at the three levels of scale, and by summarising the identified perspectives for future work.

REFERENCES

[1] Organisation for Economic Co-operation and Development, *Global Material Resources Outlook to 2060: Economic Drivers and Environmental Consequences* (OECD Publishing, 2019).

[2] World Commission on Environment and Development, *Our Common Future* (Oxford University Press, 1987).

[3] NEN, *NEN-EN 1994-1-1: Eurocode 4: Design of composite steel and concrete structures - Part 1-1: General rules and rules for buildings* (NEN, 2011).

2

LITERATURE REVIEW

There is a great deal of difference between an eager man who wants to read a book and the tired man who wants a book to read.

Gilbert Keith Chesterton

2.1. SUSTAINABLE DEVELOPMENT: A SOCIETAL CHALLENGE

Global resource demand has steadily increased since the First Industrial Revolution. The scientific and technological advances in this era facilitated the rapid production of goods and products. The seemingly abundant availability of resources and materials led to a linear take-make-dispose economy, characterised by the disregard for potential long-term environmental consequences.

2.1.1. COWBOY VS. SPACEMEN ECONOMY

The Earth's *natural capital*, consisting of all resources, living systems and ecosystem services essential to human existence [1], is in decline. Already in 1966, Boulding [2] identified that a linear "cowboy" economy, symbolic of illimitable plains and reckless behaviour, could not be sustained. The annual date by which more natural capital has been consumed than the Earth could regenerate in the same year is known as Earth Overshoot Day. Since its inception, Earth Overshoot Day shifted from December 30th (1970) to July 29th (2019), confirming Boulding's 1966 statement. In response, Boulding pleaded for the shift to a "spacemen" economy [2], built on the awareness of limited resources, implying the need for efficient and indefinite (re)use of the available materials, ecosystem services and living systems. The WOCD's[1] report *Our Common Future* [3] defined sustainable development along the same line of thought as Boulding as "development that meets the needs of the present without compromising the ability of future generations to meet their own needs". This for instance implies that sustainable development bans the extraction of natural resources at a higher rate than they can be regenerated, to prevent dependency on such "non-renewable"

---

[1]World Commission on Environment and Development

materials. This is specifically relevant for the construction sector because of its large natural resource footprint.

2.1.2. DEVELOPMENT OF GLOBAL MATERIAL DEMAND AND GDP

Raw natural resources are often allocated to one of four major categories: biomass, metal ores, non-metallic minerals and fossil energy materials. The use of biomass materials mostly depends on the size of the population, indicating that it is related to human subsistence, while the use of non-biomass materials mostly depends on the GDP per capita [4] and is therefore related to the size of the economy. Material consumption is more equally dispersed around the world than the economic activities [4], highlighting that food and shelter are more important for human existence compared to economic development.

Construction materials originate from all four natural resource categories. Examples include timber (based on biomass), polymers (oil), iron and aluminum (ores), stone and aggregates (non-metallic minerals). The annual use of construction materials rapidly increases with increasing economic development to facilitate the need for buildings and infrastructure required for industrialisation and economic growth [5]. Densely populated areas require fewer construction materials per capita to achieve the same standard of living due to efficient use of the infrastructure, smaller accommodations and low natural resource availability [5, 6].

Global material demand increased eightfold in the period 1900 - 2005 [7], whereas the global population and the global Gross Domestic Product (GDP) per capita approximately quadrupled [8]. Recent projections [9] indicate that the global population will rise from 7.6 billion (2019) to 10 billion by 2060, and that the global GDP per capita will increase from $ 11 500 to $ 37 000 . The use of primary material is forecast to grow from 89 Gt (2017) to 167 Gt by 2060. The projections indicate that, in contrast to the past, the primary material use will increase at a lower rate compared to the GDP, known as *partial decoupling*, which is attributed to the shift from an industry-based economy to a service-based economy and technological advances in production processes.

True sustainable development requires full decoupling between economic activity, resource use and environmental impact [6], which has already been achieved G7 in the period 1980 - 2010, whereas partial decoupling was observed in a number of other developed countries [10]. This decoupling was already attempted in the Roman empire by reusing architectural components [11]. The efficiency of material (re)use declined since Industrial Revolutions, because of low material costs compared to labour costs [12], but the data demonstrates that this tendency is reversing in developed countries.

2.1.3. CIRCULAR ECONOMY: CLOSING THE LOOP

Efficient and indefinite material use is achieved by *closing the loop* of their flow, by connecting the "dispose" and "take" stages of a linear economy, hereby eliminating the formation of waste. In essence this leads to *recycling* at the material level. A number of frameworks have been developed containing strategies superior to recycling, for example the "reduce, reuse, recycle" hierarchy [13] and Lansink's "prevent, reuse, recycle, energy recovery, landfill" ladder [14], amongst others [e.g. 15–19]. The shared characteristic between such frameworks is that they promote certain actions (e.g. reuse) over others (e.g. recycling), aiming to maintain the highest value of a material or product. This value-based approach was first described by Walter Stahel [20] as "...keep loops as small as possible: do not recondition

something that can be repaired, do not recycle a product that can be reconditioned economically". The contemporary overarching term for an economic system aimed at maintaining the highest value of materials, components and products is the *Circular Economy*, which is illustrated in Figure 2.1. Another graphic representation of the circular economy principles is the *Value Hill* [21, 22], illustrated in Figure 2.2, which more intuitively reflects value creation and retention.

The reuse, remanufacturing and recycling stages shown in Figures 2.1 and 2.2 can take place as a *closed loop* process, where the application does not change, as an *open loop* process, where the application changes and the inherent properties change, and as a *semi-closed loop* process, where the application changes but the inherent properties do not change [25]. Steel, the world's most recycled material [26], is suitable for all three types of processes because of its durability, its ability for upcycling and its multitude of applications. On the other hand, concrete recycling is an example of an open loop process, because the material is often downcycled for use in road foundations.

Although the Circular Economy is an appealing economic system, negative feedback loops restrict its full potential [12, 27]. For example, increased material reuse leads to a relative shortage for recycling, which could have serviced the production of newly developed and/or more functional products. Consequently, the market price for recycled material rises, reducing the incentive for reuse. Other potential barriers to the circular economy are related to undeveloped supply chains, increased project complexity, and the potential need for certification of the reclaimed members [12]. Samson & Avery [28] and Gorgolewski et al. [27] indicated that only 7-10% of the structural steel was reused in the period 2006-2012 in the UK and Canadian markets, demonstrating that there is a significant opportunity for higher value retention within the construction sector.

The finite supply of resources is not the only reason for transitioning to a more sustainable society. A healthy economy needs natural capital (resources, living systems and ecosystem services essential to human existence [1]), human capital (labour, culture, organisation), financial capital (monetary instruments) and manufactured capital (infrastructure, machines) to function [29]. In the present linear economic system, the natural capital is liquidated to fuel growth of financial and manufactured capital. To counteract this tendency, The Natural Step[2] has defined the following four system conditions for a sustainable society:

1. In order for a society to be sustainable, nature's functions and diversity will not be systematically subjected to increasing concentrations of substances extracted from the Earth's crust.

2. In order for a society to be sustainable, nature's functions and diversity will not be systematically subject to increasing concentrations of substances produced by society.

3. In order for a society to be sustainable, nature's functions and diversity must not be systematically impoverished by physical displacement, over-harvesting, or other forms of ecosystem manipulation.

4. In a sustainable society, resources are used fairly and efficiently in order to meet basic human needs globally.

---

[2]https://thenaturalstep.org/approach/

2

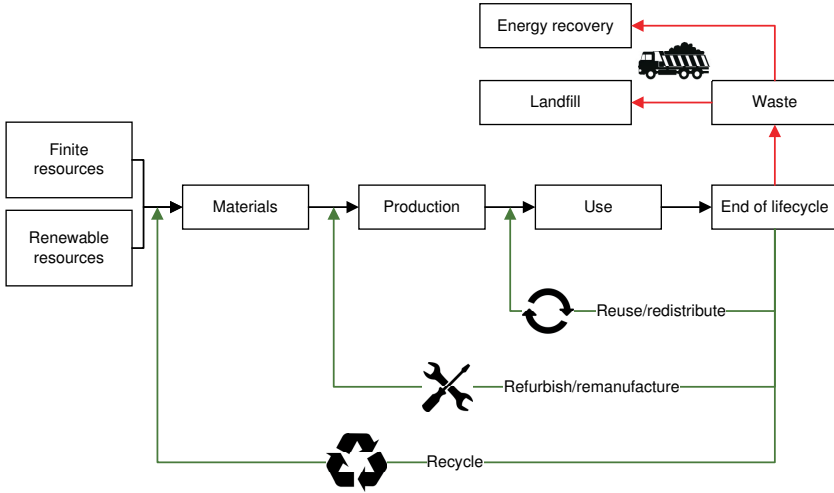**Figure 2.1 |** Schematic of the *Circular Economy,* aimed at maintaining the highest value of materials by *closing the loop* (drawn after Craven [23] and the Ellen MacArthur Foundation [24]).
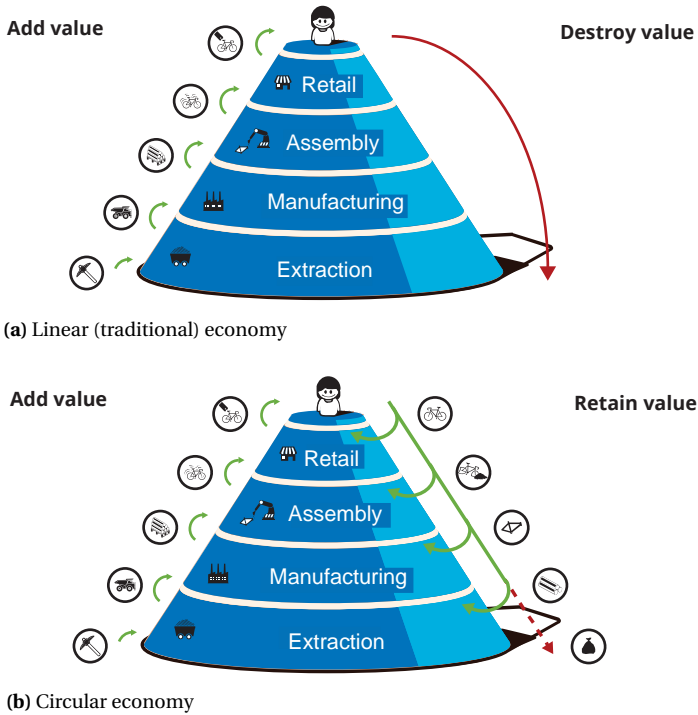

(a) Linear (traditional) economy

(b) Circular economy

Figure 2.2 | The *Value Hill*: an alternative representation of the circular economy principles (extracted from Achterberg et al. [22]).

These four system conditions offer starting points for legislators to create policies aimed at sustainable development.

2.1.4. POLICIES TOWARDS SUSTAINABLE DEVELOPMENT

Policy makers are increasingly addressing the need for sustainable development. For example, the Dutch government has the ambition to 'efficiently (re)use natural resources, without harmful emissions to the environment', to 'extract only sustainable primary resources if necessary' and to 'design products and materials such that they can be reused with the highest value retention' by the year 2050 [30]. Similar ambitions by 2050 exist on European level within the *Green Deal*[3]: the European Commission is currently working on a European Climate Law [31] to enable the enforcement of the Green Deal objectives for all member states, with the ultimate goal to become the world's first climate-neutral continent.

In 2015 the United Nations adopted its '2030 Agenda for Sustainable Development' [32], which does not only focus on climate and resources, but, like the Natural Step, also on human well-being and the quality of ecological resources. Figure 2.3 illustrates the United Nations' seventeen *Sustainable Development Goals* which together form a comprehensive strategy to improve the quality of existence for all humankind, with items nine, eleven and twelve being the most relevant in the context of this dissertation.

2.1.5. DESIGNING AND CONSTRUCTING FOR DEMOUNTABILITY AND REUSE: STRATEGIES, BENEFITS AND PERCEIVED BARRIERS

The *longevity* of a structure depends on its ability to maintain both structural integrity and desirability, in terms of function and style, over a long period of time [33]. The longevity of a structure is a function of internal expected variations (e.g. changes in functional requirements, aesthetic shifts) and environmental uncertainties (e.g. changes in markets, adoption of new standards and codes) [34] and therefore requires both durability and adaptability of the building components.

HISTORIC AND SUSTAINABLE PERCEPTIONS OF BUILDINGS

Historically, structures are perceived as single and rigid entities [35], whose inflexibility results in demolition due to the inability to address the changing functional needs [23]. To develop a more sustainable building stock, adaptability and flexibility of the assets are required without compromising on the durability, for example by structural over-design, by providing additional space for future services, and by enabling the modification of the facade and internal partitions [23]. This strategy is also known as *layering* of an asset, for example by subdividing a building into (i) its site, (ii) its skin, (iii) its structure, (iv) its services, (v) its space plan and (vi) its users' content [36–39]. Spatial, structural, and element and material transformations then enable the continuity of the use of the space, building components, and materials, respectively [40, 41], which is possible because of the *modularisation* of the building constituents. The continuous functional use eliminates the need for both demolition and the construction of a replacement building, and hereby contributes to a more sustainable built environment.

---

[3]https://ec.europa.eu/info/strategy/priorities-2019-2024/european-green-deal_en

2

Figure 2.3 | The United Nations' *Sustainable Development Goals* [32].

CLOSED-LOOP BUILDING MATERIALS STRATEGY
The modularisation of buildings directly addresses the *cardinal rules* for a closed-loop building materials strategy, defined by Kibert [42] as:

  i. Buildings must be deconstructable;

 ii. Products must be disassemblable (demountable);

iii. Materials must be recyclable;

 iv. Products and materials must be harmless in production and in use;

  v. Materials dissipated from recycling must be harmless.

However, the above rules are enablers for sustainable development within the construction sector, but do not prioritise any of the actions. Clearly, the cardinal rules must be considered in relation to other existing frameworks, such as the "reduce, reuse, recycle" hierarchy [13], Lansink's ladder [14] or other alternative formulations [e.g. 15–19].

SUSTAINABLE BUILDING PRODUCTS
Wilson [43] distinguishes five major categories of sustainable building products that can be combined with Kibert's cardinal rules [42] to further improve sustainable development within the construction sector. These categories include:

  i. Products made from environmentally attractive materials;

 ii. Products that are green because of what is not there;

iii. Products that reduce environmental impacts during construction, renovation, or demolition;

 iv. Products that reduce the environmental impacts of building operation;

v. Products that contribute to a safe, healthy indoor climate.

In addition, Cooper & Gutowski [44] state that generic sustainable products should be long-lived and thus substitute production, and have a high level of embodied carbon dioxide.

Demountable and reusable composite floor systems - the focal point of this dissertation - are type (iii) building products (or modules/sub-assemblies). However, there are certainly opportunities to activate other categories as well, for example by using sustainable materials, by minimising the material use through design optimisation (accounting for the environment to which the structural element is exposed [45]) and by improving the energy footprint and indoor climate. Therefore designing sustainable (sub)assemblies is an integral process.

It should be noted that the sustainability of structural components can increase over time, for example in case of concrete, where recent developments have led to the possibility of (also) recycling the crushed concrete fines [46] or to the possibility of applying self-healing concretes [47]. An potentially interesting group of materials for reusable structures are fibre-reinforced polymers (FRPs) [48], mainly because of their high strength to weight ratio, but this type of material is not well recyclable yet and thus does not address point (iii) of Kibert's cardinal rules [42] .

REUSE FRAMEWORK AND ITS GENERAL BENEFITS

A wider framework is necessary to support the physical activities related to the demountability and reusability of structural components. Fujita & Iwata [49] proposed a framework that facilitates the reuse of steel structures. This framework addresses the need for (i) a stock of reusable members, (ii) reuse management models, (iii) database procedures, (iv) establishment of storage sites, (v) careful demolition, (vi) performance evaluation procedures for reusable members and (vii) fabrication procedures for reusable members. This approach is also valid for structures of other or multiple materials, and functions as an overarching framework of relevant processes relevant to demountable and reusable structures. Such a well-developed reuse framework leads to benefits beyond advantages in terms of only climate and pollution, for instance [50]:

i. Reduced extraction of non-renewable resources and reduced landfill waste;

ii. Reduced energy consumption to manufacture new components;

iii. Simplified maintenance procedures;

iv. Increased adaptability of the building to address future needs for functional changes;

v. Increased opportunities for resale and reuse of the extracted structural components;

vi. Reduced costs and hindrance for dismantling compared to non-reusable buildings;

vii. Reduced financial risks related to costs associated to future repair or dismantling.

Wang et al. [51] addressed the reduced financial risks by statistical analyses to quantify the net present value (NPV) of functionally equivalent demountable and traditional structures. It was concluded that the overall investment risk of demountable structures is lower due to a narrower NPV probability distribution, despite the higher initial investment cost.

In particular, the risk of negative NPVs (lost capital) is significantly reduced due to opportunities to transform the structure, which prevents its obsoleteness in relation to points (iv) and (v) in the list above. The mean added value in terms of the NPV of the reversible design was quantified as 9%, although the maximum possible NPV was slightly lower due to the higher initial investment costs.

Fawcett et al. [52] also revealed through Monte Carlo analysis that flexible design may yield cost benefits. This was demonstrated through a case study focusing on building insulation in relation to the fluctuation of oil prices. Their approach could be extended to demountable structures, which would enable more comprehensive and detailed analysis of potential cost benefits than performed by Wang et al. [51] by considering price and market (supply vs. demand) fluctuations more accurately.

STRATEGIES AND PREREQUISITES FOR DEMOUNTABILITY AND REUSE

The cardinal rules (p. 12), product categories (p. 12), and benefits of designing for reuse (p. 13) provide a basis to implement sustainable design strategies, but do not provide any practical guidance on how to achieve the objectives. Based on the generic cardinal rules, Pulaski et al. [53] derived a set of concrete *design principles* for practical implementation within the construction sector, see Figure 2.4, and identified the potential contributions of the project partners. Particularly relevant to this dissertation are the principles "simplify and standardise connection details" and "select fittings, fasteners, adhesives and sealants that allow for quicker disassembly and facilitate the removal of reusable materials".

According to Sassi [54], the most important prerequisites for the demountability and reusability of buildings include:

i. The availability of information in the form of as-built drawings, a maintenance log and an overview of points of disassembly;

ii. The ease and safety of the access to building elements and their connections with minimal machinery requirements;

iii. Simple connection systems that enable removal by hand tools and that account for realistic tolerances for assembly and disassembly;

iv. Components and connections should be able to withstand risks associated to the (dis)assembly process and to withstand repeated use;

v. The dimensions and weight of prefabricated components should be aligned with practical issues (transportability, special cranes, etc.);

vi. The number of parts, types and number of connections should be minimised, and their design should allow for parallel (dis)assembly.

Item (i) clearly indicates the need accurate documentation and identification [27], for example through *Building Information Modelling* (BIM) to keep track of all structural components, their properties and their relation to other elements, which could be integrated with the structural design and a construction sequence simulation [55]. The items (ii)-(vi) reflect the need to keep the design as simple, repetitive and resilient as possible, which enables the construction site to function as a modern assembly facility.

Design Principles	Owners	Architects	Engineers	General Contractor/ CM	Specialty/ Subcontractors	Fabricators/ Manufacturers	Suppliers
1 Design for prefabrication, preassembly and modular construction		High	High	Medium	High	High	
2 Simplify and standardize connection details		Medium	High	High	High	High	Medium
3 Simplify and separate building systems		High	High	High			
4 Consider worker safety during deconstruction & construction		Medium	Medium	High	High	Medium	
5 Minimize building components and materials		High	High				
6 Select fittings, fasteners, adhesives and sealants that allow for quicker disassembly and facilitate the removal of reusable materials		Medium	High	High	High	High	High
7 Design to accommodate deconstruction logistics		High	Medium				
8 Reduce building complexity	Medium	High	High	Medium			
9 Design to reusable materials	Medium	High	High	High	Medium	Medium	Medium
10 Design for flexibility and adaptability	High	High	Medium				

High relevance
Medium relevance

Figure 2.4 | Design principles for demountable buildings according to Pulaski et al. [53] and the potential contributions of the project partners.

Other lists with prerequisites can, amongst others [e.g. in 39, 56–59], be found in the work of Crowther [35], who reviewed the relevant literature until 2001 and assigned the relevance of each prerequisite for recycling, component remanufacture, component reuse and building relocation (reuse). Wahlström [60] extended the lists of prerequisites with the need to verify if the building elements do not contain restricted compounds (that may have been legal when the building was first constructed), and that the components are not polluted nor aged.

In addition to the above, Dunant et al. [61] identified the influence of steel prices on the probability of reuse. It was found that a lower steel price promotes the reuse of structural elements and buildings. Another important prerequisite for markedly lower costs of reused steel is if the testing of individual elements is not required [61]. Also it was reported that partial structure reuse, i.e. the reuse of parts of buildings or buildings as a whole, is the most cost-effective strategy compared to other alternatives (e.g. reinforcing old structures, reusing single elements from a demolition site), because it simplifies fabrication, limits reconditioning costs and prevents additional material costs [61]. This strategy eliminates the need of items (i) - (iv) of the system proposed by Fujita & Iwata [49] (see p. 13) and therefore offers a more convincing and viable business model.

(PERCEIVED) BARRIERS FOR DEMOUNTABILITY AND REUSE

The reusability of the structural elements, for example of composite floor systems, does not only depend on strategies and prerequisites related to the demountability of the connection between the constituent elements, but also on the technical conditions, the demand and supply, and other (perceived) barriers. According to Durmisevic [62], potential barriers for the design and implementation of reusable buildings include:

i. The lack of instruments for certification of reclaimed elements;

ii. The lack of reversed logistic strategies;

iii. The lack of market strategies and market demand;

iv. Unknown investment risks;

v. Higher costs related to reusable compared to new building components.

The condition of the reclaimed elements (point i) is addressed by Sassi [54] through a criteria matrix, and distinguishes between three main categories: suitability for general disassembly, suitability for reuse as a second-hand item and suitability for reuse as new. The difference between second-hand and as new components is only considered in terms of the aesthetic appearance, whereas Hurley [63] also acknowledges the uncertainty related to the current conditions due to the unknown in-service history. Webster & Costello [58] state that only one material grade must be used in a structure, to avoid any uncertainty and to avoid the propagation thereof in the reuse value.

Densley Tingley & Davidson [59] reviewed the literature on barriers for reuse over the period 2001 - 2005. Their findings are summarised in Table 2.1 and include, amongst others, that composite construction is one of the key barriers in the design for deconstruction. However, this dissertation will demonstrate that composite construction is not necessarily a barrier to reuse. Kibert [64] noted that the application of manufactured, site-installed, low-mass products (e.g. paints, sealers, mastics) strongly reduces the reuse potential, in addition to site-processed products (e.g. drywall, wiring, insulation) and off-site processed, site-finished products (e.g. cast in-situ concrete). The latter implies that the use of grout (or *wet joints*) in demountable floor systems should be considered as unacceptable. An example of a 'demountable' floor system with (supposedly unacceptable) wet joints can be found in the temporary court house in Amsterdam, where mortar was used to establish a connection between a hollow core slab and an integrated steel beam, see Figure 2.5.

A recent study by Dunant et al. [65] provided an overview of the perceived and real barriers for the reuse of steel elements in the UK market. The study was based on a survey distributed among architects, clients, structural engineers, main contractors, fabricator, stockists and demolition contractors. It was reported that 60% had experience with steel reuse, and that 80% had heard about it. Remarkably, none of the respondents said they were motivated to implement reuse to reduce carbon emissions, although 85% of their companies had such policies in place. The top two barriers for reuse are outlined in Table 2.2 for each group of actors. The barrier *design for deconstruction* is only important for structural engineers and demolition contractors, implying that they have a knowledge and experience gap, whereas the main contractors do not see this as a significant barrier at all and thus demonstrate their confidence of applying such demountable structural systems in

Table 2.1 | Summary of the 2001-2005 literature review on (perceived) barriers for reuse by Densley Tingley & Davidson [59].

Rank	Barrier to design for deconstruction and material reuse
1	• Perceived risk in specifying reused materials • Lack of reused materials market • Time constraints: deconstruction can take longer • Financial constraints: Design for deconstruction likely more expensive • Accessibility of jointing and the types of joints for existing structures • Composite construction
2	• Perception of second-hand materials
3	• Lack of legislation for design for deconstruction and reused materials • Performance guarantees for reused materials • Contamination of materials • Storage for recovered materials • Lack of information about materials and techniques for existing structures
4	• Additional design costs • Insurance constraints: it may be unfavourable to use reused materials • Design codes generally encourage use of new materials • Loss of craft skills to create aesthetically pleasing exposed connections • Perception that design for demountability will compromise value, aesthetics, and safety • Steel coatings may contain banned chemicals • Steel coatings may contaminate the shot used to remove the coating • Additional fabrication on steel sections • Visible aesthetic degradation of reused materials

Figure 2.5 | A wet (grouted) 'demountable' connection between a hollow core slab and an integrated steel beam in the temporary Amsterdam court house (Cepezed Projects).

2

practice. Fabricators and stockists are most concerned about the quality and certification and the old/new perception, respectively, which reflects their main interests and liabilities. A similar concern regarding quality and certification was reported based on a wide Finnish market survey [66], which further strengthens the need for the development of adequate and appropriate standardisation and legislation for reusable structural elements.

To mitigate the perception of inadequate quality, the Steel Construction Institute (SCI) recently released its recommendations for the reusability assessment of dominantly statically loaded steel members [67]. The guidelines state that any sign of plastic deformation is a reason for rejection, implying that only quasi-new steel elements are suitable for reuse. This definition mitigates any perception of inconsistent quality. It should be noted that the SCI, in a companion publication [68], still considers plastic design as a viable option for demountable composite floor systems. Obviously, plastic design is in contrast with the need to prevent plasticity, and therefore the condition of all structural members must be assessed to determine their reusability, which increase costs and time [61] compared to an elastic design case. Suggestions have been made to limit the utilisation factor or unity check to a magnitude below 1.00 for plastic design to avoid plasticity [69], although clearly elastic design is more appropriate in this case because it inherently mitigates the risk of plasticity. The contradictory guidance is hypothesised to follow from a *lock-in*: no major design changes are proposed in fear of non-acceptance in current engineering practice, although a *paradigm change* is what is really necessary to accomplish the transition to a more sustainable construction sector. The effect of plastic versus elastic design on the risk of developing plasticity during the service lifetime of a structural component is discussed in Appendix G.

The lack of reversed logistic and market strategies, insufficient availability, lack of experience and the unknown investment risks mentioned in Tables 2.1 and 2.2 cannot be mitigated until the market has sufficiently matured and as their effects become evident. The perceived higher costs related to reusable structures, however, can be countered by considering the *total cost of ownership*, the *life cycle costs* or the *whole-life cost* [e.g. in 70], instead of only the costs directly associated with the execution. This may require regulation by relevant authorities, for example by imposing criteria related to material efficiency, and by developing guidelines and legislation to support reuse [50].

Environmental benefits

There is a general consensus on the environmental benefits of the circular economy, which can be applied to a multitude of industries and products. A well-established approach to quantify relative environmental benefits is *life cycle assessment* (LCA), the principles and framework of which are laid down in ISO 14040 [71]. Life cycle assessment aims to (i) iden-

Table 2.2 | Top two barriers against steel reuse per actor, according to the survey of Dunant et al. [65].

Actor	Top barrier	Second barrier
Architects and clients	Trust/lack of communication	Old/new perception
Structural engineers	Design for deconstruction	Availability/dimension
Main contractors	Availability/dimensions	Uncommon practice
Fabricators	Quality/certification/traceability	Uncommon practice
Stockists	Old/new perception	Quality/certification/traceability
Demolition contractors	Design for deconstruction	Programme (delays)

tify opportunities to improve environmental performance, (ii) inform decision-makers, (iii) select relevant indicators of environmental performance and (iv) to provide the ability to market environmental claims. This requires LCAs to consider the environmental impact during the full life cycle of a product, i.e. from raw material extraction to production, and to include the service life and the end of life treatment. Economic and social aspects are not considered.

LCAs consists of four distinct phases, (i) goal and scope definition, (ii) inventory analysis, (iii) impact assessment and (iv) interpretation. The goal reflects the intended application of the product, whereas the scope reflects, amongst others, the product system to be studied and requires the definition of a *functional unit*. The functional unit defines the performance characteristics of the product. The inventory analysis aggregates all input and output related to the product, either in terms of materials, energy or emissions. The impact assessment aggregates the impact of the inventory for certain environmental impacts categories. The interpretation phase considers the results of the impact assessment and leads to conclusions about the relative environmental effects that are aligned with the definition of the goal and scope. The requirements and guidelines to carry out LCAs in line with the general principles and framework are laid down in ISO 14044 [72].

Construction works assessment information																	
Construction works life cycle information																Supplementary information beyond construction works life cycle	
Product stage			Construction process stage		Use stage							End of life stage				Benefits and loads beyond the system boundary	
A1	A2	A3	A4	A5	B1	B2	B3	B4	B6	B7	B8	C1	C2	C3	C4	D	
Raw material supply	Transport	Manufacturing	Transport	Construction installation process	Use stage	Maintenance	Repair	Replacement	Refurbishment	Replacement	Refurbishment	Deconstruction Demolition	Transport	Waste processing	Disposal	Reuse, recovery and/or recycling potential	

(Stage / Module / Description row labels on left.)

Figure 2.6 | Modules for the life cycle assessment of construction works (drawn after EN 15804 [74]).

The environmental impacts of buildings can be quantified using EN 15978 [73], which is based on the LCA approach defined in ISO 14040 [71] and ISO 14044 [72]. The functional unit of a building must reflect (i) the building type, (ii) its relevant technical and functional requirements, (iii) its pattern of use and (iv) its required service life. The building is separated into (i) its constituent parts, (ii) related processes (e.g. transport, construction) and (iii) its operational use, to distinguish between the different phases during the service life. These phases of impact are also referred to as *modules* and are extensively defined in EN 15804 [74]. An overview of the modules is given in Figure 2.6: here modules A-C reflect the different stages during the lifetime of the building, whereas module D accounts for any benefits outside the system boundary. The environmental impact categories for buildings include global warming potential (GWP), depletion potential of the stratospheric ozone layer (ODP), acidification potential of land and water (AP), eutrophication potential (EP), formation potential of tropospheric ozone photochemical oxidants (POCP), abiotic resource depletion for elements (ADPE) and abiotic depletion potential of fossil fuels (ADPF). There is no scientific basis to aggregate the impact of each category [72], although this is sometimes

done in monetary units, known as the environmental cost indicator (ECI), to compute the *shadow price* of a building or product.

A recent study by Brambilla et al. [75] investigated the environmental advantages of demountable compared to traditional composite floor systems based on LCA. This was done for a case study building with a typical layout of a four storey office building of 13.5 m wide and 48 m long, and considered only the frame superstructure (steel columns and the composite floor system). Three steel-concrete composite floor systems were considered:

1. A reusable composite floor system with friction-type demountable shear connectors;

2. A composite slab composite floor system with profiled sheeting and welded headed studs;

3. Precast hollow core slabs where composite interaction is achieved by welded headed studs and cast in-situ concrete.

In a previous publication [76], Brambilla verified the structural resistance of all three alternatives to enable a fair comparison. The reusable alternative was considered to be entirely disassembled after 50 years and reused elsewhere for an additional 50 year period. The non-reusable, traditional alternatives are assumed to be demolished after 50 years and to be replaced by a completely new floor system which should last for an additional 50 years. Therefore, in all cases, the reference service life is 100 years. The analysis was carried out in accordance with ISO 14040 [71], ISO 14044 [72], EN 15804 [74] and EN 15978 [73]. It was concluded that the demountable and reusable floor system led to the most favourable scoring for all impact categories, except the depletion potential of the stratospheric ozone layer (ODP) [75]. The ODP impact increased due to the longer operation of diesel-burning trucks and machinery during deconstruction and transport. Such effects could be mitigated by using more efficient or electric alternatives. The demountable alternative scored best in terms of all other impact categories because the majority of the impact occurred during the production stage. The benefits during the reference service life therefore arose due to the lack of a second production stage compared to the non-reusable, traditional alternatives. The reusable alternative was environmentally viable for transport distances up to 300-500 km, implying that reusable composite floor systems could be viable in densely populated regions. The relative contributions for steel and concrete to the impact during the production stage varied per impact category. For example, steel was responsible for approximately 60% of the the global warming potential, but only 10-15% for the abiotic depletion potential for fossil resources. In conclusion, the work of Brambilla [75] highlighted the environmental benefits of designing for reuse. Obviously, the relative environmental benefits could be further increased if the structure would be demounted and reused more frequently, e.g. every 10-20 years.

The reduced environmental impact due to the longer potential service life of demountable and reusable composite floor systems can be considered through the Estimated Service Life (ESL) method. The ESL approach is laid down in ISO 51686[4] [70], and is used to determine the ESL based on a reference service life (RSL) and actual in-use conditions, such as component quality, design level, execution level, indoor and outdoor environment, and maintenance conditions. The ESL is calculated as:

---

[4]this approach was first reported by the Architectural Institute of Japan [77]

$$T_{ESL} = T_{RSL} \cdot \varphi_A \cdot \varphi_B \cdot \varphi_C \cdot \varphi_D \cdot \varphi_E \cdot \varphi_F \cdot \varphi_G, \tag{2.1}$$

where $\varphi_{A...G}$ are factors relating to the aforementioned actual in-use conditions. Van den Dobbelsteen [78] noted that it is extremely complicated to determine the preceding factors for buildings as a whole, and suggested to define the ESL for buildings based on considerations related to the flexibility of the building, because this offers great opportunities to prevent obsolescence by allowing for other types of future use. Geraedts et al. [79] developed a determination method to quantify and promote the flexibility of structures that could be evaluated in terms of th ESL. However, Straub [80] reports that, based on a Dutch expert survey, objections to using the ESL method include:

i. It is doubtful whether the factors can be quantified: the flexibility may be best expressed qualitatively;

ii. The potential interdependence between the factors;

iii. The applicability of the method to describe building services.

Straub [80] thus recognised the potential benefits of the ESL method, but in an analytical instead of a mathematical way.

2.2. DEMOUNTABLE SHEAR CONNECTORS

2.2.1. HISTORY AND BENEFITS OF STEEL-CONCRETE INTERACTION

The beneficial effects of combining steel and concrete were first recognised in the late 19th century. In 1882, Melan [81] combined steel trusses and concrete to develop economically competitive arch bridges. However, the potential benefits of composite interaction between the two materials were not utilised until Von Emperer studied concrete columns reinforced with iron sections [82]. Von Emperer relied on friction and bonding to achieve beneficial interaction, but this which was later proven to be inadequate: a mechanical connection was necessary instead [83, 84].

The practical application of steel-concrete composite beams initiated in the 1930s [85] and was based on achieving composite interaction through mechanical shear connectors. In 1941, Maier-Leibnitz [86] proposed a design method for composite beams, well ahead of its inclusion in design codes in the 1970s [85]. Research and development of welded headed studs as shear connectors, a concept originating from the 1920s [87] and illustrated in Figure 2.7, matured in the 1940s and, in the 1950s [88] and 1960s [89], it became increasingly ready for implementation in engineering and construction practice. Viest [90] was the first to perform push-out tests for welded headed studs to obtain a relation between load and deformation, and found that three main failure modes may occur depending on the height to diameter ratio: (i) shear failure of the stud, (ii) concrete crushing and (iii) a combination of the two. Ample research on the static and cyclic response of welded headed studs followed, an extensive overview of experimental results and prediction models in the period 1956-2005 is presented in the work of Pallarés & Hajjar [91].

Research in the field of welded headed studs continues to present date, for example by Araujo et al. [92], Ding et al. [93], Ling et al. [94], Kruszeweski et al. [95], Molkens et al. [96] and others [97–100]. However, welded headed studs cannot be demounted because of

2

the permanent connection between the steel and concrete: therefore an obvious contradiction exists between the characteristics of welded studs and the need for more sustainable structural systems that was identified in Section 2.1.

2.2.2. DEMOUNTABLE ALTERNATIVES TO WELDED HEADED STUDS

Welded headed studs are inherently non-demountable, and therefore the steel and concrete can only be separated by demolition. The transition to a more sustainable construction sector calls for development of demountable shear connector systems to enable the non-destructive separation of the structural elements. This section discusses available demountable alternatives to welded headed studs, based on which a novel demountable shear connector is synthesised that addressed all desired characteristics.

BOLTED HEADED STUDS

One of the most obvious technical solutions is to replace the welded headed stud by a *bolted* headed stud, protruding through the flange and secured by a nut, see Figure 2.7. The bolted headed stud may be a modified (threaded) headed stud or a standard bolt and may or may not extend beyond the top facing of the concrete. The behaviour of bolted headed studs is, amongst others, described by Dallam [101], Marshall et al. [102], Hawkins [103], Pavlovic et al. [104], Lam et al. [105–108] and Ataei et al. [109–112]. The comparatively lower shear connector stiffness cause bolted headed studs to be inferior to welded headed studs [108, 113], because the beneficial effects of composite interaction in a composite beam depends (amongst others) on the connector stiffness.

The connection stiffness of the bolted headed stud was improved by using one or more embedded nuts [100, 104, 114–117], see Figure 2.7, to mitigate the rotation of the bolt in the hole. However, the stiffness was still lower compared to the welded headed stud, which was attributed to the tolerances, causing an uneven load distribution among the specimen's fasteners. The bolt may be preloaded to mitigate the reduced initial stiffness, however the friction resistance is overcome at relatively small load levels [115, 117, 118], rendering the shear connection largely ineffective. This type of shear connection is also known as "Full-Zero-Full" because of the initially stiff behaviour, followed by a plateau on the load-slip curve because the friction resistance is overcome, after which the load again increases as the connector starts against to bear against the bolt hole.

Depending on the design of the connector, part of the connector permanently protrudes from the concrete element and is thus vulnerable to damage during execution and storage. Kozma et al. [119] developed a through-bolted shear connector based on the original design by Marshall et al. [102] that does not exhibit the aforementioned risk, and which uses a cast-in steel cylinder to prevent the pretension loss due to through-thickness concrete creep. The latter was not sufficiently addressed in prior research: for example, Chen et al. [120] used a PVC cylinder instead.

Marshall et al. [102] were the first to test bolted headed studs in beam tests. Later work includes that of Moynihan & Allwood [121], who successfully demounted and reassembled their specimens. Kozma [122] presented the results of push-out and beam tests for a through-bolt system with cast-in steel cylinders, and proved the demountability of the composite floor system. Therefore the bolted shear connector is proven to be practically useful for demountable composite floor systems, although the mechanical behaviour of this type of connector is not as good as that of welded headed studs.
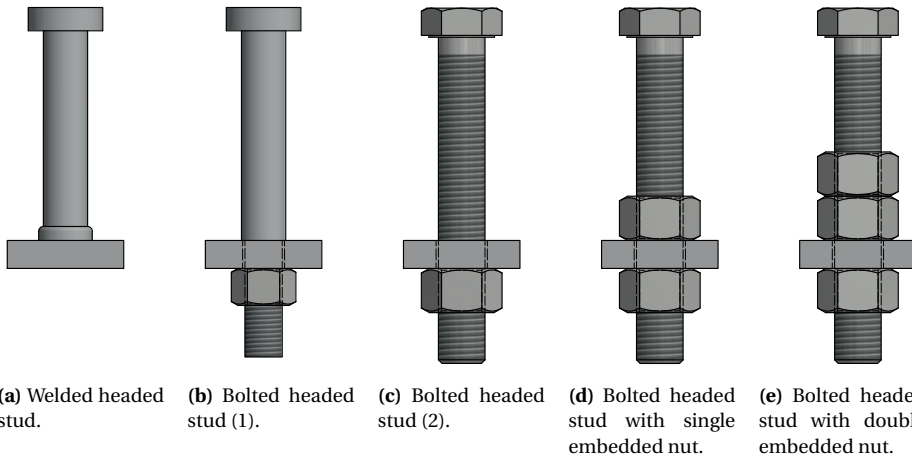
2

(a) Welded headed stud.

(b) Bolted headed stud (1).

(c) Bolted headed stud (2).

(d) Bolted headed stud with single embedded nut.

(e) Bolted headed stud with double embedded nut.

Figure 2.7 | Welded and bolted headed studs.

BLIND BOLTS

Blind bolts are generally used as shear connectors to strengthen and rehabilitate existing (composite) structures and require access from (only) one side. This type of shear connector is installed after hardening of the concrete, and is therefore inherently demountable. The blind bolts can be installed from the top by removing part of the concrete and drilling a hole in the flange, or vice versa from below. It should be noted that the connection can generally not be considered as demountable if the connector is installed from the top, due to the subsequent grouting necessary to ensure contact between the connector and the remainder of the concrete floor system.

Mirza et al. [123] and Pathirana et al. [124] performed experimental and numerical studies on two types of post-installed shear connectors, see Figure 2.8a-b, and it was concluded that the connector stiffness was substantially lower compared to welded headed studs [124]. Uy et al. [125] numerically investigated a shear connector design similar as in Figure 2.8b, which also demonstrated low shear connector stiffness. A similar finding was reported for adhesive anchors, see Figure 2.8c, by Kwon et al. [115], who attribute the reduced stiffness to the lack of a significant pretension force. In addition, Kwon et al. [100] investigated three more types of (adhesive) anchors with minor design changes compared to Figure 2.8c.

In another publication, Pathirana et al. [126] present the results of experimental and numerical beam tests using their blind bolt connectors, and conclude that demountability was possible until 40% of the ultimate resistance. Blind bolts were also applied as shear connectors in composite beam-column connections, for example by by Loh et al. [127], Wang et al. [128] and Mirza & Uy [129], and in steel-to-FRP connections [130].

It should be noted that, in principle, all types of shear connectors could be used to strengthen and rehabilitate existing structures. A large number of combinations of connector components can be made to form new post-installed shear connectors that can be installed from one side only. However, with respect to demountability, only blind-bolt connector systems installed from below are considered useful. From this perspective, blind

2

bolts are considered to be suitable only for rehabilitation work of composite beams where alternatives with better mechanical properties cannot be applied.

FRICTION-BASED SHEAR CONNECTOR / LOCKING NUT SHEAR CONNECTOR

Suwaed & Karavasilis developed two types of demountable shear connectors, the Friction-Based Shear Connector (FBSC) [131] and the Locking Nut Shear Connector (LNSC) [132]. Their designations already indicate the difference between the shear connector systems: the former transfers the load by friction, whereas the latter transfers the load mechanically through bearing of a (conical) nut. Both alternatives are nearly identical in terms of their physical appearance, see Figure 2.9.

Both systems consist of a high-strength steel rod with a relatively short threaded length. The upper part of the bolt hole is a countersunk seat (hole), where either a conical nut (LNSC) or retaining washer (FBSC) is installed, the function of the latter is to prevent the bolt from falling. The prefabricated concrete slab consist of *pockets*: countersunk slotted holes with an inclination of approximately 5°, in which (smaller) inverted conical precast concrete plugs are placed. The clearance between the pocket and plug is used to account for geometrical and dimensional tolerances, and is later grouted to enable interaction between both parts by bearing. The steel rod passes through the (i) plugs, (ii) the conical nut (LNSC) or retaining washer (FBSC) and (iii) the beam flange, and is secured on both sides by nuts. The FBSC is pretensioned by turning one of the nuts, enabling shear force transfer at the steel-concrete interface.

Both shear connector systems are reported as superior to welded and bolted headed studs in terms of their mechanical performance (stiffness, resistance, and ductility), as proven both by push-out tests [131, 132] and beam tests [133] (here only FBSC was considered). However, a major downside of both systems is the need for grouting: although the structural components can be demounted, their reuse is impaired because the shear connector system cannot accommodate any deviations in the second life cycle without mechanically separating the plug from the pocket. Therefore these shear connector systems are considered to enable swift execution (due to the large clearances) in the first life cycle, but are not considered to be suitable for reuse of the structural components.

PRETENSIONED CHANNEL CONNECTOR

Another example of a pretensioned connector with a distinctly different design compared to bolted/welded headed studs is presented by Wang et al. [134, 135], and consists of precast concrete elements with cast-in T-shaped channels perpendicular to the steel beam span. Clamps and bolts connect the cast-in channels to the beam flange and transfer the external load by friction, see Figure 2.10. The benefit of this system is that no bolt holes are necessary for the load transfer, reducing the sensitivity of the connection to geometrical and dimensional deviations. Both push-out tests and beam tests were conducted with this connector type. The push-out tests demonstrated that only 60% of the nominal shear resistance of the bolt could be transferred by friction, and that no subsequent increase of the load was possible because the movement of the bolt was not physically restrained by a bolt hole. This suggests that the guaranteed ability to install the connector is counteracting the mechanical performance.
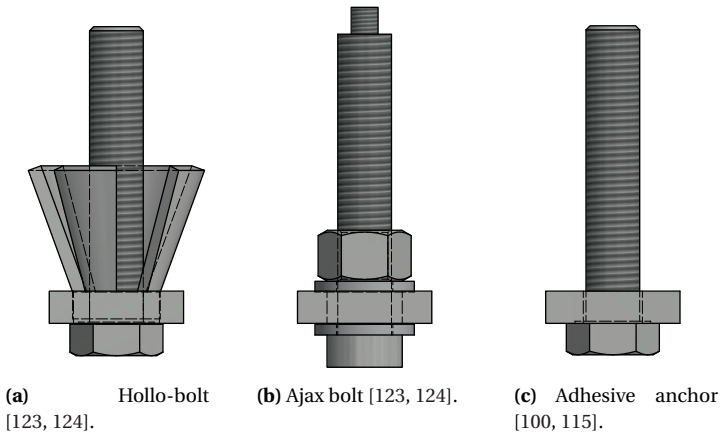
(a) Hollo-bolt [123, 124]. **(b)** Ajax bolt [123, 124]. **(c)** Adhesive anchor [100, 115].

Figure 2.8 | Blind bolts as post-installed shear connectors.

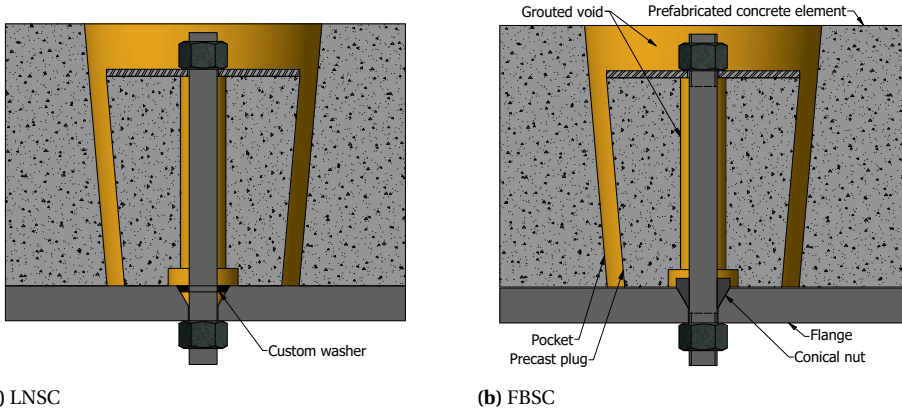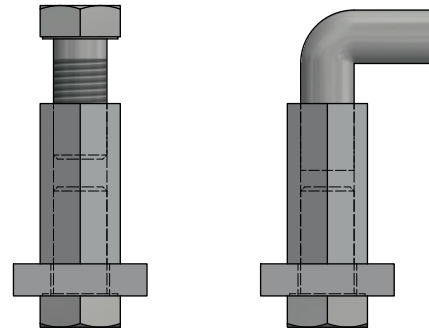**(a)** LNSC   **(b)** FBSC

Figure 2.9 | Friction-Based Shear Connector (FBSC) [131] and Locking Nut Shear Connector (LNSC) [132].

2

Figure 2.10 | Pretensioned channel connector [134, 135].

(a) With embedded bolt [119, 122, 136].

(b) With embedded reinforcement bar [137].

Figure 2.11 | Embedded coupler systems.

EMBEDDED COUPLER SHEAR CONNECTOR

Yang et al. [136], Milosavljevic et al. [137] and Kozma et al. [119, 122] (in consultation with present work) performed push-out tests on embedded coupler shear connectors. This type of shear connector consists of a steel coupler embedded in a prefabricated concrete element, anchored by an embedded bolt [119, 122, 136, see Figure 2.11a] or a reinforcement bar [137, see Figure 2.11b]. The connection between the steel beam and the concrete element is achieved by installing an external bolt in the coupler, see Figure 2.11. The external access to this bolt enables its replacement, and its absence during execution and storage prevents any damage because no components protrude from the concrete element.

The external bolt can be non-pretensioned [136, 137] or pretensioned [119, 122], and influences the response of the connector because of the inherent nominal hole clearances. However, the friction resistance is overcome at relatively small load levels (approximately at 30% of the short-term resistance [119, 122]), and therefore no significantly different shear connector behaviour (particularly in terms of secant stiffness) could be expected compared to non-pretensioned connections once this threshold force is overcome.

2.2.3. PROPOSED DESIGN OF DEMOUNTABLE SHEAR CONNECTOR

The shear connectors presented in Section 2.2.2 are all demountable in a technical sense, but do not necessarily answer to the prerequisites for demountable composite floor systems. The most relevant prerequisites for the demountability and reusability according to Sassi [54] (see p. 14 for the complete list) include:

i. The ease and safety of the access to building elements and their connections with minimal machinery requirements;

ii. Simple connection systems that enable removal by hand tools and that account for realistic tolerances for assembly and disassembly;

iii. Components and connections should be able to withstand risks associated to the (dis)assembly process and to withstand repeated use.

Each of the identified demountable shear connectors could suitably address point (i) and could also facilitate removal by hand tools. However, only the FBSC/LNSC and the pretensioned channel connector provide the ability to account for realistic tolerances for assembly and disassembly. However, these connectors may not be suitable for repeated use because of the degradation of the contact surfaces due to shear force transfer by friction and due to surface damage during transportation and execution. Similar risks exists for connectors where parts of non-replaceable components permanently protrude from the concrete elements. Therefore none of the identified shear connectors address all of the prerequisites (i)-(iii).

The non-pretensioned embedded coupler shear connector system is considered as most favourable in terms of minimal risks of potential damage because (i) all components are internal and (ii) because no major rework is necessary to make the floor elements suitable for reuse (as opposed to the FBSC/LNSC systems). However, in their present form, the expected beneficial effects due to shear interaction are small (due to the nominal hole clearances reducing the connector stiffness) and are expected to be even lower when larger nominal hole clearances are used to account for realistic tolerances for assembly and disassembly.

A technical solution exists which could solve the seemingly contradictory requirement between the need for large nominal hole clearances during execution, and the need for composite interaction during the service life. The solution is to use oversized holes during execution, and to subsequently inject the bolt-to-hole clearance with an epoxy resin system through the head of the external bolt. This type of connection is also known as an *injected bolted connection*. An overview of the proposed resin-injected demountable shear connector is presented in Figure 2.12. A stiff and load-bearing connection is obtained once the epoxy resin system hardens, despite of the initial nominal hole clearance - the magnitude of which is only limited by practical considerations. The connector can be demounted by
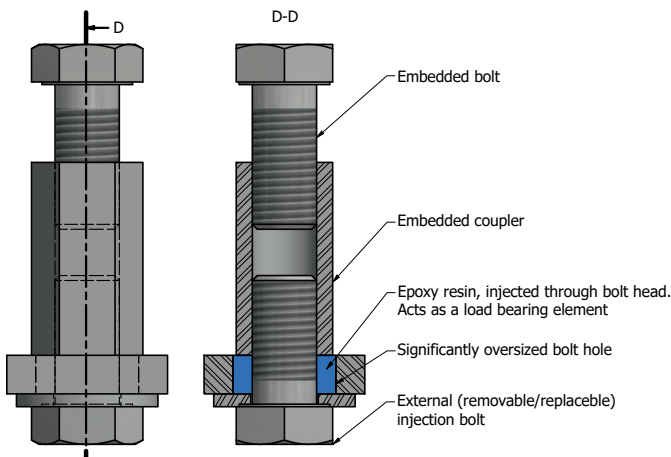

Figure 2.12 | Proposed demountable shear connector system, based on the embedded coupler system, but with an injection bolt in a significantly oversized bolt hole to accommodate large execution tolerances. After hardening, the epoxy resin acts as a stiff load-bearing element.

unscrewing the external bolt. The epoxy resin can be easily removed from the bolt hole by hand and disposed of. This proposed system therefore does not propagate any damage to the injectant during the full technical lifetime of the structural components of the composite floor system: new epoxy resin is injected in each subsequent life cycle.

The history, development and behaviour of injected bolted connections is discussed in Section 2.3. The proposed resin-injected demountable shear connector is at the heart of this dissertation, and is subjected to short- and long-term push-out tests in Part II to derive the relation between applied load and slip. Experiments on the injection material are conducted in Part I, and the proposed connector is applied an experimental composite floor system in Part III.

2.3. INJECTED BOLTED CONNECTIONS

2.3.1. INTRODUCTION AND GENERALITIES

The demountable shear connector proposed in Section 2.2.3 uses injection bolts to establish shear interaction despite inherent nominal hole clearances. The principle of the injection bolts was invented in the 1970s to extend the service lifetime of railway bridges with deteriorated riveted connections. Replacing the old rivets by new ones was considered infeasible because the riveting process was no longer common practice. Substituting the rivets by bolts was only permitted in case these were pretensioned, because conventional bolts were (and are) not allowed to be used for connections subject to reversed cyclic loading. However, the use of pretensioned connections was considered to be impractical because the actual condition of the faying surfaces (coefficient of friction) is generally unknown and could locally vary, for instance due to corrosion. Fitted bolts were considered impractical because of the considerable in-situ work and the associated delays and costs of the refurbishment.

Rivets and pretensioned and fitted bolts are considered as slip-resistant, meaning that the slip (relative displacement between connected elements) during the service lifetime does not exceed a nominal threshold value, e.g. 0.30 mm [138]. The challenge therefore was to find an alternative connection type that (i) does not rely on friction, (ii) is slip-resistant and (iii) limits the required in-situ labour.

The solution to this quest was the injection bolt, which is mostly a conventional bolted connection, with the exception that the bolt-hole clearance is injected with an epoxy resin, a process that takes 1-2 minutes [139, 140]. The injection is enabled by a hole in the bolt head and special washers, all standardised in EN 1090-2 [138], although improved designs for the washer under the bolt head are presented by Qureshi & Mottram [141] to improve the injectability of high-viscosity epoxy resins. A cross-section of an injected bolted connection is shown in Figure 2.13. After curing, the epoxy resin acts as a load bearing element, which has a substantially higher resistance than its uniaxial compression strength due to the natural confinement provided by the bolt hole. Obviously, the behaviour of injected bolted connections is not as good as that of fitted bolts, as demonstrated by Carvalho [142]. However, the application of injection bolts must be put into perspective: injection bolts provide a more *competitive* and *practical* solution than fitted bolts.

The remainder of this introductory section focuses on general aspects of injected bolted connections, and their mechanical behaviour under sustained and cyclic loads is discussed in Section 2.3.2 and 2.3.3, respectively.
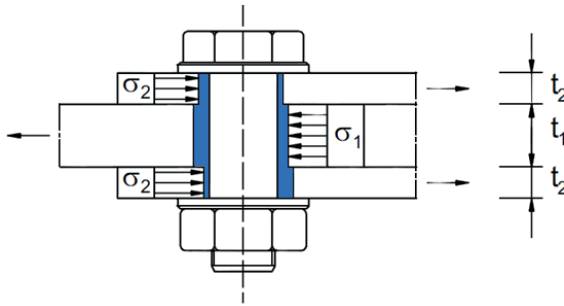
Figure 2.13 | Double lap injected bolted shear connection [138], the epoxy resin is shown in blue.

TOOLS AND DISPOSABLES REQUIRED FOR EXECUTION
Injected bolted connections require few additional tools compared to normal bolted con-
nections. Only a manual, electric or pneumatic injection gun is necessary to inject the
epoxy resin into the bolt hole cavity. Leakage of resin within the plate package is prevented
by tightening the bolts to 30-100 Nm to close any gaps between adjacent surfaces. This
comparatively small torque can be generated by using a normal wrench. Off-the-shelf dis-
posable injection nozzles and tubes can be used in the injection process and, after curing,
can be disposed of as regular waste.

ADVANTAGES, DISADVANTAGES AND APPLICATIONS OF INJECTED BOLTED CONNECTIONS
A key benefit of injected bolted connections compared to pretensioned connections is that
no sudden slip can occur because the movement of the bolt is physically restrained by the
hardened injectant [139, 143]. This advantage has led to the application of pretensioned in-
jected bolted connections in critical applications, for example in the Maeslant Storm Surge
Barrier. This type of connection transfers the load initially by friction and the epoxy resin
partakes in the load transfer once the friction resistance is overcome. Further applications
of injected bolted connections include [139] crane girders, towers for wind turbines, sta-
dium roofs, highway bridges, glass roofs [143, 144], aluminium helicopter decks and FRP-
to-FRP double lap shear connections [141, 145].

Another advantage of injected bolted connections is that the bolt hole is protected against
corrosion by the epoxy resin [140]. A potential disadvantage is the lead time for modified
washers and bolts, which are typically not stock-items but are modified upon order. How-
ever, this is strictly speaking a matter of demand and supply: widespread use of injection
bolts could eliminate this current disadvantage. A second potential disadvantage is that
the quality of the connection depends on the weather conditions, although Bouwman &
Kluwen [146] have shown that no difference in quality of connections injected with epoxy
resin system Araldite SW404 + HY404 should be expected if the injection takes place one day
after it has last rained. In addition, Koper [147] experimentally demonstrated that the curing
temperature (in the range 8-24°C) does not have a significant effect for this epoxy resin sys-
tem either. A third challenge is to make an injected bolted connection that is demountable,
one of the key selling points for steel structures with bolted connections. This prerequisite
implies that the resin should not adhere to the connection components. Smits & Bouw-
man [148] used separating liquids for this purpose, but later Nijgh [149] demonstrated that
liquids should be avoided and that wax-based release sprays provide the demountability

2

potential without detrimental effects on the connection behaviour. Kortis [150] demonstrated that if rivets and injection bolts are combined in a connection, particular attention is required to the quality of the injection to guarantee a uniform transfer of the load among the fasteners, although the injection quality should be adequate if the prescribed standardised special washers under the nut are used [138] and if the formation of large air voids is adequately prevented [149].

EPOXY RESIN SYSTEMS

All two-component epoxy resins complying to the conditions in EN 1090-2 [138] may be used in injected bolted connections. These conditions relate to the viscosity of the epoxy resin (its ability to fill all cavities), its thixotropic behaviour (it should not flow once the injection pressure is removed) and its pot time (at least 15 minutes to ensure workability). Several epoxy resin systems are considered in literature, for example Araldite CW 214 + XB 2571 [146], Araldite GY 250 + XB 2571 [146], Araldite SW 404 + HY 404 (and its successor RenGel SW 404 + HY 2404/5159) [e.g. in 145–147], Sikadur 30 [e.g. in 145, 147, 151], Sikadur 33 [152], Sikadur 52 [153], Sika AnchorFix [152], Sika Injection-451 [147], Edilon Dex R2K [147] and Edilon Dex G20 [147]. Experiments revealed that the viscosity of the epoxy resins was typically too high (Sikadur 30) or too low (Araldite CW 214/GY 250 + XB 2571 and Sika Injection-451). In other acases the experimental scatter in connection tests was considerable (Edilon Dex R2K) or the connection slip was substantially higher compared to other injectants (Edilon Dex G20). For example, Zafari et al. [145] studied FRP injected bolted connections and found that Sikadur 30 leads to 65% larger connection slip than RenGel SW 404 + HY 2404/5159. Good workability and mechanical properties were reported for RenGel SW 404 + HY 2404/5159: this epoxy resin system is the only system certified for use in projects for the Dutch Ministry of Infrastructure and Water Management [154] and has been continuously considered in experimental research since the inception of injected bolted connections in the 1970s.

Nijgh [149, 155] developed *steel-reinforced* epoxy resin (SRR), consisting of spherical steel particles in an epoxy resin matrix, see Figure 2.14. The volume fraction of the steel particles is approximately 60%. The double lap shear connections with steel-reinforced resin in large oversized holes (bolt diameter + 12 mm) exhibited a larger instantaneous stiffness (+71%) and smaller time-dependent deformations (38%) compared to resin-injected specimens. This finding suggests that steel-reinforced resin offers the opportunity to greatly reduce slip, or to enable the use of (larger) oversized holes without compromising on the stiffness of the connection.

2.3.2. CREEP

The relative displacement between the connected elements (slip) increases over time due to the time-dependent behaviour of the epoxy resin injectants. The nominal bearing strength of the epoxy resin, denoted by $f_{\mathrm{b,resin}}$, is defined by EN 1090-2 [138] as the nominal bearing stress that leads to 0.30 mm cumulative connection slip after 50 years. This is the same criterion used for pretensioned connections, and extrapolation on the slip-time curve on linear-logarithmic axes is permitted to estimate the slip after 50 years [138]. The background of the maximum slip criterion is not well documented; its arbitrariness is exemplified by the RCSC specification [156], which in contrast to EN 1090-2 [138] does not limit the total connection
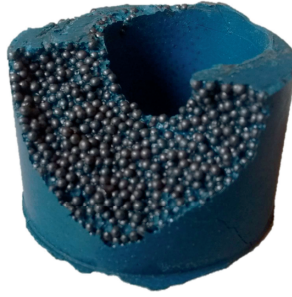
Figure 2.14 | Steel-reinforced epoxy resin: a polymer matrix containing spherical steel particles [149].

slip, but limits the slip increase between t = 0.5 h and t = 1000 h to 0.005" (0.127 mm) for pretensioned connections.

EN 1090-2 [138] and EN 1993-1-8 [157] focus on double lap resin-injected bolted shear connections, consisting of a centre plate with thickness t_1 and two cover plates with thickness t_2, see Figure 2.13. This type of connection is considered as slip resistant if

$$F_{b,Rd,resin} = \frac{k_t k_s \beta d\, t_{b,resin} f_{b,resin}}{\gamma_{M,4}} \geq F_{Ed}, \tag{2.2}$$

where d represents the bolt diameter, k_t is a constant depending on the limit state, k_s accounts for increased nominal hole clearances, and β and $t_{b,resin}$ describe the effect of the plate thicknesses t_1 and t_2 in accordance with Table 2.3. The resistance of injected bolted connections decreases by 10% for every mm the holes are oversized, following the relation $k_s = 1 - 0.1m$. This is a simplified expression based on a limited number of tests with limited variations in the magnitude of the oversized holes [140], and is based on the assumption that the holes in both the centre and cover plates are oversized. Based on experiments the magnitude of $f_{b,resin}$ can be determined for a specific epoxy resin system.

It should be noted that $f_{b,resin} \propto F/d\, t_{b,resin}$ is a nominal, averaged measure, that facilitates practical implementation in design, and does not reflect the actual bearing stress distribution, which is in the form [149]

$$\sigma_{b,resin}(\theta) = \frac{4}{\pi} \frac{F}{d\, t} \cos(\theta)^2, \tag{2.3}$$

where $-\pi/2 \leq \theta \leq \pi/2$ is the angle between the line perpendicular to a point on the hole edge with respect to the direction of the force.

Table 2.3 | Magnitudes of β and $t_{b,resin}$ according to EN 1993-1-8 [157].

t_1 / t_2 (-)	β (-)	$t_{b,resin}$ [L]
≥ 2	1	$\min(2t_2, 1.5d)$
$1 < t_1 / t_2 < 2$	$1.66 - 0.33\, t_1 / t_2$	$\min(t_1, 1.5d)$
≤ 1	1.33	$\min(t_1, 1.5d)$

2

NOMINAL BEARING STRENGTH

Bouwman [158] was the first to quantify the nominal bearing strength $f_{b,resin}$ for epoxy resin system Araldit SW 404 + HY 404, the predecessor of the current epoxy resin system RenGel SW404 + HY2404/5159. Double-lap shear connections consisting of mild steel plates with various plate thickness ratios (t_1/t_2) and grade 10.9 M20 bolts were studied. The bolts were positioned in their normal clearance hole such that the potential connection slip was maximised. The current EN 1993-1-8 design rules for injected bolted connections are to a large extent based on these tests. Bouwman [158] suggested that $f_{b,resin} = 150$ MPa for $t_1 \geq 2t_2$, increasing to $f_{b,resin} = 200$ MPa for $t_1 \leq t_2$.

In 1996, injection bolts were applied during the renovation of a steel bridge (1934) in Oranienburg, Germany. The authorities requested verification that the maximum slip criterion would not be violated at the nominal design bearing stress $f_{b,resin,d} = 150$ MPa. Gresnigt et al. [159] fabricated three specimens (A, B, and C) with characteristics identical to those in the existing steel bridge ($t_1 = 20$ mm $= 2t_2$) and subjected these to sustained loads for a period of four years, with the bolts (M24) in the most unfavourable positions in their normal clearance holes. It was concluded that a nominal design bearing stress of 150 MPa would not violate the EN 1090-2 [138] slip criterion, and that the nominal bearing strength could be raised to 175 - 200 MPa. It was noted that the circumstances in practice were generally more favourable than in the laboratory, because in practice the position of the bolts their holes was more at random and the sustained load was not constantly at the level of the design load.

The experiments of Gresnigt et al. [159] continued for an additional four years, the results obtained in this period remained unpublished. Figure 2.15 illustrates the development of the slip over the full eight years during which the specimens were subject to a sustained load. Although the data acquisition rate was low, the results obtained over this extended time period provide an indication that the slip can be represented by a straight line on a linear-logarithmic plot. This observation supports the EN 1090-2 [138] assumption the slip after 50 years can be approximated by extrapolation on a linear-logarithmic slip-time diagram. Companion experiments [159] at elevated temperature (70°C) indicated that the deformations increased by approximately 25% compared to ambient temperature.

Additional research to determine $f_{b,resin}$ for RenGel SW404 + HY2404/5159 was performed by Gresnigt & Beg [143] to prove the suitability of injected bolted connections to connect glass roof panels of the Amsterdam central bus station. Two sets of standardised EN 1090-2 [138] specimens ($t_1 = 2t_2$) were considered: one set with bolts at random positions in the bolt holes and one set with bolts in the most unfavourable position with respect to the potential connection slip (as prescribed). For the latter it was found that $f_{b,resin} = 170$ MPa, which is 13% larger than the value reported by Gresnigt et al. [159]. For a random disposition of the fasteners, the nominal bearing strength increased to 200 MPa.

2.3.3. FATIGUE

Injection bolts may be subject to cyclic loading and therefore the fatigue of the injected bolted connection is an important aspect. According to EN 1993-1-9 [160] the fatigue resistance of injected bolted connections is equal to that of a connection with fitted bolts, but is reduced compared to pretensioned connections.

In relation to failure of the net section due to fatigue, the injected bolted connection can nominally withstand 2 million cycles at a nominal stress range of 90 MPa (detail category
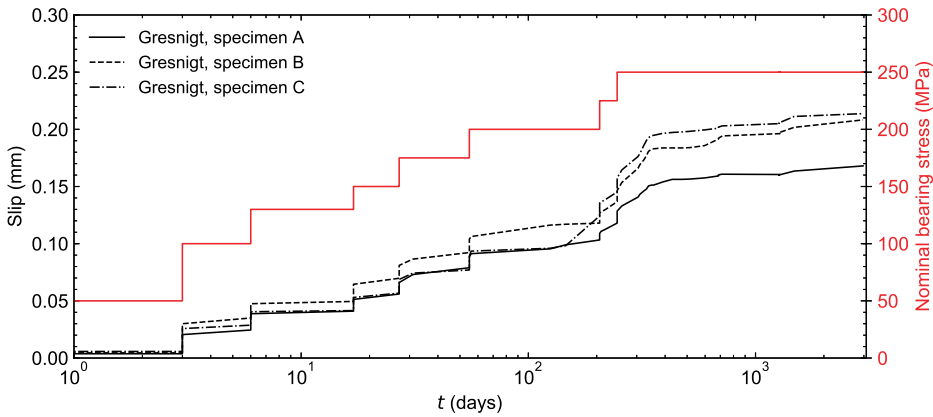
Figure 2.15 | Results of creep tests on resin-injected bolted connections (M24, $t_1 = 20$ mm $= 2t_2$) by Gresnigt et al. [159] over a period of eight years (2.9×10^3 days).

90), compared to 112 MPa for pretensioned connections [160]. For single lap shear connections this difference is smaller (detail category 80 vs. 90). Pretensioned injected bolted connections do not provide additional benefits compared to pretensioned connections for this failure mode. However, De Jesus et al. [151] reported a reduction in fatigue strength for single and double lap *pretensioned* injected bolted connections of puddle iron and structural steel, and hypothesised that this reduced resistance was due to the decreased contact pressure as a result of a more uniform bearing stress distribution through the epoxy resin layer compared to connections that were only pretensioned. Correia et al. [161] performed finite element analysis to obtain the stress intensity factor for the specimens of De Jesus et al. [151], and concluded that pretensioned injected bolted connections ought to improve the fatigue life in the crack initiation phase compared to pretensioned non-injected bolted connections. Further experiments by Pedrosa et al. [162] confirmed that the fatigue resistance of injected and non-injected pretensioned bolted connections is similar, and indicated that the location of the fracture surface moves from the gross to the net cross-section for increasing stress ranges. Van Wingerde et al. [163] studied non-pretensioned FRP double lap shear connections and concluded that the fatigue endurance in case of full load reversal is 100x larger for injected than non-injected bolted connections, although the FRP-dominated failure mode does not enable generalisation of this conclusion to steel-to-steel connections.

A second failure mode is the fatigue shear failure of the bolt. EN 1993-1-9 [160] prescribes that the threaded part of the bolt may not be at the level of the shear plane. If this condition is fulfilled, the detail category is 100, regardless if the connection is injected or not. However, the more uniform bearing stress distribution for injected bolted connections leads to the hypothesis of a favourable effect on the shear fatigue strength, although no literature is available to confirm or reject this hypothesis.

A third failure mode is the accumulation of excessive slip, although this is mostly a nominal failure mode. Gresnig & Beg [143] carried out fatigue tests on steel double lap injected bolted connections, and reported that the slip stabilised after 10-20 cycles. Their finding is in contrast with that of Zafari et al. [145], who report stabilisation of the slip after 300

2

000 cycles for FRP double lap injected bolted connections. This discrepancy could either be due to the difference in load application (displacement- and force controlled, respectively) or due to accumulating deformations in the FRP. Roupakas [164] reported stabilisation between 100 000 - 200 000 cycles for an injected tailor-made setup representing a steel-to-steel connection. However, companion cyclic confined compression material tests on this epoxy resins system by Buecking [165] demonstrated that stabilisation of the response occurred at a comparatively smaller number of cycles (< 10 000). Therefore further research is necessary to separate the influence of the epoxy resin and the influence of the test setup to understand cyclic slip accumulation.

2.4. Mechanical behaviour of injectants in IBCs

All two-component (epoxy) resins complying to the conditions in EN 1090-2 [138] may be used in injected bolted connections (IBCs). These conditions relate to the viscosity of the epoxy resin (its ability to fill all cavities), its thixotropic behaviour (it should not flow once the injection pressure is removed) and its pot time (at least 15 minutes to ensure workability).

The majority of the research on injected bolted connections focuses on their global behaviour, and the mechanical properties of the injectant are then fitted (e.g. in terms of the nominal bearing strength $f_{b,resin}$) to match the experimental connection response. The results of this type of research were shown in Sections 2.3.2 and 2.3.3.

A more fundamental approach requires the determination of the injectant's properties based on material tests, which can be used to predict the connection behaviour. Only Carvalho [142] performed compression tests on epoxy resin system Sikadur 30 and implemented a material model in commercial finite element software to analyse the short-term behaviour of injected bolted connections. Wedekamper [166] determined the compressive, tensile and shear properties of the (for IBCs) popular epoxy resin system Araldite SW 404 + HY404, but did not apply his findings to a specific application.

To describe the short-term and long-term behaviour of IBCs, it is necessary to have (time-dependent) data regarding the response of the (epoxy) resin system. Particularly relevant is the material response when subject to multiaxial compression: this stress-state originates from the (compressive) bearing stress and the natural confinement generated by the typical design of IBCs.

In the following sections, the general features of epoxy resin systems are discussed and their behaviour when subjected to short- and long-term compression is discussed. In addition, strategies to obtain the response of polymer matrix composites, such as steel-reinforced resin (introduced in Section 2.3.1), are reviewed.

2.4.1. Epoxy resin systems

Epoxy resins were first discovered by Prileschajew in 1909, while their commercial application initiated at the end of the 1940s [167]. They belong to the broader family of polymers, and consist of reactive prepolymers and polymers containing epoxide groups. Polymers, literally *many parts*, are macromolecules consisting of many smaller polymerised monomers. Two-component epoxy resins require hardeners to establish three-dimensional cross-linking of the polymer chains (see Figure 2.16), also known as curing, which leads to a solid thermoset polymer. The stiffness and resistance increase with increased degrees of cross-linking due to the comparatively more rigid material structure [168]. A more general

metric for the performance of an epoxy resin is the *glass transition temperature*, denoted by T_g, which is the temperature at which the polymer starts to exhibit viscous or rubbery instead of solid-like (glassy) behaviour. In addition to the degree of cross-linking, T_g depends on the composition of the resin molecules, the polar nature of the resin molecule's functional groups, the curing agent, and the curing conditions [169]. The glass transition temperature expresses the molecular mobility: higher values thus represent stiffer materials. Long polymeric chains contribute to the strength properties, but increase viscosity and thus decrease workability [170], as a result of *chain entanglement*, see Figure 2.16. The multitude of possible combinations of epoxy resins, hardeners and fillers enable a tailor-made solution for many types of applications.

VISCOELASTICITY

Polymers are viscoelastic materials, which are characterised by instantaneous and time-dependent contributions to the stress-strain response, for example due to relaxation or creep. The latter is the flow of an apparently solid material under sustained external loads, and its magnitude depends on the material properties, the temperature, the level of the imposed stress and its duration. Time-dependent effects also cause the behaviour to be rate-dependent: lower loading speeds lead to larger deformations, whereas higher loading speeds inhibit smaller deformations.

The creep strain rate is maximum immediately after applying the external load, but decreases with time. This stage is commonly referred to as primary creep, and is followed by a secondary creep stage which is characterized by a quasi-constant strain rate. Specimens loaded in tension may undergo a tertiary creep phase, during which the strain rapidly increases with time as a result of necking.

Creep deformation in polymers originates from the initial entanglement of polymer chains and their untangling over time, occurring for three main reasons [172]. Firstly, an increase of the thermal energy leads to an increase in molecular mobility, reducing the positive effects of chain entanglement. Secondly, the molecular mobility increases in the direction of an applied stress due to a reduction of the number of chain entanglements compared to the initial state. Lastly, physical ageing decreases the molecular mobility for polymers below their glass transition temperature T_g because of the transition of the material towards thermodynamic equilibrium, leading to an increased resistance against deformation over time [173].
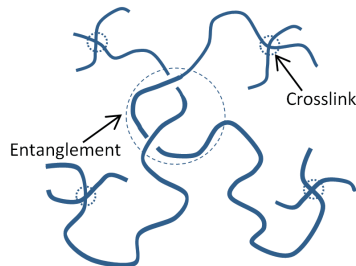

Figure 2.16 | Polymer chain entanglement and cross-linking, extracted from [171].

2

The ratio of total strain $\varepsilon(t)$ over the constant stress σ_0 is known as the *creep compliance*, expressed by

$$D(t) = \frac{\varepsilon(t)}{\sigma_0}. \tag{2.4}$$

The creep compliance $D(t)$ consists of an instantaneous and transient contribution, denoted by D_0 and $\Delta D(t)$, respectively.

LINEAR VISCOELASTICITY

In case of linear viscoelasticity, the stress is proportional to the total strain at each point in time, and every loading step can be linearly superimposed to describe the final deformation. This response can be generalised in the form

$$\varepsilon(t) = D_0\sigma + \int_0^t \Delta D(t-\tau)\frac{\mathrm{d}\sigma}{\mathrm{d}\tau}\mathrm{d}\tau, \tag{2.5}$$

which is known as the Boltzmann superposition integral, the Hereditary integral, or the Volterra integral, where τ accounts for the stress history of the material. This approach is only valid for relatively low stress levels: at increased stresses the viscoelastic behaviour becomes non-linear.

NON-LINEAR VISCOELASTICITY

The time, stress and temperature dependence of the creep strain $\varepsilon_{\mathrm{cr}} = \varepsilon(t) - \varepsilon(t=0)$ can be described in the form

$$\varepsilon_{\mathrm{cr}} = f(\sigma, t, T), \tag{2.6}$$

which is more generic than the formulation for linear viscoelasticity, and enables the opportunity to include non-linear stress, time and temperature dependencies. Penny & Marriott [174] defined the previous function in a more convenient, commutative form, given by

$$\varepsilon_{\mathrm{cr}} = f_1(\sigma)\, f_2(t)\, f_3(T) \tag{2.7}$$

and remarked that this separation of functions for stress and time is implicitly assumed in most creep models. Separating the influence of temperature, however, is considered less intuitive, and is sometimes included in combination with time [e.g. in 175].

The most elementary function $f_1(\sigma)$ is that of Norton [176], and is given by $f_1(\sigma) = K\sigma^m$, where K and m are a constant and a stress exponent, respectively. Other forms have been presented by Dorn [175] and Soderberg [177] (exponential function), McVetty [178] (hyberbolic sine function), Johnson, Henderson & Kahn [179] (summation of Norton functions) and Garofalo [180] (hyperbolic sine function with exponent). According to Garofalo [180], the function $f_1(\sigma) = K\sinh^m(\sigma/\sigma_0)$ is most convienient because it reduces to the Norton function for low stresses and to the exponential form for high stresses. In principle, all of the aforementioned functions may be fitted to experimental data, because their differences are typically negligible compared to the scatter in the experimental data [174].

The function $f_2(t)$ can typically be written in formats similar as the stress function $f_1(\sigma)$. A suitable function $f_2(t)$ uses one or multiple functions that describe the physical phenomena, although a more empirical and practical approach is to use a single (lumped) expression that accounts for all deformation mechanisms. The latter gives good results if the

material is subject to constant stress, but is not suitable to describe the response for variable stresses [174]. The two basic models to describe creep of materials subject to variable stresses are the time-hardening and strain-hardening models. For the former, the creep rate is expressed as

$$\frac{\mathrm{d}\varepsilon_{\mathrm{cr}}}{\mathrm{d}t} = f_1(\sigma)\frac{\mathrm{d}f_2(t)}{\mathrm{d}t}f_3(T),\tag{2.8}$$

for constant temperature, whereas the strain-hardening formulation is written in the form

$$\frac{\mathrm{d}\varepsilon_{\mathrm{cr}}}{\mathrm{d}t} = f_1(\sigma)f_2(\varepsilon_{\mathrm{c}})f_3(T).\tag{2.9}$$

The time-hardening formulation implies that only time-dependent changes of the material influence the creep rate, whereas strain-hardening implies effects of changes of the material structure (hardening) on the creep rate. Therefore the strain-hardening formulation is mostly suitable to describe primary creep, whereas secondary and tertiary creep are more suitable to be described by a time-hardening formulation [174]. A combined strain-time-hardening theory has also been put forward to approximate the combined effects [179, 181, 182], but none of these formulations account for creep recovery. An overview of more complex formulations is given by Penny & Marriott [174], who conclude that none of the available theories is fully satisfactory to describe the behaviour of materials subject to variable loading.

Dorn [175] observed a relation between the temperature and creep strain, which is represented by $f_3(T) = \exp(-Q/RT)$, where Q is the activation energy, R is the Boltzmann constant and T is the absolute temperature (in Kelvin). If the temperature variations are sufficiently small, the function $f_3(T)$ can be implicitly included in $f_1(\sigma)$ by specifying the material constants as a range [179].

Multi-axial stress states

The tensile and compression response of polymers differs significantly: the uniaxial strength and ductility in tension is typically smaller than in compression, which can be explained by the physical characteristics of the material. More importantly, this implies that the yield surface of polymers is pressure-dependent, and that the Von Mises yield criterion, given by

$$f(J_2) = \sqrt{J_2} - k = 0,\tag{2.10}$$

where k is the yield stress of the material in pure shear and J_2 is the second deviatoric stress invariant, is not applicable to epoxy resin systems. Pressure-dependency can be introduced by augmenting the previous equation with the first stress invariant $I_1 = \sigma_1 + \sigma_2 + \sigma_3$, where σ_i are the principal stresses. This results for example in the following yield criterion

$$f(I_1, J_2) = BI_1 + \sqrt{J_2} - k = 0,\tag{2.11}$$

which is known as the Drucker-Prager yield criterion and where B is an experimentally obtained constant.

Typically, creep tests are conducted on uniaxially loaded specimens, and the uniaxial response is used to predict the creep behaviour under multiaxial stress conditions. This requires the definition of an equivalent stress $\overline{\sigma}$, e.g. based on Von Mises for metals or Drucker-Prager for polymers.

2.4.2. POLYMER MATRIX COMPOSITES

Polymer matrix composites contain reinforcing fibres and/or particles to strengthen and stiffen the polymer (or epoxy resin) matrix. In fact, most epoxy resin systems could be classified as polymer matrix composites, simply because a substantial volume percentage consists of fillers. However, in the context of this dissertation, polymer matrix composites are considered to be materials that are not supplied as one product system by the supplier. An example central to this dissertation is that of steel-reinforced resin [149, 155], which consists of a polymer matrix and spherical steel particles, see Figure 2.14.

The properties of polymer matrix composites (PMCs) depend on the matrix (polymer), the reinforcing particles (e.g. steel, glass fibre) and the interface. The coarse-scale mechanical properties of PMCs can be determined by experimental research, but the results do not provide any explanations for the underlying mechanisms. Fine-scale modelling of PMCs enables the prediction of the homogenised coarse-scale material properties; after validation, the fine-scale model can be used generically for other combinations of materials as long as the underlying assumptions remain valid.

ANALYTICAL PREDICTION OF COMPOSITE RESPONSE

An iconic example of homogenised coarse-scale response based analytical modelling is that of a two-phase linear-elastic composite, consisting of materials with Young's Moduli E_1 and E_2. The constituent materials can be oriented parallel and perpendicular to the direction of loading. Voigt [183] and Reuss [184] derived a prediction model to determine the homogenised response for these two load cases. The Reuss and Voigt models provide upper and lower bound analytical solutions for the homogenised Young's Modulus E_c, which are are given by

$$E_{c,\text{upper}} = V_f E_1 + (1 - V_f) E_2, \tag{2.12}$$

$$E_{c,\text{lower}} = \left(\frac{V_f}{E_1} + \frac{1 - V_f}{E_2} \right)^{-1}, \tag{2.13}$$

where V_f and $(1 - V_f)$ denote the volume fractions of the materials with Young's Moduli E_1 and E_2, respectively. This type of method is generally only suitable for relatively simple geometries and interface conditions, such as in the example above.

HOMOGENISATION METHODS FOR COMPLEX COMPOSITES

The determination of the homogenised response of more complex composites, see the example in Figure 2.17, inherently requires the definition of a representative volume element (RVE) or unit cell. The RVE should generally meet the following criteria:

- it shall be "entirely typical of the whole mixture on average" [185],

- it shall be "the smallest material volume element of the composite for which the usual spatially constant (overall modulus) macroscopic constitutive representation is a sufficiently accurate model to represent mean constitutive response" [186].

Key requirements for homogenisation of composites are that (i) the fine-scale and coarse-scale model are of different length scales ($\overline{x} \gg x$ in Figure 2.17) and (ii) that the fine-scale model is characteristic and repetitive in space, i.e. it is periodic. Other requirements are (iii)

the availability of individual material models of the constituents, (iv) the definition of stress and strain averaging theorems, and (v) compliance to the Hill-Mandel macro-homogeneity principle [187, 188].

The coarse-scale homogenised response of composites (e.g. PMCs) can be determined based on analytical[5], numerical and computational homogenisation methods. The latter two are similar, but in case of numerical homogenisation the macroscopic constitutive model (relating force to deformation) is assumed prior to the (finite element) analysis and the associated material constants are fitted to match experimental results. In contrast, computational homogenisation does not require the definition of a macroscopic constitutive model: the purpose of the method is to predict the coarse-scale constitutive response[6]. More complex FE[2] models [192, 193] rely on simultaneously solving the mechanical response at a larger scale (i.e. at the level of a component or structure) and at the fine scale (i.e. the heterogeneous material), eliminating the need to provide macroscopic constitutive relations.

The homogenised coarse-scale Cauchy stress components of a representative volume element (or unit cell) with domain Θ can be determined by [190]

$$\sigma_{ij}^{c} = \frac{1}{|\Theta|} \int_{\Theta} \sigma_{ij}^{f} d\Theta, \tag{2.14}$$

where superscripts 'c' and 'f' denote the coarse and fine-scale stress components, respectively. The fine-scale strain ε_{ij}^{f} can be decomposed in terms of the coarse-scale strain ε_{ij}^{c} and a variation ε_{ij}^{*} by

$$\varepsilon_{ij}^{f} = \varepsilon_{ij}^{c} + \varepsilon_{ij}^{*}. \tag{2.15}$$

A similar decomposition can be made in terms of displacement, hence

$$u_{i}^{f}(\mathbf{x}, \mathbf{y}) = \varepsilon_{ij}^{c} y_{j} + u_{i}^{*}(\mathbf{x}, \mathbf{y}), \tag{2.16}$$

---

[5]An extensive overview of analytical techniques is presented by Fish [190] and Nemat-Nasser & Hori [191]. See also the Reuss and Voigt example above.

[6]Because of its objective, computational homogenisation is also referred to as multiscale constitutive modelling.
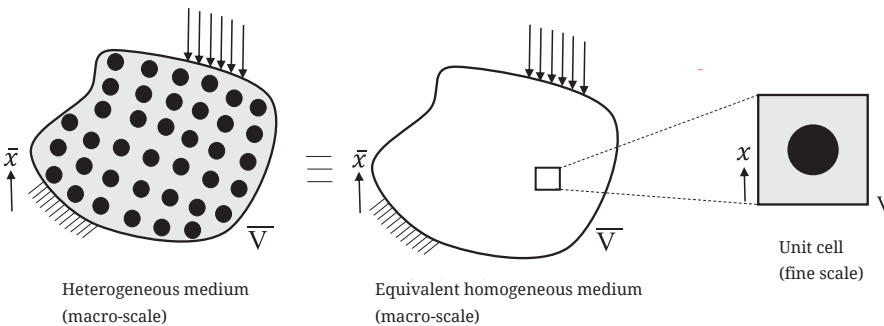
Figure 2.17 | Schematic overview of numerical/computational homogenisation, extracted from and modified after Tikarrouchine et al. [189]. Separation of length scales occurs for $\overline{x} \gg x$.

2

where the coarse-scale and fine-scale coordinates in the deformed state are denoted by $\mathbf{x} = (x_1, x_2)$ and $\mathbf{y} = (y_1, y_2)$, respectively. The fine-scale displacement and the variation of the fine-scale displacement are represented by $u_i^{\mathrm{f}}(\mathbf{x}, \mathbf{y})$ and $u_i^*(\mathbf{x}, \mathbf{y})$, respectively. If two nodes, M and S, are located at opposite faces of a unit cell, their fine-scale displacement is given by

$$
\begin{aligned}
u_i^{\mathrm{f}}(\mathbf{x}, \mathbf{y}^{\mathrm{M}}) &= \varepsilon_{ij}^{\mathrm{c}} y_j + u_i^*(\mathbf{x}, \mathbf{y}^{\mathrm{M}}), \\
u_i^{\mathrm{f}}(\mathbf{x}, \mathbf{y}^{\mathrm{S}}) &= \varepsilon_{ij}^{\mathrm{c}} y_j + u_i^*(\mathbf{x}, \mathbf{y}^{\mathrm{S}}).
\end{aligned}
\tag{2.17}
$$

For a periodic unit cell subject to a uniform coarse-scale deformation, it holds that the variations of the fine-scale displacement at both nodes are equal. This requirement can be rewritten in terms of the macro-scale displacement and the correction term as

$$
u_i^*(\mathbf{x}, \mathbf{y}^{\mathrm{M}}) - u_i^*(\mathbf{x}, \mathbf{y}^{\mathrm{S}}) = \varepsilon_{ij}^{\mathrm{c}} (y_j^{\mathrm{M}} - y_j^{\mathrm{S}}).
\tag{2.18}
$$

This condition can be implemented using *mixed boundary conditions*, given by [190]

$$
\begin{aligned}
\int_{\partial \Theta_Y} \left[u_i^{\mathrm{f}}(\mathbf{x}, \mathbf{y}) - \varepsilon_{ik}^{\mathrm{c}} y_k \right] N_j^{\Theta} d\gamma_Y &= 0, \\
\left| u_i^{\mathrm{f}}(\mathbf{x}, \mathbf{y}) - \varepsilon_{ik}^{\mathrm{c}} y_k \right| &\leq \text{Tolerance},
\end{aligned}
\tag{2.19}
$$

where N_j^{Θ} is the unit normal to the unit cell boundary. These conditions can be enforced either analytically or by implementing the underlying strategy in commercial finite element packages, for example by defining double nodes on the boundary and connecting these nodes by (non)-linear springs. Alternatively, third-party plug-ins can be used to automatically impose the periodic boundary conditions. Examples of available plug-ins for ABAQUS are EasyPBC [194] and Homtools [195].

An important contribution to homogenisation methods was made by Needleman [196], who provided the basis for the present traction-separation models by deriving a unified description for initiation and propagation of the separation of two interfaces. Such traction-separation models provide the ability to account for interface damage of composite materials, and are also known as *cohesive damage models*. Examples of cohesive damage models can, amongst others, be found in the work of Geubelle & Baylor [197], Needleman [196, 198], Xu & Needleman [198], Tvergaard & Hutchinson [199] and Benzeggagh & Kenane [200]. Commercially available finite element simulation packages, such as ABAQUS, offer a wide array of the cohesive damage models presented in the literature to be used for numerical homogenisation of composite materials.

Finite element software packages can be used for both numerical and computational homogenisation, and enable the use of built-in and previously established material models and interaction laws, despite their underlying theoretical complexity. Computational homogenisation has been successfully used to predict coarse-scale properties for a wide range of composite materials, for instance concrete [201], additive-manufactured materials [202, 203], and (G)FRP laminates [204–209]. In addition to predicting short-term properties, homogenisation methods can also be used to predict electromechanical, fatigue and creep properties of inhomogeneous materials: a wide array of examples applied to PMCs can be found in reference [210].

2.5. Design of composite floor systems according to Eurocode 4

Eurocode 4 [211] governs the design of steel-concrete composite structures. The most relevant parts of this code to this dissertation are related to the design verifications regarding the resistance in the Ultimate Limit State (ULS) and regarding the deformation in the Serviceability Limit State (SLS), which are separately discussed in the following sections.

2.5.1. Ultimate Limit State

Composite beams must be checked for the resistance of critical cross-sections[7], resistance to lateral-torsional buckling, resistance to shear buckling and transverse forces on webs, and the resistance to longitudinal shear [211].

EN 1994-1-1 [211] defines a so-called *effective width* for the verification of cross-sections to account for shear lag effects. For simply-supported composite beams the effective width is the lesser of $L/4$ (with L representing the span) and the physical width of the concrete element. Elastic and plastic design verification of the bending moment resistance is permitted: in the following subsections the background and requirements for each type of analysis is presented.

Plastic bending resistance

The plastic bending moment resistance according to EN 1994-1-1 [211] is based on the assumption that only one plastic neutral axis exists, which implies that the shear connection is infinitely stiff (rigid). The effective concrete area above the plastic neutral axis is assumed to be stressed to $0.85 \times f_{cd}$, where f_{cd} is the design concrete compressive strength. The steel is assumed to be stressed to its design yield strength over the full height of the cross-section, which must be of cross-section class 1 or 2 sections conform EN 1993-1-1 [212]. If the shear connectors are spaced at distances less than $22t_f\sqrt{235/f_y}$ for a slab in contact over the full length of the steel beam with yield strength f_y and flange thickness t_f, then also cross-section class 3 flanges are permissible for plastic design. In any case the maximum spacing of the shear connectors is the lesser of 6 times the concrete thickness and 800 mm. The shear connectors may be spaced equidistantly along the span.

The location of the plastic neutral axis can be determined based on a plastic stress distribution by solving for internal equilibrium of forces. Subsequently the plastic bending moment resistance $M_{pl,R}$ can be obtained. This approach assumes that either the steel or concrete is loaded to its resistance against axial force, which is only possible in case a sufficient number of shear connectors are present to transfer the force to the other component to achieve internal force equilibrium. In this case the sum of the design resistances of the shear connectors ($\sum P_{Rd}$) must be equal to or larger than the axial resistances of the steel and concrete. In such case the composite beam is said to have *full shear connection*. If the aggregated resistance of the connectors is smaller than the governing axial force resistance, the beam is said to have *partial shear connection*.

EN 1994-1-1 [211] assumes that shear connectors have an idealised rigid-plastic response. In case of partial shear connection, the connectors are required to be ductile, which

---

[7]i.e. sections of maximum bending moment, supports, sections subjected to concentrated loads or reactions, or places where a sudden change of cross-section occurs [211].

2

is defined as having a characteristic slip capacity of at least 6 mm[8]. The degree of shear connection η is defined as the ratio of the number of connectors over the number of connectors required for full shear connection. The plastic bending moment resistance $M_{pl,R}$ for a given value of η can be determined after the location of the plastic neutral axis has been determined based on internal force equilibrium. The use of partial shear connection is limited to $\eta \geq 0.4$, although recent research [216] initiated an attempt to decrease the acceptable magnitude of η in favour of a more economic design.

ELASTIC BENDING RESISTANCE
In EN 1994-1-1 [211], the elastic bending resistance of composite beams is determined based on the assumption that cross-sections remain plane during bending. The shear connectors should be spaced in accordance with the longitudinal shear flow based on elastic theory and are subject to the same spacing requirements as for plastic design (i.e. spaced at no more than the lesser of 6 times the concrete thickness and 800 mm). The stiffness of the shear connector is assumed as the secant stiffness at 70% of the characteristic resistance P_{Rk}. Appropriate allowance must be made for the effects of creep and shrinkage: in case of building structures it may be assumed that the long-term effects of concrete creep can be accounted for by an effective Young's Modulus $E_{c,eff} = 0.5 \times E_{cm}$ for both short-term and long-term loading, given that no pretension exists and the building is not mainly used for storage.

The elastic bending resistance is governed by limiting the stresses to the concrete design compressive strength f_{cd}, the reinforcement strength, and the steel yield strength in the respective elements. It should be noted that the use of f_{cd} implies that the elastic bending resistance does not represent a fully elastic stress state. However, the elastic design principle can be adjusted to align with the need to prevent plasticity to enable the reuse of the structural elements, as required by the SCI guidelines [67].

2.5.2. SERVICEABILITY LIMIT STATE
EN 1994 [211] includes three types of design verifications in the serviceability limit state, related to (i) stresses, (ii) deformations and (iii) cracking of concrete. Only the deformation-based criteria are further discussed, because stress limitations do not apply to buildings if no fatigue verifications are required [211] and because cracking of concrete is not considered within the scope of this dissertation.

The deflection of the composite beam can be determined based on a rigid shear connection if the following conditions are satisfied:

i. The design of the shear connection is in accordance with the ULS requirements

ii. Either not less shear connectors are used than half the number for full shear connection, or the forces resulting from an elastic behaviour and which act on the shear connectors in the serviceability limit state do not exceed P_{Rd}

iii. In case of a ribbed slab with ribs transverse to the beam, the height of the ribs does not exceed 80 mm

---

[8]More advanced methods to predict the required slip capacity for specific composite beam designs are presented by Oehlers and Bradford [213], Eggert [214], and Bärtschi [215].

The aforementioned conditions imply that the effects of incomplete interaction due to the flexibility of the shear connectors can be neglected in most cases. However, the work presented in this dissertation relates to the case where so few shear connectors are present (and not conform the spacing requirements) that the effects of incomplete interaction can no longer be neglected. The time-dependent effects of the concrete can be accounted for by an effective Young's Modulus $E_{c,eff} = 0.5 \times E_{cm}$ for both short-term and long-term loading, given that no pretension exists and the building is not mainly used for storage. The deflection should not exceed a certain predefined magnitude, e.g. $L/250$ with L representing the beam span.

2.6. Serviceability behaviour of composite floor systems

This section presents an overview of prediction models that describe the behaviour of composite floor systems under serviceability or quasi-elastic conditions, focusing specifically on internal actions (to obtain stresses), deflection and time-dependent effects. These models are specifically relevant in case the effects of the flexibility of the shear connection on the resistance and deflection cannot be neglected.

2.6.1. Deflection and internal actions

The deflection of a demountable composite floor system must be limited during its use-phase to comply with serviceability requirements. In the comparative study of Ranzi et al. [217], four different modelling methods for composite beams are outlined:

   i. Exact analytical methods

  ii. Finite difference methods

 iii. Finite element methods

  iv. Direct stiffness methods

All four modelling strategies are briefly discussed in the following. An overview of the comparative performance of the methods can be found in the work of Ranzi et al. [217] based on a case study example.

Exact analytical methods

Exact analytical methods are based on solving differential equations obtained by considering the strain diagram and internal equilibrium of composite beams. The elastic mechanical behaviour of composite beams with flexible (non-rigid) shear connectors was first described analytically by Newmark et al. [218]. The Newmark model consists of two Euler-Bernoulli beams (one representing the steel beam, and the other representing the concrete floor element) which are coupled at their interface using a uniformly distributed shear connection. Girhammar & Pan [219] and Girhammar [220] studied the elastic behaviour of composite beams using the Newmark approach, whereas Xu & Wu [221] and Schabl et al. [222] also implemented shear deformation in their models by using Timoshenko beam theory. Yam & Chapman [223] extended the original Newmark model to account for nonlinear material and shear connector behaviour. The exact analytical methods are not directly suitable for accounting for non-uniform shear connector arrangements. An attempt to model

2

non-uniform shear connector arrangements using analytical methods was made by Lawson et al. [224] by assuming the slip distribution to be cosinusoidal, which is typically acceptable for quasi-uniform shear connection and for prismatic composite beams. Coelho [69] demonstrated that for a non-uniform shear connection the slip function is not cosinusoidal. Therefore a universal shape function of the slip distribution cannot be readily predefined, particularly not for non-prismatic composite beams with (highly) non-uniform shear connector arrangements.

FINITE DIFFERENCE METHODS

Finite difference methods approximate the behaviour of composite beams numerically by assuming derivatives of the equilibrium conditions in the form of algebraic expressions. This modelling method has been developed extensively by Adekola [225], Roberts [226], and Al-Amery & Roberts [227], and requires the discretisation of the composite beam into parts. Given the boundary conditions, the system of equations can be solved and the deformed shape of the composite beam is obtained.

FINITE ELEMENT METHODS

Finite element methods provide numerical solutions and are robust and reliable in case suitable shape functions are chosen [12] to approximate the displacements. The finite element formulations are based on Euler–Bernoulli beam theory [e.g. in 228, 229], Timoshenko beam theory [e.g. in 230, 231] or higher order beam theories [e.g. in 232, 233]. The latter type of model aims to account for shear deformations in a more exact way than in case of Timoshenko beam theory. The solution strategy of finite element methods relies on the principle of virtual work, where the equilibrium condition for the composite beam can be expressed by the cumulative contributions of all its finite elements.

DIRECT STIFFNESS METHOD

The direct stiffness method is based on an initially undeformed element that is subjected to a unit rotation or translation in one of the degrees of freedom (DOF), whilst restraining all other DOFs. The direct stiffness method is presented in the work of Ranzi et al. [234], and later extended by Ranzi & Bradford [235] to account for time-dependent effects of composite floor systems. It should be noted that the direct stiffness method is at the heart of the majority of commercial finite element software packages. This discrepancy in naming illustrates the context-dependence of the solution strategy. The direct stiffness method leads to the same solution as the exact analytical methods, because the stiffness matrix is determined by solving the same differential equation that is used for the exact analytical solution [217].

2.6.2. TIME-DEPENDENT EFFECTS

The mechanical behaviour of steel-concrete composite floor systems, subject to sustained loads, is inherently time-dependent due to the creep and shrinkage of the concrete. The time-dependent response of the concrete affects the deformations and the internal actions in the serviceability state, and its influence is mainly governed by the mix design, element geometry and dimensions, load history and the environmental conditions [236]. In addition, the time-dependency also affects the stress concentration around the shear connector and thereby its fatigue life [237].

The first authors to model the time-dependent variations of the deflection and internal actions of composite beams assumed rigid composite interaction, i.e. without interface slip, and assigned a creep model to only the concrete element [238]. Later, more refined models were developed that accounted for the shear connector flexibility, which was assumed to be constant in time [e.g. in 235, 239–249]. However, a comprehensive experimental-numerical study by Al-deen et al. [250, 251] demonstrated that also the time-dependent deformation of the shear connector must be accounted for. If the variation of the shear connector deformation is neglected, the additional deflection due to creep is underestimated. This calls for long-term push-out tests to characterise the time-dependent behaviour of the shear connectors, results of which are scarce in the open literature [250–252] or are solely based on finite element studies without model validation [253] or without providing sufficient details thereof [254]. The most comprehensive work on long-term behaviour of shear connectors was carried out by Song et al. [252] and Liu et al. [237], and consisted of both experimental work and numerical analysis.

Experimental work on the time-dependent behaviour of composite beams is limited, and was reported by Bradford & Gilbert [255], Xue et al. [256], Al-deen et al. [250, 251], Liu et al. [257] and Ban et al. [258]. The broad scope of a parameter study by Ban et al. [258] led to a number of generic conclusions, for example that the relative time-dependent deflection is insensitive to the distribution of shear connectors along the beam length, and that high-strength concrete and additional compressive reinforcement may significantly reduce the creep sensitivity of the composite floor system.

Although Al-deen et al. [250, 251] recognised the importance of including the time-dependent shear connector behaviour, a phenomenological creep model for the shear connection was implemented that was not based on companion long-term push-out tests. A similar discrepancy exists in the work of Ban et al. [258], who implemented the same phenomenological time-dependent shear connector model as Al-deen et al. [250, 251], thus acknowledging its importance, but only carried out short-term push-out tests to determine the instantaneous response. The implementation of phenomenological creep models by both author groups suggests that there is no well-defined relation between time-dependent response of shear connectors in push-out tests and in beam tests, and that adjustments to the push-out response are necessary to correctly predict time-dependent effects of the composite beam.

2.7. SUMMARY

The literature review indicates the urgency for sustainable development *to meet the needs of the present without compromising the needs of future generations to meet their own needs.* An important and well-established concept in this field is the Circular Economy, which aims at maintaining the highest value of products and materials and facilitates the decoupling between resource use and pollution from economic growth. Government policies, either at national or international level, increasingly address the need for sustainable development.

The construction sector has the ability to play an important role in the transition to sustainable development, mainly because of its significant resource use, its polluting processes and because it generates substantial amounts of waste. The historic perception of buildings, as single and rigid entities, is a limiting factor to sustainable structures. Modularisation of building components offers both flexibility and adaptability, and enables the reuse of structural elements over multiple functional life cycles, either at the same location or at another.

An important prerequisite for this approach is that the building is demountable. Another condition for sustainable development is that all components shall be recyclable at the end of their technical life span.

Advantages of demountable and reusable structures are not limited to environmental aspects, but also include simplified maintenance procedures, increased adaptability, reduced costs and hindrance during disassembly compared to demolition, and reduced financial risks because the building can be repurposed. Several authors have presented strategies and prerequisites to design for demountability and reuse to mitigate any perceived barriers to the new design approach. However, market surveys show that all actors in the construction sector still perceive barriers, for example related to traceability and certification of structural elements or related to the development of new construction techniques.

Particular gains in terms of sustainability can be obtained in the field of steel-concrete composite floor systems. This is because the conventional construction method, using welded headed studs, led to an inherently non-demountable building which required demolition to recover the construction materials. A multitude of demountable alternatives to welded headed studs are presented, based on which the design of a novel shear connector system was derived. This novel demountable shear connector addresses both the need for composite interaction and the need for execution tolerances for rapid assembly, by using oversized holes in the beam flange, which are later injected with a (steel-reinforced) epoxy resin.

The literature on non-composite injected-bolted connections demonstrates the sensitivity of this type of connection to sustained and repeated loading. Therefore the long-term properties of the proposed demountable shear connector are governing the design. A review of the epoxy resin injectants is made, based on which a novel material, steel-reinforced resin offers the highest Young's Modulus and lowest creep sensitivity. The established methods to predict the properties of such a *polymer matrix composite* are presented.

The chapter culminates by presenting an overview of design and prediction methods for composite floor systems, addressing the verification of deflection and resistance criteria in case the shear connection can be considered as rigid and in case the flexibility of the shear connection cannot be neglected. An overview is provided of the time-dependent behaviour of composite floor system due to concrete creep and shrinkage and due to time-dependency of the shear connector stiffness.

REFERENCES

[1] E. Schumacher, *Small is beautiful: A study of economics as if people mattered* (Blond & Briggs, 1973).

[2] K. E. Boulding, *Environmental Quality in a Growing Economy,* (John Hopkins University Press, 1966) Chap. The Economics of the Coming Spaceship Earth, pp. 3–14.

[3] World Commission on Environment and Development, *Our Common Future* (Oxford University Press, 1987).

[4] J. K. Steinberger, F. Krausmann, and N. Eisenmenger, *Global patterns of materials use: A socioeconomic and geophysical analysis,* Ecological Economics **69**, 1148 (2010).

[5] H. Weisz, F. Krausmann, C. Amann, N. Eisenmenger, K.-H. Erb, K. Hubacek, and M. Fischer-Kowalski, *The physical economy of the European Union: Cross-country comparison and determinants of material consumption,* Ecological Economics **58**, 676 (2006).

[6] United Nations, *Decoupling Natural Resource Use and Environmental Impacts from Economic Growth*, edited by International Resource Panel (United Nations Environment Programme, 2011).

[7] F. Krausmann, S. Gingrich, N. Eisenmenger, K.-H. Erb, H. Haberl, and M. Fischer-Kowalski, *Growth in global materials use, GDP and population during the 20th century,* Ecological Economics **68**, 2696 (2009).

[8]   A. Maddison, *The World Economy: Historical statistics* (Organisation for Economic Co-operation and Development, 2003).

[9]   Organisation for Economic Co-operation and Development, *Global Material Resources Outlook to 2060: Economic Drivers and Environmental Consequences* (OECD Publishing, 2019).

[10] Organisation for Economic Co-operation and Development, *Policy Guidance on Resource Efficiency* (OECD Publishing, 2016).

[11] M. Ghyoot and L. Devlieger, *Déconstruction et réemploi. Comment faire circuler les éléments de construction* (PPUR, 2018).

[12] J. M. Allwood, M. F. Ashby, T. G. Gutowski, and E. Worrell, *Material efficiency: A white paper,* Resources, Conservation and Recycling **55**, 362 (2011).

[13] Department of the Environment, Transport and the Regions, *Making waste work: a strategy for sustainable waste management in England and Wales* (Her Majesty's Stationery Office, 1995).

[14] A. G. W. J. Lansink, *Ladder van Lansink,* Parliamental procedure (1979).

[15] R. U. Ayres and L. W. Ayres, *Industrial Ecology: Towards Closing the Materials Cycle,* 1st ed. (Edward Elgar, 1996).

[16] N. M. J. Guequierre and J. Kristinsson, *Product features that influence the end of a building.* in *Eighth International Conference on Durability of Building Materials and Components* (1999) pp. 2021–2032.

[17] C. J. Kibert and A. R. Chini, *Overview of deconstruction in selected countries,* isbn 0-9643886-3-4 ed. (International Council for Research and Innovation in Building Construction Task Group 39: Deconstruction, 2000).

[18] T. Graedel and B. R. Allenby, *Industrial Ecology and Sustainable Engineering: International Edition,* 2nd ed. (Pearson Education, 2010).

[19] E. B. Magrab, S. K. Gupta, F. P. McCluskey, and P. Sandborn, *Integrated Product and Process Design and Development,* 2nd ed. (Taylor & Francis, 2019).

[20] W. Stahel, *The Product Life Factor,* (1982) Chap. 4, pp. 72–96.

[21] J. Hinfelaar, E. Achterberg, and E. Kerkhof, *Kansen voor circulaire businessmodellen,* Tijdschrift Milieu (2016).

[22] E. Achterberg, J. Hinfelaar, and N. Bocken, *The Value Hill business model: identifying gaps and opportunities in a circular network,* (2016).

[23] D. J. Craven, H. M. Okraglik, and I. M. Eilenberg, *Construction waste and a new design methodology,* in *Proceedings of the First Conference of CIB TG,* Vol. 16 (1994) pp. 89–98.

[24] Ellen MacArthur Foundation, *Towards a circular economy: Business rationale for an accelerated transition,* Online (2015).

[25] T. N. Ligthart and A. A. M. Ansems, *Modelling of Recycling in LCA,* in *Post-Consumer Waste Recycling and Optimal Production* (Intech Open, 2012).

[26] World Steel Association, *Steel in the circular economy - A life cycle perspective* (World Steel Association, 2015).

[27] M. Gorgolewski, V. Straka, J. Edmonds, and C. Sergio, *Facilitating greater reuse and recycling of structural steel in the construction and demolition process,* Tech. Rep. (Ryerson University, 2006).

[28] M. Sansom and N. Avery, *Briefing: Reuse and recycling rates of UK steel demolition arisings,* Proceedings of the Institution of Civil Engineers - Engineering Sustainability **167**, 89 (2014).

[29] P. Hawken, A. B. Lovins, and L. H. Lovins, *Natural Capitalism* (Taylor & Francis Ltd., 2012).

[30] Rijksoverheid, *Nederland circulair in 2050,* (2016).

[31] European Commision, *Proposal for a regulation of the European Parliament and of the Council establishing the framework for achieving climate neutrality and amending Regulation EU 2018/1999 (European Climate Law)* (EUR-Lex, 2020).

[32] United Nations, *A/Res/70/1: Transforming our world: the 2030 Agenda for Sustainable Development,* (2015).

[33] D. S. Macozoma, *Building deconstruction,* CIB Publications (2001).

[34] N. Sadafi, M. F. M. Zain, and M. Jamil, *Design criteria for increasing building flexibility: Dynamics and prospects,* Environmental Engineering and Management Journal **13**, 407 (2014).

[35] P. Crowther, *Developing and inclusive model for design for deconstruction,* CIB Publications (2001).

[36] N. J. Habraken, *Supports: an alternative to mass housing* (The Architectural Press, 1972).

[37] F. Duffy and A. Henney, *The Changing City* (Bulstrode Press, 1989).

[38] S. Brand, *How Buildings Learn: What happens after they're built* (Penguin Publishing Group, 1995).

[39] A. R. Chini and S. Balachandran, *Anticipating and responding to deconstruction through building design,* in *Design for Deconstruction and Materials Reuse: Proceedings of the CIB Task Group 39 - Deconstruction Meeting on 9 April 2002,* edited by A. R. Chini and F. Schultmann (2002).

[40] E. S. Slaughter, *Design strategies to increase building flexibility,* Building Research & Information **29**, 208 (2001).

[41] E. Durmisevic and J. Brouwer, *Design aspects of decomposable building structures,* in *Design for Deconstruction and Materials Reuse: Proceedings of the CIB Task Group 39 - Deconstruction Meeting on 9 April 2002,* edited by A. R. Chini and F. Schultmann (2002).

[42] C. J. Kibert, *Sustainable Construction* (John Wiley & Sons Inc, 2016).

[43] A. Wilson, *Building Materials: What Makes a Product Green?* Environmental Building News **9**, 10 (2000).

[44] D. R. Cooper and T. G. Gutowski, *The Environmental Impacts of Reuse: A Review,* Journal of Industrial Ecology **21**, 38 (2015).

[45] W. P. S. Dias, *Factors influencing the service life of buildings,* Engineer **46**, 1 (2013).

[46] S. Lotfi and P. Rem, *Recycling of end of life concrete fines into hardened cement and clean sand,* Journal of Environmental Protection **07**, 934 (2016).

[47] H. M. Jonkers and H. E. J. G. Schlangen, *Self-healing of cracked concrete: a bacterial approach,* in *High performance concrete, brick masonry and environmental aspects,* edited by A. Carpinteri, P. Gambarova, G. Ferro, and G. Plizzari (Taylor & Francis, 2007) pp. 1821–1826.

[48] N. Taranu, G. Oprisan, I. Entuc, M. Budescu, V. Munteanu, and G. Taranu, *Composite and hybrid solutions for sustainable development in civil engineering,* Environmental Engineering and Management Journal **11**, 783 (2012).

[49] M. Fujita and M. Iwata, *Reuse system of building steel structures,* Structure and Infrastructure Engineering **4**, 207 (2008).

[50] A. Talja, *Re-use of structural elements: Environmentally efficient recovery of building components,* (VTT Technical Research Centre of Finland, 2014) Chap. Design for deconstruction and reuse, pp. 46–54.

[51] K. Wang, S. de Regel, W. Debacker, J. Michiels, and J. Vanderheyden, *Why invest in a reversible building design?* IOP Conference Series: Earth and Environmental Science **225**, 012005 (2019).

[52] W. Fawcett, M. Hughes, H. Krieg, S. Albrecht, and A. Vennström, *Flexible strategies for long-term sustainability under uncertainty,* Building Research & Information **40**, 545 (2012).

[53] M. Pulaski, C. Hewitt, M. Horman, and B. Guy, *Design for deconstruction,* Modern Steel Construction **44**, 33 (2004).

[54] P. Sassi, *Study of current building methods that enable the dismantling of building structures and their classifications according to their ability to be reused, recycled or downcycled,* (in-house publishing, Rotterdam (Netherlands), 2002).

[55] A. Gritsenko, *Towards demountable composte steel-concrete flooring systems,* Master's thesis, Delft University of Technology (2018).

[56] P. Crowther, *Developing guidelines for design for deconstruction,* in *Proceedings of the "Deconstruction - Closing the Loop" conference* (BRE, 2000).

[57] P. Crowther, *Design for buildability and the deconstruction consequences,* in *Design for Deconstruction and Materials Reuse: Proceedings of the CIB Task Group 39 - Deconstruction Meeting on 9 April 2002,* edited by A. R. Chini and F. Schultmann (2002).

[58] M. D. Webster and D. T. Costello, *Designing structural systems for deconstruction: How to extend a new building's useful life and prevent it from going to waste when the end finally comes,* in *Proceedings of the Greenbuild Conference* (2005).

[59] D. Densley Tingley and B. Davison, *Design for deconstruction and material reuse,* Proceedings of the Institution of Civil Engineers - Energy **164**, 195 (2011).

[60] M. Wahlström, *Re-use of structural elements: Environmentally efficient recovery of building components,* (VTT Technical Research Centre of Finland, 2014) Chap. Quality Aspects, pp. 43–45.

[61] C. F. Dunant, M. P. Drewniok, M. Sansom, S. Corbey, J. M. Cullen, and J. M. Allwood, *Options to make steel reuse profitable: An analysis of cost and risk distribution across the UK construction value chain*, Journal of Cleaner Production **183**, 102 (2018).

[62] E. Durmisevic, P. Beurskens, R. Adrosevic, and R. Westerdijk, *Systemic view on reuse potential of building elements, components and systems: comprehensive framework for assessing reuse potential of building elements*, in *Hiser International Conference* (2017) pp. 275–280.

[63] J. W. Hurley, *Design for deconstruction: tools and practices*, in *Design for Deconstruction and Materials Reuse: Proceedings of the CIB Task Group 39 - Deconstruction Meeting on 9 April 2002*, edited by A. R. Chini and F. Schultmann (2002).

[64] C. J. Kibert, *Deconstruction's role in an ecology of construction*, in *Design for Deconstruction and Materials Reuse: Proceedings of the CIB Task Group 39 - Deconstruction Meeting on 9 April 2002* (2002) pp. 219–230.

[65] C. F. Dunant, M. P. Drewniok, M. Sansom, S. Corbey, J. M. Allwood, and J. M. Cullen, *Real and perceived barriers to steel reuse across the UK construction value chain*, Resources, Conservation and Recycling **126**, 118 (2017).

[66] P. Hradil, *Re-use of structural elements: Environmentally efficient recovery of building components*, (VTT Technical Research Centre of Finland, 2014) Chap. Introduction, pp. 6–12.

[67] Steel Construction Institute (SCI), *Protocol for reusing structural steel*, Tech. Rep. (SCI, 2019).

[68] A. M. Girão Coelho, M. Lawson, D. Lam, and J. Yang, *Guidance on demountable composite construction systems for UK practice*, p428 ed. (SCI, 2020).

[69] A. M. G. Coelho, R. M. Lawson, and E. S. Aggelopoulos, *Optimum use of composite structures for demountable construction*, Structures **20**, 116 (2019).

[70] ISO, *ISO 15686: Building Construction - Service Life Planning* (ISO, 2011).

[71] ISO, *ISO 14040: Environmental management - Life cycle assessment - Principles and framewor* (ISO, 2006).

[72] ISO, *ISO 14044: Environmental management - Life cycle assessment - Requirements and guidelines* (ISO, 2006).

[73] NEN, *NEN-EN 15978: Sustainability of construction works - Assessment of environmental performance of buildings - Calculation method* (NEN, 2011).

[74] NEN, *NEN-EN 15804: Sustainability of construction works - Environmental product declarations - Core rules for the product category of construction products* (NEN, 2019).

[75] G. Brambilla, M. Lavagna, G. Vasdravellis, and C. A. Castiglioni, *Environmental benefits arising from demountable steel-concrete composite floor systems in buildings*, Resources, Conservation and Recycling **141**, 133 (2019).

[76] G. Brambilla, *Sustainable composite steel-concrete construction*, Ph.D. thesis, Politecnico de Milano (2018).

[77] N. K. Gakkai, *The English edition of the Principal guide for service life planning of buildings* (Architectural Institute of Japan, 1993).

[78] A. A. J. F. van den Dobbelsteen, *The Sustainable Office: An exploration of the potential for factor 20 environmental improvement of office accommodation*, Ph.D. thesis, Delft University of Technology (2004).

[79] R. Geraedts, M. Hermans, H. Remoy, and E. van Rijn, *Adaptive capacity of buildings: a determination method to promote flexible and sustainable construction*, in *Proceedings of the International Union of Architects World Congress* (2014).

[80] A. Straub, *Estimating the service lives of building products in use*, Journal of Civil Engineering and Architecture **9** (2015), 10.17265/1934-7359/2015.03.011.

[81] H. Eggemann and K.-E. Kurrer, *On the international propagation of the Melan Arch System since 1892*, in *Proceedings of the Third International Congress on Construction History* (2009).

[82] H. Eggemann, *Development of composite columns: Emperger's effort*, in *Proceedings of the First International Congress on Construction History* (2003).

[83] M. Koenen, *Über die gefährlichen Abscherflächen in Beton eingebetteter Eisenstäbe*, Beton und Eisen **4**, 148 (1905).

[84] L. Cambournac, *Poutrelles en acier enrobees de beton (beams of encased rolled steel sections)*, in *Abhandlungen der Internationalen Vereinigung für Brückenbau und Hochbau* (1932) pp. 25–34.

[85] K.-E. Kurrer, *The History of the Theory of Structures* (Ernst und Sohn, 2018) pp. 616–621.

[86] H. Maier-Leibnitz, *Zusammenwirken von I-Trägern mit Eisenbetondecken*, Die Bautechnik **19**, 265 (1942).

[87] K. Sattler, *Betrachtungen über neuere Verdübelungen im Verbundbau,* Der Bauingenieur **37**, 1 (1962).

[88] W. Wapenhans, *Zur Entwicklung des Stahlverbundbaus in Deutschland bis 1992* (Wapenhans und Richter, 1992).

[89] H. Muess, N. Sauerborn, and J. Schmitt, *Höhepunkte im modernen Verbundbau - eine beispielhafte Entwicklungsgeschichte,* Stahlbau **73**, 791 (2004).

[90] I. M. Viest, *Investigation of stud shear connectors for composite concrete and steel T-beams,* Journal of the American Concrete Institute **27**, 875 (1956).

[91] L. Pallarés and J. F. Hajjar, *Headed steel stud anchors in composite structures, Part I: Shear,* Journal of Constructional Steel Research **66**, 198 (2010).

[92] D. de Lima Araújo, M. W. R. Sales, S. M. de Paulo, and A. L. H. de Cresce El Debs, *Headed steel stud connectors for composite steel beams with precast hollow-core slabs with structural topping,* Engineering Structures **107**, 135 (2016).

[93] F.-X. Ding, G.-A. Yin, H.-B. Wang, L. Wang, and Q. Guo, *Static behavior of stud connectors in bi-direction push-off tests,* Thin-Walled Structures **120**, 307 (2017).

[94] Y. Ling, Z. Zheng, T. Y. Yang, and H. Ma, *Behaviour and Modeling of the Bearing Capacity of Shear Stud Connectors,* International Journal of Steel Structures **19**, 650 (2018).

[95] D. Kruszewski, A. E. Zaghi, and K. Wille, *Finite element study of headed shear studs embedded in ultra-high performance concrete,* Engineering Structures **188**, 538 (2019).

[96] T. Molkens, J. Dobrić, and B. Rossi, *Shear resistance of headed shear studs welded on welded plates in composite floors,* Engineering Structures **197**, 109412 (2019).

[97] D. Lam and E. El-Lobody, *Behavior of headed stud shear connectors in composite beam,* Journal of Structural Engineering **131**, 96 (2005).

[98] S. J. Hicks, *Resistance and ductility of shear connection: Full-scale beam and push tests,* in *Proceedings of the 6th International Conference on Steel & Aluminium Structures* (2007) pp. 613–620.

[99] O. Mirza and B. Uy, *Effects of strain regimes on the behaviour of headed stud shear connectors for composite steel-concrete beams, Volume 6 Number 1,* Advanced Steel Construction **6**, 635 (2010).

[100] G. Kwon, B. Hungerford, H. Kayir, B. Schaap, Y. Kyu Ju, R. Klingner, and M. Engelhardt, *Strengthening existing non-composite steel bridge girders using post-installed shear connectors,* Tech. Rep. (Centre for Transportation Research of The University of Texas at Austin, 2007).

[101] L. N. Dallam, *High-strength bolt shear connectors - Pushout tests,* Journal of the America Concrete Institute (1968).

[102] W. T. Marshall, H. M. Nelson, and H. K. Banerjee, *An experiment study of the use of high-strength friction grip bolts as shear connectors in composite beams,* Structural Engineer (1971).

[103] N. M. Hawkins, *Strength in shear and tension of cast-in-place anchor bolts,* Anchorage to Concrete **103**, 233 (1987).

[104] M. Pavlović, Z. Marković, M. Veljković, and D. Buđevac, *Bolted shear connectors vs. headed studs behaviour in push-out tests,* Journal of Constructional Steel Research **88**, 134 (2013).

[105] D. Lam, X. Dai, and E. Saveri, *Behaviour of Demountable Shear Connectors in Steel-Concrete Composite Beams,* in *Proceedings of the 2013 Composite Construction in Steel and Concrete Conference* (American Society of Civil Engineers, 2016).

[106] X. H. Dai, D. Lam, and E. Saveri, *Effect of concrete strength and stud collar size to shear capacity of demountable shear connectors,* Journal of Structural Engineering **141**, 04015025 (2015).

[107] N. Rehman, D. Lam, X. Dai, and A. Ashour, *Experimental study on demountable shear connectors in composite slabs with profiled decking,* Journal of Constructional Steel Research **122**, 178 (2016).

[108] N. Rehman, D. Lam, X. Dai, and A. Ashour, *Testing of composite beam with demountable shear connectors,* Proceedings of the Institution of Civil Engineers - Structures and Buildings **171**, 3 (2018).

[109] A. Ataei, M. Bradford, and X. Liu, *Sustainable composite beams and joints with deconstructable bolted shear connectors,* in *Proceedings of the 23rd Australasian Conference on the Mechanics of Structures and Materials (ACMSM23)* (2014).

[110] A. Ataei, M. A. Bradford, and H. R. Valipour, *Experimental study of flush end plate beam-to-CFST column composite joints with deconstructable bolted shear connectors,* Engineering Structures (2015).

[111] A. Ataei, M. A. Bradford, and X. Liu, *Experimental study of flush end plate beam-to-column composite joints with precast slabs and deconstructable bolted shear connectors,* Structures **7**, 43 (2016).

[112] A. Ataei, M. A. Bradford, H. R. Valipour, and X. Liu, *Experimental study of sustainable high strength steel flush end plate beam-to-column composite joints with deconstructable bolted shear connectors,* Engineering Structures **123**, 124 (2016).

[113] V. Patel, B. Uy, S. Pathirana, S. Wood, M. Singh, and B. Trang, *Finite element analysis of demountable steel-concrete composite beams under static loading,* Advanced Steel Construction (2018), 10.18057/ijasc.2018.14.3.5.

[114] D. Dedic and F. Klaiber, *High-Strength Bolts as Shear Connectors in Rehabilitation Work,* Concrete International **6**, 41 (1984).

[115] G. Kwon, M. D. Engelhardt, and R. E. Klingner, *Behavior of post-installed shear connectors under static and fatigue loading,* Journal of Constructional Steel Research **66**, 532 (2010).

[116] M. M. Lawan, M. M. Tahir, and J. Mirza, *Bolted shear connectors performance in self-compacting concrete integrated with cold-formed steel section,* Latin American Journal of Solids and Structures **13**, 731 (2016).

[117] J. Chen, W. Wang, F.-X. Ding, P. Xiang, Y.-J. Yu, X.-M. Liu, F. Xu, C.-Q. Yang, and S.-G. Long, *Behavior of an Advanced Bolted Shear Connector in Prefabricated Steel-Concrete Composite Beams,* Materials **12**, 2958 (2019).

[118] X. Liu, M. A. Bradford, and M. S. S. Lee, *Behavior of high-strength friction-grip bolted shear connectors in sustainable composite beams,* Journal of Structural Engineering **141**, 04014149 (2015).

[119] A. Kozma, C. Odenbreit, M. Braun, M. Veljkovic, and M. Nijgh, *Push-out tests on demountable shear connectors of steel-concrete composite structures,* Structures **21**, 45 (2019).

[120] Y.-T. Chen, Y. Zhao, J. West, and S. Walbridge, *Behaviour of steel–precast composite girders with through-bolt shear connectors under static loading,* Journal of Constructional Steel Research **103**, 168 (2014).

[121] M. C. Moynihan and J. M. Allwood, *Viability and performance of demountable composite connectors,* Journal of Constructional Steel Research **99**, 47 (2014).

[122] A. S. Kozma, *Demountable composite beams: Design procedure for non-conventional shear connections with multilinear load-slip behaviour,* Ph.D. thesis, University of Luxembourg (2020).

[123] O. Mirza, B. Uy, and N. Patel, *Behavior and strength of shear connectors utilising blind bolting,* in *Proceedings of the 4th International Conference on Steel and Composite Structures* (2010) pp. 21–23.

[124] S. W. Pathirana, B. Uy, O. Mirza, and X. Zhu, *Bolted and welded connectors for the rehabilitation of composite beams,* Journal of Constructional Steel Research **125**, 61 (2016).

[125] B. Uy, V. Patel, D. Li, and F. Aslani, *Behaviour and design of connections for demountable steel and composite structures,* Structures **9**, 1 (2017).

[126] S. W. Pathirana, B. Uy, O. Mirza, and X. Zhu, *Flexural behaviour of composite steel–concrete beams utilising blind bolt shear connectors,* Engineering Structures **114**, 181 (2016).

[127] H. Loh, B. Uy, and M. Bradford, *The effects of partial shear connection in composite flush end plate joints part i — experimental study,* Journal of Constructional Steel Research **62**, 378 (2006).

[128] J.-F. Wang, L.-H. Han, and B. Uy, *Behaviour of flush end plate joints to concrete-filled steel tubular columns,* Journal of Constructional Steel Research **65**, 925 (2009).

[129] O. Mirza and B. Uy, *Behaviour of composite beam–column flush end-plate connections subjected to low-probability, high-consequence loading,* Engineering Structures **33**, 647 (2011).

[130] F. Csillag, *Demountable deck-to-girder connection of FRP-steel hybrid bridges,* Master's thesis, Delft University of Technology (2018).

[131] A. S. H. Suwaed and T. L. Karavasilis, *Removable shear connector for steel-concrete composite bridges,* Steel and Composite Structures **29**, 107 (2018).

[132] A. S. H. Suwaed and T. L. Karavasilis, *Novel demountable shear connector for accelerated disassembly, repair, or replacement of precast steel-concrete composite bridges,* Journal of Bridge Engineering **22**, 04017052 (2017).

[133] A. S. Suwaed and T. L. Karavasilis, *Demountable steel-concrete composite beam with full-interaction and low degree of shear connection,* Journal of Constructional Steel Research **171**, 106152 (2020).

[134] L. Wang, M. D. Webster, and J. F. Hajjar, *Behavior of deconstructable steel-concrete shear connection in composite beams,* in *Structures Congress 2015* (American Society of Civil Engineers, 2015).

[135] L. Wang, L. N. Troup, K. Coleman, M. J. Eckelman, and J. F. Hajjar, *Deconstructable systems for sustainable design of steel and composite structures*, Tech. Rep. (American Institute of Steel Construction, 2016).

[136] F. Yang, Y. Liu, Z. Jiang, and H. Xin, *Shear performance of a novel demountable steel-concrete bolted connector under static push-out tests,* Engineering Structures **160**, 133 (2018).

[137] B. Milosavljevic, I. Milicevic, M. Pavlovic, and M. Spremic, *Static behaviour of bolted shear connectors with mechanical coupler embedded in concrete,* Steel and Composite Structures **29** (2018).

[138] NEN, *NEN-EN 1090-2: Execution of steel structures and aluminium structures - Part 2: Technical requirements for steel structures* (Nederlandse Norm (NEN), 2018).

[139] A. M. Gresnigt and J. W. B. Stark, *Design of bolted connections with injection bolts,* in *Proceedings from the Third International Workshop on Connections in Steel Structures: Behaviour, Strength and Design*, edited by R. Bjorhovde, A. Colson, and R. Zandonini (1995) pp. 77–87.

[140] ECCS, *European recommendations for bolted connections with injection bolts*, 79 (ECCS, 1994).

[141] J. Qureshi and J. T. Mottram, *Resin injected bolted connections: a step towards achieving slip-resistant joints in FRP bridge engineering,* in *Proceedings of the FRP Bridges Conference* (2012) pp. 56–66.

[142] B. J. P. M. Carvalho, *Modelação por Elementos Finitos do Comportamento de Ligações Aparafusadas Sem e Com Resina Injetada*, Master's thesis, Universidade de Trás-os-Montes e Alto Douro (2013).

[143] A. M. Gresnigt and D. Beg, *Design bearing stresses for injection bolts with short and long duration high loads,* in *Proceedings of the Fifth International Conference on Structural Engineering, Mechanics and Computation*, edited by A. Zingoni (2013) pp. 1317–1322.

[144] H. J. van Lint, J. C. van Wolfswinkel, and A. M. Gresnigt, *Bouwen met Staal: Vakblad over staal en staalconstructies,* (Bouwen met Staal, 2012) Chap. Besparen op injectiebouten, pp. 44–49.

[145] B. Zafari, J. Qureshi, J. T. Mottram, and R. Rusev, *Static and fatigue performance of resin injected bolts for a slip and fatigue resistant connection in FRP bridge engineering,* Structures **7**, 71 (2016).

[146] L. P. Bouwman and H. Kluwen, *De invloed van water op de mechanisme eigenschappen van 3 verschillende hars/harder systemen*, Tech. Rep. (Technische Hogeschool Delft, 1973).

[147] A. Koper, *Assessment of epoxy resins for injected bolted shear connections*, Master's thesis, Delft University of Technology (2017).

[148] H. J. Smits and L. P. Bouwman, *Investigation to the application of separating liquids for injected bolt-connections*, Tech. Rep. (Technische Hogeschool Delft, 1972).

[149] M. P. Nijgh, *New Materials for Injected Bolted Connections: A Feasibility Study for Demountable Connections*, Master's thesis, Delft University of Technology (2017).

[150] J. Korti̇s, *The numerical solution of the bolted connection with the low-quality injected bolts,* in *Proceedings of the 9th International Conference on New Trends in Statics and Dynamics of Buildings*, edited by N. Jendzelovsky and M. Nagyova (2011).

[151] A. M. P. de Jesus, J. F. N. da Silva, M. V. Figueiredo, A. S. Ribeiro, A. A. Fernandes, J. A. F. O. Correia, A. L. L. da Silva, and J. M. C. Maeiro, *Fatigue behaviour of resin-injected bolts: An experimental approach,* in *Proceedings of the Iberian Conference on Fracture and Structural Integrity* (2010).

[152] A. M. Gresnigt and P. A. de Vries, *Injection bolts: update on research and applications,* in *Proceedings of the AISC-ECCS workshop* (2016).

[153] M. Rodrigues, P. C. Raposa, B. Pedrosa, J. A. F. O. Correia, S. Blasón, M. Calvente, A. M. P. Jesus, C. Rebelo, R. A. B. Calcada, and A. Fernandez-Canteli, *Fatigue characterisation of structural resins used in reinforcement of old bridges,* in *Proceedings of the XI Congresso de Construçã Metálica e mista* (2017).

[154] Rijkswaterstaat Steunpunt Opdrachtgeversschap, *Eisen voor voegovergangen*, Tech. Rep. (Rijkswaterstaat, 2007).

[155] M. P. Nijgh, *Injected bolted connection,* (2018).

[156] Research Council on Structural Connections, *Specification for Structural Joints Using High-Strength Bolts* (Research Council on Structural Connections, 2014).

[157] NEN, *NEN-EN 1993-1-8: Eurocode 3: Design of steel structures - Part 1-8: Design of joints* (NEN, 2005).

[158] L. P. Bouwman, *De invloed van de dikteverhoudingen van hoofd- en stuikplaten op de toelaatbare stuikspanning bij verbindingen met injectiebouten,* Tech. Rep. (Technische Hogeschool Delft, 1974).

[159] A. Gresnigt, G. Sedlacek, and M. Paschen, *Injection bolts to repair old bridges,* in *Proceedings of Connections in Steel Structures IV* (2000).

[160] NEN, *NEN-EN 1993-1-9: Eurocode 3: Design of steel structures - Part 1-9: Fatigue* (NEN, 2006).

[161] J. A. F. O. Correia, A. M. P. de Jesus, J. C. M. Pinto, and R. A. B. Calcada, *Fatigue behaviour of single and double shear connections with resin-injected preloaded bolts,* in *Proceedings of the 19th IABSE Congress: Challenges in the Design and Construction of an Innovative and Sustainable Built Environment* (2016).

[162] B. Pedrosa, C. Rebelo, H. Gervásio, L. S. da Silva, and J. A. Correia, *Fatigue of preloaded bolted connections with injection bolts,* Structural Engineering International **30**, 102 (2019).

[163] A. M. van Wingerde, D. R. V. van Delft, and E. S. Knudsen, *Fatigue behaviour of bolted connections in pultruded FRP profiles,* Plastics, Rubber and Composites **32**, 71 (2003).

[164] K. Roupakas, *Fatigue behavior of resin and steel reinforced resin used in IBCs,* Master's thesis, Delft University of Technology (2019).

[165] L. Bücking, *Behaviour of steel-reinforced epoxy resin exposed to compressive-compressive cyclic loading in confined conditions,* Master's thesis, Leibniz Universität Hannover, Delft University of Technology (2019).

[166] F. J. Wedekamper, *Avaliação de resinas epóxi para aplicação em end fittings de dutos flexíveis,* Master's thesis, Universidade Federal do Rio Grande do Sul (2017).

[167] C. A. May, *Epoxy Resins - Chemistry and Technology,* (Marcel Dekker, 1987) Chap. Introduction to Epoxy Resins, 2nd ed.

[168] R. J. Varley, J. H. Hodgkin, and G. P. Simon, *Toughening of Trifunctional Epoxy System. V. Structure - Property Relationships of Neat Resin,* Journal of Applied Polymer Science **77**, 237 (2000).

[169] T. W. Tamulevich, *The Significance Of Glass Transition Temperature On Epdxy Resins For Fiber Optic Applications,* in *Integration and Packaging of Optoelectronic Devices,* edited by D. H. Hartman, R. L. Holman, and D. P. Skinner (SPIE, 1987).

[170] L. H. Sperling, *Introduction to Physical Polymer Science* (Wiley, 2005).

[171] Polymer Properties Database, *Rubber elasticity,* Online.

[172] E. T. J. Klompen, *Mechanical properties of solid polymers: constitutive modelling of long and short term behaviour,* Ph.D. thesis, Eindhoven University of Technology (2005).

[173] L. C. Brinson and T. S. Gates, *Effects of physical aging on long term creep of polymers and polymer matrix composites,* International Journal of Solids and Structures **32**, 827 (1995).

[174] R. K. Penny and D. L. Marriott, *Design for Creep* (Springer, 1995).

[175] J. E. Dorn, *Some fundamental experiments on high temperature creep,* Journal of the Mechanics and Physics of Solids **3**, 85 (1955).

[176] F. H. Norton, *The Creep of Steel at High Temperatures* (McGraw-Hill, 1929).

[177] C. R. Soderberg, *The interpretation of creep tests for machine design,* Transactions of the American Society of Mechanical Engineers **65** (1936).

[178] P. G. McVetty, *Creep of metals at elevated temperatures - the hyperbolic sine relation between stress and creep rate,* Transactions of the American Society of Mechanical Engineers **58**, 733 (1943).

[179] A. E. Johnson, J. Henderson, and B. Khan, *Multiaxial Creep-Strain/Complex-Stress/Time Relations for Metallic Alloys with Some Applications to Structures,* Proceedings of the Institution of Mechanical Engineers, Conference Proceedings **178**, 2 (1963).

[180] F. Garofalo, *Fundamentals of creep and creep-rupture in metals* (MacMillan, 1965).

[181] I. Finnie and W. R. Heller, *Creep of Engineering Materials* (McGraw-Hill, 1959).

[182] S. S. Manson, *Creep under non-steady temperatures and stresses,* edited by J. E. Dorn (McGraw-Hill, 1961).

[183] W. Voigt, *Ueber die Beziehung zwischen den beiden Elasticitätsconstanten isotroper Körper,* Annalen der Physik **274**, 573 (1889).

[184] A. Reuss, *Berechnung der Fließgrenze von Mischkristallen auf Grund der Plastizitätsbedingung für Einkristalle,* Zeitschrift für Angewandte Mathematik und Mechanik **9**, 49 (1929).

[185] R. Hill, *Elastic properties of reinforced solids: Some theoretical principles,* Journal of the Mechanics and Physics of Solids **11**, 357 (1963).

[186] W. Drugan and J. Willis, *A micromechanics-based nonlocal constitutive equation and estimates of representative volume element size for elastic composites,* Journal of the Mechanics and Physics of Solids **44**, 497 (1996).

[187] R. Hill, *A self-consistent mechanics of composite materials,* Journal of the Mechanics and Physics of Solids **13**, 213 (1965).

[188] J. Mandel, *Plasticité Classique et Viscoplasticité* (Springer-Verlag, 1971).

[189] E. Tikarrouchine, G. Chatzigeorgiou, F. Praud, B. Piotrowski, Y. Chemisky, and F. Meraghni, *Three-dimensional FE2 method for the simulation of non-linear, rate-dependent response of composite structures,* Composite Structures **193**, 165 (2018).

[190] J. Fish, *Practical Multiscaling* (John Wiley & Sons, 2014).

[191] S. Nemat-Nasser and M. Hori, *Micromechanics: overall properties of heterogeneous materials* (Elsevier, 2013).

[192] F. Feyel, *Multiscale FE2 elastoviscoplastic analysis of composite structures,* Computational Materials Science **16**, 344 (1999).

[193] F. Feyel, *A multilevel finite element method (FE2) to describe the response of highly non-linear structures using generalized continua,* Computer Methods in Applied Mechanics and Engineering **192**, 3233 (2003).

[194] S. L. Omairey, P. D. Dunning, and S. Sriramula, *Development of an ABAQUS plugin tool for periodic RVE homogenisation,* Engineering with Computers **35**, 567 (2019).

[195] S. Lejeunes and S. Bourgeois, *Une Toolbox Abaqus pour le calcul de propriétés effectives de milieux hétérogènes,* in *Proceedings of the 10e Colloque National en Calcul des Structures* (2011).

[196] A. Needleman, *A continuum model for void nucleation by inclusion debonding,* Journal of Applied Mechanics **54**, 525 (1987).

[197] P. H. Geubelle and J. S. Baylor, *Impact-induced delamination of composites: a 2d simulation,* Composites Part B: Engineering **29**, 589 (1998).

[198] X.-P. Xu and A. Needleman, *Numerical simulations of fast crack growth in brittle solids,* Journal of the Mechanics and Physics of Solids **42**, 1397 (1994).

[199] V. Tvergaard and J. W. Hutchinson, *The relation between crack growth resistance and fracture process parameters in elastic-plastic solids,* Journal of the Mechanics and Physics of Solids **40**, 1377 (1992).

[200] M. L. Benzeggagh and M. Kenane, *Measurement of mixed-mode delamination fracture toughness of unidirectional glass/epoxy composites with mixed-mode bending apparatus,* Computer Sciences and Technology **56**, 439 (1996).

[201] D. Tal and J. Fish, *Stochastic multiscale modeling and simulation framework for concrete,* Cement and Concrete Composites **90**, 61 (2018).

[202] H. Xin, W. Sun, and J. Fish, *A surrogate modelling approach for additive-manufactured materials,* International Journal for Multiscale Computational Engineering **15**, 525 (2017).

[203] H. Xin, W. Sun, and J. Fish, *Discrete element simulations of powder-bed sintering-based additive manufacturing,* International Journal of Mechanical Sciences **149**, 373 (2018).

[204] H. Xin, A. S. Mosallam, Y. Liu, C. Wang, and J. He, *Experimental and numerical investigation on assessing local bearing behavior of a pultruded GFRP bridge deck,* Composite Structures **204**, 712 (2018).

[205] H. Xin, Y. Liu, A. S. Mosallam, J. He, and A. Du, *Evaluation on material behaviors of pultruded glass fiber reinforced polymer (GFRP) laminates,* Composite Structures **182**, 283 (2017).

[206] H. Xin, A. Mosallam, Y. Liu, Y. Xiao, J. He, C. Wang, and Z. Jiang, *Experimental and numerical investigation on in-plane compression and shear performance of a pultruded GFRP composite bridge deck,* Composite Structures **180**, 914 (2017).

[207] T. Vaughan and C. McCarthy, *Micromechanical modelling of the transverse damage behaviour in fibre reinforced composites,* Composites Science and Technology **71**, 388 (2011).

[208] M. Romanowicz, *A numerical approach for predicting the failure locus of fiber reinforced composites under combined transverse compression and axial tension,* Computational Materials Science **51**, 7 (2012).

[209] H. Xin, A. Mosallam, Y. Liu, C. Wang, and Y. Zhang, *Analytical and experimental evaluation of flexural behavior of FRP pultruded composite profiles for bridge deck structural design,* Construction and Building Materials **150**, 123 (2017).

[210] R. M. Guedes, ed., *Creep and Fatigue in Polymer Matrix Composites* (Woodhead Publishing, 2010).

[211] NEN, *NEN-EN 1994-1-1: Eurocode 4: Design of composite steel and concrete structures - Part 1-1: General rules and rules for buildings* (NEN, 2011).

[212] NEN, *NEN-EN 1993-1-1: Eurocode 3: Design of steel structures - Part 1-1: General rules and rules for buildings* (NEN, 2006).

[213] D. Oehlers and M. Bradford, *Composite Steel and Concrete Structural Members: Fundamental Behaviour* (Pergamon Press, 1995).

[214] F. Eggert, *Einfluss der Verdübelung auf das Trag-und Verformungsverhalten von Verbundträgern mit und ohne Profilblech*, Ph.D. thesis, Universität Stuttgart (2019).

[215] R. Bärtschi, *Load-bearing behaviour of composite beams in low degress of partial shear connection*, Ph.D. thesis, ETH Zurich (2005).

[216] R. Lawson, E. Aggelopoulos, R. Obiala, F. Hanus, C. Odenbreit, S. Nellinger, U. Kuhlmann, F. Eggert, D. Lam, X. Dai, and T. Sheehan, *Development of Improved Shear Connection Rules in Composite Beams (DISCCO)*, Tech. Rep. (European Commission - Dictorate-General for Research and Innovation, 2017).

[217] G. Ranzi, F. Gara, G. Leoni, and M. A. Bradford, *Analysis of composite beams with partial shear interaction using available modelling techniques: A comparative study,* Computers & Structures **84**, 930 (2006).

[218] N. M. Newmark, *Test and analysis of composite beams with incomplete interaction,* Proceedings of the Society for Experimental Stress Analysis **9**, 75 (1951).

[219] U. A. Girhammar and D. H. Pan, *Exact static analysis of partially composite beams and beam-columns,* International Journal of Mechanical Sciences **49**, 239 (2007).

[220] U. A. Girhammar, *A simplified analysis method for composite beams with interlayer slip,* International Journal of Mechanical Sciences **51**, 515 (2009).

[221] R. Xu and Y. Wu, *Static, dynamic, and buckling analysis of partial interaction composite members using Timoshenko's beam theory,* International Journal of Mechanical Sciences **49**, 1139 (2007).

[222] S. Schnabl, M. Saje, G. Turk, and I. Planinc, *Analytical solution of two-layer beam taking into account interlayer slip and shear deformation,* Journal of Structural Engineering **133**, 886 (2007).

[223] L. C. P. Yam and J. C. Chapman, *The inelastic behaviour of simply supported composite beams of steel and concrete,* Proceedings of the Institution of Civil Engineers **41**, 651 (1968).

[224] R. M. Lawson, D. Lam, E. S. Aggelopoulos, and S. Nellinger, *Serviceability performance of steel–concrete composite beams,* Proceedings of the Institution of Civil Engineers - Structures and Buildings **170**, 98 (2017).

[225] A. O. Adekola, *Partial interaction between elastically connected elements of a composite beam,* International Journal of Solids and Structures **4**, 1125 (1968).

[226] T. M. Roberts, *Finite difference analysis of composite beams with partial interaction,* Computers & Structures **21**, 469 (1985).

[227] R. I. M. Al-Amery and T. M. Roberts, *Nonlinear finite difference analysis of composite beams with partial interaction,* Computers & Structures **35**, 81 (1990).

[228] M. J. S. Hirst and M. F. Yeo, *The analysis of composite beams using standard finite element programs,* Computers & Structures **11**, 233 (1980).

[229] M. R. Salari, E. Spacone, P. B. Shing, and D. M. Frangopol, *Nonlinear analysis of composite beams with deformable shear connectors,* Journal of Structural Engineering **124**, 1148 (1998).

[230] S. Schnabl, M. Saje, G. Turk, and I. Planinc, *Locking-free two-layer timoshenko beam element with interlayer slip,* Finite Elements in Analysis and Design **43**, 705 (2007).

[231] A. Zona and G. Ranzi, *Finite element models for nonlinear analysis of steel–concrete composite beams with partial interaction in combined bending and shear,* Finite Elements in Analysis and Design **47**, 98 (2011).

[232] A. Chakrabarti, A. H. Sheikh, M. Griffith, and D. J. Oehlers, *Analysis of composite beams with partial shear interactions using a higher order beam theory,* Engineering Structures **36**, 283 (2012).

[233] A. Uddin, A. H. Sheikh, D. Brown, T. Bennett, and B. Uy, *A higher order model for inelastic response of composite beams with interfacial slip using a dissipation based arc-length method,* Engineering Structures **139**, 120 (2017).

[234] G. Ranzi, M. A. Bradford, and B. Uy, *A direct stiffness analysis of a composite beam with partial interaction,* International Journal for Numerical Methods in Engineering **61**, 657 (2004).

[235] G. Ranzi and M. A. Bradford, *Analysis of composite beams with partial interaction using the direct stiffness approach accounting for time effects,* International Journal for Numerical Methods in Engineering **78**, 564 (2009).

[236] S. L. Bakoss, R. I. Gilbert, K. A. Faulkes, and V. A. Pulmano, *Long-term deflections of reinforced concrete beams,* Magazine of Concrete Research **34**, 203 (1982).

[237] R. Liu, Z. Feng, H. Ye, and Y. Liu, *Stress redistribution of headed stud connectors subjected to constant shear force,* International Journal of Steel Structures (2019), 10.1007/s13296-019-00295-3.

[238] M. A. Bradford and R. I. Gilbert, *Non-linear behaviour of composite beams at service loads,* The Structural Engineer **67**, 263 (1989).

[239] A. M. Tarantino and L. Dezi, *Creep effects in composite beams with flexible shear connectors,* Journal of Structural Engineering **118**, 2063 (1992).

[240] M. A. Bradford and R. I. Gilbert, *Composite beams with partial interaction under sustained loads,* Journal of Structural Engineering **118**, 1871 (1992).

[241] L. Dezi and A. M. Tarantino, *Creep in composite continuous beams. i: Theoretical treatment,* Journal of Structural Engineering **119**, 2095 (1993).

[242] B. Jurkiewiez, S. Buzon, and J. Sieffert, *Incremental viscoelastic analysis of composite beams with partial interaction,* Computers & Structures **83**, 1780 (2005).

[243] F. Virtuoso and R. Vieira, *Time dependent behaviour of continuous composite beams with flexible connection,* Journal of Constructional Steel Research **60**, 451 (2004).

[244] G. Ranzi and M. Bradford, *Analytical solutions for the time-dependent behaviour of composite beams with partial interaction,* International Journal of Solids and Structures **43**, 3770 (2006).

[245] F. Gara, G. Ranzi, and G. Leoni, *Time analysis of composite beams with partial interaction using available modelling techniques: A comparative study,* Journal of Constructional Steel Research **62**, 917 (2006).

[246] M. A. Bradford, *Generic modelling of composite steel–concrete slabs subjected to shrinkage, creep and thermal strains including partial interaction,* Engineering Structures **32**, 1459 (2010).

[247] Q.-H. Nguyen, M. Hjiaj, and B. Uy, *Time-dependent analysis of composite beams with continuous shear connection based on a space-exact stiffness matrix,* Engineering Structures **32**, 2902 (2010).

[248] F. Gara, G. Ranzi, and G. Leoni, *Short- and long-term analytical solutions for composite beams with partial interaction and shear-lag effects,* International Journal of Steel Structures **10**, 359 (2010).

[249] X. Liu, M. A. Bradford, and R. E. Erkmen, *Time-dependent response of spatially curved steel-concrete composite members. i: Computational modeling,* Journal of Structural Engineering **139**, 04013004 (2013).

[250] S. Al-deen, G. Ranzi, and Z. Vrcelj, *Full-scale long-term experiments of simply supported composite beams with solid slabs,* Journal of Constructional Steel Research **67**, 308 (2011).

[251] S. Al-deen, G. Ranzi, and Z. Vrcelj, *Full-scale long-term and ultimate experiments of simply-supported composite beams with steel deck,* Journal of Constructional Steel Research **67**, 1658 (2011).

[252] R. Song, Y. lin Zhan, F. Liu, and R. da Zhao, *Long-term push out test and finite element analysis of steel-concrete composite specimens,* Journal of Traffic and Transportation Engineering (2019).

[253] O. Mirza and B. Uy, *Finite element model for the long-term behaviour of composite-steel concrete push tests,* Steel and Composite Structures **10**, 45 (2010).

[254] O. Mirza and B. Uy, *Numerical modelling of short and long term behaviour of headed stud shear connector in composite steel-concrete beams,* in *Incorporating Sustainable Practice in Mechanics of Structures and Materials: Proceedings of the 21st Australian Conference on the Mechanics of Structures and Materials,* edited by S. Fragomeni, S. Venkatesan, N. T. K. Lam, and S. Setunge (2010) pp. 91–96.

[255] M. A. Bradford and R. I. Gilbert, *Time-dependent behaviour of simply-supported steel-concrete composite beams,* Magazine of Concrete Research **43**, 265 (1991).

[256] W. Xue, M. Ding, C. He, and J. Li, *Long-term behavior of prestressed composite beams at service loads for one year,* Journal of Structural Engineering **134**, 930 (2008).

[257] X. Liu, M. A. Bradford, and R. E. Erkmen, *Time-dependent response of spatially curved steel-concrete composite members. II: Curved-beam experimental modeling,* Journal of Structural Engineering **139**, 04013003 (2013).

[258] H. Ban, B. Uy, S. W. Pathirana, I. Henderson, O. Mirza, and X. Zhu, *Time-dependent behaviour of composite beams with blind bolts under sustained loads,* Journal of Constructional Steel Research **112**, 196 (2015).

I

MATERIALS FOR INJECTED BOLTED CONNECTIONS

3

SHORT-TERM MECHANICAL PROPERTIES OF (STEEL-REINFORCED) RESIN

The important work of moving the world forward
does not wait to be done by perfect men.

George Eliot

INTRODUCTION

This chapter examines the mechanical properties of (steel-reinforced) epoxy resin systems RenGel SW 404 + HY 2404/5159 under short-term loads. The literature review identified this epoxy resin system as the most suitable for application in injected bolted connections. Its steel-reinforced variant is considered to understand its potential benefits in terms of stiffness and resistance compared to the conventional epoxy resin system.

This chapter is subdivided into five sections. Section 3.1 presents the design and results of experimental compression tests on confined and unconfined specimens. A hybrid homogenisation method is developed in Section 3.2 to predict the uniaxial elastic compression behaviour of steel-reinforced resin. Section 3.3 covers the prediction of the tensile response of the steel-reinforced resin by performing computational homogenisation using the finite element method. The chapter proceeds with Section 3.4, where Drucker-Prager parameters for (steel-reinforced) resin are derived to enable implementation of the pressure-dependent material properties in commercial finite element software packages. The chapter concludes with Section 3.5, summarising the main findings of this chapter.

3.1. Experimental work

3.1.1. Specimen design and experimental details

In relation to this chapter, a series of uniaxial compression tests was conducted on cylindrical (steel-reinforced) resin specimens under confined and unconfined conditions. Two epoxy resin systems were considered: RenGel SW 404 with hardener HY 2404, and RenGel SW 404 with hardener HY 5159. The steel-reinforced resin specimens consisted of epoxy resin and spherical steel particles of nominal size class S330 conform standard J444 [4] in a loose random packing, corresponding to a nominal particle volume fraction of 60%.

The unconfined specimens had dimensions Ø26 × 50 mm. The aspect ratio $L/d \approx 2$ ensured that the effect of interface friction on the Young's Modulus was smaller than <2% [5]. An aspect ratio of 1 (Ø22 × 22 mm) was adopted for the confined specimens. These specimens were passively confined by a Ø30 × 50 mm S235 steel tube with a wall thickness of 4 mm. The load was transferred from the hydraulic actuator to the confined specimens by a snug-fit Ø21.5 × 40 mm solid steel pin. An overview of the design of both types of specimens is illustrated by Figure 3.1.

The compressive force F was applied using a stroke-controlled regime at a speed of 0.01 mm/s, equivalent to a nominal strain rate of 0.0002 s^{-1}. Two Ono Sokki GS-551 linear gauge sensors with a range of 0.001–5 mm were used to measure the axial deformation of the RenGel SW 404 + HY 2404 specimens: the experimental set-up including the gauge sensors is illustrated in Figure 3.2. For the RenGel SW 404 + HY 5159 specimens, five potentiometers were used: four at exterior corners of the frame and one adjacent to the specimen's surface.

The experimental test matrix is given in Table 3.1, which summarises the number of tests for each type of specimen. One unconfined resin and one steel-reinforced specimen based on RenGel SW 404 + HY 2404 were instrumented with strain gauges in axial and tangential directions to determine the respective Poisson ratios.

3.1.2. Results and discussion - unconfined specimens

The engineering stress-strain curves for the unconfined resin and steel-reinforced resin specimens are illustrated in Figure 3.3. The engineering stress and strain are defined as

$$\sigma = \frac{F}{A_0} \text{ and } \varepsilon = \frac{\delta}{L_0}, \tag{3.1}$$

respectively, where F represents the actuator force, A_0 is the initial cross-sectional area, and δ and L_0 are the contraction and initial length of the specimen, respectively.

The Young's Modulus E, the ultimate compression strength f_u, and the ductility (strain at $0.9 f_u$ on the descending branch of the curve) of the (steel-reinforced) resin specimens are summarised in Table 3.2 and Table 3.3 for the epoxy resins system with hardeners HY 2404

Table 3.1 | Test matrix of small-scale specimen.

Condition	Nominal geometry	RenGel SW 404 + HY 2404		RenGel SW 404 + HY 5159	
		Resin	Steel-reinforced resin	Resin	Steel-reinforced resin
Unconfined	Ø26.3 mm x 50 mm	5	5	3	3
Confined	Ø22 mm x 22 mm	5	5	-	-

(a) Unconfined condition.

(b) Confined condition.
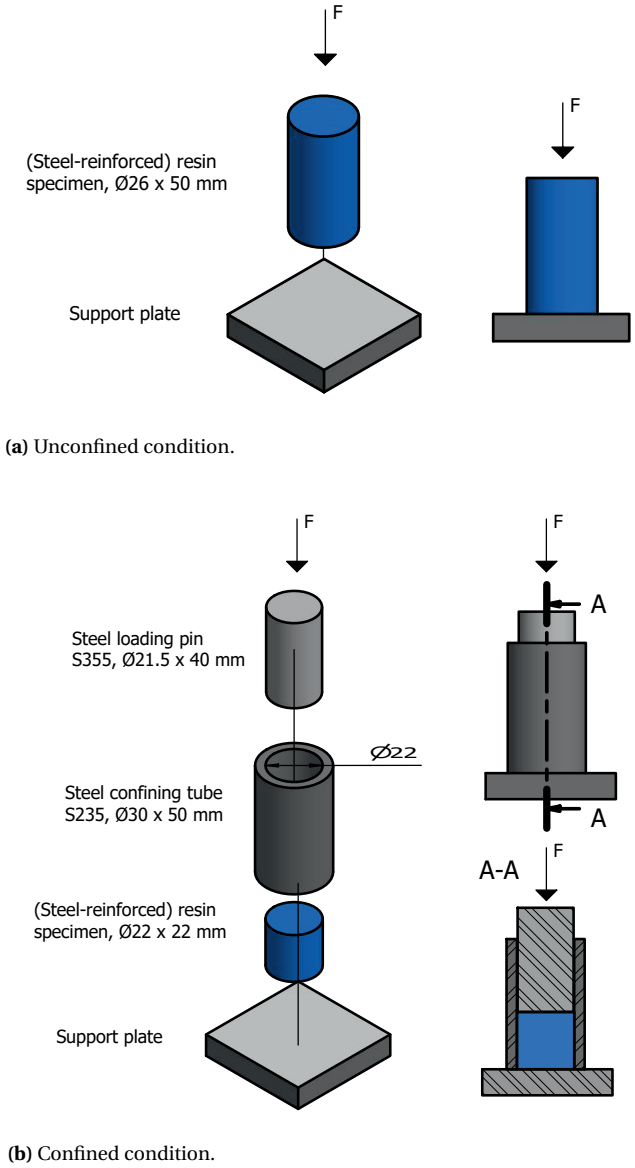
Figure 3.1 | Overview of small-scale (steel-reinforced) resin specimen test assemblies subject to an external force *F*.
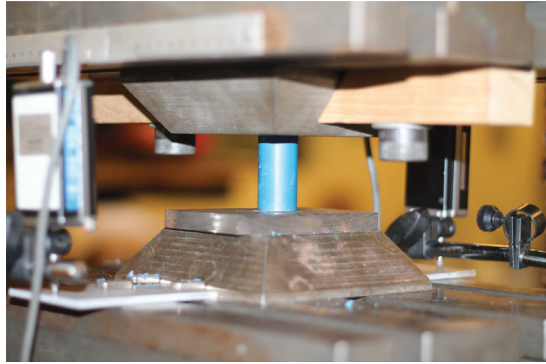
Figure 3.2 | Unconfined RenGel SW 404 + HY 2404 epoxy resin specimen in the experimental compression test set-up.
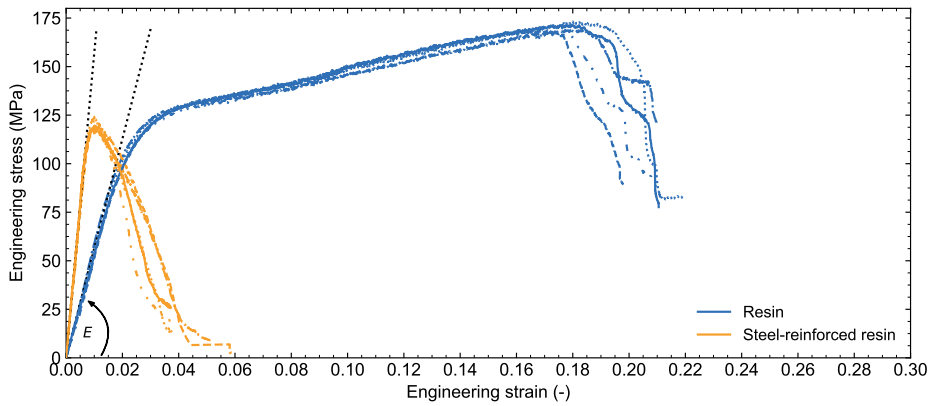
(a) RenGel SW 404 + HY 2404.
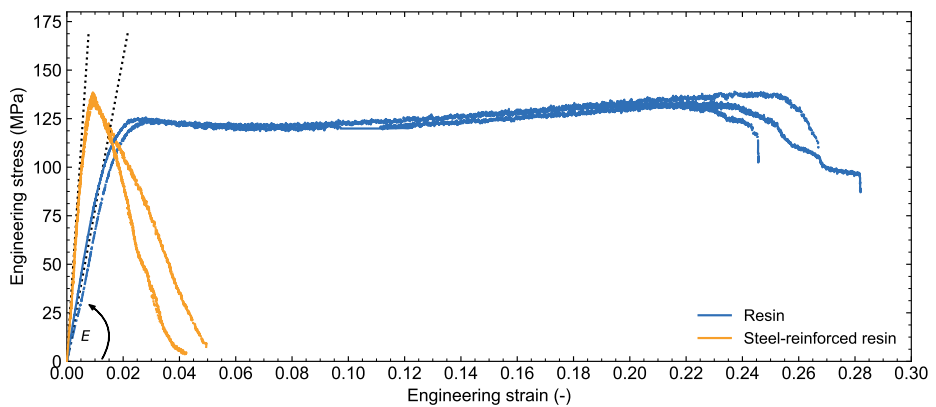
(b) RenGel SW 404 + HY 5159.

Figure 3.3 | Engineering stress-strain curves for the unconfined resin and steel-reinforced resin specimens.

and HY 5159, respectively. The Young's Modulus was determined over an interval of 40 MPa (approximately one-third of the stress at the onset of non-linearity) for which the slope of the curve was largest, to avoid the influence of initial settling of the specimen in the setup. This 40 MPa range was taken either between 20 and 60 MPa or 30 and 70 MPa, depending on the shape of the stress-strain curve.

The Young's Modulus of the non-reinforced epoxy resin systems exhibited little scatter between different but nominally identical specimens, with a weighted coefficient of variation of 6.8%. In addition, the stress at the onset of non-linearity and the ultimate compression strength did not vary significantly either. The nominal strain at failure was in the range of 19-26%, indicating that the non-reinforced epoxy resin system was highly ductile for both hardeners. Prior to failure, longitudinal and diagonal cracks developed in the specimen. Final failure occurred through explosive spalling along these cracks. The Poisson ratio, determined in the linear branch of the stress-strain curve of one of the RenGel SW 404 + HY 2404 specimens, was $\nu_r = 0.315$.

Figure 3.4 shows a comparison between the compressive stress-strain curves for the epoxy resin specimens, including the results obtained by Wedekamper [6] for hardener HY 404 (the predecessor of HY 2404). Specimens with hardeners HY 404 and HY 2404 showed a similar elastic behaviour, but demonstrated a significantly different post-elastic response: where specimens with hardener HY 404 demonstrated a stress plateau, specimens with hardener HY 2404 exhibited strain hardening. Similarly to the former, specimens with hardener HY 5159 also demonstrated a stress plateau, although these specimens on average showed a 39% higher Young's Modulus compared to the HY 2404 specimens. This increase can be attributed to its higher nominal *glass transition temperature* of 100 °C compared to 80 °C for HY 2404 according to the manufacturer: a higher glass transition temperature is a proxy for a stiffer polymer [7, 8].

The unconfined steel-reinforced specimens showed significantly higher Young's Moduli compared to the epoxy resin specimens, with a 178% and 180% increase for hardeners HY 2404 and HY 5159, respectively. The results suggest that the Young's Moduli of the steel-reinforced epoxy resin specimens increase proportionally to the increase of the Young's Modulus of the non-reinforced epoxy resin specimens. The variation of the Young's Modulus for the steel-reinforced specimens is in the same order of magnitude as for the resin specimen (weighted coefficient of variation 3.9%). The ductility of the two-phase composite material significantly decreased compared to the resin specimens: on average the strain at $0.9 f_u$ on the descending branch of the stress equalled 1.6%. Failure was initiated by separation of the epoxy resin and steel particles at average stress levels of 120.3 MPa and 136.2 MPa for hardeners HY 2404 and HY 5159, respectively. The Poisson ratio of the composite material was determined as $\nu_{srr} = 0.22$, which is outside the bounds of the Poisson ratios of the constituents ($\nu_r = 0.315$, $\nu_s = 0.30$), a phenomenon typical for composite materials [9, 10].

The density of each steel-reinforced specimen was determined to derive the volume fraction of the spherical steel particles. On average, the density of the steel-reinforced resin was $\rho_{srr} = 5.26$ g/cm^3, and the average densities of the resin and shot were $\rho_r = 1.86$ g/cm^3 and $\rho_s = 7.49$ g/cm^3, respectively. Based on the mean densities, the representative particle volume fraction was determined as $V_f = 60.1\%$. According to the supplier [11], the density and the bulk density of the spherical steel particles are 7.4 g/cm^3 and 4.4 g/cm^3, respec-

Table 3.2 | Experimental results of compression tests on unconfined specimens for epoxy resin system Ren-Gel SW 404 + HY 2404.

(a) Resin specimens.

Specimen	Young's Modulus (GPa)	Ultimate compression strength, f_u (MPa)	Strain at $0.9 f_u$ (%)
1	5.30	171.7	19.56
2	6.15	168.9	19.35
3	5.83	173.2	20.05
4	5.45	168.7	18.06
5	5.49	166.6	18.67
Mean	5.64	169.8	19.14
St. dev.	0.34	2.62	0.78

(b) Steel-reinforced resin specimens.

Specimen	Young's Modulus (GPa)	Ultimate compression strength, f_u (MPa)	Strain at $0.9 f_u$ (%)
1	15.9	118.0	1.66
2	16.3	119.5	1.55
3	15.5	124.1	1.39
4	15.6	122.1	1.78
5	15.1	118.0	1.41
Mean	15.7	120.3	1.56
St. dev.	0.41	2.72	0.165

Table 3.3 | Experimental results of compression tests on unconfined specimens for epoxy resin system Ren-Gel SW 404 + HY 5159.

(a) Resin specimens.

Specimen	Young's Modulus (GPa)	Ultimate compression strength, f_u (MPa)	Strain at $0.9 f_u$ (%)
1	8.55	134.1	25.4
2	7.47	133.7	24.7
3	7.43	139.0	26.6
Mean	7.81	135.6	25.5
St. dev.	0.63	2.62	1.07

(b) Steel-reinforced resin specimens.

Specimen	Young's Modulus (GPa)	Ultimate compression strength, f_u (MPa)	Strain at $0.9 f_u$ (%)
1	23.3	138.6	1.66
2	21.8	134.5	1.60
3	20.6	135.8	1.42
Mean	21.9	136.2	1.56
St. dev.	1.33	2.14	0.13
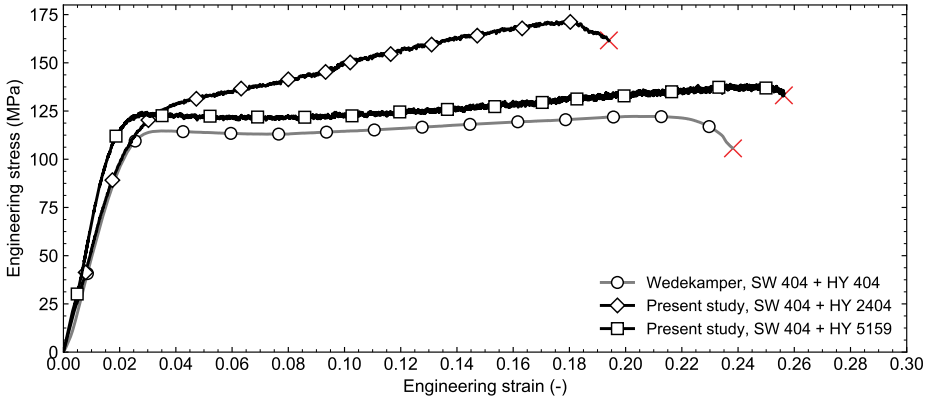
Figure 3.4 | Comparison between experimental compression tests (averaged) on RenGel SW 404 with three different types of hardener (HY 404, HY 2404, and HY 5159).

tively. This is equivalent to a particle volume fraction of 59.5%, which is consistent with the magnitude obtained based on the measurable characteristics of the specimens.

3.1.3. Results and discussion - confined specimens

The nominal engineering stress-strain curves for the confined resin and steel-reinforced resin specimens of epoxy resin system RenGel SW 404 + HY 2404 are illustrated in Figure 3.5, with the nominal engineering stress and strain defined by Equation 3.1.

Initially the stress increased linearly with increasing strain: the apparent Young's Moduli $\overline{E}$ (an observed value, not a material property) was determined in this linear branch over an interval of 60 MPa (approximately one-third of the stress at the onset of non-linearity) for which the slope of the curve was largest. This was done to avoid influence due to initial settling of the specimen. The magnitude of $\overline{E}$ for each specimen is presented in Table 3.4. The mean apparent Young's Moduli of the resin and steel-reinforced resin were $\overline{E}_{\mathrm{r}}$ = 7.6 GPa and $\overline{E}_{\mathrm{srr}}$ = 17.6 GPa, respectively.

Table 3.4 | Experimental results of compression tests on confined specimens for epoxy resin system RenGel SW 404 + HY 2404.

(a) Resin.

Specimen	Apparent Young's Modulus, $\overline{E}$ (GPa)
1	7.2
2	7.5
3	6.6
4	8.6
5	7.9
Mean	7.6
St. dev.	0.76

(b) Steel-reinforced resin.

Specimen	Apparent Young's Modulus, $\overline{E}$ (GPa)
1	15.4
2	20.0
3	18.9
4	17.9
5	16.1
Mean	17.6
St. dev.	1.9
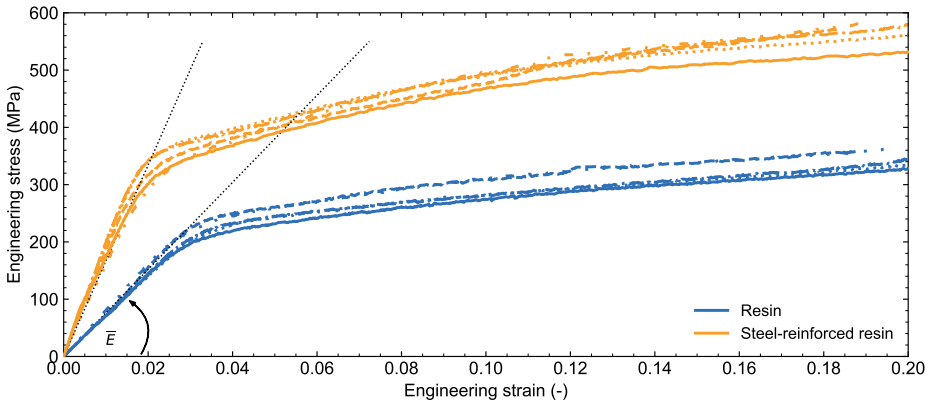
Figure 3.5 | Engineering stress-strain curves for the confined resin and steel-reinforced resin specimens, epoxy resin system RenGel SW 404 + HY 2404.

An analytical prediction method for the apparent Young's Modulus $\overline{E}$ can be derived based on Hooke's Law as

$$\overline{E} = E \left[\frac{1}{\frac{-v^2(Ed_t - 2E_t t_t)}{t_t E_t(v-1)} + 1} \right] \geq E, \tag{3.2}$$

where E and v are the Young's Modulus and Poisson ratio of the unconfined material, d_t and t_t are the centre line diameter and thickness of the confining tube, respectively, and E_t is the Young's Modulus of the tube. For the present geometrical (d_t = 26 mm, t_t = 4 mm) and material properties, the analytical solution for the apparent Young's Modulus of the confined resin and steel-reinforced resin is $\overline{E}_R = 1.36E_R$ and $\overline{E}_{SRR} = 1.10E_{SRR}$, respectively. This is in good agreement with the averaged experimental results $\overline{E}_R = 1.35E_R$ and $\overline{E}_{SRR} = 1.12E_{SRR}$, confirming that the Poisson ratio of the materials was accurately determined.

The non-linear branch of the stress-strain curve originated from (i) the non-linear behaviour of the material and (ii) yielding of the confining steel tube. The latter caused a reduction of the lateral confinement of the specimen, hence the experimentally obtained stress at the onset of non-linearity is a lower bound value. The plastic deformation of the steel tube is more pronounced for resin than steel-reinforced resin specimens, which can be attributed to the comparatively higher lateral expansion due to the higher Poisson ratio. It must be noted that the confined specimens could not be loaded to failure and that therefore the ultimate strength and ductility of these specimens was not determined.

3.2. HYBRID HOMOGENISATION METHOD: PREDICTING THE YOUNG'S MODULUS

3.2.1. INTRODUCTION AND OBJECTIVE

The mechanical response of steel-reinforced resin can be analysed at a *coarse* and *fine* scale: the former focuses on global *homogenised* material response, whereas the latter concentrates on the zoomed-in behaviour and interaction of the *material system*. Experimental

work, as described in Section 3.1, inherently focuses on coarse-scale behaviour, but does not provide explanations for the observations. Fine-scale modelling of steel-reinforced resin enables the prediction of the homogenised coarse-scale material properties; after validation, the fine-scale model can be used generically for other combinations of materials as long as the underlying assumptions remain valid.

An iconic example of homogenised coarse-scale response based fine-scale modelling is that of a two-phase linear-elastic composite, consisting of materials with Young's Moduli E_1 and E_2. The constituent materials can be oriented parallel and perpendicular to the direction of loading. Voigt [12] and Reuss [13] derived a fine-scale prediction model to determine the homogenised response for these two load cases. The Reuss and Voigt models provide upper and lower bound analytical solutions for the homogenised modulus E_c, respectively, and are expressed by

$$E_{c,upper} = V_f E_1 + (1 - V_f) E_2, \text{ and} \tag{3.3}$$

$$E_{c,lower} = \left(\frac{V_f}{E_1} + \frac{1 - V_f}{E_2} \right)^{-1}, \tag{3.4}$$

where V_f and $(1 - V_f)$ denote the volume fractions of the materials with Young's Moduli E_1 and E_2, respectively.

The dispersion of the materials in steel-reinforced resin fulfils the assumptions of neither the Voigt nor the Reuss model. To determine the actual stress-strain relationship of steel-reinforced resin, a hybrid (analytical-numerical) homogenisation method was developed. The main objective of this method is to predict the Young's Modulus of the steel-reinforced resin, and its secondary objective is to determine the suitability of the model to simulate the non-linear behaviour.

3.2.2. Unit cell and representative volume element (RVE)

A three-dimensional *unit cell* with a body-centred cubic dispersion of reinforcing shot particles, see Figure 3.6, is assumed to represent the actual packing of the spheres in a connection or specimen. A cross-section of the unit cell is illustrated in Figure 3.7(a). By definition, the 3D unit cell has unity dimensions of $1 \times 1 \times 1$ mm.

To validate the assumption that a body-centred cubic packing of spheres is representative for the actual dispersion of spheres in steel-reinforced resin, a significantly larger cell ($6 \times 6 \times 12$ mm) with more (≈ 1000) and randomly distributed spherical particles was considered. This larger cell with random sphere dispersion is considered as a *representative volume element* (RVE) because it meets the following criteria:

- it is "entirely typical of the whole mixture on average" [14],

- it is "the smallest material volume element of the composite for which the usual spatially constant (overall modulus) macroscopic constitutive representation is a sufficiently accurate model to represent mean constitutive response" [15],

The validation of the assumed unit cell using a representative volume element is important to ensure accurate characterisation of the structural complexity of the composite material [16, 17]. Several methods are available in literature that are capable of randomly distributing spherical particles, e.g. the Dropping and Rolling Method [18], the Optimized Dropping

and Rolling Method [19] and the Gravitational Sphere Packing Method [20]. All aforementioned models require the definition of several algorithms, e.g. to determine if spheres are touching, whether the position of the sphere is stable, how a stable sphere position can be achieved, etc. To simplify the generation of a random-packed sphere skeleton, the gravity principle of the Gravitational Sphere Packing Method was used, but the dropping of and interaction between spheres was solved using 3D simulation package Blender. A large number of nominally identical spheres was generated and dropped into a rectangular container. The remaining voids were assumed to be filled with resin. The mechanical behaviour of the generated 3D sphere skeleton and resin matrix, see Figure 3.6, was analysed using the same method as for the body-centred cubic unit cell, which will be discussed in the following sections.

3.2.3. MODEL DERIVATION

Given a sample of steel-reinforced resin material, the volume fraction V_f of reinforcing spherical particles is expressed by

$$V_f = \frac{\frac{m}{V} - \rho_r}{\rho_s - \rho_r},$$
(3.5)

where m and V represent the mass and volume of the specimen, respectively, and ρ_r and ρ_s denote the density of the resin matrix and the steel particles, respectively. Based on this volume fraction and the number of spheres q in the unit cell, the sphere radius r can be determined by

$$r = \sqrt[3]{\frac{1}{q} \cdot \frac{3}{4} \frac{V_f}{\pi}},$$
(3.6)

where $q = 2$ for a body-centred cubic packing, see Figure 3.6.

The three-dimensional unit cell shown in Figure 3.6 is subdivided into $n \times n$ $(= n^2)$ equally sized elements in the xy plane. A cross-section of the unit cell is illustrated in Figure 3.7(a). Based on the volume fraction and dispersion of the reinforcing spheres, the average total height of the steel spheres $h_s(x_i, y_j)$ for each of the n^2 elements on the xy plane can be determined by

$$h_s(x_i, y_j) = \sum_{p=1}^{q} h_{s,p}(x_i, y_j),$$
(3.7)

where $1 \le i \le n$ and $1 \le j \le n$ identify the discrete element under consideration. The remainder of the discrete element consists of epoxy resin, therefore the height of the resin in each of the elements can be determined by

$$h_r(x_i, y_j) = 1 - h_s(x_i, y_j).$$
(3.8)

The equivalent composition of the discrete element introduced in Figure 3.7(a) is represented in 3.7(b). The resin and steel are modelled as two springs in series for each of the n^2 elements, see Figure 3.7(c). The equivalent spring stiffness of the steel and resin in each element can be determined by
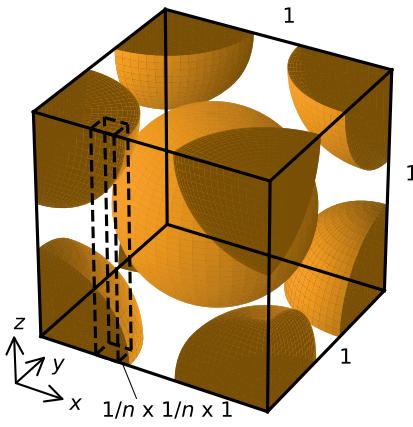
(a) Body-centered cubic arrangement, indicating a discrete element with size $1/n$ x $1/n$ x 1 within the unit cell.
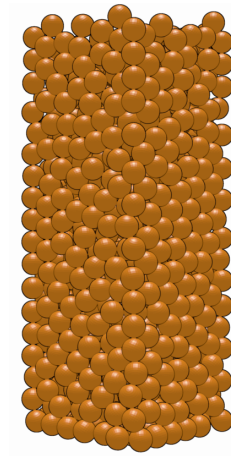
(b) Random distribution of steel spheres generated using Blender.

Figure 3.6 | Arrangements of spherical steel particles (orange).
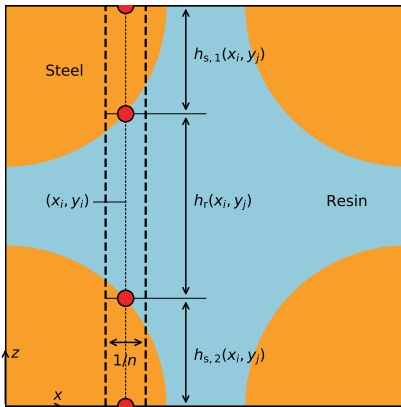
(a) Cross-sectional view of the unit cell, introducing the variables related to a discrete element.
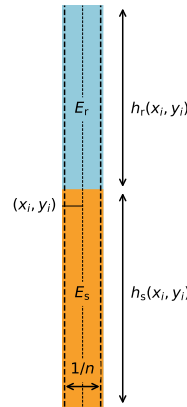
(b) Aggregated height of steel and resin of the discrete element.
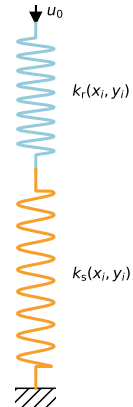
(c) Mechanical representation of subfigure (b).

Figure 3.7 | A cross-sectional view of the unit cell and the conversion of a discrete element into an equivalent mechanical spring.

$$k_s\left(x_i, y_j\right) = \frac{E_s \cdot \frac{1}{n^2}}{h_s\left(x_i, y_j\right)}, \text{ and} \tag{3.9}$$

$$k_r\left(x_i, y_j\right) = \frac{E_r \cdot \frac{1}{n^2}}{h_r\left(x_i, y_j\right)}, \tag{3.10}$$

respectively, where E_s and E_r respectively denote the Young's Moduli of the steel and resin. The equivalent spring stiffness k_{eq} of these two springs in series is given by

$$k_{eq}\left(x_i, y_j\right) = \frac{k_r\left(x_i, y_j\right) \cdot k_s\left(x_i, y_j\right)}{k_r\left(x_i, y_j\right) + k_s\left(x_i, y_j\right)}. \tag{3.11}$$

The Young's Modulus of the steel-reinforced resin can be computed by summing the equivalent spring stiffness of all n^2 elements, expressed by

$$E_{SRR} = \sum_{i=1}^{n} \sum_{j=1}^{n} k_{eq}\left(x_i, y_j\right). \tag{3.12}$$

The non-linear behaviour of each of the constituent materials can be implemented to estimate the non-linear branch of the stress-strain relationship of the two-phase material. This is not the main objective of the proposed method, but for completeness the principles and solution strategy are given in the following. An axial deformation u_0 is applied to each element within the unit cell. A trial solution of the deformation of the resin in each of the n^2 elements is assumed through the analytical solution for the linear-elastic stage, given by

$$u_r\left(x_i, y_j\right) = \frac{u_0}{1 + \frac{k_r(x_i, y_j)}{k_s(x_i, y_j)}}. \tag{3.13}$$

The strain in the resin layer can then be computed by

$$\varepsilon_r\left(x_i, y_j\right) = \frac{u_r\left(x_i, y_j\right)}{h_r\left(x_i, y_j\right)}, \tag{3.14}$$

which can be used to determine the stress $\sigma_r\left(x_i, y_j\right)$ based on the stress-strain curve of the matrix. Because the resin matrix and steel particles are in series, the stress through both materials is identical for each individual element, hence $\sigma_r\left(x_i, y_j\right) = \sigma_s\left(x_i, y_j\right) = \sigma\left(x_i, y_j\right)$. The resulting axial deformation of the steel is given by

$$u_s\left(x_i, y_j\right) = \varepsilon_s\left(x_i, y_j\right) \cdot h_s\left(x_i, y_j\right), \tag{3.15}$$

where $\varepsilon_s\left(x_i, y_j\right)$ can be determined based on stress-strain curve of the steel for the computed value of $\sigma\left(x_i, y_j\right)$.

The total actual deformation amounts to $u_r\left(x_i, y_j\right) + u_s\left(x_i, y_j\right)$. Iteration is carried out until the absolute difference between the applied deformation u_0 and actual deformation is sufficiently small, represented by the condition

$$\left| u_0 - \left[u_r\left(x_i, y_j\right) + u_s\left(x_i, y_j\right) \right] \right| \le |\Delta u_{max}|, \tag{3.16}$$

where $|\Delta u_{\max}| = u_0/5000$ is the convergence tolerance. If Eq. 3.16 is satisfied, the stress $\sigma(x_i, y_j)$ is stored. After iterating for all of the n^2 elements, the stress and strain of the homogenised two-phase material are determined by

$$\sigma = \frac{1}{n^2} \cdot \sum_{i=1}^{n} \sum_{j=1}^{n} \sigma(x_i, y_j), \text{ and} \tag{3.17}$$

$$\varepsilon = u_0, \tag{3.18}$$

respectively. Carrying out above procedure for a sufficient number of deformations u_0, the stress-strain curves of the steel-reinforced resin can be derived. The process of determining a point in the stress-strain curve of steel-reinforced resin is summarised by the flowchart provided in Figure 3.8.

3.2.4. Validation against experimental results

Figure 3.9 illustrates the predicted and experimentally obtained engineering stress-strain curve for the unconfined steel-reinforced resin specimens. Good agreement is observed in terms of the linear ascending branch. The hybrid homogenisation method overestimates the Young's Modulus by 5.7% as 16.6 GPa using the body-centred cubic unit cell for hardener HY 2404, whereas it is overestimated by 2.7% as 22.5 GPa for hardener HY 5159.

One of the possible reasons for the difference between actual and predicted Young's Modulus is that the reinforcing spherical particles are not completely solid. According to SAE J827 [21] and J444 [4], imperfections such as voids, shrinkage, cracks and deviations in particle shape are accepted to a certain extent, which have a negative influence on the mechanical properties of the composite material. Another reason for the discrepancy is that the model assumes perfect bonding between the models, whereas in reality this is not the case.

For the larger volume of $6 \times 6 \times 12$ mm with randomly generated sphere dispositions, a $5.5 \times 5.5 \times 11.5$ mm domain was selected to reflect the global particle volume fraction of 60%. This domain was analysed using the same hybrid homogenisation method as previously outlined, and the results are shown in Figure 3.9. The results demonstrate that the behaviour based on the unit cell and on the larger volume with random sphere disposition is very similar in terms of the Young's Modulus (difference < 1%) and the inelastic response. Therefore the assumption of a body-centred cubic packing of spheres is justified for uniaxial compression and under the assumption of perfect bonding between matrix and particles.

The implementation of a damage model is required to capture the descending part of the curve. However, there is no solid foundation to implement a phenomenological damage model to the proposed non-linear hybrid homogenisation method. This is because the model does not account for the (lateral) boundary effects of the unit cell: in the analytical model the deformation perpendicular to the direction of the applied load is not considered nor restrained. In addition, the model does not reflect the adhesion between the matrix and particles, which leads to a higher maximum compressive strength for steel-reinforced resin specimens with hardener HY 5159 than the resistance of the matrix itself. The complex interaction at the matrix-sphere interface is considered in more detail through computational homogenisation in Section 3.3.

3
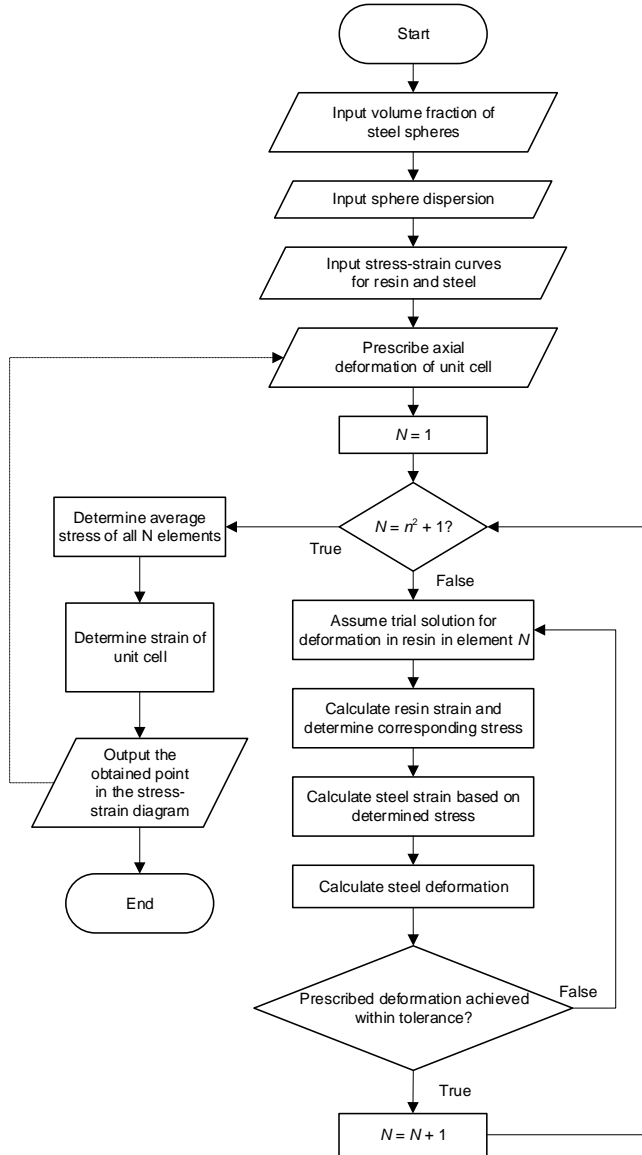
Figure 3.8 | Flowchart of the hybrid homogenization model for the determination of a point on the stress-strain curve of steel-reinforced resin. Repetition of the process for multiple prescribed axial deformations u_0 provides the complete stress-strain curve.
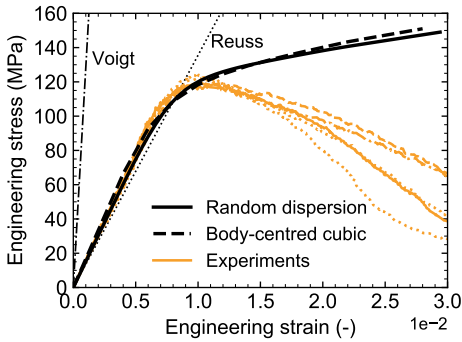
(a) RenGel SW 404 + HY 2404.
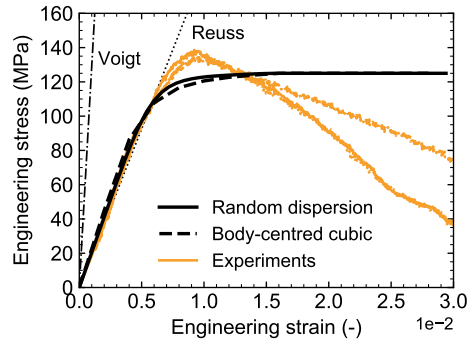
(b) RenGel SW 404 + HY 5159.

Figure 3.9 | Experimental and predicted stress-strain curves for unconfined steel-reinforced resin using the hybrid homogenisation method.

3.3. COMPUTATIONAL HOMOGENISATION: PREDICTING TENSILE RESISTANCE

3.3.1. INTRODUCTION AND OBJECTIVE

The coarse-scale homogenised response of steel-reinforced resin can be determined both analytically (see Section 3.2) and computationally. The latter approach involves the numerical evaluation of the fine-scale problem, for example using the finite element method. Despite its comparative (theoretical) complexity (see Section 2.4), the advantage of computational homogenisation using commercial finite element software is that readily available material models and interaction laws can be implemented in the fine-scale model to predict coarse-scale material properties.

In this section, the objective is to obtain data on the tensile properties of the steel-reinforced resin specimens through computational homogenisation. The fabrication of such physical specimens is hindered by the need for a certain undisturbed length: the injection pressure is not sufficient to inject the epoxy resin over longer distances. The injection of the epoxy resin at multiple locations induces imperfections, which may have a pronounced effect on the experimental results. Therefore, the tensile properties of the steel-reinforced resin are not obtained experimentally, but through computational homogenisation, and are used to obtain the material parameters to describe the pressure-dependent Drucker-Prager yield surface in Section 3.4.2.

3.3.2. UNIT CELLS

Two alternative two-dimensional unit cells are assumed based on the three-dimensional body-centred cubic unit cell considered in Section 3.2, see Figure 3.10 The unit cells are considered in 2D to reduce computational time. The volume fraction of steel spheres is identical for both alternatives, and the assumption is that a unique set of modelling parameters exists that lead to identical numerically obtained results for both alternative 2D unit cells.

The two alternative 2D unit cells are modelled using the commercial finite element

(a) 3D body-centred cubic unit cell.   **(b)** 2D unit cell - Alternative 1.   **(c)** 2D unit cell - Alternative 2.
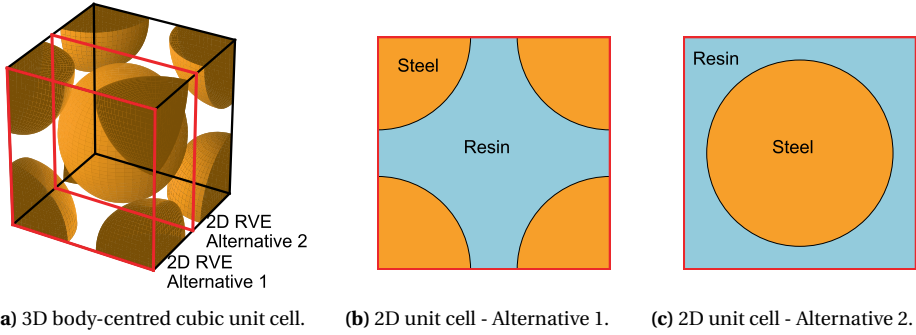
Figure 3.10 | Two alternative two-dimensional unit cells based on a 3D unit cell.

package `ABAQUS`, with periodic boundary conditions generated by `Homtools` [22]. The periodic boundary conditions enforce that the deformation at two opposite points on the boundary is the same, whereas the stresses at these points are equal but with opposite sign.

3.3.3. MATRIX, PARTICLE AND TRACTION-SEPARATION BEHAVIOUR

The material properties of the epoxy resin systems are described by the Drucker-Prager material models developed in Section 3.4. The steel particles are modelled as linear-elastic, characterised by a Young's Modulus $E_s = 210$ GPa.

The resin-steel interface behaviour is described by a traction-separation model, which includes linear-elastic behaviour, a damage initiation criterion and a damage evolution law. The traction vector **t** consists of a normal component t_n and shear components t_s and t_t, accompanied by a normal separation δ_n and shear separations δ_s and δ_t. The elastic interface behaviour is expressed by

$$\mathbf{t} = \begin{pmatrix} t_n \\ t_s \\ t_t \end{pmatrix} = \begin{bmatrix} k_n & 0 & 0 \\ 0 & k_s & 0 \\ 0 & 0 & k_t \end{bmatrix} \begin{pmatrix} \delta_n \\ \delta_s \\ \delta_t \end{pmatrix}, \tag{3.19}$$

based on the assumption of uncoupled behaviour, where k_n and $k_s = k_t$ are the normal and shear interface stiffness, respectively. The shear behaviour is assumed equal in both directions based on the isotropic nature of the material. The interface stiffness is determined according to

$$k_n = \frac{E_r}{t} \;\;;\;\; k_s = k_t = \frac{G_r}{t}, \tag{3.20}$$

where E_r and G_r denote the Young's Modulus and Shear Modulus of the resin matrix, respectively, and where t represents the interface thickness, assumed as 1% of the unit cell height.

The normal and shear interface strengths are denoted by t_n^0 and $t_s^0 = t_t^0$, respectively, where the superscript '0' indicates that damage initiates at these stress levels. A phenomenological quadratic traction criterion is used to predict the onset of damage initiation under a combination of normal and shear traction. This criterion is given by [23]

$$\left(\frac{t_\text{n}}{t_\text{n}^0}\right)^2 + \left(\frac{t_\text{s}}{t_\text{s}^0}\right)^2 + \left(\frac{t_\text{t}}{t_\text{t}^0}\right)^2 = 1, \tag{3.21}$$

where the variables without superscripts relate to the actual traction components. It should be noted that only positive normal traction (tension) contributes to the first damage initiation term in Eq. 3.21.

The damage evolution is assumed to follow the Benzeggagh-Kenane (BK) fracture criterion [24], which is particularly useful if the critical fracture energies in the two shear directions are the same, i.e. $G_\text{s}^\text{C} = G_\text{t}^\text{C}$. The BK fracture criterion is given by

$$G^\text{C} = G_\text{n}^\text{C} + \left(G_\text{s}^\text{C} - G_\text{n}^\text{C}\right)\left(\frac{G_\text{s} + G_\text{t}}{G_\text{n} + G_\text{s} + G_\text{t}}\right)^\eta, \tag{3.22}$$

where G_n, G_s and G_t denote the work done by the normal traction and both shear tractions, respectively, and where G^C represents the mixed-mode fracture energy. The normal critical fracture energy G_n^C, the shear critical fracture energies $G_\text{s}^\text{C} = G_\text{t}^\text{C}$ and the material parameter η are fitting parameters for the BK criterion, the latter is taken as $\eta = 1.8$ [25].

3.3.4. Results and discussion

The parameters t_n^0, $t_\text{s}^0 = t_\text{t}^0$, G_n^C and G_s^C were iteratively fitted to match the experimental compression results of the unconfined resin specimens in terms of the ultimate compression strength, subject to the constraint that both unit cell alternatives provide the same coarse-scale stress-strain curve. The calibrated values of the parameters are $t_\text{n}^0 = 45$ MPa, $t_\text{s}^0 = t_\text{t}^0 = 50$ MPa, $G_\text{n}^\text{C} = 0.18$ kJ/mm and $G_\text{s}^\text{C} = 0.40$ kJ/mm for the epoxy resin system with hardener HY 2404, and $t_\text{n}^0 = 58$ MPa, $t_\text{s}^0 = t_\text{t}^0 = 65$ MPa, $G_\text{n}^\text{C} = 0.18$ kJ/mm and $G_\text{s}^\text{C} = 0.35$ kJ/mm in case of hardener HY 5159 .

The Von Mises stress distribution and the deformed shape of the 2D unit cell alternatives are illustrated in Figure 3.11 during the softening stage of the steel-reinforced resin loaded in compression. The separation between resin matrix and steel particles occurs parallel to the direction of loading. The deformation and stress distribution for the 2D unit cells loaded in tension are shown in Figure 3.12: in this case separation occurs perpendicular to the direction of loading. The homogenised coarse-scale stress-strain curve of the steel-reinforced resin is illustrated in Figure 3.13 for both 2D unit cell alternatives.

The 2D unit cells are characterised by ultimate compressive strengths $f_\text{u} = 133.2$ MPa and $f_\text{u} = 134.9$ MPa for alternatives 1 and 2, respectively, for the epoxy resin system with hardener HY 5159. In case of hardener HY 2404, the ultimate compressive strengths are $f_\text{u} = 122.0$ MPa and $f_\text{u} = 120.3$ MPa for alternatives 1 and 2, respectively. For both epoxy resins systems good agreement is observed with the experimental results presented in Section 3.1. The tensile resistance of the steel-reinforced resin, central to this Section, equals on average (based on unit cell alternatives 1 and 2) 43.0 MPa in case of hardener HY 2404 and 54.6 MPa in case of hardener HY 5159.

The attention is drawn to the uncertainty of the tensile softening branch in Figure 3.13; the numerical model does not account for tensile fracture of the resin matrix. However, the tensile softening is not critical for the development of a material model aimed at application in bolted connections, where a dominantly multiaxial compressive stress state is prevalent. In any case, the ultimate tensile strength of the composite materials is smaller than that of the matrix, equal to 64.3 MPa according to Wedekamper [6] for hardener HY 404.

(a) Alternative 1.

(b) Alternative 2.
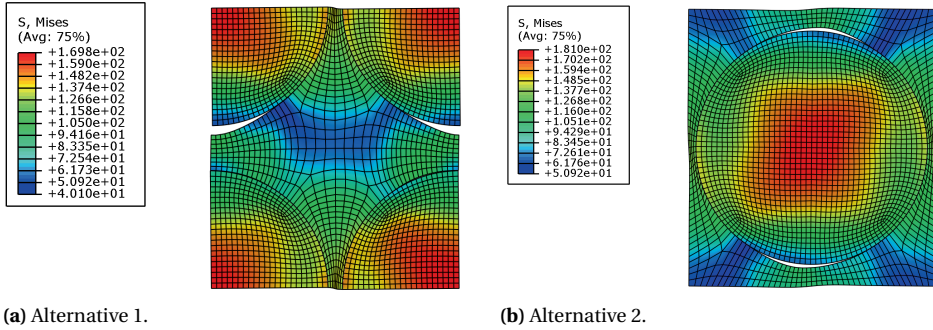
Figure 3.11 | Stress distribution and deformed shape of the unit cell at 1.5% coarse-scale compressive strain, for epoxy resin system RenGel SW 404 + HY 2404.

(a) Alternative 1.

(b) Alternative 2.
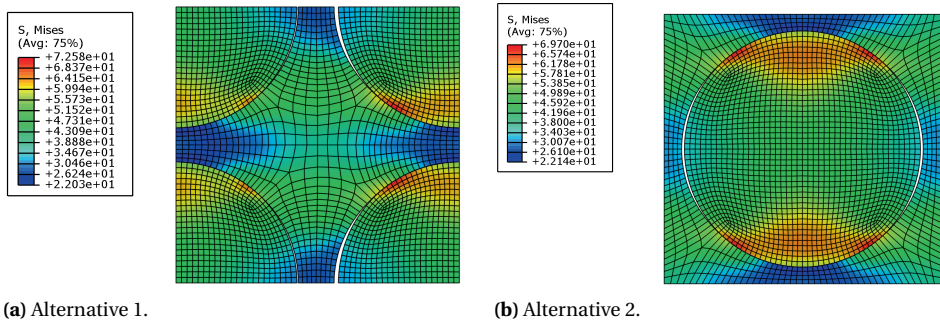
Figure 3.12 | Stress distribution and deformed shape of the unit cell at the maximum coarse-scale tensile stress, for epoxy resin system RenGel SW 404 + HY 2404.

(a) RenGel SW 404 + HY 2404.

(b) RenGel SW 404 + HY 5159.
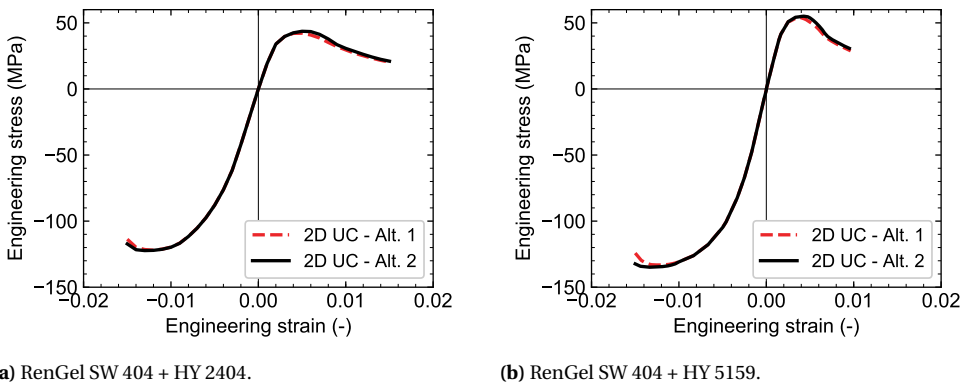
Figure 3.13 | Coarse-scale stress-strain curve of the steel-reinforced resin 2D unit cells (UC) obtained by numerical homogenisation.

The Poisson ratio of the composite material is determined numerically as $\nu_{\text{srr}} = 0.19$ and 0.20 for hardeners HY 2404 and HY 5159, which is slightly less than the experimentally obtained value of 0.22. The latter is adopted in the remainder of this work, because it is based on a physical three-dimensional rather than a digital two-dimensional specimen.

3.4. DRUCKER-PRAGER MATERIAL MODEL

This section presents the background to the Drucker-Prager material model, which describes the pressure-dependent yield surface of (for example) polymeric materials. The material properties established in Sections 3.1, 3.2 and 3.3 for the (steel-reinforced resin) systems RenGel SW 404 + HY 2404/5159 are used to establish Drucker-Prager material models. These material models can be implemented in commercially available finite element packages to predict the behaviour of the (steel-reinforced) epoxy under different conditions, for example in the confined environment of an injected bolted connection.

The Drucker-Prager criterion is a smooth pressure-dependent version of the Von Mises yield criterion, the latter given by

$$f(J_2) = \sqrt{J_2} - k = 0, \tag{3.23}$$

where k is the yield stress of the material in pure shear and J_2 is the second deviatoric stress invariant, defined by

$$J_2 = \tfrac{1}{6}\left[(\sigma_1 - \sigma_2)^2 + (\sigma_2 - \sigma_3)^2 + (\sigma_3 - \sigma_1)^2\right], \tag{3.24}$$

where $\sigma_1 \geq \sigma_2 \geq \sigma_3$ represent the principal stresses. The Von Mises yield criterion in terms of principal stresses is expressed by

$$\sqrt{\frac{1}{2}\left[(\sigma_1 - \sigma_2)^2 + (\sigma_2 - \sigma_3)^2 + (\sigma_3 - \sigma_1)^2\right]} = f_{\text{y,t}}, \tag{3.25}$$

where $f_{\text{y,t}}$ denotes the uniaxial tensile yield stress. In three-dimensional principle stress space, Eq. 3.25 represents a cylinder along a line equally inclined with respect to the principal stress axes (also known as the space diagonal). This implies that the yield strength in compression is equal to that in tension, which is not true for polymeric materials because their yield surface is pressure-dependent.

The Drucker-Prager criterion introduces pressure dependency to the Von Mises criterion by augmenting Eq. 3.23 with the first stress invariant $I_1 = \sigma_1 + \sigma_2 + \sigma_3$. This results in the yield criterion

$$f(I_1, J_2) = B I_1 + \sqrt{J_2} - k = 0, \tag{3.26}$$

where B and k are derived from experiments. The Drucker-Prager yield criterion is expressed in terms of the principal stresses as

$$\sqrt{\frac{1}{6}\left[(\sigma_1 - \sigma_2)^2 + (\sigma_2 - \sigma_3)^2 + (\sigma_3 - \sigma_1)^2\right]} = a + b\,(\sigma_1 + \sigma_2 + \sigma_3), \tag{3.27}$$

with a and b functions of the uniaxial tensile yield stress $f_{\text{y,t}}$ and the uniaxial compression yield stress $f_{\text{y,c}}$. Eq. 3.27 represents a cone along the space diagonal in three-dimensional principle stress space. In the meridional plane ($p - t$ plane) the linear Drucker-Prager yield

surface is represented by a straight line with slope β (also known as the friction angle) that intersects the t-axis at $(0, d)$, see Figure 3.14. The yield surface is described by

$$F = t - p \tan \beta - d = 0, \tag{3.28}$$

where p denotes the hydrostatic pressure, d is the material cohesion, and

$$t = \frac{1}{2} q \left[1 + \frac{1}{K} - \left(1 - \frac{1}{K} \right) \left(\frac{r}{q} \right)^3 \right]. \tag{3.29}$$

The Von Mises equivalent stress q is always positive and therefore so is t. Parameter K denotes the ratio of the yield stress in triaxial tension to the yield stress in triaxial compression, and is bound by $0.778 \leq K \leq 1$ to ensure convexity of the yield surface. Parameter r denotes the third invariant of the deviatoric stress.

The cohesion d of the material is related to the friction angle β and the uniaxial compression yield stress by

$$d = \left(1 - \frac{1}{3} \tan \beta \right) f_{y,c}, \tag{3.30}$$

if hardening is defined in compression. Isotropic hardening is included by updating Eq. 3.30 to the updated compression yield stress.

PLASTIC FLOW
The flow potential G for the Drucker Prager model is introduced as

$$G = t - p \tan \psi, \tag{3.31}$$

where ψ is the dilatation angle in the $p - t$ plane with respect to the t-axis. The plastic strain increment $d\epsilon^{\mathrm{pl}}$ is assumed to follow the potential flow rule given by

$$d\varepsilon^{\mathrm{pl}} = \frac{d\bar{\varepsilon}^{\mathrm{pl}}}{c} \frac{\partial G}{\partial \sigma}, \tag{3.32}$$

where c depends on how the hardening is defined. For hardening described in uniaxial compression, c is given by

$$c = \left(1 - \frac{1}{3} \tan \psi \right). \tag{3.33}$$

The plastic flow (or plastic strain increment) is perpendicular to the yield surface on the π-plane in case of associated flow, hence $\psi = \beta$. In case of non-associated flow, the plastic strain increment is not perpendicular to the yield surface ($\psi \neq \beta$). A characteristic subtype of non-associated flow is non-dilatant flow, for which $\psi = 0$. In the remainder of this Section, both non-dilatant and associated flow are considered.
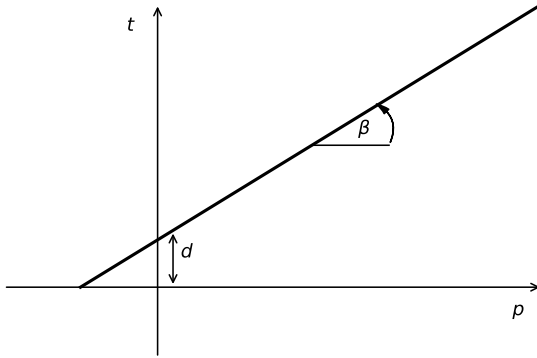
Figure 3.14 | Linear Drucker-Prager yield surface in the $p - t$ plane.

3.4.1. DRUCKER-PRAGER PARAMETERS WITHOUT TRIAXIAL DATA

The determination of the Drucker-Prager model parameters requires triaxial experimental data of the material. If this triaxial experimental data is not available, as is the case in this chapter, the Drucker-Prager model parameters can be obtained by matching the smooth Drucker-Prager yield surface to the hexagonal Mohr-Coulomb yield surface. The Mohr-Coulomb failure criterion is defined by

$$\frac{\sigma_1 - \sigma_2}{2} = \left[\frac{\sigma_1 + \sigma_2}{2}\right] \sin(\phi) + c\cos(\phi);$$

$$\frac{\sigma_2 - \sigma_3}{2} = \left[\frac{\sigma_2 + \sigma_3}{2}\right] \sin(\phi) + c\cos(\phi); \tag{3.34}$$

$$\frac{\sigma_3 - \sigma_1}{2} = \left[\frac{\sigma_3 + \sigma_1}{2}\right] \sin(\phi) + c\cos(\phi),$$

where ϕ and c represent the angle of internal friction and the cohesion, respectively. The Mohr-Coulomb material parameters c and ϕ can be obtained by solving the set of equations in Eq. 3.35, provided that the uniaxial tensile yield stress $f_{y,t}$ and uniaxial compressive yield stress $f_{y,c}$ are known.

$$f_{y,t} = \frac{2c\cos\phi}{1 + \sin\phi}$$

$$f_{y,c} = \frac{2c\cos\phi}{1 - \sin\phi} \tag{3.35}$$

The Drucker-Prager model parameters d and β are expressed in terms of Mohr-Coulomb parameters c and ϕ by

$$\tan\beta = \frac{\sqrt{3}\sin\phi}{\sqrt{1 + \frac{1}{3}\sin^2\phi}}, \text{ and}$$

$$\frac{d}{c} = \frac{\sqrt{3}\cos\phi}{\sqrt{1 + \frac{1}{3}\sin^2\phi}}, \tag{3.36}$$

in case of associated flow with $\psi < \beta$. For non-dilantant flow ($\psi = 0$)

$$\tan\beta = \sqrt{3}\sin\phi, \text{ and}$$

$$\frac{d}{c} = \sqrt{3}\cos\phi. \tag{3.37}$$

The parameter K (ratio of the yield stress in triaxial tension to the yield stress in triaxial compression) can be determined by

$$K = \frac{3 - \sin\phi}{3 + \sin\phi} \geq 0.778. \tag{3.38}$$

3.4.2. FROM EXPERIMENTAL RESULTS TO DRUCKER-PRAGER MATERIAL MODEL

The Drucker-Prager material parameters for the (steel-reinforced) resin are determined (i) based on the experimentally obtained compression stress-strain curves of the unconfined specimens, (ii) based on the tensile stress-strain curve for the epoxy resin SW 404 + HY 404 obtained by Wedekamper [6], see Figure 3.15, and (iii) based on the numerically obtained tensile response of the steel-reinforced resin.

The engineering stress-strain curves were converted in terms of true stress and true strain, through the expressions

$$\varepsilon' = -\ln(1 - \varepsilon) \text{ and}$$

$$\sigma' = \sigma(1 - \varepsilon), \tag{3.39}$$

in case of uniaxial compression and by

$$\varepsilon' = \ln(1 + \varepsilon) \text{ and}$$

$$\sigma' = \sigma(1 + \varepsilon), \tag{3.40}$$

in case of uniaxial tension, where subscript "$'$" distinguishes the true from the engineering values.

RESIN

The uniaxial true yield strength of the epoxy resin in compression, $f'_{\text{y,c,R}}$, was determined as 80 MPa for both hardeners HY 2404 and HY 5159, because at this point the non-linear compressive response initiates, see Figure 3.15. Hardening in compression is defined for $\sigma' \geq 80$ MPa based on the experimentally obtained results. Because the Drucker-Prager model can only account for one type of hardening (compression, or tension, or shear), the tensile hardening is implicitly included by defining $f'_{\text{y,t,R}}$ (tensile yield strength of the resin) as the ultimate tensile strength (taken as 64.3 MPa based on Wedekamper [6]), rather than at the onset of the non-linear branch of the stress-strain curve. This approach is justified

because the specimens loaded in tension do not exhibit any significant hardening nor any substantial plastic deformation, see Figure 3.15.

The Drucker-Prager material parameters for the epoxy resin are thus derived based on $f'_{y,c} = 80$ MPa and $f'_{y,t} = 64.3$ MPa. The intermediary Mohr-Coloumb parameters are $c = 35.9$ MPa and $\phi = 6.26°$ for both hardeners, although the (compressive) hardening definition is different, see Appendix A. The corresponding Drucker-Prager material parameters are summarised in Table 3.5.

STEEL-REINFORCED RESIN

The uniaxial true yield strength of the steel-reinforced resin in compression was taken as the ultimate compression strength, which is justified because no significant non-linear behaviour is observed in the ascending branch of the experimental results and because of the absence of any hardening. Based on this assumption and based the results obtained in Section 3.1, it follows that $f'_{y,c,SRR} = 120.3$ MPa for hardener HY 2404 and $f'_{y,c,SRR} = 136.2$ MPa for hardener HY 5159. Softening in compression is defined based on descending branch of the experimentally obtained stress-strain curve, the associated softening parameters are presented in Appendix A. The tensile yield strength of the steel-reinforced resin is taken equal to the ultimate tensile strength as $f'_{y,t,SRR} = 43.0$ MPa for hardener HY 2404 and as $f'_{y,t,SRR} = 56.4$ MPa for hardener HY 5159, see Section 3.3 for the determination of these values. This assumption is justified because the specimens loaded in tension do not exhibit any significant hardening, see Figure 3.13. The intermediary Mohr-Coloumb parameters are $c = 35.9$ MPa and $\phi = 28.2°$ for hardener HY 2404 and $c = 43.1$ MPa and $\phi = 25.3°$ for hardener HY 5159. The corresponding Drucker-Prager material parameters are summarised in Table 3.5.

3.4.3. VALIDATION AGAINST EXPERIMENTAL RESULTS

UNCONFINED SPECIMENS

The Drucker-Prager models were implemented in ABAQUS and assigned to a finite element representation of the nominal geometry of the unconfined compression specimens, which
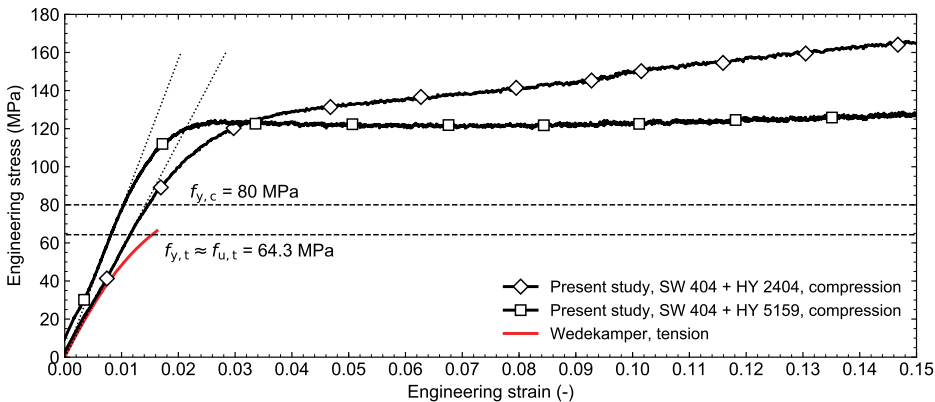
Figure 3.15 | Engineering stress-strain curve showing experimentally obtained results (averaged) in uniaxial tension (based on Wedekamper [6]) and uniaxial compression for resin specimens (based on present work).

Table 3.5 | Drucker-Prager parameters for RenGel SW 404 + HY 2404/5159.

Material	Associated flow			Non-dilatant flow		
	β	K	ψ	β	K	ψ
Resin, RenGel SW 404 + HY 2404	10.33°	0.93	10.33°	10.70°	1.00	0.00°
Resin, RenGel SW 404 + HY 5159	10.33°	0.93	10.33°	10.70°	1.00	0.00°
Steel-reinforced resin, RenGel SW 404 + HY 2404	38.30°	0.78	38.30°	39.44°	1.00	0.00°
Steel-reinforced resin, RenGel SW 404 + HY 5159	35.74°	0.78	35.74°	36.54°	1.00	0.00°

are modelled using C3D8R solid elements. The Young's Modulus of the (steel-reinforced)resin specimens were taken as the average values summarised in Tables 3.2 and 3.3 for hardeners HY 2404 and HY 5159, respectively.

Figures 3.16 and 3.17 show the experimentally and numerically obtained engineering stress-strain curves for the unconfined resin and steel-reinforced resin specimens, respectively. Good agreement is observed, indicating the material models were appropriate to model the uniaxial response of unconfined (steel-reinforced) resin over their full strain range. The results for "associated flow" and "non-dilatant flow" did not significantly differ.

CONFINED SPECIMENS

The Drucker-Prager models were also implemented in a finite element representation of the confined resin specimens. The confining steel tube (steel grade S235, $E = 210$ GPa), the steel loading pin (steel grade S355 $E = 210$ GPa) and the resin specimen (material properties according to Appendix A) were modelled using C3D8R solid elements. All translation degrees of freedom on the bottom surface of the steel base were fixed. An axial displacement was applied on the top surface of the steel loading pin to load the specimen until failure. An isotropic hardening model was defined for the steel parts based on their nominal material properties.

The numerically obtained engineering stress-strain curves of the confined resin and steel-reinforced resin specimens are illustrated in Figure 3.18, alongside the experimental results. A good agreement between the experiments and the numerical prediction is observed for the associated flow rule, indicating the suitability of these Drucker-Prager models to account for the confinement effects. The non-dilatant flow rule for the steel-reinforced resin led to an underestimation of the hardening behaviour; therefore in the remainder of this dissertation the associated flow rule is used unless stated otherwise. The deformed shape at $\varepsilon \approx 20\%$ of the actual and numerical resin specimens were in good agreement, see Figure 3.19. A similar agreement was found for the steel-reinforced resin specimens.
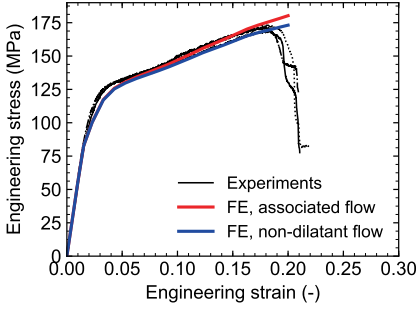
(a) RenGel SW 404 + HY 2404.
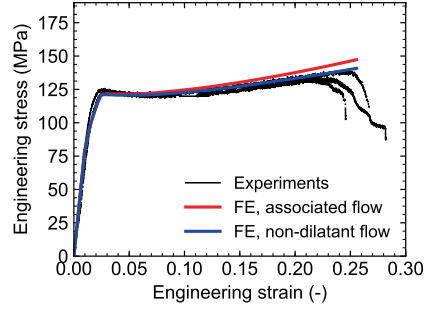
(b) RenGel SW 404 + HY 5159.

Figure 3.16 | Engineering stress-strain curve illustrating experimentally and numerically obtained results for unconfined resin specimens.
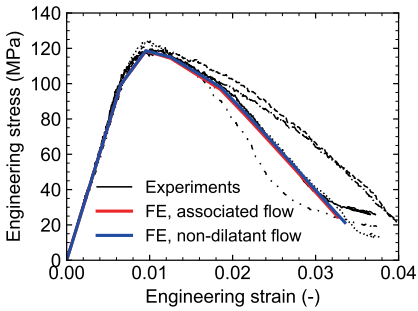
(a) RenGel SW 404 + HY 2404.
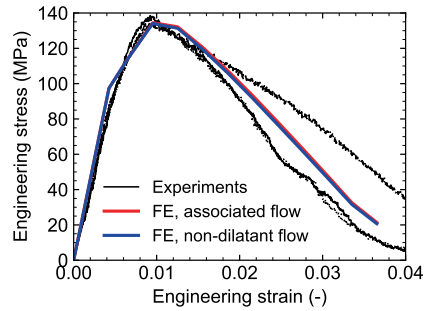
(b) RenGel SW 404 + HY 5159.

Figure 3.17 | Engineering stress-strain curve illustrating experimentally and numerically obtained results for unconfined steel-reinforced resin specimens.
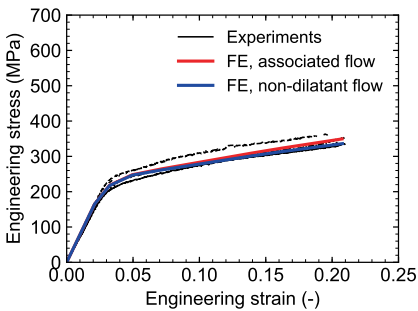
(a) Resin.
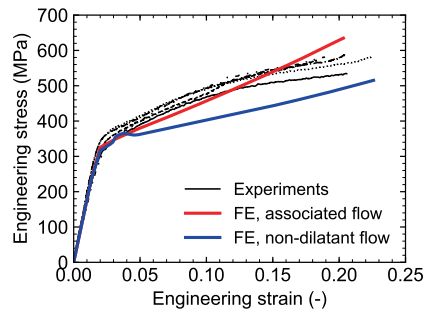
(b) Steel-reinforced resin.

Figure 3.18 | Experimental and numerical stress-strain curve for confined (steel-reinforced) RenGel SW 404 + HY 2404 specimens.

(a) Confining steel tube.

(b) Cross-section of numerical model of confined resin specimen.
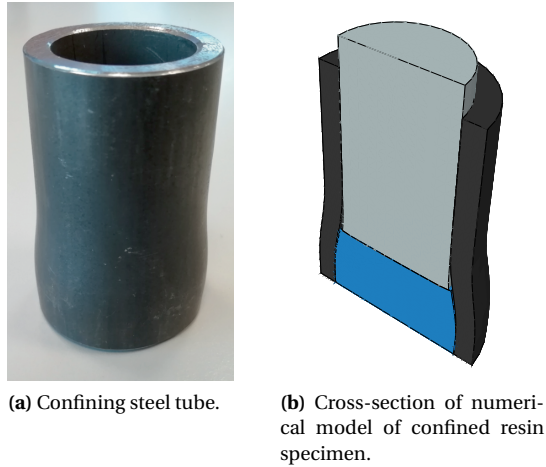
Figure 3.19 | Plastic deformation of confined resin specimen at 20% engineering strain.

3.5. CONCLUSIONS

This Chapter presented the short-term mechanical properties of the (steel-reinforced) epoxy resin system RenGel SW 404 + HY 2404/5159, which were derived based on experimental research and computational/numerical homogenisation. The main findings of the work are:

- The unconfined compressive stress-strain relationships for epoxy resin systems Ren-Gel SW 404 + HY 2404/5159 were determined experimentally. The results demonstrated that hardener HY 5159 led to a 39% higher Young's Modulus compared to HY 2404 ($E = 7.8$ GPa vs. $E = 5.6$ GPa, respectively), which was attributed to the higher glass transition temperature of RenGel SW 404 + HY 5159. Specimens with hardener HY 5159 did not exhibit substantial strain hardening, as opposed to specimens with hardener HY 2404. Both epoxy resin systems were highly ductile and failed in the range of 19 - 26% engineering strain at an average compression strength of 169.8 MPa and 135.6 MPa for hardeners HY 2404 and HY 5159, respectively. The Poisson ratio of the epoxy resin system was determined as $\nu_r = 0.315$.

- The unconfined compressive stress-strain relationships for the steel-reinforced versions of the epoxy resin systems RenGel SW 404 + HY 2404/5159 were determined experimentally as well. Also in this case hardener HY 5159 led to a higher (+39%) Young's Modulus compared to hardener HY 2404 ($E = 21.9$ GPa vs. $E = 15.7$ GPa, respectively), suggesting that the Young's Moduli of the epoxy resin and steel-reinforced epoxy resin specimens increase proportionally. The steel-reinforced resin specimens did not exhibit any hardening but failed on average at 1.6% engineering strain. The average compression strength of the steel-reinforced specimens was 120.3 MPa and 136.2 MPa for hardeners HY 2404 and HY 5159, respectively. The Poisson ratio of the steel-reinforced epoxy resin was determined as $\nu_{srr} = 0.22$.

- Experiments on confined epoxy resin and steel-reinforced epoxy resin specimens demonstrated apparent Young's Moduli $\overline{E}$ 35% and 12% higher, respectively, than the (un-

confined) Young's Modulus E. These results match well with existing analytical predictions ($\overline{E}/E = 1.36$ and $\overline{E}/E = 1.10$, respectively) that are based on the Poisson ratio and the characteristics of the confining element.

- A hybrid homogenisation method to predict the Young's Modulus of steel-reinforced epoxy resins was developed and validated against experimental results. The assumption of a body-centred cubic unit cell was validated by comparing to results obtained for a random disposition of spherical reinforcing steel particles in a larger volume. Good agreement between the predicted and experimentally obtained Young's Moduli was observed: on average, E was overestimated by 5.7% and 2.6% for hardeners HY 2404 and HY 5159, respectively.

- Computational homogenisation was used to predict the tensile response of steel-reinforced resin. Two two-dimensional unit cells were defined and it was assumed that a unique set of interaction parameters should lead to identical results for both unit cells. The traction-separation behaviour at the matrix-particle interface was calibrated against the experimental compression data. The predicted tensile strength of the steel-reinforced epoxy resins equalled 43.0 MPa and 54.6 MPa for hardeners HY 2404 and HY 5159, respectively.

- A linear Drucker-Prager material model was derived for epoxy resin systems Ren-Gel SW 404 + HY 2404/5159 based on the compression experiments and based on tensile test data presented in the literature. A similar approach was followed for the steel-reinforced specimens, but the tensile strength was predicted using computational homogenisation. The model parameters (β, K, ψ) were iteratively calibrated to match the experimental results and are summarised in Appendix A. The Drucker-Prager material model was implemented in `ABAQUS` and demonstrated good agreement with the data obtained for unconfined and confined specimens over the full strain range. No substantial difference between material models based on non-dilatant and associated flow was observed, except for the confined steel-reinforced resin specimens, for which the associated flow rule was most appropriate .

4

Uniaxial creep response of (steel-reinforced) resin

*Each problem that I solved became a rule
which served afterwards to solve other problems.*

René Descartes

How much easier it is to be critical than to be correct.

Benjamin Disraeli

Introduction

This chapter examines the time-dependent deformation of (steel-reinforced) epoxy resin system RenGel SW 404 + HY 5159 under sustained uniaxial compressive stress. Creep experiments at three stress levels (30, 60 and 90 MPa) are conducted, and the results provide input to fit phenomenological creep models for both injectants. Subroutines are developed for use in `ABAQUS` to complement the short-term material models (derived in Chapter 3) with the calibrated creep law.

This chapter is subdivided into three sections. Section 4.1 presents the design and results of uniaxial compressive creep tests on (steel-reinforced) epoxy resin specimens. The experimental results are used in Section 4.2 to derive a phenomenological creep model for both injectants. These creep models are implemented in `ABAQUS` through a user-defined `CREEP` subroutine and are validated against the experimental results. The chapter concludes with Section 4.3, summarising the main findings of this chapter.

4.1. EXPERIMENTAL WORK

4.1.1. SPECIMEN DESIGN AND EXPERIMENTAL DETAILS

The previous chapter addressed the short-term mechanical properties of (steel-reinforced) epoxy resin systems RenGel SW 404 + HY 2404/5159. However, the literature review revealed that the long-term behaviour of the injected bolted connections (IBCs) typically governs the design. Because of the bearing-type force transfer of IBCs, the compressive creep properties of the injectants are the most relevant to obtain.

The experimental work presented in this chapter focuses on the (steel-reinforced) epoxy resin system RenGel SW 404 + HY 5159. The time-dependent deformation of these materials was obtained by uniaxial compressive creep tests on unconfined (steel-reinforced) epoxy resin specimens. Similar as in Chapter 3, the specimens had a nominal diameter of 26 mm. The height of the resin and steel-reinforced resin specimens were 45 mm and 50 mm, respectively, and differed because of their respective production processes. No experiments on confined specimens were conducted because companion tests focusing on the cyclic response of the aforementioned injectants revealed a large influence of friction at the interface between injectant and confining cylinder [26].

Each specimen was subjected to a constant nominal compressive stress of 30, 60 or 90 MPa for a duration of one week (6×10^5 s). This relatively short time period was considered to be adequate for acquisition of benchmark data while awaiting delivery of a more advanced parallel testing apparatus. The three different stress levels correspond to approximately 22%, 44% and 66% of the short-term uniaxial compression resistance of the (steel-reinforced) epoxy resin specimens. The external load was applied by a hydraulic actuator at rate of 0.5 kN/mm. Four Ono Sokki GS-551 LVDTs with a range of 0.001-5 mm measured the contraction of the specimen at the corners of the square loading plates. Two specimens for each load level and material were tested, which led to a total duration of the experimental campaign of 12 weeks. To reduce the duration of future test series, a parallel testing apparatus was developed.

DEVELOPMENT OF PARALLEL TESTING APPARATUS

The long-term character of creep experiments calls for parallel testing of multiple specimens to reduce the time required to complete a research programme. To this extent, an experimental setup that addresses the need for long-term parallel testing of specimens under uniaxial compression was developed in collaboration with the Electronic and Mechanical Support Division (DEMO) of Delft University of Technology. Using this experimental setup, both resin and steel-reinforced resin specimens could be tested parallel in time, and the natural variation between test repetitions is accounted for by using multiple specimens of each type.

Figure 4.1 provides an overview of the proposed setup, which is colloquially known as the *creep tower* because of its appearance and function. The creep tower consists of 10 specimen layers, each consisting of three nominally identical specimens concentrically placed around the centroidal axis of the setup on an aluminium plate stabilised by leaf springs. The relative deformation between two plates is measured using potentiometers at three locations around their circumference, and resembles the (time-dependent) deformation of the specimen. Every component of the experimental setup can resist temperatures up to 80°C to enable accelerated creep testing.

An hydraulic actuator is located at the base of the creep tower, directly below the speci-
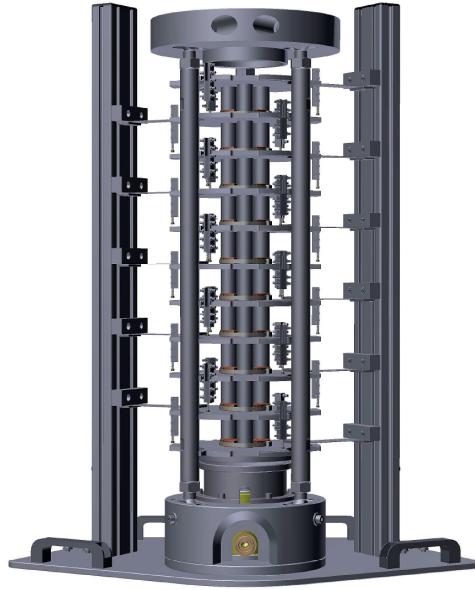
Figure 4.1 | Overview of *creep tower*: an experimental setup under development in collaboration with DEMO to obtain the uniaxial creep response of (injection) materials more efficiently compared to single-specimen testing.

men layers and a load cell. At the top of the setup is a stainless steel plate, connected to the base of the setup by three Ø30 mm stainless steel tension rods. These rods provide internal force equilibrium. A ball bearing mitigates any effects related to potential skewness of the assembly because of geometrical or dimensional imperfections of the specimens. The hydraulic actuator is manually controlled to reduce the complexity of the setup. The reduction of force over time because of the creep deformation of the specimens is mitigated by the use of an hydraulic accumulator, in favour of a set of spring plates. If the actuator force drops below a threshold (nominal value minus accepted tolerance) the force must be manually readjusted. However, because of the hydraulic accumulator, only infrequent adjustments are expected to be necessary outside the first few hours after the initial load application.

The creep tower is nearing completion and preliminary tests are scheduled to validate its results against those obtained by single specimens, for example those obtained in this chapter. The validated creep tower is expected to contribute to an efficient and effective determination of the uniaxial creep properties of (steel-reinforced) resin.

4.1.2. RESULTS AND DISCUSSION

The experimental results are considered in terms of the *creep strain*, which was defined as the accumulated engineering strain since the time the load was first fully applied. The creep strain is expressed by the equation

$$\varepsilon_{\mathrm{cr}}\left(t\right) = \varepsilon\left(t + t_0\right) - \varepsilon\left(t_0\right), \tag{4.1}$$

where t_0 is the time instant where the load was first fully applied, and t denotes the time variable representing the duration of the sustained load.

Figure 4.2 illustrates the development of the creep strain over time for the (steel-reinforced) resin specimens. The results of the epoxy resin specimens indicated that not only the magnitude of the creep strain, but also that the shape of the creep strain curve depended on the magnitude of the nominal stress. For the steel-reinforced resin specimens the shape of the creep strain curve did not significantly vary between the three stress levels (e.g. see Figure 4.7). The averaged creep strain after 7 days (6×10^5 s) is summarised in Figure 4.3, which shows that both injectants demonstrated non-linear viscoelastic behaviour, although this was more pronounced for resin compared to steel-reinforced resin specimens.

Figure 4.4 shows the ratio of the resin creep strain $\varepsilon_{\mathrm{cr,r}}$ over the steel-reinforced resin creep strain $\varepsilon_{\mathrm{cr,srr}}$ for equal nominal stress σ as a function of time. It was observed that at $\sigma = 30$ MPa the ratio $\varepsilon_{\mathrm{cr,r}}/\varepsilon_{\mathrm{cr,srr}}$ was quasi-constant over time and, on average, equalled 3.50. This implies that at this stress level both injectants were characterised by a similar time dependency, but that the creep strain of the steel-reinforced resin specimens was only 28% of that of the resin specimens. For stress levels $\sigma = 60$ and 90 MPa, the ratio $\varepsilon_{\mathrm{cr,r}}/\varepsilon_{\mathrm{cr,srr}}$ increased over time, suggesting that the creep rate of resin specimens reduced less rapidly than for steel-reinforced resin specimens. For a stress of 90 MPa, the creep strain of the resin specimens was 23.5 times that of the steel-reinforced resin: the shape of the curve suggests that the ratio $\varepsilon_{\mathrm{cr,r}}/\varepsilon_{\mathrm{cr,srr}}$ will increase further over time. Therefore the results suggest that the benefit of steel-reinforced resin to reduce creep deformation becomes more pronounced at higher compressive stresses, although the cause for this observation was not examined in the context of this dissertation.

4.2. NUMERICAL CREEP MODEL

4.2.1. GENERALITIES

A user-defined CREEP subroutine was derived for implementation in ABAQUS to represent the time-dependent behaviour of the experimental specimen subject to uniaxial compression. This finite element software package uses the notion of *equivalent creep stress* in case of Drucker-Prager material models to define the sensitivity of an element to creep based on the stress state and based on the yield surface. The equivalent creep stress $\overline{\sigma}_{\mathrm{cr}}$ is determined based on the combination of the Von Mises stress q, the pressure p and the friction angle β through the equation [27]

$$\overline{\sigma}_{\mathrm{cr}} = \frac{q - p\tan\beta}{1 - \frac{1}{3}\tan\beta},$$

(4.2)

for creep defined in uniaxial compression.

The equivalent creep stress is associated with an equivalent creep strain $\overline{\varepsilon}_{\mathrm{cr}}$ which is defined by a creep law. The creep strain components can be derived based on a creep flow rule G_{cr}, an auxiliary parameter f_{cr} and the stress state [27]. Because ABAQUS only supports $K = 1^1$ for Drucker-Prager material models during creep analyses, it was chosen to augment the injectants' short-term material models for non-dilatant flow ($K = 1$, $\psi = 0°$, see Chapter 3 and/or Appendix A) with a creep law. For $\psi = 0°$, the incremental creep strain components over a time increment Δt are expressed by the (simplified) expression [27]

$$\Delta\boldsymbol{\varepsilon}_{\mathrm{cr}} = \frac{3}{2}\frac{1}{\overline{\sigma}_{\mathrm{cr}}}\mathbf{S}\Delta\overline{\varepsilon}_{\mathrm{cr}},$$

(4.3)

---

[1] ratio of yield stress in triaxial tension to the yield stress in triaxial compression
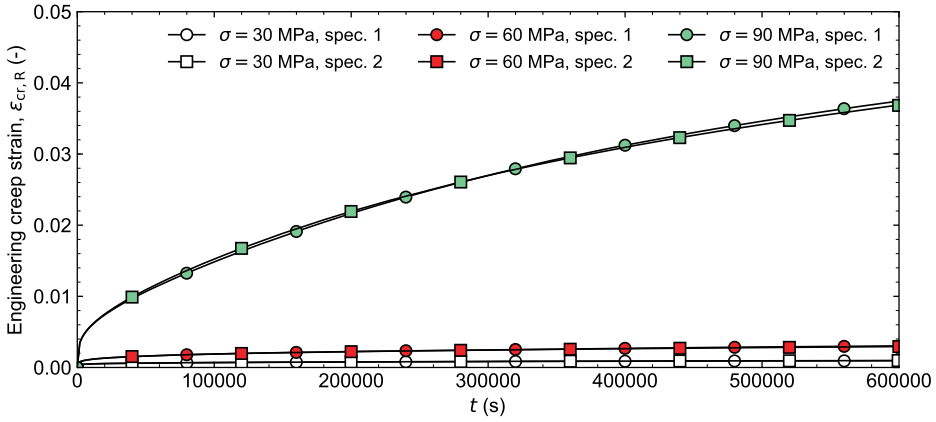
(a) Resin specimens
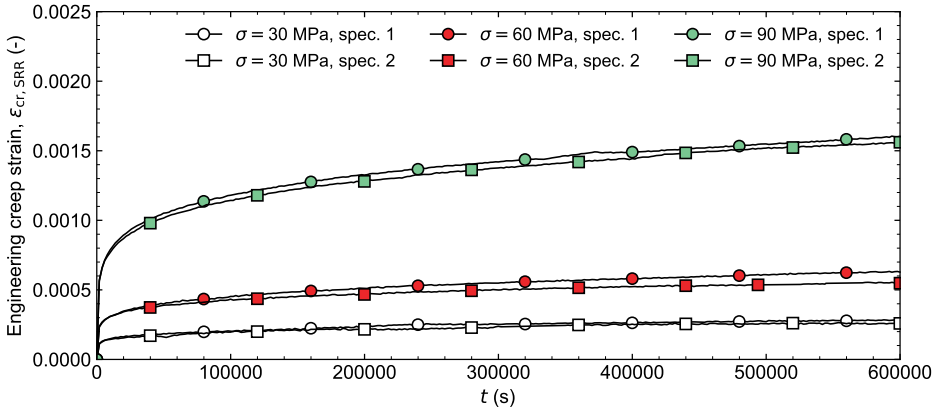
(b) Steel-reinforced resin specimens

Figure 4.2 | Creep strain vs. time for specimens subject to uniaxial compressive stress σ.
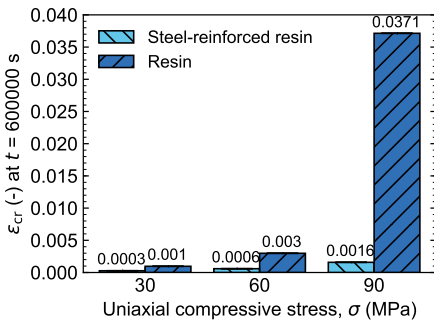
Figure 4.3 | Average creep strain at $t = 600000$ s.
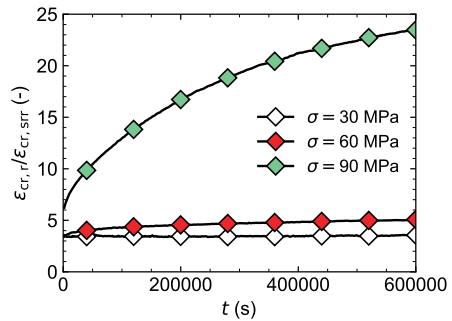
Figure 4.4 | Ratio of average resin creep strain over average steel-reinforced resin creep strain vs. time.

where $\mathbf{S}$ denotes the deviatoric stress matrix. For a uniaxial compressive creep test at $\sigma_{xx} = \sigma_{yy} = 0$ and $\sigma_{zz} = -\sigma$, the previous equation becomes

$$\Delta \boldsymbol{\varepsilon}_{\mathrm{cr}} = \frac{3}{2} \frac{1}{\overline{\sigma}_{\mathrm{cr}}} \begin{bmatrix} \sigma/3 & 0 & 0 \\ 0 & \sigma/3 & 0 \\ 0 & 0 & -\sigma + \sigma/3 \end{bmatrix} \Delta \overline{\varepsilon}_{\mathrm{cr}}. \tag{4.4}$$

Equation 4.4 implies that a positive strain increment perpendicular to the direction of loading occurs which is equal to half the (negative) longitudinal creep strain increment. It can be proven that this combination of strains corresponds to approximate volume conservation[2]. This is an important observation in case of confined environments, and its implications for injected bolted connections will be further discussed in Chapter 6.

4.2.2. CREEP LAW FORMULATION AND VALIDATION
The evaluation of Equation 4.4 requires the definition of the equivalent uniaxial creep strain increment $\Delta \overline{\varepsilon}_{\mathrm{cr}}$ based on experimental data. The equivalent creep strain increment is related to the total equivalent creep strain $\overline{\varepsilon}_{\mathrm{cr}}$. Therefore a phenomenological creep law of the form

$$\overline{\varepsilon}_{\mathrm{cr}} = t^{C_1 \overline{\sigma}_{\mathrm{cr}}^2 + C_2 \overline{\sigma}_{\mathrm{cr}} + C_3} \cdot \exp\left(C_4 \overline{\sigma}_{\mathrm{cr}} + C_5/\overline{\sigma}_{\mathrm{cr}} + C_6\right), \tag{4.5}$$

was fitted to the experimental results for each of the two injectants in terms of engineering stress and strain. The form of this creep law was iteratively chosen to describe the experimental results - none of the creep formulations identified in the literature review could adequately replicate the experimental findings. It should be noted that for the uniaxial creep tests $p = q/3$ and thus $\overline{\sigma}_{\mathrm{cr}} = |\sigma|$. The magnitudes of the material constants C_i ($i = 1 \dots 6$) were determined by minimising the sum of the squared residuals between the creep law and the experimental results, and are summarised in Table 4.1 for both injectants. The phenomenological creep law was implemented in `ABAQUS` through a user-defined `CREEP` subroutine. Figure 4.5 illustrates the excellent agreement between the experimental results and the results obtained by finite element simulation.

4.2.3. DISCUSSION
The phenomenological character of the creep law implies that it describes an empirical relationship, but that it was not derived based on a fundamental theory. Figure 4.6 demonstrates that this creep law leads to an exponential increase of the creep strain with increasing stress, in line with the experimental observations. Secondly, Figure 4.7 shows that for resin subject to $\overline{\sigma}_{\mathrm{cr}} > 120$ MPa the creep strain increases more progressively than time due to a time exponent $C_1 \overline{\sigma}_{\mathrm{cr}}^2 + C_2 \overline{\sigma}_{\mathrm{cr}} + C_3 > 1$. Based on these two observations, the derived creep law is expected to generate non-conservative predictions for stress levels higher than those considered in the experimental programme.[3] It should be noted that the creep law for the

---

[2]For a cylindrical specimen with original volume $0.25\pi d^2 h$ subject to longitudinal strain $\varepsilon_{\mathrm{cr}}$, it follows that ratio of the original diameter d to the new diameter d_* based on volume conservation equals $d_*/d = 1/\sqrt{1 - \varepsilon_{\mathrm{cr}}}$ which is represented by the Taylor Series expansion $1 - \frac{\varepsilon_{\mathrm{cr}}}{2} + \frac{3\varepsilon_{\mathrm{cr}}^2}{8} - \frac{5\varepsilon_{\mathrm{cr}}^3}{16} + O(x^4)$ around $\varepsilon_{\mathrm{cr}} = 0$. Therefore the transversal strain can indeed be approximated by $d_*/d - 1 \approx -0.5\varepsilon_{\mathrm{cr}}$ at relatively small creep strains.

[3]It should be noted that a time exponent > 1 for resin specimens with $\overline{\sigma}_{\mathrm{cr}} > 120$ MPa is physically unrealistic, but that it does provide a non-conservative prediction nonetheless. Also it should be noted that the injectants cannot withstand higher uniaxial compressive stresses than determined in Section 3.1 (approximately 135 MPa).
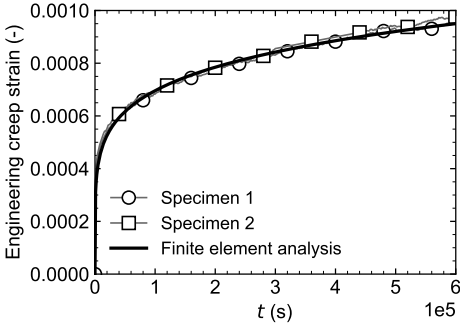
(a) Resin, $\sigma = 30$ MPa.
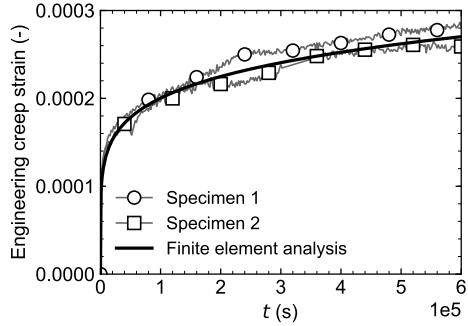
(b) Steel-reinforced resin, $\sigma = 30$ MPa.
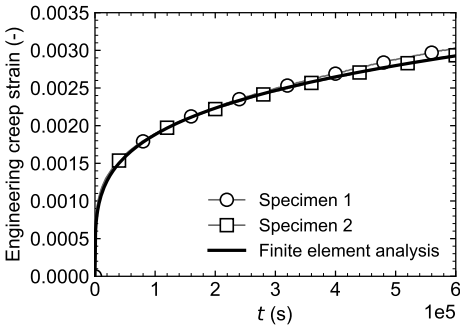
(c) Resin, $\sigma = 60$ MPa.
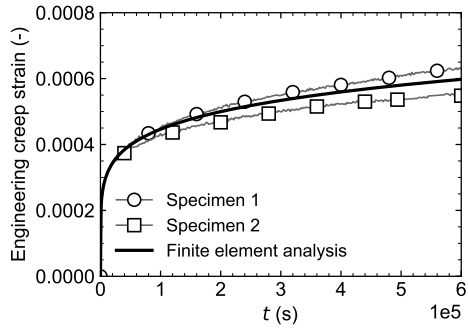
(d) Steel-reinforced resin, $\sigma = 60$ MPa.
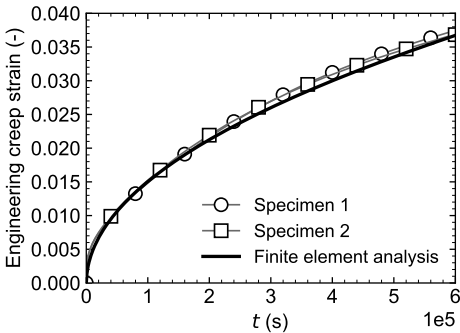
(e) Resin, $\sigma = 90$ MPa.
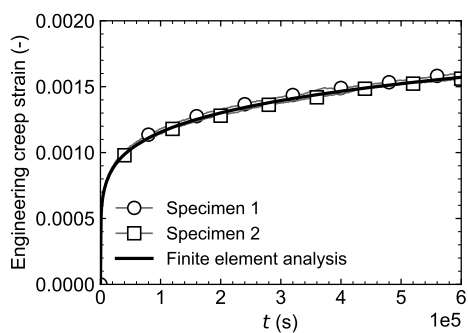
(f) Steel-reinforced resin, $\sigma = 90$ MPa.

Figure 4.5 | Validation of the numerical creep material model against experimental results.

steel-reinforced resin leads to a small creep strain (e.g. 1.5×10^{-4} after 7 days) for $\sigma = 0$. This phenomenon is not physically realistic but the magnitude of the creep strain is sufficiently small to be neglected: further tests over a wider range of stress levels could suggest modifications to Equation 4.5 to avoid occurrence of the phenomenon. The combined short- and long-term material models for the injectants will be applied in Chapter 6 to determine their suitability to describe the behaviour of injected bolted connections.

4.3. CONCLUSIONS

This Chapter presented the long-term (seven-day) uniaxial compressive response of the (steel-reinforced) epoxy resin system RenGel SW 404 + HY 5159 for nominal stress levels of 30, 60, and 90 MPa. The main findings of the work are:

- Steel-reinforced resin leads to smaller uniaxial creep deformation compared to non-reinforced resin. For a nominal stress of 30 MPa, the resin creep strain $\varepsilon_{\mathrm{cr,srr}}$ was 3.5 times that of the steel-reinforced resin (denoted by $\varepsilon_{\mathrm{cr,srr}}$) over the entire test duration. For stress levels of 60 and 90 MPa, the ratio $\varepsilon_{\mathrm{cr,r}}/\varepsilon_{\mathrm{cr,r}}$ increased over time, demonstrating that the creep rate of resin specimens reduced less rapidly than for steel-reinforced resin specimen. At a stress level of 90 MPa, the resin specimens underwent 23.5 times the creep strain of the steel-reinforced resin specimens after 7 days of constant loading. Therefore the results suggest that the benefit of steel-reinforced resin to reduce creep deformation becomes more pronounced for higher load levels.

- Based on the need for longer-term testing, a tailor-made experimental setup was designed that can simultaneously subject multiple (maximum 30) specimens to sustained compression. This experimental setup was not used to obtain data for this dissertation because it was still under construction, but will contribute to future work focusing on the efficient determination of the time-dependent behaviour of (steel-reinforced) epoxy resins.

- A phenomenological creep model of the form

$$\overline{\varepsilon}_{\mathrm{cr}} = t^{C_1 \overline{\sigma}_{\mathrm{cr}}^2 + C_2 \overline{\sigma}_{\mathrm{cr}} + C_3} \cdot \exp\left(C_4 \overline{\sigma}_{\mathrm{cr}} + C_5 / \overline{\sigma}_{\mathrm{cr}} + C_6\right)$$

was derived based on the long-term uniaxial compressive creep tests on the (steel-reinforced) resin specimens. The constants C_i ($i = 1 \ldots 6$) were calibrated for both injectants. The short-term Drucker-Prager material models for (steel-reinforced) epoxy resin, developed in Chapter 3, were augmented with the derived creep law by a user-defined CREEP subroutine. The material models were implemented in ABAQUS and demonstrated excellent agreement with the experimental creep results for both injectants.

Table 4.1 | Magnitudes of the constants C_i ($i = 1 \ldots 6$) corresponding to the creep law given by Equation 4.5.

Constant	Magnitude	
	Resin	Steel-reinforced resin
C_1	9.85×10^{-5}	7.22×10^{-6}
C_2	-6.44×10^{-3}	-7.87×10^{-4}
C_3	2.78×10^{-1}	1.84×10^{-1}
C_4	-4.11×10^{-2}	2.83×10^{-2}
C_5	8.37×10^{1}	0
C_6	-5.24	-1.13×10^{1}

4
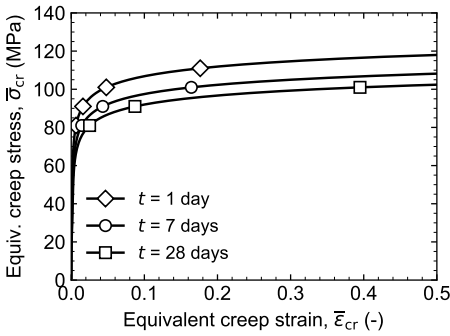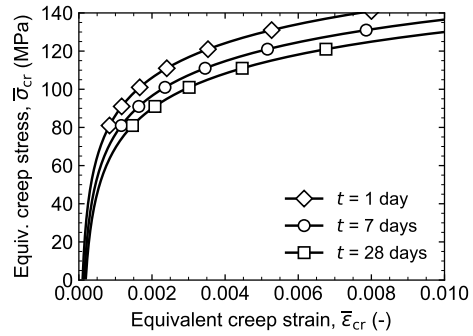
(a) Resin

(b) Steel-reinforced resin

Figure 4.6 | Equivalent creep stress $\overline{\sigma}_{cr}$ vs. equivalent creep strain $\overline{\varepsilon}_{cr}$ isochrones. Note the significantly different scale on the equivalent creep strain axis.
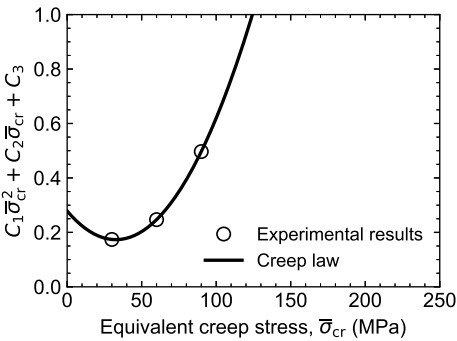
(a) Resin
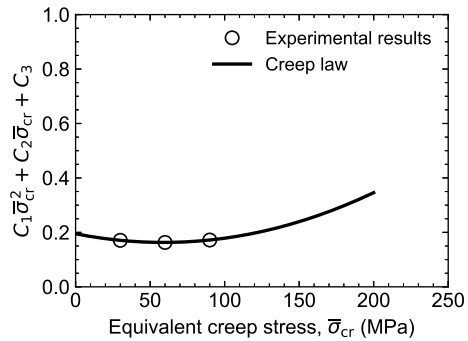
(b) Steel-reinforced resin

Figure 4.7 | Time exponent $C_1\overline{\sigma}_{cr}^2 + C_2\overline{\sigma}_{cr} + C_3$ (see Equation 4.5) vs. equivalent creep stress $\overline{\sigma}_{cr}$.

REFERENCES PART I

REFERENCES

[1] M. P. Nijgh, H. Xin, and M. Veljkovic, *Non-linear hybrid homogenization method for steel-reinforced resin,* Construction and Building Materials **182**, 324 (2018).

[2] H. Xin, M. Nijgh, and M. Veljkovic, *Computational homogenization simulation on steel reinforced resin used in the injected bolted connections,* Composite Structures **210**, 942 (2019).

[3] H. Xin, M. P. Nijgh, and M. Veljkovic, *Computational homogenization simulation on steel reinforced resin used in the injected bolted connections,* in *Proceedings of the 13th World Congress on Computational Mechanics* (2018).

[4] SAE International, *J444: Cast Shot and Grit Size Specifications for Peening and Cleaning* (SAE International, 2012).

[5] J. Williams and C. Gamonpilas, *Using the simple compression test to determine Young's modulus, Poisson's ratio and the Coulomb friction coefficient,* International Journal of Solids and Structures **45**, 4448 (2008).

[6] F. J. Wedekamper, *Avaliação de resinas epóxi para aplicação em end fittings de dutos flexíveis,* Master's thesis, Universidade Federal do Rio Grande do Sul (2017).

[7] T. W. Tamulevich, *The Significance Of Glass Transition Temperature On Epdxy Resins For Fiber Optic Applications,* in *Integration and Packaging of Optoelectronic Devices,* edited by D. H. Hartman, R. L. Holman, and D. P. Skinner (SPIE, 1987).

[8] L. H. Sperling, *Introduction to Physical Polymer Science* (Wiley, 2005).

[9] R. W. Zimmerman, *Behavior of the poisson ratio of a two-phase composite material in the high-concentration limit,* Applied Mechanics Reviews **47**, S38 (1994).

[10] C. Hsieh and W. Tuan, *Poisson's ratio of two-phase composites,* Materials Science and Engineering: A **396**, 202 (2005).

[11] A. Abrasives, *High Carbon Steel Shot & Grit,* Online (2016).

[12] W. Voigt, *Ueber die Beziehung zwischen den beiden Elasticitätsconstanten isotroper Körper,* Annalen der Physik **274**, 573 (1889).

[13] A. Reuss, *Berechnung der Fließgrenze von Mischkristallen auf Grund der Plastizitätsbedingung für Einkristalle,* Zeitschrift für Angewandte Mathematik und Mechanik **9**, 49 (1929).

[14] R. Hill, *Elastic properties of reinforced solids: Some theoretical principles,* Journal of the Mechanics and Physics of Solids **11**, 357 (1963).

[15] W. Drugan and J. Willis, *A micromechanics-based nonlocal constitutive equation and estimates of representative volume element size for elastic composites,* Journal of the Mechanics and Physics of Solids **44**, 497 (1996).

[16] P. Sheng, J. Zhang, and Z. Ji, *An advanced 3d modeling method for concrete-like particle-reinforced composites with high volume fraction of randomly distributed particles,* Composites Science and Technology **134**, 26 (2016).

[17] B. Cox and Q. Yang, *In quest of virtual tests for structural composites,* Science **314**, 1102 (2006).

[18] Y. Shi and Y. Zhang, *Simulation of random packing of spherical particles with different size distributions,* Applied Physics A **92**, 621 (2008).

[19] K. Hitti and M. Bernacki, *Optimized dropping and rolling (ODR) method for packing of poly-disperse spheres,* Applied Mathematical Modelling **37**, 5715 (2013).

[20] M. M. Roozbahani, B. B. Huat, and A. Asadi, *Effect of rectangular container's sides on porosity for equal-sized sphere packing,* Powder Technology **224**, 46 (2012).

[21] SAE International, *J827: High-Carbon Cast-Steel Shot* (SAE International, 2013).

[22] S. Lejeunes and S. Bourgeois, *Une Toolbox Abaqus pour le calcul de propriétés effectives de milieux hétérogènes,* in *Proceedings of the 10e Colloque National en Calcul des Structures* (2011).

[23]   *ABAQUS User Manual: 33.1.10 Surface-based cohesive behaviour* ().

[24]   M. L. Benzeggagh and M. Kenane, *Measurement of mixed-mode delamination fracture toughness of unidirectional glass/epoxy composites with mixed-mode bending apparatus,* Computer Sciences and Technology **56**, 439 (1996).

[25]   K. Song, C. G. Davila, and C. A. Rose, *Guidelines and Parameter Selection for the Simulation of Progressive Delamination,* in *Proceedings of the 2008 Abaqus Users' Conference* (2008).

[26]   L. Bücking, *Behaviour of steel-reinforced epoxy resin exposed to compressive-compressive cyclic loading in confined conditions,* Master's thesis, Leibniz Universität Hannover, Delft University of Technology (2019).

[27]   *ABAQUS Theory Manual: 4.4.2 Models for granular or polymer behaviour* ().

II

DEMOUNTABLE INJECTED BOLTED SHEAR CONNECTORS

5

SHORT-TERM BEHAVIOUR OF THE PROPOSED DEMOUNTABLE SHEAR CONNECTOR

You have to be confused before you can reach a new level of understanding anything.

Dudley Robert Herschbach

INTRODUCTION

This chapter focuses on the short-term mechanical behaviour of the (steel-reinforced) resin-injected demountable shear connector proposed in Chapter 2. Based on the literature review, this type of demountable shear connector was considered to be most suitable because it enables large nominal hole clearances to facilitate execution, and because the injectant provides instantaneous shear interaction during the service life of a composite floor system despite these clearances. The favourable effect of the injectant on the connector response is proven in this chapter comparing the behaviour of injected connections to the response of pretensioned (non-injected) connections.

This chapter is subdivided into four sections. Section 5.1 presents the design and results of experimental *push-out* tests to obtain the load-deformation relationship for the demountable (steel-reinforced) resin-injected shear connectors. Extensive finite element modelling is performed in Section 5.2 to valid numerical models against the experimental results obtained through the push-out tests. This finite element modelling is performed based on the (steel-reinforced) resin material models derived in Chapter 3, and based on the actual material properties of the other shear connector constituents. The chapter proceeds with Section 5.3, where the validated finite element model is used to perform a parametric study to derive the sensitivity of the demountable shear connector system to design variations. The chapter concludes with Section 5.4, summarising the main findings of the this chapter.

5.1. Experimental work

5.1.1. Specimen design and experimental details

A series of *push-out tests* was designed and carried out to determine the relation between applied load and relative deformation between the steel and concrete elements (slip) for the resin-injected demountable shear connector synthesised in Chapter 2. The specimens consisted of four prefabricated concrete elements, one steel section and eight demountable shear connectors, see Figure 5.1.
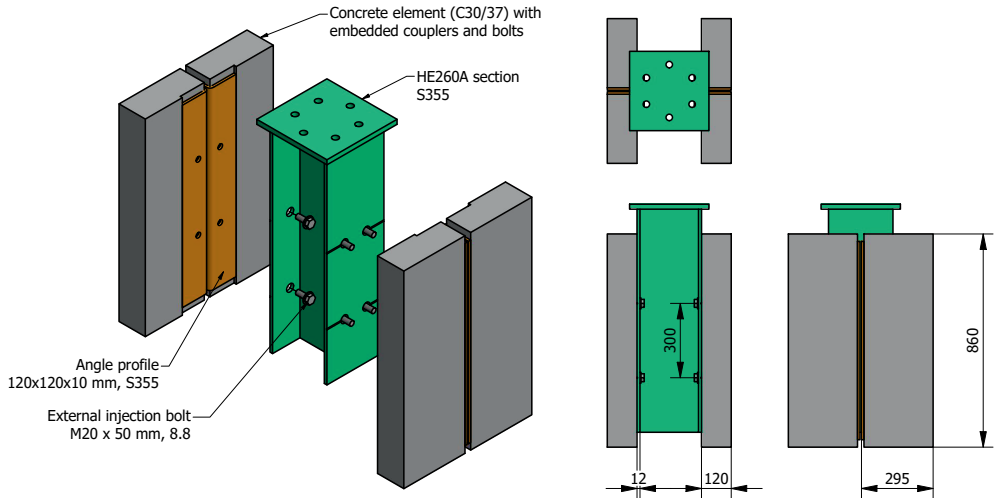
Figure 5.1 | Overview of *push-out test* specimen. Dimensions in mm.

Specimen design

The demountable shear connectors consisted of an M20 coupler (grade 10.9[1]) and M20 bolt (grade 8.8, ISO 4017 [2]) embedded in a 120m mm thick concrete element with a 25 mm top cover, see Figure 5.2. The embedded parts of the shear connector were connected to the flange of a HE260A section with an external M20 injection bolt (grade 8.8, ISO 4017 / EN 1090-2 [3]). The coupler was stronger than the bolt to ensure that damage related to the overloading of a shear connector would accumulate in the replaceable external bolt in a practical application.

An HE260A steel section was used because of its thinner flanges compared to the HE260B section prescribed by Eurocode 1994-1-1 [4]. The reduced flange thickness reflected the conditions of the (steel-reinforced) resin in the experiments on a demountable composite floor system, introduced in Chapter 7.

The bolt holes in the flanges had a diameter of 32 mm to enable the swift execution of large-scale demountable composite floor systems. The significant hole clearance (32 - 20 = 12 mm) is beyond the allowable limits (1-4 mm) for M20 bolts imposed by the current version of EN 1090-2 [3]. The injection bolts were concentric with respect to the bolt hole: this constraint was enforced during the assembly by the use of custom alignment

---

[1]All fastener grades were conform ISO 898-1 [1].
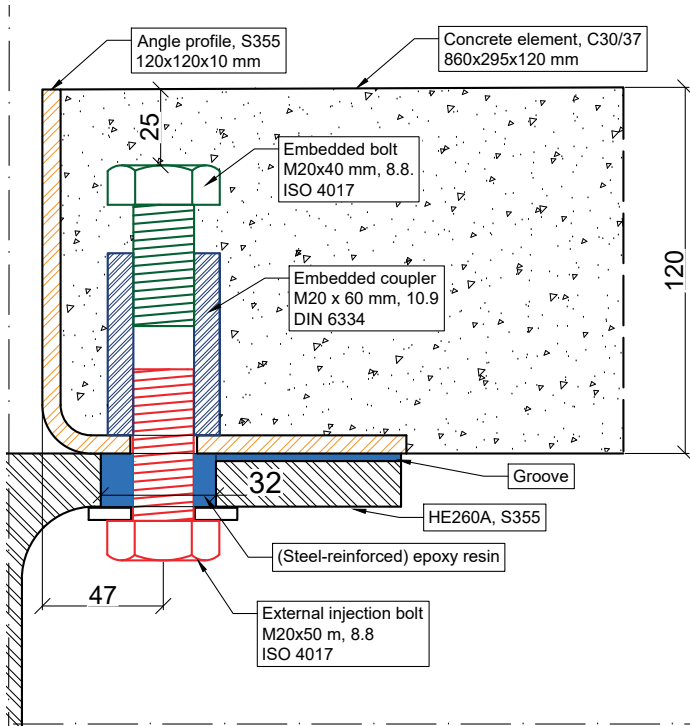
Figure 5.2 | Cross-section of demountable shear connector considered in *push-out tests.* Dimensions in mm.

pins. The hole clearance was injected with the (steel-reinforced) epoxy resin system RenGel SW 404 + HY 5159, which was introduced Chapters 2 and 3. Five resin-injected and four steel-reinforced resin-injected push-out specimens were tested. Adhesion was prevented by applying a wax-layer to all connection components. A groove in the flange at the steel-concrete interface prevented air inclusions in the epoxy resin and provided visual confirmation of a successful injection procedure. Two specimens were tested without any injectant: for these specimens the bolts were already nominally bearing against the edge of the bolt hole at the start of the experiments.

Angle profiles ($120 \times 120 \times 10$ mm, $L = 800$ mm, S355) prevented damage to the bottom edges of the prefabricated concrete elements ($860 \times 295 \times 120$ mm) during transportation and assembly of the specimens. In practical applications the angle profile could therefore improve the reusability of the concrete floor elements. An additional expected benefit was that the angle profile confines the concrete, and hereby introduces a favourable multi-axial compressive stress state in the region of the shear connector.

All four prefabricated concrete elements of each specimen were placed in a 10 mm thick mortar bedding, which was left to cure for at least 24 hours. The mortar ensured that all four concrete elements were in full contact with the support plate. Any mortar between the support plate and the angle profile was removed to guarantee that the load was fully transferred by the demountable shear connector into the concrete element.

CONCRETE AND REINFORCEMENT

The nominal strength class of the concrete elements was C30/37 conform EN 1992-1-1 [5]. The average 28-day compressive strength of five concrete cubes, cast from the same batch and at the same time as the concrete elements, was $f_{cm,cube} = 48.2$ MPa, and the coefficient of variation was 2.5%. The tensile strength of the concrete was not experimentally obtained, but has been derived based on EN 1992-1-1 [5] as $f_{ctm} = 0.30 f_{ck}^{(2/3)} = 2.9$ MPa where $f_{ck} = 0.8 f_{cm,cube} - 8 = 30.6$ MPa.

The reinforcement consisted of Ø8 mm U-shaped rebar (grade B500B [6]) placed around the embedded shear connector system, and of stirrups longitudinal and perpendicular to the height of the elements, see Figure 5.3. The purpose of the U-bar was to prevent concrete splitting to due to the small edge distance $e = 47$ mm indicated in Figure 5.2.

LOADING

The experiments were conducted using a hydraulic actuator with maximum compression capacity of 2000 kN. The loading procedure for standard push-out tests conform EN 1994-1-1 [4] includes 25 load cycles between 5% and 40% of the expected failure load to break any adhesion between the load bearing elements. To determine the failure load, a preliminary test of a resin and steel-reinforced resin injected specimen was conducted without any repeated loading. Subsequently tests were carried out with either of the following loading regimes:

- Twenty-five load-controlled cycles between 5% and 40% of the failure load obtained from the preliminary test. Hereafter, the specimen was loaded to failure at a rate of 1 mm/minute.

- Twenty-five load-controlled cycles between 5% and 40% of the failure load obtained from the preliminary test. Several unloading-loading cycles after 0.5 – 1 mm increments of slip to determine the residual (permanent) relative deformation. Hereafter, the specimen was loaded to failure at a rate of 1 mm/minute.

These two distinct load regimes were adopted to reflect the same loading conditions as in the experimental work of Kozma et al. [7].

MEASUREMENTS

The relative displacement between the steel section and the prefabricated concrete elements, or *slip*, was measured at the centreline of each demountable shear connector by potentiometers with a 25 mm stroke. The transverse separation between the bottom of the steel section and the concrete elements was determined using 12 mm stroke potentiometers. The data acquisition frequency was set as 1 Hz.

5.1.2. EXPERIMENTAL RESULTS

The experimental results of the push-out tests are represented by load-slip curves. Figure 5.4 shows the relation between the nominally applied force per connector P and the averaged connection slip s for the resin and steel-reinforced resin injected specimens. The results are quantitatively summarised in Table 5.1 in terms of the resistance P_u, the slip at failure s_u, defined as the slip at 90% of the resistance P_u on the descending branch, and the secant connector stiffness at 40% and 70% of P_u.
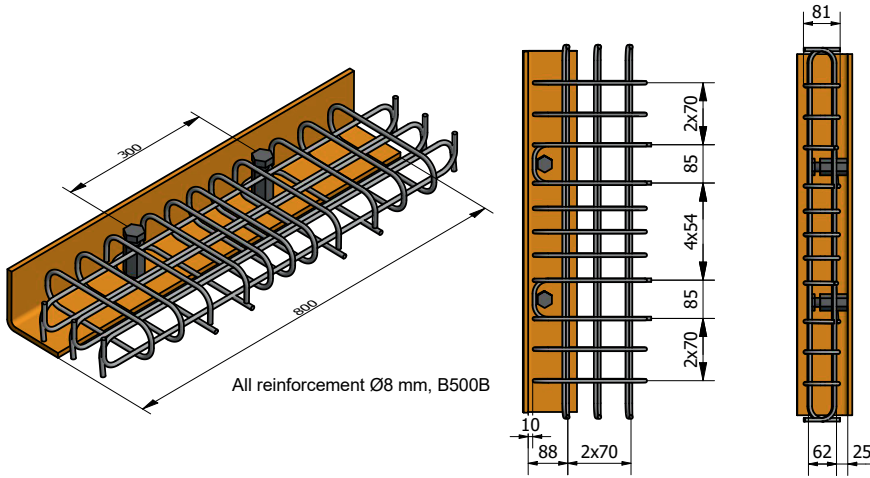
Figure 5.3 | Prefabricated reinforcement cages consisting of Ø8 mm rebar of grade B500B [6], dimensions in mm.

Table 5.1 | Experimental results of push-out tests. The average resistance P_u of all specimens equals 117.7 kN.

Injectant	Specimen	P_u (kN)	s_u (mm)	Secant stiffness at $0.7P_u$ (kN/mm)	Secant stiffness at $0.4P_u$ (kN/mm)
Resin	1	117.2	20.7	35.0	91.4
	2	115.5	5.8	66.0	107.4
	3	110.2	7.1	52.8	110.8
	4	117.3	19.0	41.5	101.1
	5	117.6	20.8	36.0	67.0
	Mean	115.6	-	46.3	95.5
	Coeffic. of var.	2.7%	-	28.4%	18.4%
Steel-reinforced resin	1	118.2	14.9	136.2	272.0
	2	123.6	5.7	123.3	148.1
	3	117.6	20.6	83.4	151.6
	4	113.3	21.2	49.0	113.7
	Mean	118.2	-	98.0	171.6
	Coeffic. of var.	3.6%	-	41%	40%
None	1	126.0	6.6	34.0	30.6
	2	118.7	6.3	34.3	30.4
	Mean	122.4	6.4	34.1	30.5
	Coeffic. of var.	4.2%	3.6%	0.6%	0.5%
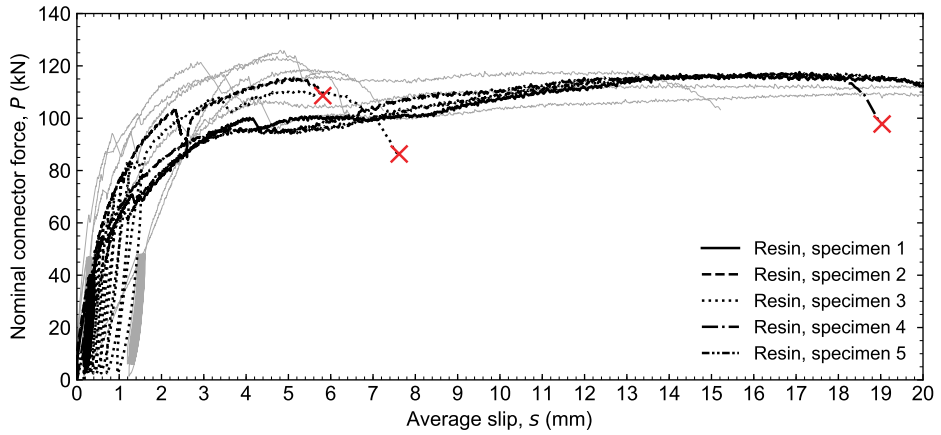
(a) Resin-injected specimens
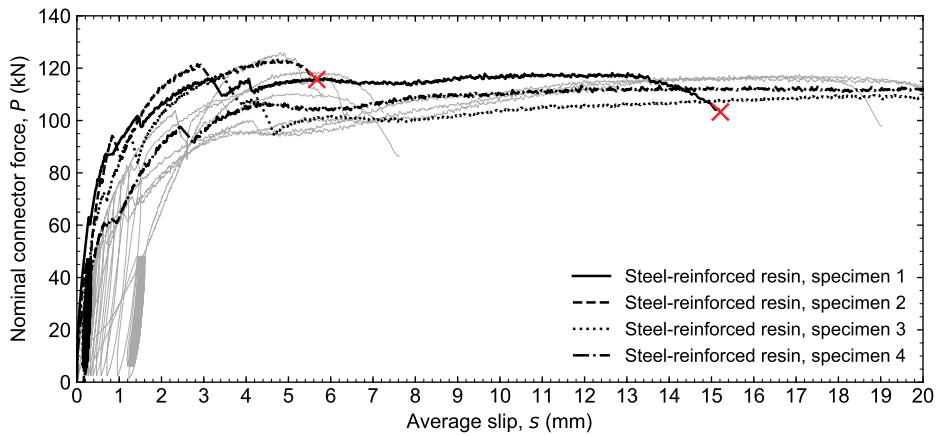
(b) Steel-reinforced resin-injected specimens
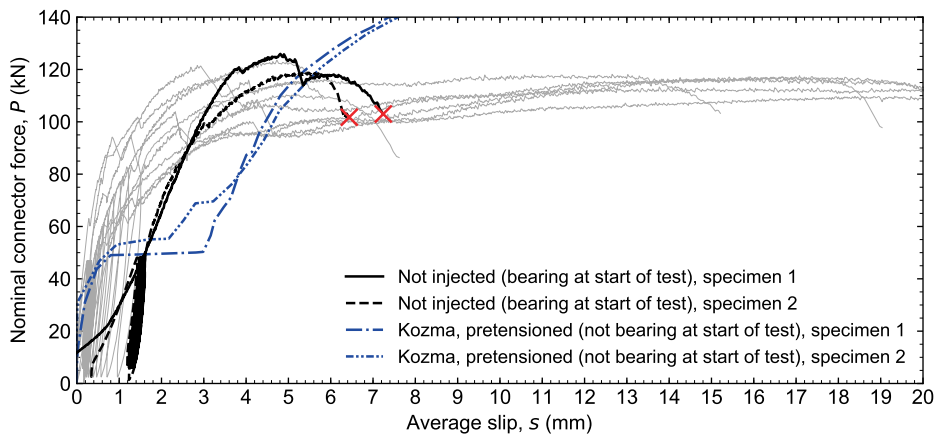
(c) Non-injected specimens

Figure 5.4 | Damage to connection components for specimens with significant slip (> 15 mm) at failure.

RESISTANCE

The mean value μ and standard deviation σ of the resistances P_u of the (steel-reinforced) resin-injected specimens were used to determine the characteristic resistance P_{Rk}. The characteristic resistance is defined as the 5% fractile, conform EN 1990 [8] expressed by

$$P_{Rk} = \mu - k_n \frac{\sigma}{\mu}, \tag{5.1}$$

where k_n accounts for the limited number of test results, based on the most conservative assumption that the ratio σ/μ was not known a priori. The characteristic resistances are summarised in Table 5.2, except for the non-injected specimens, because too few experiments within this subgroup were performed to enable a meaningful statistical evaluation.

No statistical difference between the average resistances of resin-injected and steel-reinforced resin-injected specimens was observed based on a two-tailed Student's t-test ($p = 0.347$). Similarly no statistical difference was found between injected and non-injected specimens ($p = 0.403$), and therefore it was concluded that the presence and type of injectant had no significant influence on the resistance P_u of demountable shear connector. The insensitivity of the resistance to the injectant can be attributed to the bolt-dominated failure mode, illustrated in Figure 5.5, which was apparently not related to the behaviour of the injectant.

On average, the shear resistance of the injection bolts could be described by

$$P_u = 0.547 A_s f_{ub} = 117.7 \text{ kN}, \tag{5.2}$$

where A_s is the shear area of the bolt and $f_{ub} = 879$ MPa is the actual average ultimate tensile strength of the bolt, see Appendix B. The factor $0.547 < 1/\sqrt{3} = 0.577$ indicates that the average resistance was 5.2% smaller than expected according the Von Mises criterion based on pure shear.

According to the hand calculation model (HCM) of Pavlovic [9] for bolted shear connectors with single embedded nuts the bolt shear resistance is equal to

$$P_{b,u} = 0.6 \left(\frac{34}{d} \right)^a f_{ub} A_s, \tag{5.3}$$

Pavlovic [9] fitted the exponent a to account for the increase of the resistance due to friction, embedment and catenary effects. However, frictional and embedment effects are not relevant for the demountable shear connector considered in this work because the angle profile prevents any direct contact between the coupler and the HE260A section. Setting $a = 0$ gives $P_{b,u} = 124.3$ kN, which is 5.6% larger than the average experimental resistance of

Table 5.2 | Statistical evaluation of connector resistance.

Injectant	Number of specimens (-)	k_n (-) [8]	Resistance (kN)		
			Mean, μ	Standard deviation, σ	Characteristic value (5% fractile)
Resin	5	2.33	115.6	3.1	108.4
Steel-reinforced resin	4	2.63	118.2	4.2	107.1
None	2	-	122.4	5.1	-

all specimens, and 1.6% larger than the average experimental resistance of the non-injected specimens. For the concrete resistance, Pavlovic [9] derived the prediction formula

$$P_{c,u} = 55\alpha_c d^{1.9} \left(\frac{f_{cm} h_{sc}}{d} \right)^{0.4} + 22000, \tag{5.4}$$

which gives the resistance in Newtons, and where h_{sc} is the height of the shear connector (total embedded length), and where α_c is expressed by

$$\alpha_c = \frac{22.5}{d+1} \le 1, \tag{5.5}$$

with the bolt diameter d expressed in millimetres. Because Pavlovic [9] did not observe any substantial difference between the resistance in case of one or two embedded nuts, it was hypothesised that Equation 5.4 is also valid for a coupler, the height of which is approximately equal to three nuts. For the actual material properties, Equation 5.4 gives $P_{c,u} = 144.6$ kN, which confirms that concrete resistance was not governing during the push-out experiments (see page 111). Therefore good agreement was observed between the experiments and the hand calculation model of Pavlovic in terms of the failure mode (bolt shear failure) and the failure load.

The observed average resistance per shear connector (117.7 kN) was lower than in case of push-out tests by Kozma [10] (142 kN, see Figure 5.4c) on similar shear connectors with embedded couplers. In these experiments the M20 bolts were pretensioned to 70% of the bolt tensile resistance, but the 6 mm nominal hole clearance was not injected. The difference in the resistance (+21%) was due to additional force transfer by friction, although the resistance was reached at significantly larger slip due to (temporarily) unopposed translation of the bolt in the oversized bolt hole that initiated at 0.3-0.4P_u. Experiments by Milosavljevic et al. [11] on similar but non-injected and non-pretensioned specimens with M20 bolts led to an average resistance $P_u = 0.598 A_s f_{ub}$. Therefore the resistance observed in their test series was 0.598/0.547 = 9 % higher than in present work, which can be attributed to beneficial friction and embedment effects at the coupler-flange interface.

SECANT STIFFNESS
The average secant stiffness of the non-injected specimens was substantially lower compared to the (steel-reinforced) resin-injected specimens: at 0.4P_u it was (on average) only 31% of the secant stiffness of the resin-injected specimens and only 18% of the secant stiffness of the steel-reinforced resin-injected specimens. The (steel-reinforced) resin had a favourable effect on the secant stiffness because (i) the injectant ensured that all connectors are instantaneously and simultaneously load-bearing and (ii) the injectant partially restrained the deformation of the external injection bolt (e.g. due to bending, shear) within the oversized hole. These benefits are supported by the observation that for non-injected specimens the secant connector stiffness with increasing load, see Figure 5.4c, which results from (i) initial non-uniform bearing of the injection bolts due to fabrication tolerances and (ii) local thread penetration in the flange.

Figure 5.4 demonstrates the superiority of the injected shear connectors compared to similar pretensioned (non-injected) shear connectors tested by Kozma [10]. For pretensioned specimens substantial slip occurred (approximately equal to half the nominal hole clearance) once the friction resistance was overcome, which led to a significant reduction of the secant stiffness. However, for injected specimens the position of the bolt was fixated

by the (steel-reinforced) epoxy resin: therefore injected shear connectors were considered to be more suitable to develop significant composite interaction in a steel-concrete floor system.

No firm conclusions can drawn on the magnitude of the secant stiffness for the injected specimens, mainly because resin layers formed at the flange-angle profile interface during the injection due to geometrical imperfections of the specimen components. The size of the resin layer was largest for the steel-reinforced resin due to the higher injection pressure. Although the interfaces were lubricated, the large coefficients of variations in Table 5.1 (18 - 41%) indicate that adhesion between the components could not be fully prevented nor mitigated. The influence of the adhesive layer on the secant stiffness is confirmed by a comparatively small scatter (0.5-0.6%) for the non-injected specimens.

Despite the large variation in the secant stiffness, the experimental results clearly identified the benefits in terms of stiffness for the steel-reinforced resin-injected specimens compared to the resin-injected specimens. The secant stiffness at $0.4P_u$ and $0.7P_u$ increased by 80% and 111%, respectively. A more qualitatively accurate comparison between non-injected, resin-injected and steel-reinforced resin-injected specimens is made through finite element analysis in Section 5.2.

FAILURE MODE

The results showed two subgroups of specimens, (i) those that failed after moderate slip (5-8 mm) and those that failed after substantial slip (> 15 mm). The majority of the latter specimens demonstrated a relatively early onset of non-linearity in the force-slip response, followed by a plateau and subsequent increase of the load until the bolt fractures at large slip. The specimens that failed after moderate slip (5-8 mm) showed a comparatively longer quasi-linear branch, followed by fracture of the bolt shortly after the maximum load was reached. For both subgroups, the bolt fracture occurred at the interface between the steel section and the angle profile, see Figure 5.5(a).

No damage to the concrete and the embedded coupler was observed for specimens failing at moderate slip. For the more ductile specimens, significant damage to the coupler occurred, see Figure 5.5(b). Local yielding of the coupler due to bearing of the injection bolt generated additional slip and led to an inclination of the injection bolt in the bolt hole. Consequently, the confinement of the (steel-reinforced) resin in the bolt hole was reduced, causing additional slip due to the embedment of the bolt in the (steel-reinforced) epoxy resin infill, see Figure 5.5(c).

The existence of two subgroups of results in terms of behaviour at failure for nominally identical specimens was surprising, particularly because every step in the assembly of the specimens and their loading was identical. Hypotheses for the existence of two subgroups of experimental results are investigated by finite element analysis in Section 5.2.

5

(a) Coupler with part of fractured bolt.

(b) Ovalisation of coupler.

(c) Embedment of steel-reinforced resin due to reduction of confinement effects.

(d) Injection bolts after testing.

Figure 5.5 | Damage to connection components for specimens with significant slip (> 15 mm) at failure.

5.2. FINITE ELEMENT MODELLING

A finite element representation of the *push-out* specimens, introduced in Section 5.1, was developed using `ABAQUS` to (i) validate the finite element model against the experimental results and (ii) to use the validated finite element model for a parameter study to identify opportunities for design optimisation and to recognise sources of compliance.

An overview of the finite element model is illustrated in Figure 5.6. A quarter of the physical push-out specimen was modelled to increase computational efficiency. The following subsections elaborate on the details of the finite element model.
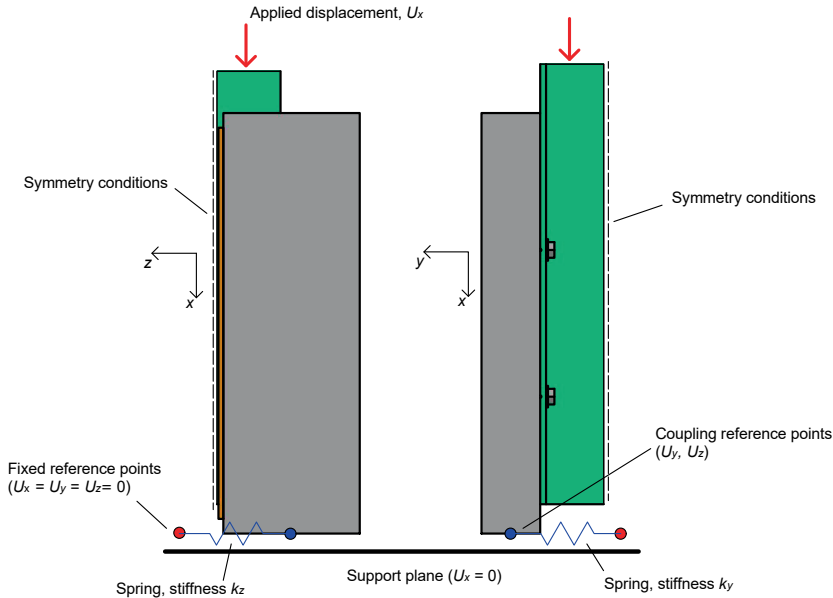
Figure 5.6 | One-quarter finite element model of the experimental *push-out* specimen.

5.2.1. ANALYSIS METHOD

The dynamic explicit solver of `ABAQUS` was used to perform the geometrical and material non-linear analysis (GMNLA), which enabled the use of damage plasticity models and is more robust because it prevents typical convergence issues for implicit solvers. Because the quasi-static response of the shear connector is sought, it is important to verify that any inertia-related effects are negligible.

The computational time required for an explicit analysis depends on the size of the smallest finite element and the wave propagation speed: these two factors control the maximum stable time increment. The analysis time can be reduced by mass scaling methods, which artificially increase the mass of the finite elements to match the target time increment. Non-uniform mass-scaling with a target time increment of 0.005 s has successfully been used in the literature [9, 11–13] and was also implemented in present work. It was verified that the sum of the external forces was negligibly small to prevent the influence of inertia-related effects on the results.

5.2.2. SYMMETRY CONDITIONS, BOUNDARY CONDITIONS, AND LOADING

Because only one quarter of the specimen was modelled, symmetry conditions were imposed to represent the effects of adjacent parts of the full-scale specimen, see Figure 5.6. The vertical support of the specimen was represented by fully restraining the nodes on the support plane in global x-direction.

The displacement of the nodes on the support plane in y- and z-directions was partially restrained by two orthogonal spring elements with stiffness k_y and k_z, respectively, see Figure 5.6. The springs physically represented the effects of friction and the gypsum at the support interface. The spring elements were parallel to the y and z axes and connected the reference node at the centroid of the concrete element to a fixed point in space. The translational degrees of freedom on the support plane (in y- and z-directions) of all nodes were coupled to that of the reference node. The magnitude of k_y and k_z was iteratively calibrated to match the experimental results.

A monotonically increasing vertical displacement U_x was applied at the top of the HE260A profile, see Figure 5.6. The displacement increased from $U_x = 0$ mm at $t = 0$ s to $U_x = 10$ mm at $t = 900$ s by a *smooth step* function to mitigate any inertia-induced effects.

5.2.3. COMPONENTS, MESHING AND MATERIAL PROPERTIES

EXTERNAL INJECTION BOLT

All features of the external injection bolts, including the threads, were modelled to represent the actual geometry and to capture the exact shape of the failure mechanism, see Figure 5.7(a).

The uniaxial tensile stress-strain relation of the external injection bolts, see Figure 5.8, was determined by coupon tests: progressive ductile damage models were iteratively calibrated using ABAQUS to match the numerically to the experimentally obtained stress-strain curve. The derivation of the ductile damage model for the injection bolts is extensively described in Appendix B, and was augmented with the built-in phenomenological shear damage initiation criterion and evolution law to describe the shear fracture of the bolt. The shear damage initiation was assumed to occur for a pure shear stress triaxiality ($\theta = \sqrt{3}$) at the equivalent plastic shear strain $\overline{\varepsilon}^{\text{pl}}_{\text{s,bolt}}$. The evolution of the shear damage depends on the exponential law parameter α (which accounts for the combined effects of shear and ductile damage) and the equivalent plastic displacement at failure $\overline{u}^{\text{pl}}_{\text{f,s,bolt}}$. Parameter α was taken as 0.70 based on its ability to adequately describe the failure mode in previous push-out tests [11, 12]; the other two variables were iteratively calibrated to match the experimentally obtained ductility of the connection. The washer under the bolt head was modelled with a linear-elastic material model ($E = 210$ GPa).

The part was meshed using C3D4 tetrahedral elements with a nominal mesh size of 1.2 mm in the threaded zone, which was identical to that used in the derivation of the material model to avoid mesh-size dependency. The mesh size in the bolt head was increased to 2.4 mm, reducing the total number of elements without adversely affecting the model's accuracy.

The friction coefficient between the external thread of the bolt and the internal thread of the coupler was assumed as 0.14 based on Reference [12].
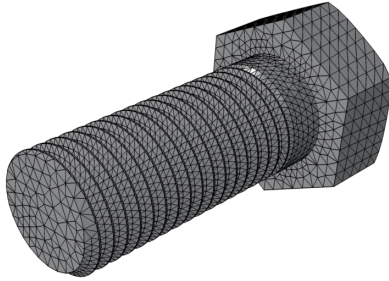
(a) Injection bolt.
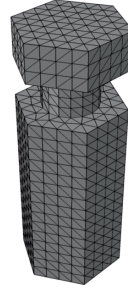
(b) Unified bolt-coupler.

(c) HE260A.
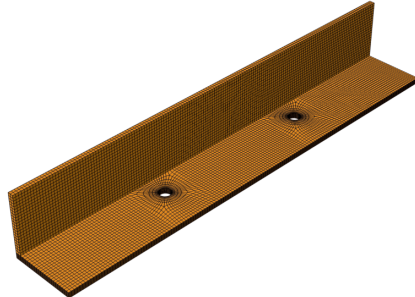
(d) Angle profile.
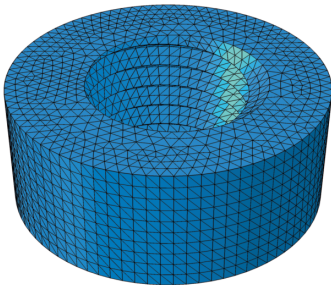
(e) (Steel-reinforced) resin.
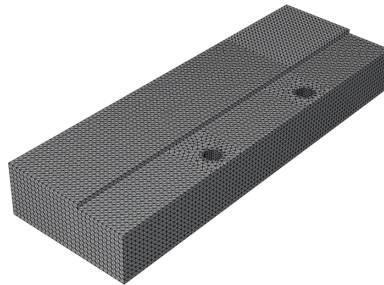
(f) Concrete.

Figure 5.7 | Geometry and mesh of the key connection components.
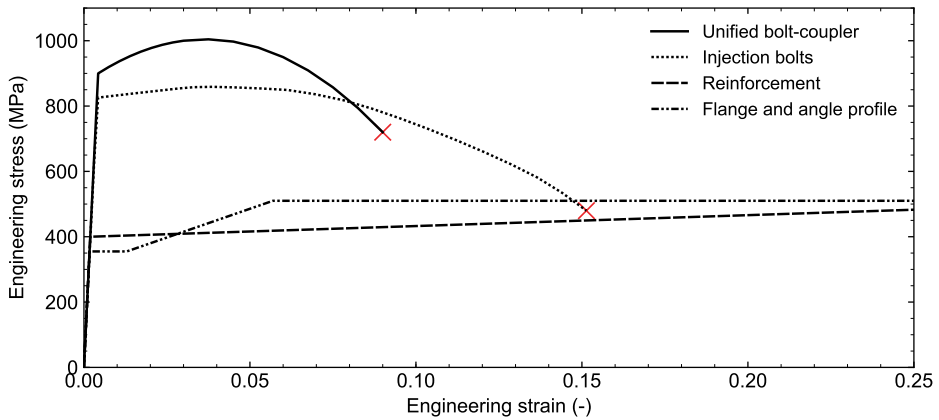
Figure 5.8 | Engineering stress-strain curves of steel components.

EMBEDDED COUPLER AND BOLT

A simplified representation of the embedded coupler and bolt was used to reduce computational time without compromising the model's accuracy. The embedded bolt and coupler were modelled as a monolithic part, see Figure 5.7(b), which is justified because their connected region is sufficiently far from the steel-concrete interface where the load is transferred and failure occurs.

The bottom of the unified part contained an internal thread, which engages with the external thread of the injection bolt. This complex geometry enabled the understanding of the deformation components in the zone where most of the imposed loads were transferred. This region was meshed using C3D4 tetrahedral elements with a nominal mesh size of 1.2 mm to match the mesh of the injection bolt. The mesh size increased to 4 mm in the other zones.

The uniaxial tensile stress-strain relation of the embedded coupler was assumed in accordance with the nominal properties of grade 10.9 bolts [1] see Figure 5.8. A similar approximation was successfully made by Milosavljevic et al. [11]. Progressive ductile damage models were iteratively calibrated using `ABAQUS` to match the numerical to the nominal stress-strain curve (see Figure 5.8) using the method outlined in Appendix B.

FLANGE AND ANGLE PROFILE

The flange of the HE260A section and the angle profile were meshed using hexagonal C3D8R elements with a nominal mesh size of 5 mm. The mesh was refined around the bolt holes to match the mesh of the (steel-reinforced) resin component. The meshed HE260A section and the meshed angle profile are illustrated in Figure 5.7(c) and (d), respectively.

A simplified tri-linear model corresponding to steel grade S355 described the stress-strain relation of the components, see Figure 5.8. No damage models were used for the HE260A and angle profile.

(STEEL-REINFORCED) RESIN

The (steel-reinforced resin) component contained an internal thread that has been match-cast from the external injection bolt. The part was meshed using C3D4 tetrahedral elements with a nominal mesh size of 1.2 mm, see Figure 5.7(e).

The non-linear material properties for the (steel-reinforced) resin RenGel SW 404 + HY 5159, derived in Chapter 3 and summarised in Appendix A for application in `ABAQUS`, were used to describe the material behaviour.

CONCRETE AND REINFORCEMENT

The prefabricated concrete elements were modelled using hexagonal C3D8R elements with a nominal mesh size of 10 mm, see Figure 5.7(f). Preliminary analyses indicated that no mesh size sensitivity (in terms of resistance or slip) occurs for mesh sizes smaller than 10 mm; a similar threshold value was found by Milosavljevic et al. (12 mm) [11] and Pavlovic (10 mm) [9]. The mesh was refined to 4 mm in the vicinity of the embedded bolt-coupler.

The concrete material model, based on the actual strength properties of the prefabricated elements, is presented in Appendix C and is based on the Concrete Damage Plasticity (CDP) model native to `ABAQUS`. The uniaxial stress-strain curve in tension and compression based on $f_{cm,cube} = 48.2$ MPa are illustrated in Figure 5.9.

The reinforcement was modelled using wire-features as embedded regions in the concrete host element. A simple bi-linear material model for the grade B500B reinforcement was used, see Figure 5.8.

5.2.4. INTERACTIONS

The contact between different components was described by *General Contact*. Normal contact was defined as *hard* and tangential behaviour was assumed to be represented by a *penalty* friction formulation. A friction coefficient of 0.14 was used for thread-thread contact [12], the same value was used for all other contacts including the the lubricated interface between angle profile and flange. Only for the non-lubricated concrete-angle interface the friction coefficient was set as 0.30.

5.2.5. VALIDATION

Figure 5.10 illustrates the numerically and experimentally obtained load-slip curves. The spring stiffnesses and material parameters were iteratively calibrated as $k_y = 40$ kN/mm, $k_z = 20$ kN/mm, $\overline{\varepsilon}^{pl}_{s,bolt} = 0.058$ and $\overline{u}^{pl}_{f,s,bolt} = 0.10$ mm. The same value for k_y was used by Pavlovic [12] and Milosavljevic et al. [11], but these authors considered $k_z = \infty$ because in their cases the concrete elements were continuous in z-direction. The magnitude of $\overline{\varepsilon}^{pl}_{s,bolt}$ falls within the bounds previously reported (0.05 - 0.08) [11, 12], although $\overline{u}^{pl}_{f,s,bolt}$ was smaller compared to prior work (0.3 mm - 2 mm) [11, 12].

SPECIMENS FAILING AT MODERATE VS. SUBSTANTIAL SLIP

Good agreement was found between the numerical and experimental results, particularly for the specimens that failed at moderate slip (5-8 mm), irrespective of the shear damage parameters, which only control the ductility but to a lesser extent the shape of the load-slip curve. To investigate a possible explanation between the specimens failing at moderate and substantial slip (> 15 mm), either of the following imperfections were introduced:

(a) Tension.

(b) Compression.
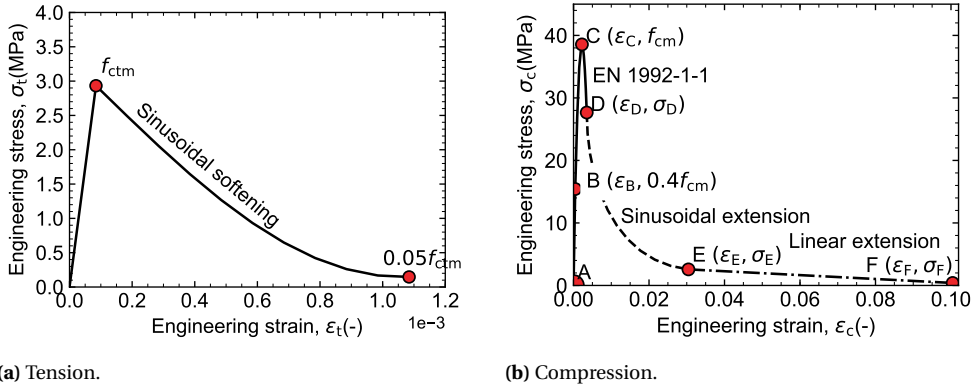
Figure 5.9 | Uniaxial stress-strain curves for the experimental concrete with $f_{cm} = 0.8 f_{cm,cube} = 38.6$ MPa. For details see Appendix C.

i. Cylindrical voids in the resin layer perpendicular to the direction of bearing. This type of imperfection could arise due to air inclusions in the epoxy resin layer.

ii. Reduced concrete strength class, C20/25 (see Appendix C), which could arise as a consequence of inadequate compaction/vibration.

iii. Reduced material properties of unified bolt-coupler, $f_y = 500$ MPa and $f_u = 600$ MPa, which could be attributed to the abundance of low-quality couplers on the market and the limited availability of grade 10.9 couplers.

iv. Reduced material properties of the injection bolts, $f_y = 640$ MPa and $f_u = 800$ MPa. The large batch of bolts (500 pcs) was purchased at once, but possibly the bolts did not originate from the same manufacturing batch.

v. Reduced lateral constraints at the supports, $k_y = 10$ kN/mm and $k_z = 5$ kN/mm.

Only the reduced concrete strength class led to a pronounced difference in the load-slip response, the good agreement between the finite element prediction and the experimental results is shown in Figure 5.10. It is therefore hypothesised that in a subgroup of prefabricated concrete elements the concrete strength is (at least) locally reduced due to inadequate compaction, which can be attributed to the relatively dense reinforcement in the shear connector zone, hindering the access of the vibration device. The local strength reduction did not influence the resistance of the connector because the failure mode remained bolt shear failure.

RESISTANCE, SECANT STIFFNESS, AND FAILURE MODE
The resistance P_u according to the finite element simulation of the resin and steel-reinforced resin specimens was 115.9 kN and 115.6 kN, respectively. Therefore the injectant only marginally influenced the ultimate resistance, which is in line with the experimental results. The secant connector stiffness of the steel-reinforced specimen at $0.4 P_u$ (see Section 5.3.2 for the
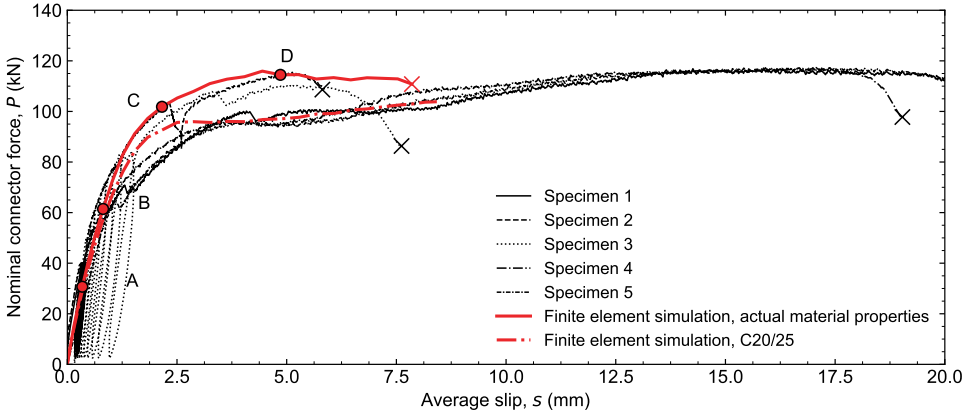
(a) Resin-injected specimens.
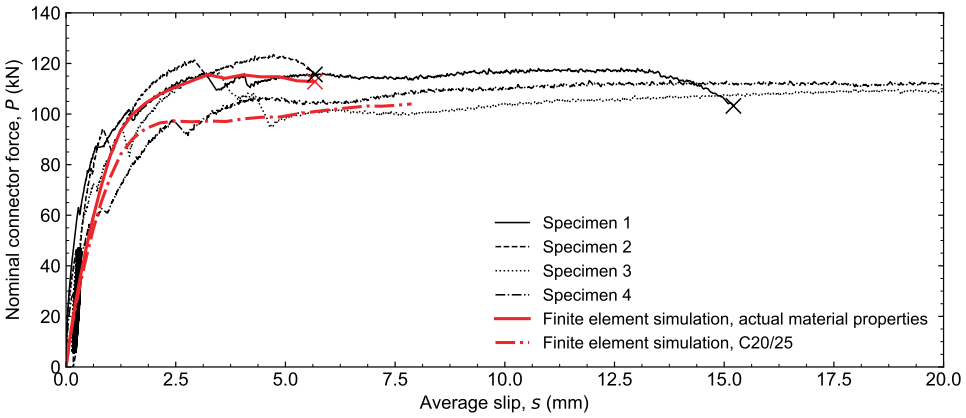
(b) Steel-reinforced resin-injected specimens.

Figure 5.10 | Experimental vs. numerical load-slip curves for the push-out specimens, points A-D provide reference to load levels in Figure 5.14.

background of this load level) was 25% higher compared to that of the resin-injected specimen, with $k_{sc,R} = 82.1$ kN/mm and $k_{sc,SRR} = 102.7$ kN/mm, respectively. The increase in connector stiffness is comparatively smaller than the increase of the Young's Moduli of the injectants ($E_{SRR} = 2.8E_R$, see Chapter 3), indicating that other deformation mechanisms (bending and shear deformation of the bolt, concrete compression, etc.) had a pronounced influence on the connection stiffness. The finite element results confirmed the effect of adhesion on the experimentally obtained magnitudes of k_{sc}: the 25% increase of k_{sc} for steel-reinforced resin-injected specimens compared to resin-injected specimens is substantially smaller than the 80% increase observed in the experiments. The comparison between experimental and finite element results is summarised in Figure 5.11. The finite element analysis enabled a more precise quantification of the beneficial effects of (steel-reinforced) resin-injected connections: the average experimental secant stiffness for the non-injected connections was 37% and 30% of the numerically predicted secant stiffness of the resin-injected and steel-reinforced resin-injected specimens, respectively.

The failure mode of the shear connector was bolt shear failure: the good agreement between the fracture surface of the numerical and experimental bolts is illustrated in Figure 5.12. Significant compressive and tensile damage occured in the concrete, see Figure 5.13, although no obvious cracking was observed on the external faces of the specimens.

CONCRETE BEARING STRESS
The concrete bearing stress over the height of the coupler is illustrated in Figure 5.14 for four different load levels (A-D, see Figure 5.10). The bearing stress was maximum at approximately 5 mm from the concrete bottom due to the comparatively stronger confinement, a similar effect was found by Pavlovic [12] for bolted headed studs with single embedded nuts. The bearing stress approaches zero at 40-55 mm from the concrete bottom, which indicates that no substantial effect of the connector height (e.g. on resistance or stiffness) could be expected beyond the physical height of the coupler. Significantly higher bearing stresses (up to 240 MPa) could be resisted compared to the uniaxial compressive strength $f_{cm} = 0.8f_{cm,cube} = 38.6$ MPa, which is attributed to the favourable multi-axial compressive stress state in the concrete as a result of the angle profile and the reinforcing U-bar. The shape of the bearing stress curve for load level D demonstrates the redistribution of the bearing stresses due to the degradation of the material properties.
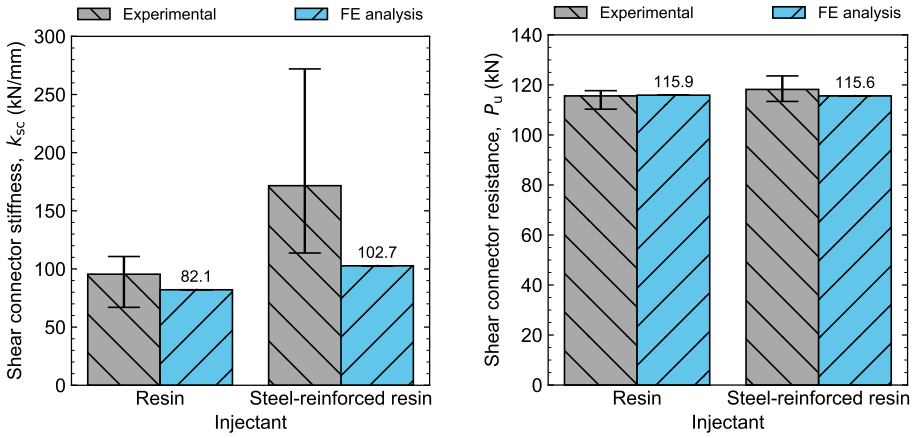
(a) Secant stiffness, k_{sc} (kN/mm) at $0.4P_u$.

(b) Resistance, P_u (kN).

Figure 5.11 | Experimental vs. finite element analysis results for push-out test.

(a) Experimental.
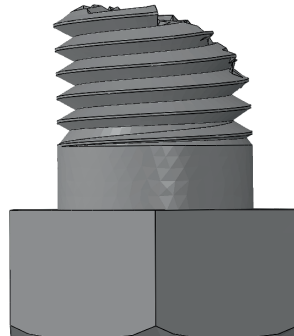
(b) Finite element simulation.

Figure 5.12 | Fracture surface of injections bolts.

5
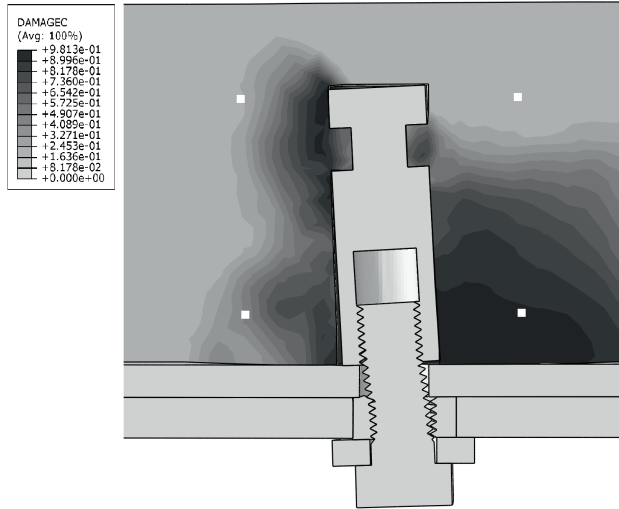
(a) Compressive damage state variable, D_c.
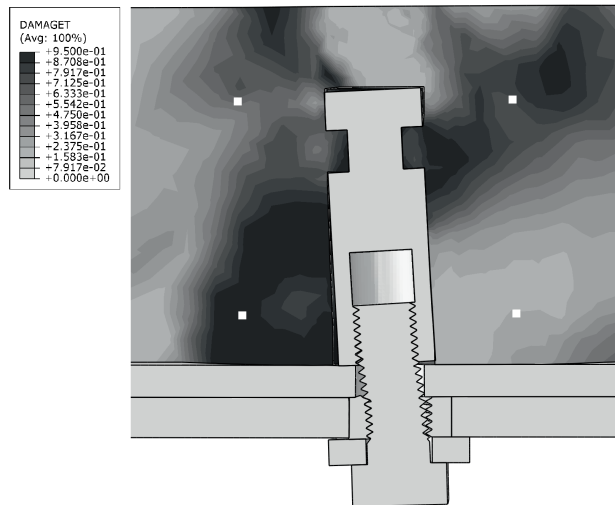
(b) Tensile damage state variable, D_t.

Figure 5.13 | Damage state variable for concrete in the region around the shear connector at the onset of bolt fracture.
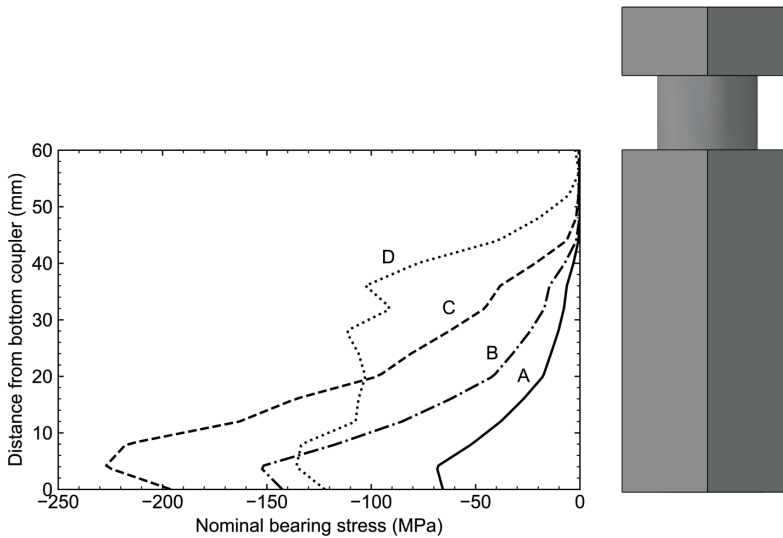
Figure 5.14 | Nominal bearing stress at coupler-concrete interface at four load levels A-D, see Figure 5.10.

5.3. Finite element parameter study

5.3.1. Design variations and material models

DESIGN VARIATIONS

The sensitivity of the shear connector system to changes in the geometry and/or strength of the components was assessed by a parameter study based on the FE model developed in Section 5.2. Variations included the bolt diameter (M20 and M24), the concrete strength class (C20/25, C30/37, C40/50), the bolt strength class (8.8, 10.9 and 12.9), and the nominal hole clearance (6, 12 and 20 mm). In addition, the influence of the reinforcing U-bar and the angle profile, both providing confinement to the concrete in the region around the shear connector, was investigated. Three connector spacings: 100 mm ($5d$), 200 mm ($10d$) and 300 mm ($15d$) were considered to determine the influence of the centre-to-centre distance on the mechanical behaviour. The connector height was not varied because the findings from Section 5.2.5 led to conclusion that its influence will be negligible.

The reference connector design is identical to the experimental geometry (see Section 5.1.1), and all parts were assigned nominal material properties. The aforementioned variations were applied to this reference connector design, while all other characteristic dimensions (spacing, edge distance, cover) and material models were kept equal unless stated otherwise.

MATERIAL MODELS

The material models for the steel components were based on their nominal (characteristic) properties and are shown in Figure 5.15 in the form of stress-strain curves. In Chapter 2 it was identified that the reusability of the shear connector system is an important prerequisite: therefore preventing the *onset* of permanent deformation is most important, while the *fracture* of the injection bolt could be avoided by the quasi linear-elastic design of both the connector and the composite floor system as a whole. For this reason the steel components

were modelled without damage initiation and evolution: at the onset of necking the engineering stress-strain curve was assumed to continue horizontally at the level of the nominal ultimate tensile strength.

The non-linear concrete material behaviour was introduced using the concrete damage plasticity (CDP) model based on the nominal (mean) properties according to EN 1992-1-1 [5]. The stress-strain curves of the different concrete grades are presented in Appendix C, where also the background to the material models can be found.

5.3.2. BASIS OF EVALUATION
The results of the parameter study were evaluated in terms of (i) the secant shear connector stiffness k_{sc} and (ii) the ultimate resistance P_u. An overview of these characteristics is given in Figure 5.16. The resistance P_u follows directly from the numerical results, whereas k_{sc} requires further definition.

The (secant) shear connector stiffness was determined at the load level $\alpha_k P_u$, such that

$$k_{sc} = \frac{\alpha_k P_u}{s(\alpha_k P_u)},\tag{5.6}$$

where $s(\alpha_k P_u)$ is the slip at load level $\alpha_k P_u$. The parameter α_k was taken as 0.40 based on preliminary analyses: this value was considered to be sufficiently small (and large) to be representative for the quasi-linear branch of the load-slip curve, and at this load level no significant damage developed in the concrete. It should be noted that the definition of the secant stiffness was done based on an *engineering sense*, but is in fact arbitrary. However, arbitrary or not, the definition enabled the objective comparison of the characteristics of the alternative shear connector designs considered in the parametric study.

5.3.3. RESULTS AND DISCUSSION
The results of the parameter study in terms of k_{sc} and P_u are summarised in Figures 5.17-5.22 for each type of design variation. The figures also illustrate the bolt shear resistance and the concrete bearing resistance according to the hand calculation model (HCM) of Pavlovic [9], expressed by Equation 5.3 and 5.4, respectively. The findings per design variation category are separately discussed in the following subsections. The full load-slip curves for all of the connection designs considered in the parametric study are presented in Appendix D.

CONNECTOR SPACING
The connector spacing was reduced from 300 mm or $15d$ (reference design, with d the bolt diameter) to 100 mm ($5d$) or 200 mm ($10d$). This reduced spacing enables an increased concentration of shear connectors to maximise the beneficial effects of composite interaction for composite floor systems.

The effects of the reduced shear connector spacing are illustrated in Figure 5.17 and indicate that the secant stiffness decreased by 5% and 9% for resin and steel-reinforced resin-injected specimens, respectively, if the spacing was reduced from 300 to 100 mm. No substantial difference in terms of the secant stiffness was observed for spacings of 200 and 300 mm, implying that in the quasi-elastic stage no interaction between the reference shear connectors exists up to a spacing of approximately $10d$.
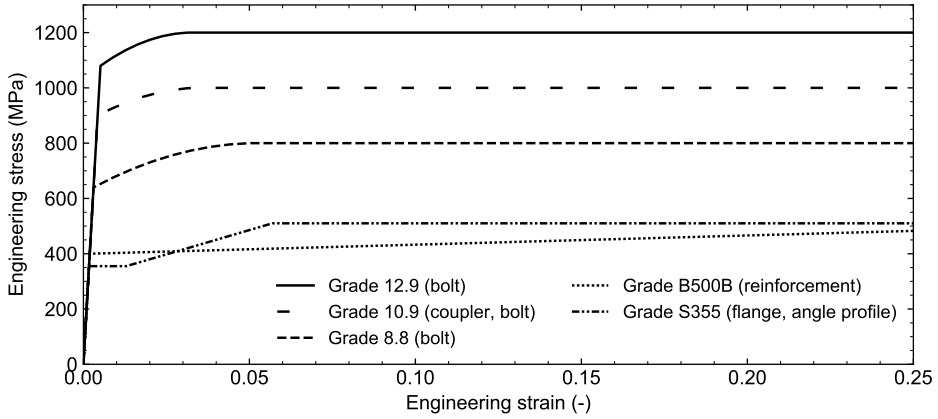
Figure 5.15 | Stress-strain curves for steel components for the parameter study.
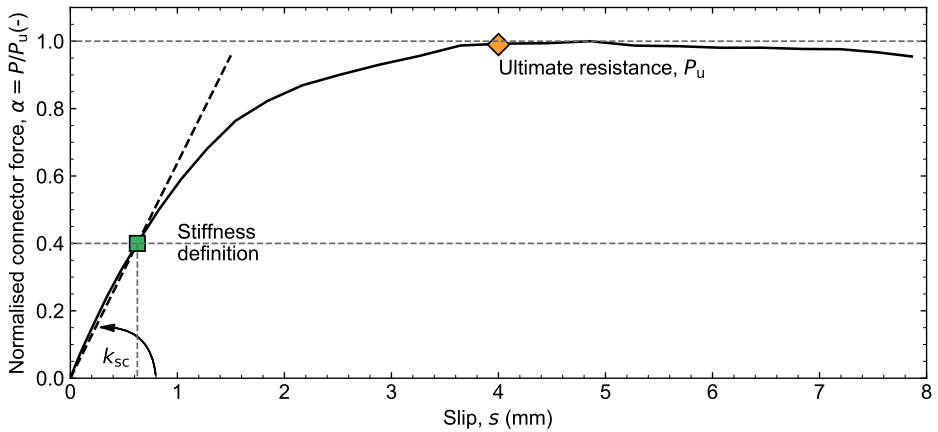
Figure 5.16 | Evaluation of the shear connector characteristics.

In contrast to the secant stiffness, the resistance decreased by approximately 10% for both 100 and 200 mm spacings compared the reference case. This strength reduction occurred due to the overlap of high stress zones in the concrete, which arose as a result of bearing of the couplers. The hand calculation model of Pavlovic [9] does not account for reduced spacing, but accurately predicted the resistance (deviation +3%) for 300 mm spacing, which was characterised by bolt shear failure. A higher grade concrete has the potential to mitigate (delay) effects related to the decrease in resistance as a result of overlapping high stress zones in the concrete.

Bolt diameter

Two nominal bolt diameters, M20 and M24, were considered on the basis of the reference connector design introduced in Section 5.3.1. Because the height of the coupler is typically $3d$, the prefabricated concrete block for the M24 bolt was 12 mm thicker compared to the reference design to maintain equal concrete cover (25 mm).

Figure 5.18 illustrates the effect of the bolt diameter on the stiffness and resistance of the shear connector. The secant stiffness increased by 27% and 30% for the resin and steel-reinforced resin-injected specimens, respectively, when replacing the M20 by M24 components. The bolt bending stiffness EI increased by 107%, but this increase was not fully not reflected in the simulation results because of the multitude of other deformation mechanisms. The comparatively stronger increase for the steel-reinforced resin-injected connector is explained by the fact that part of the deformation associated with bolt bearing was mitigated compared to the resin-injected connector: therefore any reduction of bolt bending deformation has a more pronounced effect on k_{sc}.

The resistance increased by approximately 40% for both injectants when applying M24 instead of M20 components: this gain is comparable to the 44% increase of the bolt shear area, and demonstrated that the resistance of the bolt was governing for this particular connector design. For both cases the resistance of the shear connector was accurately predicted by the hand calculation model of Pavlovic [9] (see Figure 5.18), which indicated bolt shear failure for M20 and concrete bearing failure for M24 bolts.

The increased ductility of larger diameter bolts, observed in the work of Pavlovic [12], could not be confirmed nor rejected because the parametric study did not focus on the shear fracture of the connector.

Bolt grade

Three different bolt grades (8.8, 10.9 and 12.9) were considered for the injection bolts: the effect of the bolt grade on the stiffness and resistance of the shear connector is illustrated in Figure 5.19.

The secant stiffness did not substantially vary because all three bolt grades are characterised by the same Young's Modulus E. The minor variation in k_{sc} is attributed to its definition - the behaviour of the connectors in the quasi linear-elastic stage are nominally identical.

The resistance increased by 8.5% and 13.6% for grades 10.9 and 12.9, respectively, compared to grade 8.8 for resin-injected connections, and 8.6% and 15% for the steel-reinforced resin-injected connections. These increases were not proportional to the 25% and 50% gain in terms of the ultimate tensile strength: this non-proportionality could be associated with the change of the governing failure mode from bolt shear failure to concrete failure. The
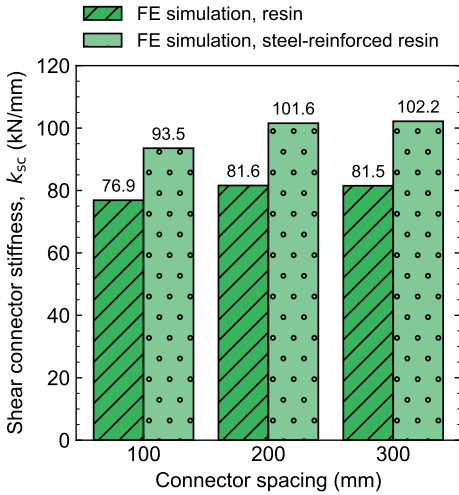
(a) Secant stiffness, k_{sc} (kN/mm).
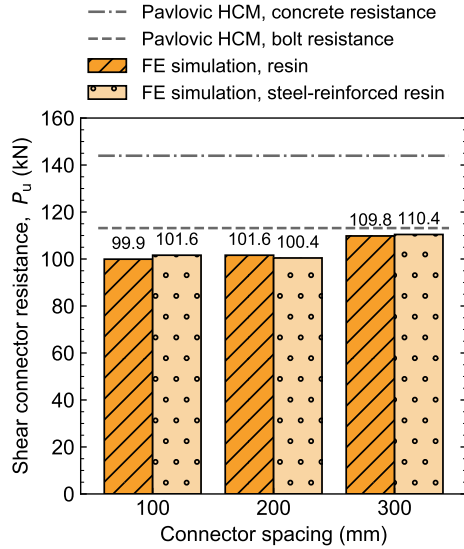
(b) Resistance, P_u (kN).

Figure 5.17 | Effect of the change in connector spacing for the reference connector design.
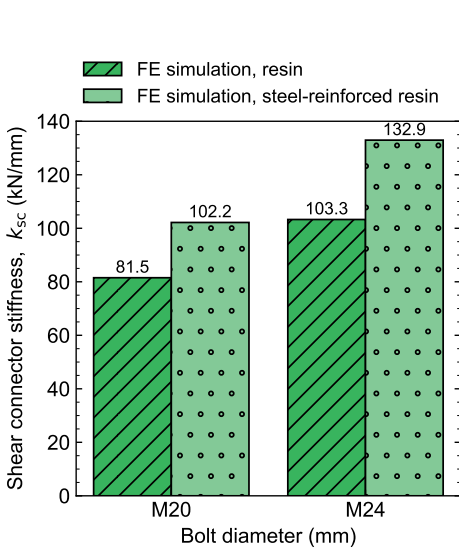
(a) Secant stiffness, k_{sc} (kN/mm).
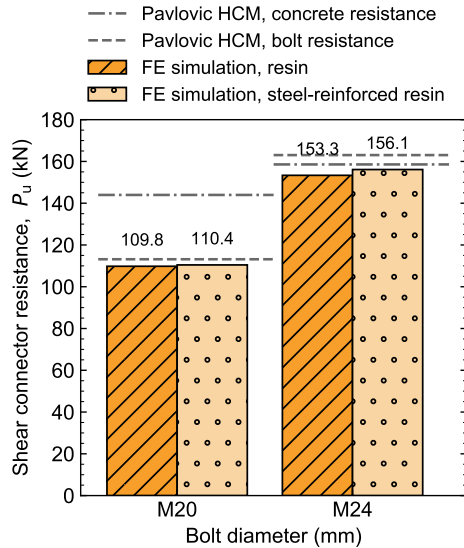
(b) Resistance, P_u (kN).

Figure 5.18 | Effect of the change in bolt diameter for the reference connector design.

hand calculation model of Pavlovic [9] confirmed that concrete bearing failure would become more dominant for higher bolt grades, but did not accurately predict the resistance for grade 10.9 and 12.9 bolts. This discrepancy indicates that either (i) there could be a mutual influence between the two failure modes that reduced the overall resistance or (ii) the concrete bearing resistance was lower because of reduced confinement effects due to the larger height of the coupler compared to the height of an embedded nut. Pavlovic [9] proved that the concrete above embedded nuts contributes more to the resistance compared to the concrete in front of the embedded nut: such beneficial effects do not occur in case of a comparatively higher coupler.

CONFINEMENT LEVEL: INFLUENCE OF U-BAR AND ANGLE PROFILE

The confinement of the concrete in the region around the shear connector is reported in literature [e.g. in 14] to influence the resistance. In the experimental work, see Section 5.1.1, the concrete was laterally restrained by the reinforcing U-bar around the coupler and by the steel angle profile. However, the main question is if both (or any) of these restraints are necessary to develop a similar resistance and stiffness.

Four alternative designs were considered: (i) with U-bar and angle profile, (ii) only U-bar, (iii) only angle profile and (iv) neither of the two. The effects of these four alternatives on the stiffness and resistance are illustrated in Figure 5.20.

The stiffness of the shear connector increased by 35-45% when the angle profile was removed but the U-bar was retained. Although this may seem contradictory, it can be explained by the reduced bending of the bolt: the bolt now passes through the flange (and injectant) directly into the coupler, without passing through the intermediary non-load bearing angle profile. A secondary explanatory factor for the higher shear connector stiffness could be the increased axial stiffness of the bolt due to its reduced effective length, leading to reduced rotation of the connector/coupler for a constant catenary force in the bolt. A slightly higher increase in the stiffness was found in the absence of both the U-bar and angle profile (case iv): inspection of the load-slip diagram (see Appendix D) reveals that this is a consequence of how k_{sc} is defined, and that in fact the stiffness is nominally identical for cases (ii) and (iv).

Shear connectors confined by an angle profile and U-bar had a similar resistance (difference < 2%) as those confined by only a U-bar. An additional benefit of the removal of the angle profile is that the quasi-linear branch was extended, see Appendix D, thus enabling a higher force transfer per connector while conforming to the principles of reusability. Shear connectors without a U-bar but with an angle profile had a 13-15% lower resistance, therefore the U-bars are considered more effective than the angle profiles. The biggest reduction in terms of resistance was 27-28% and occurred for case iv (no confining components): this suggests that the concrete needs a confining element to develop the maximum shear connector resistance. The results of the hand calculation model (HCM) of Pavlovic [9] demonstrated that the closed-form expressions are only valid in case of sufficiently confined concrete. In case of well-confined concrete the HCM overestimated the resistance by only 3%, whereas it overestimated the resistance by up to 28% in case of insufficient confinement. It should be noted that, in absence of the angle profile, the coupler (width-over-flats 32 mm) rests partially on the flange and partially on the injectant. However, because of the large nominal hole clearance (12 mm) it was assumed that no significant embedment and frictional effects arose at the coupler-flange plane because of the deformability of the injectant

on which the coupler mostly rested: therefore the exponent a in Equation 5.3 was kept as zero.

It was concluded that the application of U-bars around the couplers (case ii) is the best design strategy because it increased the connector stiffness and because it had no detrimental effect on the resistance compared to the reference connector design (case i).

CONCRETE STRENGTH CLASS

Three different concrete strength classes (C20/25, C30/37 and C40/50) were considered for the prefabricated concrete elements. The effect of the concrete strength class on the stiffness and resistance of the shear connector is illustrated in Figure 5.21.

Compared to strength class C20/25, the secant stiffness for C40/50 increased by 7% and 8.4% for resin and steel-reinforced resin-injected hole clearances, respectively. The theoretically maximum increase (based on the Young's Moduli according to EN 1992-1-1 [5]) is 16.7%, which was not reflected in the simulation results due to the compliance of other connector elements. The comparatively larger increase for the steel-reinforced resin-injected connection was due the injectant's inherently lower bearing compliance.

Comparing the same two strength classes, the connector resistance increased marginally (10-12%) compared to the potential 71% increase based on the mean concrete compressive strength according to EN 1992-1-1 [5]. This indicates that higher strength concrete is only sensible if it is accompanied by a higher bolt grade for this reference connector design. According to the hand calculation model (HCM) of Pavlovic [9], bolt shear failure is the governing failure mode for all three concrete strength classes considered. However, the HCM increasingly overstimated the resistance for lower concrete strength classes, suggesting that interaction may have existed between the concrete bearing failure mode and the bolt shear failure mode. Alternatively, the concrete bearing resistance could be lower than expected because of reduced confinement effects due to the larger height of the coupler compared to the height of an embedded nut. Pavlovic [9] proved that the concrete above embedded nuts contributes more to the resistance compared to the concrete in front of the embedded nut: such beneficial effects do not occur in case of a comparatively higher coupler, leading to an overestimation of the concrete bearing resistance by the HCM for lower concrete strength classes.

NOMINAL HOLE CLEARANCE

Three magnitudes of the nominal hole clearance were investigated: 6, 12 and 20 mm. All other geometrical and dimensional characteristics were identical to the reference design presented in Section 5.3.1.

Figure 5.22 illustrates the effect of the nominal hole clearance on the stiffness and resistance of the shear connector. The secant stiffness decreased by 10% and 21% if the hole clearance was increased from 6 to 20 mm for resin-injected and steel-reinforced resin-injected connections, respectively. Injecting steel-reinforced resin instead of resin enabled the increase of the nominal hole clearance from 6 to 20 mm while still obtaining a relative benefit in terms of the secant stiffness (k_{sc} = 96.5 vs. 89.9 kN/mm), underlining the potential of the steel-reinforced resin to *prevent* additional deformations associated to large nominal hole clearances. However, even for the 20 mm resin-injected hole clearance (k_{sc} = 71.4 kN/mm) the secant stiffness was still substantially larger compared to the experimental non-injected specimens (see Section 5.1.2) for which k_{sc} = 30.5 kN/mm. Therefore it can be concluded that injection bolts with large nominal hole clearances offer a substantial

(a) Secant stiffness, k_{sc} (kN/mm).

(b) Resistance, P_u (kN).
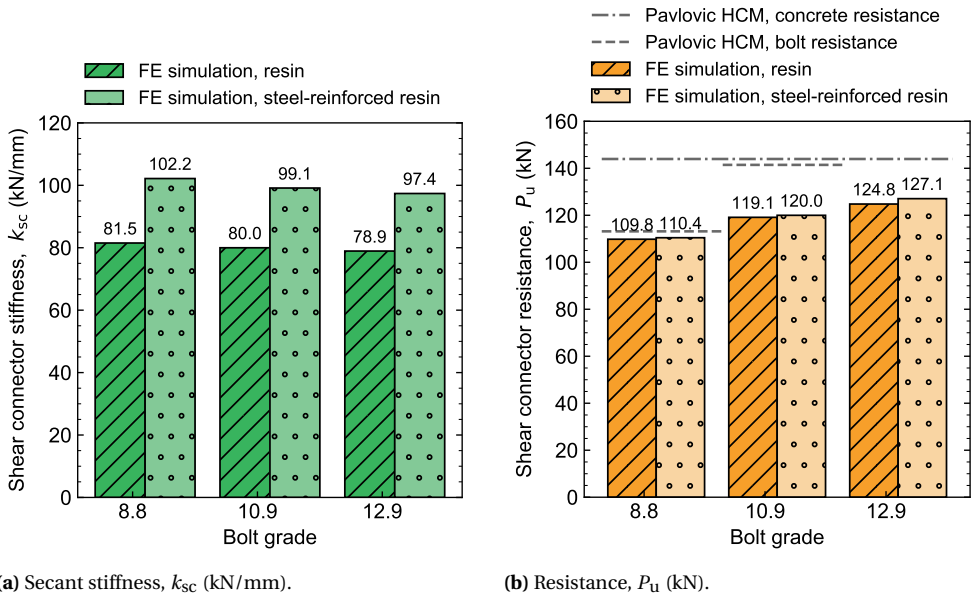
Figure 5.19 | Effect of the change in bolt grade for the reference connector design.

(a) Secant stiffness, k_{sc} (kN/mm).

(b) Resistance, P_u (kN).
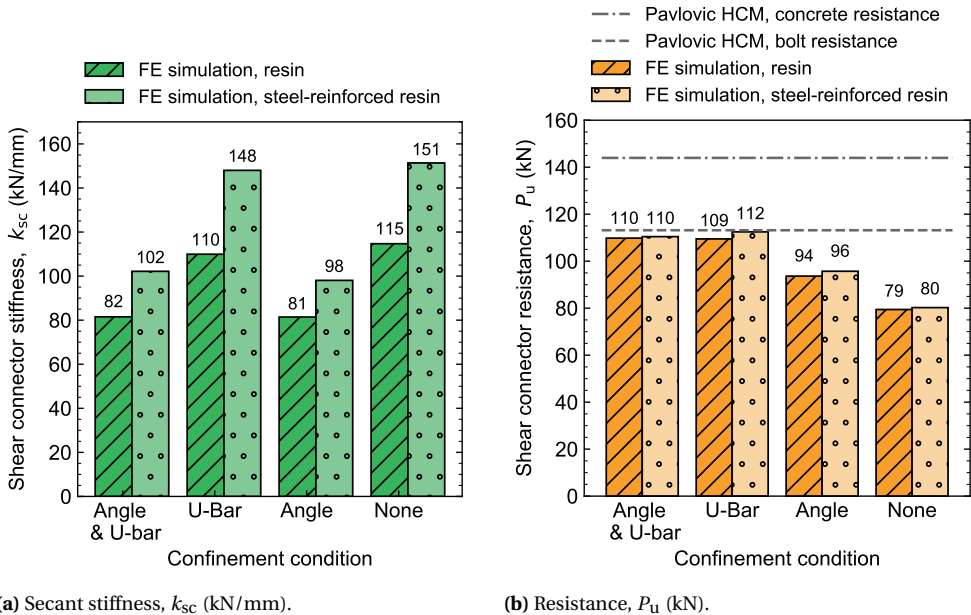
Figure 5.20 | Effect of the change in confinement conditions around the shear connector for the reference connector design.

comparative advantage to conventional bolted connections, and that the performance can be further optimised using steel-reinforced resin.

The variation of the resistance for the three alternative designs was negligible (<0.2%), implying that increased nominal hole clearances do not adversely affect the resistance of the connector. The resistance is in good agreement with the prediction based on the hand calculation model of Pavlovic [9] for all nominal hole clearances considered.

5.3.4. Design recommendation

The results of the parametric study identified opportunities to maximise the secant connector stiffness and the connector resistance. The combination of both metrics (i) increases the benefits of composite action and (ii) maximises the force that the connector can transfer quasi-elastically in a composite floor system.

The connector spacing is recommended to be $10d$ for M20 bolts to maximise the number of shear connectors in the most effective shear transfer zones in a composite floor system, without excessively compromising on connector stiffness and resistance. Larger bolt diameters increased both the stiffness and resistance, and are therefore recommended, although the bolt diameter is practically limited by the physically maximum diameter of the oversized bolt hole. This hole diameter depends on the required nominal hole clearance, which had a significant effect on the stiffness and a negligible effect on the resistance. However, even for a 20 mm nominal hole clearance, a favourable substantial net effect was found compared to non-injected connections, and therefore virtually any injected hole clearance is preferred over a non-injected connection. An increase of the bolt grade and concrete strength class is most appropriate if simultaneous: in isolation the beneficial effects were limited due to interaction of the failure modes. Confining the concrete around the shear connector with a reinforcing U-bar is most appropriate and leads to the highest stiffness and equal resistance compared to the reference design: the angle profile can therefore be omitted.

(a) Secant stiffness, k_{sc} (kN/mm).

(b) Resistance, P_u (kN).
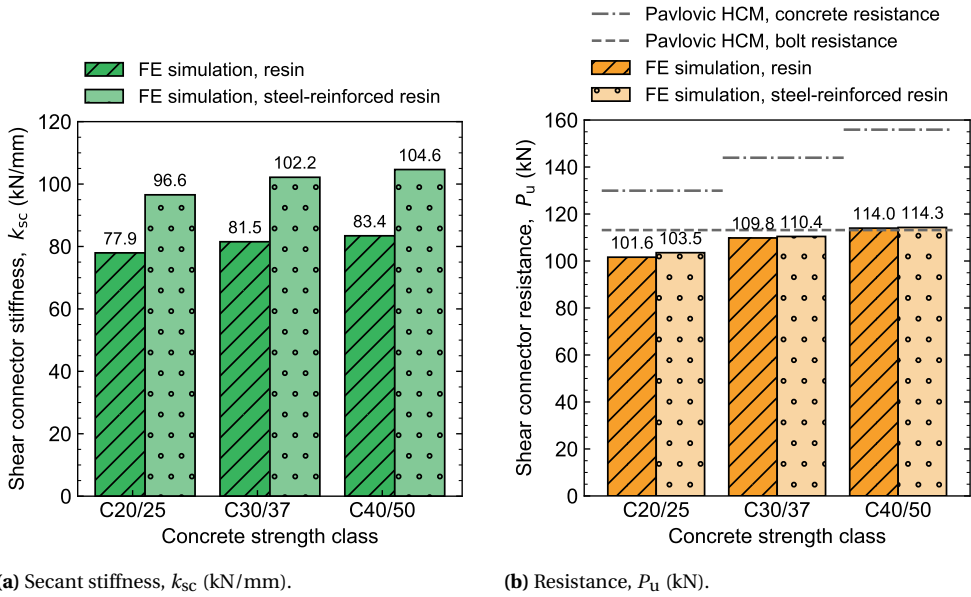
Figure 5.21 | Effect of the change in concrete strength class for the reference connector design.

(a) Secant stiffness, k_{sc} (kN/mm).

(b) Resistance, P_u (kN).
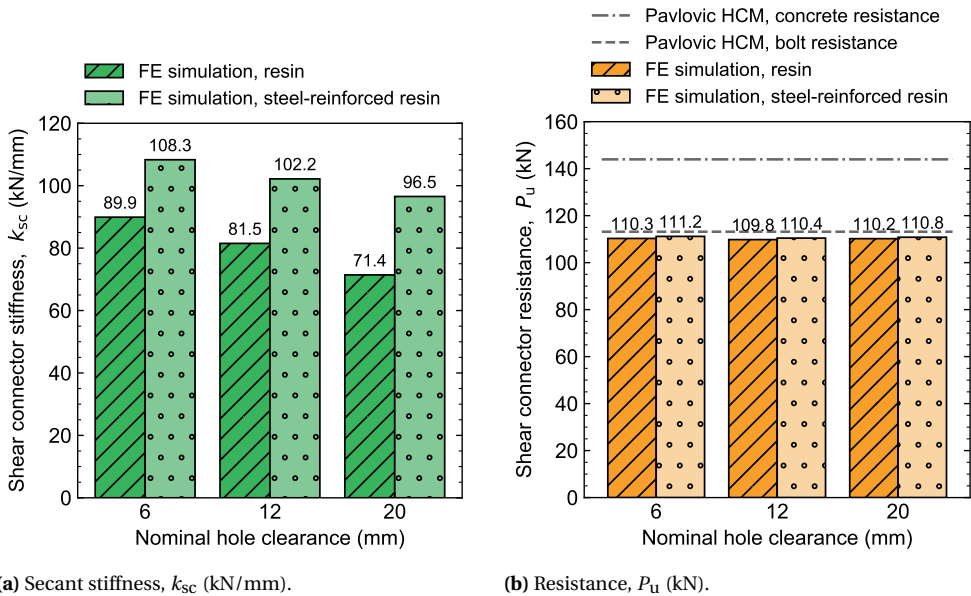
Figure 5.22 | Effect of the change in nominal hole clearance for the reference connector design.

5.4. CONCLUSIONS

This chapter presented experimental and numerical work related to the short-term behaviour of the demountable shear connector synthesised based on the literature review. Experimental push-out tests were conducted to establish the short-term relation between load and deformation for a (steel-reinforced) resin-injected demountable shear connector suitable for application in steel-concrete composite floor systems. Extensive finiteelement modelling of the push-out tests was performed using `ABAQUS` and its dynamic explicit solver. The (steel-reinforced) resin material models developed in Chapter 3 were implemented, and material models for the concrete and steel components were derived. Shear damage parameters were iteratively calibrated to match the experimentally observed shear fracture of the injection bolt. The calibrated finite element model was used to perform a parametric study to evaluate the effects of design variations on the shear connector response. Based on all experimental and numerical work, the following conclusions can be made:

- The experimental results demonstrated that the resistance P_u was invariant with the injectant ($p = 0.347$) and, for present geometry, was governed by the shear resistance of the injection bolt. No statistical difference was found between the resistance of injected and non-injected connections either ($p = 0.403$). The average resistance of the shear connectors was $P_u = 0.547 A_s f_{ub} = 117.7$ kN, which is 6% lower than predicted by the hand calculation model developed by Pavlovic [9].

- The secant stiffness at $0.4P_u$ of the steel-reinforced resin-injected specimens was on average 80% higher compared that of the resin-injected specimens, although frictional and adhesive effects caused substantial variations of this parameter for nominally identical specimens. The non-injected specimens had a significantly lower secant stiffness at $0.4P_u$: it reduced to 30% and 18% of the secant stiffness of the resininjected and steel-reinforced resin-injected specimens, respectively. Despite the scatter in k_{sc} for the injected connections, the experimental results qualitatively demonstrated the benefits of implementing injection bolts in demountable shear connectors. Finite element analysis enabled a more precise quantification of the beneficial effects of (steel-reinforced) resin-injected connections: the stiffness for the noninjected connection ($k_{sc} = 30.5$ kN/mm) was 37% and 30% of the secant stiffness of the resin-injected ($k_{sc} = 82.1$ kN/mm) and steel-reinforced resin-injected specimens ($k_{sc} = 102.7$ kN/mm, respectively.

- The experimental push-out test results were compared to those obtained by Kozma [10] for a similar shear connector type, which was pretensioned to 70% of the bolt tensile resistance but not injected. It was found that the pretensioned connector exhibited a 21% higher resistance due to additional force transfer by friction, but that substantial slip occurred once the friction resistance was overcome at approximately $0.3\text{-}0.4P_u$, which led to a significant reduction of the secant stiffness. Such substantial slip did not occur in case of injected shear connector because of the injectant fixated the location of the bolt: therefore injected shear connectors were considered to be more suitable than pretensioned shear connectors to develop significant composite interaction in a floor system.

5

- The experimental results of push-out tests showed two subgroups of specimens, (i) those that failed after moderate slip (5-8 mm) and those that failed after substantial slip (> 15 mm), irrespective of the injectant. The finite element model accurately reproduced the load-slip curves for the specimens that failed at moderate slip, and the model was modified to study the influence of material and geometrical imperfections on the results. This sensitivity study led to the hypothesis that poor concrete vibration led to a lower strength in the region around the shear connector and contributed to the deviation between the two groups.

- A finite element parameter study was performed to optimise the design of the demountable shear connector in terms of connector spacing, bolt diameter, bolt grade, concrete confinement, concrete strength class, and the nominal hole clearance (the difference between the hole and bolt diameters). One of the most important findings is that regardless of nominal hole clearance (varied in the range 6-20 mm), injected bolted shear connectors lead to higher secant stiffness compared to the experimental non-injected specimens. The stiffness increase is between 134% and 255%, corresponding to a 20 mm resin-injected nominal hole clearance and a 6 mm steel-reinforced resin-injected nominal hole clearance, respectively. A second key finding was that the angle profile around the concrete perimeter did not contribute at all to the resistance if the concrete around the connector was adequately confined by a reinforcing U-bar. However, omitting the angle profile led to a significant (35-45%) increase of the secant stiffness because of reduced bolt bending. Therefore confining the concrete around the shear connector solely by a reinforcing U-bar is the recommended design approach.

- The results of the parametric study were compared in terms of the shear connector resistance to the prediction based on the hand calculation model (HCM) derived by Pavlovic [9]. Generally good agreement was observed, although the HCM led to incorrect results in case of insufficient confinement of the concrete and in case of connector spacings of $5d$ and $10d$. Also the HCM led to incorrect results for a number of combinations of concrete strength classes and bolt grades: whenever the concrete bearing resistance was governing, the resistance was overestimated. This effect was hypothesised to be related to the absence of beneficial confinement effects typically observed above embedded nuts: the larger height of the coupler was hypothesised to prevent such beneficial effects from arising.

6

LONG-TERM BEHAVIOUR OF (STEEL-REINFORCED) RESIN-INJECTED CONNECTIONS

The trouble with being punctual is that nobody is there to appreciate it.

Franklin P. Jones

INTRODUCTION

This chapter focuses on the long-term behaviour of injected bolted shear connections subject to sustained loading. In this chapter, push-out specimens similar to those considered in Chapter 5 are subjected to sustained loads during a fourteen-day period. Experiments on steel-to-steel (steel-reinforced) resin-injected double lap shear connections reveal the influence of the injectant on time-dependent slip. By aligning the magnitudes of the nominal bearing stress in the injectant for both types of experiments, the relative contributions of the injectant and concrete to the time-dependent slip of push-out specimens is determined.

This chapter is subdivided into four sections. Section 6.1 presents the design and results of experimental long-term *push-out* tests on steel-reinforced resin-injected demountable shear connectors synthesised in Chapter 2. Experimental details and results of steel-to-steel (steel-reinforced) resin-injected double lap shear connections are presented in Section 6.2. These experiments were performed to obtain information on the short- and long-term response of the injectant at the same nominal bearing stress levels as considered in the long-term push-out tests. The chapter proceeds with Section 6.3, where the results of the long-term push-out and double-lap shear connection experiments are analysed to determine the relative contribution of the injectant and concrete to the time-dependent slip observed in push-out specimens. The chapter concludes with Section 6.4, summarising the main findings of this chapter.

6.1. Long-term push-out tests

6.1.1. Specimen design and experimental details

Five push-out specimens were subjected to sustained loads to investigate the creep sensitivity of the demountable shear connector synthesised in Chapter 2. The specimens had a nominally identical geometry as the short-term specimen presented in Chapter 5 and were subjected to identical external conditions unless mentioned otherwise. The only difference in the geometry with respect to the short-term tests was the position of the bolt in the hole: for the long-term tests the bolts were positioned in the most unfavourable positions with respect to the potential connection slip (resulting in a 12 mm load-bearing injection layer). Only the steel-reinforced variant of epoxy resin system RenGel SW 404 + HY 5159 was considered in the long-term push-out tests.

An overview of the test matrix is given in Table 6.1. Two nominal load levels were considered: 43.8 kN and 56.3 kN per shear connector, equivalent to 37% and 48% of the short term resistance, respectively. The load levels correspond to nominal bearing stresses $\sigma_{b,nom}$ = 175 and 225 MPa, respectively, in the steel-reinforced resin. All specimens, except POT-C-225-3, were loaded to their respective nominal force per shear connector at a rate of 2.5 kN/s. Specimen POT-C-225-3 was first subjected to 25 cycles between $0.05P_u$ = 5.9 kN and $0.4P_u$ = 47.3 kN per shear connector prior to attaining the long-term load $0.48P_u$ = 56.3 kN per shear connector. This specimen was subject to a different loading pattern to reduce any sudden slip during the initial phases of the long-term test which was observed in three of the four other experiments. After 14 days of sustained loading the specimens were first unloaded, and then loaded to failure by displacement control at a rate of 1 mm/minute.

The prefabricated concrete blocks were cast approximately 15 months before the first external load was applied. This was not a conscious decision, but was a consequence of the progress with the static push-out tests and other logistical challenges. The true time-dependent deformation of the concrete would have increased if load would have been first applied at a typical concrete age, e.g. 28 days after casting.

6.1.2. Results and discussion

Figure 6.1 illustrates the relation between force and slip during load application. Specimens POT-C-175-2, POT-C-225-1 and POT-C-225-2 demonstrated a sudden increase of the slip by up to 0.6 mm during load application. Based on this observation, specimen POT-C-225-3 was first subjected to 25 force-controlled cycles between $0.05P_u$ and $0.40P_u$ before reach-

Table 6.1 | Test matrix for long-term push-out tests. All specimens had steel-reinforced resin-injected shear connectors: the bolts were installed in the most unfavourable position in the bolt hole to obtain the maximum potential connection slip.

Specimen	Nominal bearing stress, $\sigma_{b,nom}$ (MPa)	External force per shear connector, F (kN)	Load application
POT-C-175-1	175	43.8 ($0.37P_u$)	Monotonically to F at 2.5 kN/s
POT-C-175-2	175	43.8 ($0.37P_u$)	Monotonically to F at 2.5 kN/s
POT-C-225-1	225	56.3 ($0.48P_u$)	Monotonically to F at 2.5 kN/s
POT-C-225-2	225	56.3 ($0.48P_u$)	Monotonically to F at 2.5 kN/s
POT-C-225-3	225	56.3 ($0.48P_u$)	Twenty-five force-controlled cycles between $0.05P_u$ and $0.40P_u$ at f = 0.02 Hz before reaching F

ing its designated load of $0.48P_{\mathrm{u}}$. This specimen did not exhibit sudden slip to the same extent as the other specimens: only a sudden minor increase occurred at the peak of one of the load cycles. The combined set of short-term (Chapter 5) and long-term (Chapter 6) push-out tests indicated that the sudden slip did not occur due to the loading type (force-vs. deformation-controlled). Neither was the effect likely to be related to dynamic effects: the monotonically loaded long-term specimens had a smaller loading rate (2.5 kN/s) compared to the short-term specimens subject to the twenty five cycles (6.6 kN/s). Therefore, the sudden slip was hypothesised to have occurred due to material imperfections in the push-out specimens, the effects of which were mitigated by prior cyclic loading in case of specimen POT-C-225-3.

Figure 6.2 illustrates the development of the slip over time, where the whiskers represent the slip range of the eight individual shear connectors per specimen. Specimen POT-C-175-1, which did not show sudden slip during load application, demonstrated sudden slip of 0.6 mm after approximately 5 hours of constant loading. A similar sudden slip, although with reduced magnitude, occurred for specimen POT-C-225-1 after approximately 2 days. Specimen POT-C-225-3 was the only specimen that did not exhibit sudden slip during load application and during the sustained loading phase. Although subjected to a 29% higher load level, the latter specimen developed on average a 10% reduced slip over the fourteen-day period compared to the POT-C-175-1/2 specimens. The results suggest that cyclic loading prior to creep testing could be essential to obtain reliable long-term shear connector behaviour, although further tests are necessary to strengthen this suggestion.

The sudden slip during load application and during the constant load impeded any accurate comparison of the absolute (time-dependent) slip between the different specimens. To enable a meaningful comparison, the incremental slip for $4 \leq t \leq 14$ days was used to exclude any influences related to sudden slip during the early testing stage. Figure 6.3 illustrates the slip since $t = 4$ days for all long-term push-out specimens. Nominally identical specimens showed similar time-dependent behaviour. Only specimen POT-C-225-3 demonstrated a reduced creep increment (-46% at $t = 14$ days) compared to the other two nominally identical (apart from the loading regime) specimens. It was hypothesised that this difference was caused by the cyclic loading which settled the specimen and mitigated material imperfections, hereby reducing the creep potential. The average accumulated creep slip for the push-out test specimens (not considering POT-C-225-3) increased approximately linearly (+34%) with the increase in applied load from $0.37P_{\mathrm{u}}$ to $0.48P_{\mathrm{u}}$ (+29%).

Figure 6.4 illustrates the load-slip curve until failure of the push-out specimens. No significant difference was observed between the response of specimens subject to 37% or 48% of the short-term resistance. However, the specimens subjected to sustained loads exhibit an earlier and more pronounced onset of non-linear behaviour than the short-term specimens considered in Chapter 5. The long-term specimens exhibited hardening after approximately 8 mm of slip, and had an average shear connector resistance of $P_{\mathrm{u}} = 119.4$ kN. The resistance did not significantly differ from the short-term specimens ($P_{\mathrm{u}} = 118.2$ kN), and therefore it was concluded that the sustained loads did not influence the resistance for the load levels and load duration considered in the experiments. Contrary to the short-term specimens, all long-term specimens demonstrated significant ductility (at least 15 mm slip capacity), although for both specimen types failure occurred due to shear failure of the bolts. Therefore there was no proof that the failure mechanism changed as a result of sustained loading.

(a) $0.37P_u \equiv \sigma_{b,nom} = 175$ MPa.

(b) $0.48P_u \equiv \sigma_{b,nom} = 225$ MPa.
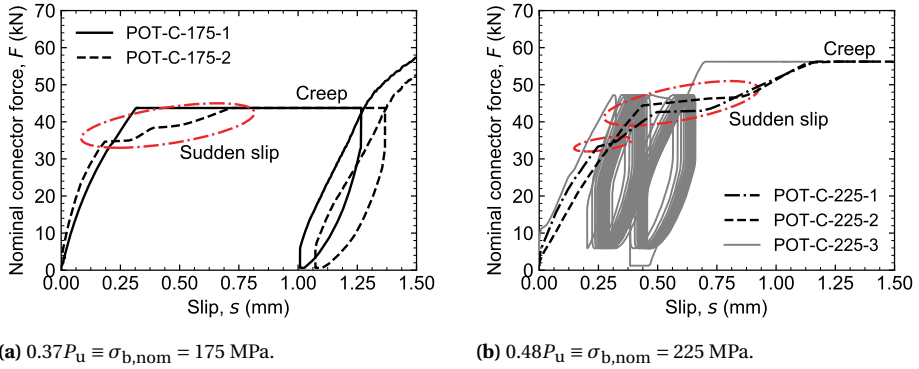
Figure 6.1 | Averaged force vs. slip diagrams of the load application phase for the long-term push-out specimens.

(a) $0.37P_u \equiv \sigma_{b,nom} = 175$ MPa.

(b) $0.48P_u \equiv \sigma_{b,nom} = 225$ MPa.
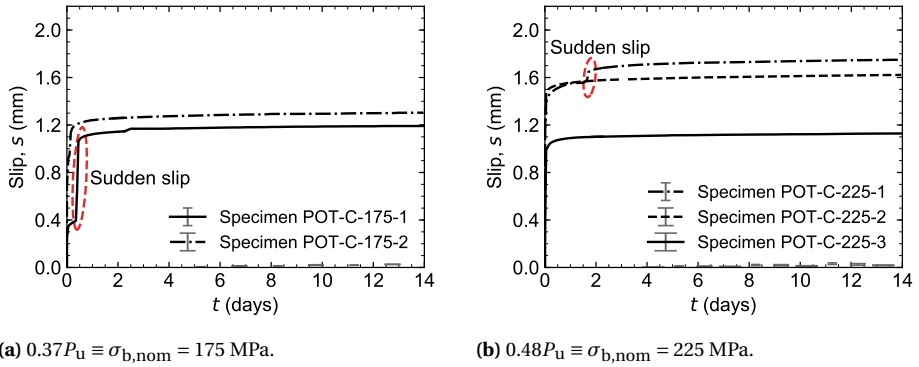
Figure 6.2 | Averaged slip vs. time diagrams of the long-term push-out specimens. Whiskers indicate range of eight connectors per specimen.

(a) $0.37P_u \equiv \sigma_{b,nom} = 175$ MPa.

(b) $0.48P_u \equiv \sigma_{b,nom} = 225$ MPa.
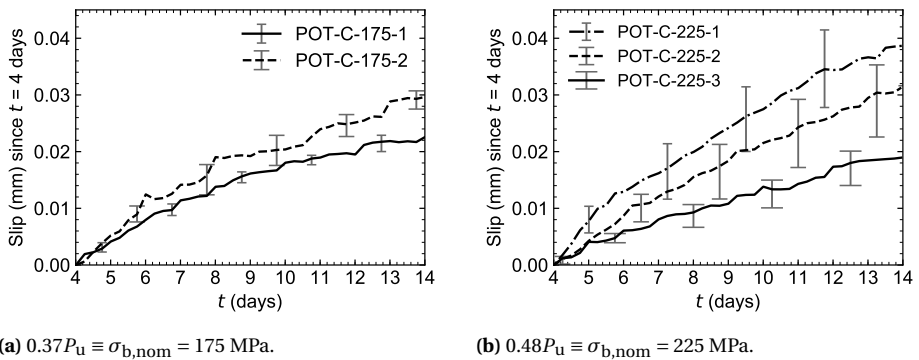
Figure 6.3 | Averaged incremental slip since $t = 4$ days vs. time diagrams of the long-term push-out specimens.
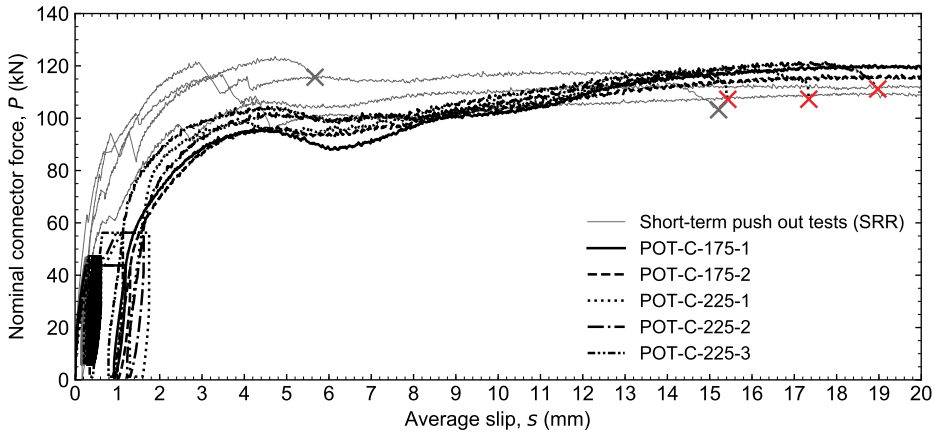
Figure 6.4 | Short- and long-term (fourteen-day) load slip curves of the steel-reinforced resin-injected (SRR) demountable shear connector.

6.2. LONG-TERM EXPERIMENTS ON INJECTED BOLTED DOUBLE LAP SHEAR CONNECTIONS

6.2.1. SPECIMEN DESIGN AND EXPERIMENTAL DETAILS

The creep behaviour of (steel-reinforced) resin-injected double-lap injected bolted connections with significantly oversized holes in the centre plates was determined experimentally. These steel-to-steel connections reflected the geometry and condition of the (steel-reinforced) resin that was part of the long-term push-out specimens described in Section 6.1. This design enables the comparison between (steel-reinforced) resin-injected steel-to-concrete and steel-to-steel connections, which will be the subject of Section 6.3.

Resin- and steel-reinforced resin-injected double-lap shear connections with 20 mm thick centre plates, 10 mm thick cover plates, and grade 10.9 M20 bolts were subjected to sustained loads for a period of 100 days, followed by 14 days of recovery at zero imposed load. An overview of the double-lap shear connection specimens and their dimensions is illustrated in Figure 6.5. The bolts were positioned such that they were bearing on the normal clearance holes in the cover plates, but were in the most negative position in the Ø32 mm centre plate holes with respect to potential slip. This positioning strategy mitigated the influence of the cover plates on the creep deformation, and attempted to replicate the long-term conditions of the bolt and injectant in the single-lap demountable shear connection considered in the long-term push-out tests. The specimens were produced under laboratory conditions, and care was taken prevent air inclusions in the (steel-reinforced) resin by implementing an air vent in the centre plates [15]. The injection bolts were non-preloaded.

Three strings consisting of four serial specimens were tested at nominal bearing stress levels $\sigma_{b,nom}$ of 125, 175 and 225 MPa. The latter two nominal bearing stress levels were also considered in the long-term push-out tests. Each string consisted of two resin-injected and two steel-reinforced resin-injected double-lap shear specimens, totalling four connections of each type per load level. In addition, two strings containing only resin-injected double lap shear connections were subject to nominal bearing stress levels of 75 and 275 MPa, re-
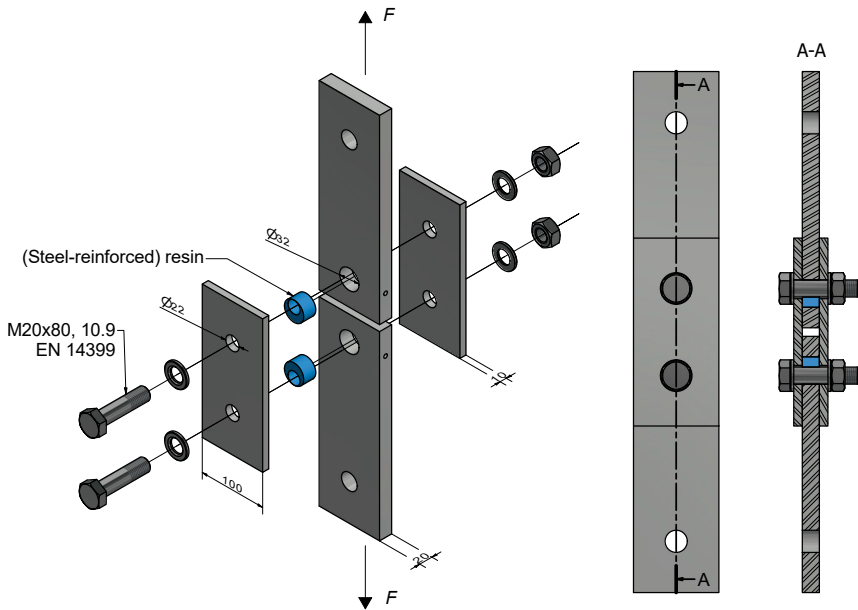
Figure 6.5 | Double-lap shear specimens used to evaluate the creep behaviour of resin-injected bolted connections with significantly oversized holes. Dimensions in mm.

spectively. These additional strings were tested because of the lack of a clear and reliable trend for the results of the specimens subjected to $\sigma_{b,nom}$ = 125, 175 and 225 MPa.

The relative displacement between the centre and cover plates was measured using LVDTs mounted at the cover plate edge. The results obtained for the two connections within one specimen were averaged because their results were mutually influenced due to the alignment constraints during assembly.

6.2.2. Results and discussion
The results of the creep tests on the double lap shear connections are illustrated in Figure 6.6 in terms of the connection slip s, which was defined as the relative displacement between the centre plates and the edge of the cover plate. The attention of the reader is drawn to the small scatter in the experimental data, which can be attributed to the reliability of the injection procedure which causes all macroscale voids within the connection to be filled. This limited variation suggests that the larger scatter in the long-term push-out tests (see Section 6.1) originates from the concrete element. Secondly, none of the double-lap shear connections exhibited measurable sudden slip over the 100-day testing period, indicating that the sudden slip observed in the long-term push-out tests was due to the concrete element.

The results are separately discussed in terms of the instantaneous slip, defined at the instant where full load has just been applied, the total slip, defined as the instantaneous slip plus the accumulated slip between $t = 0\dots100$ days since load application, and the residual slip after unloading and the fourteen-day recovery period.

(a) Resin-injected connections.

(b) Steel-reinforced resin-injected connections.
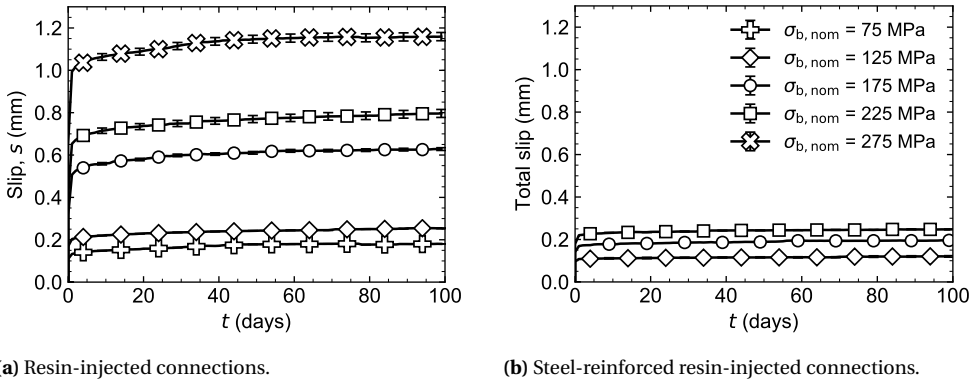
Figure 6.6 | Slip vs. time diagrams of the long-term double lap shear connection specimens.

INSTANTANEOUS SLIP

The instantaneous slip is illustrated in Figure 6.7a. The instantaneous slip of the steel-reinforced resin-injected specimens was 57%, 44% and 43% of that of the resin-injected specimens at nominal bearing stresses of 125, 175 and 225 MPa, respectively, clearly demonstrating the stiffer short-term response of steel-reinforced resin-injected specimens. The results suggest that the benefits of steel-reinforced resin-injected specimens compared to resin-injected specimens become more pronounced for larger values of $\sigma_{b,nom}$.

The instantaneous slip was compared to a prediction based on finite element analysis based on the injectants' short-term material properties derived in Chapter 3 and a nominal friction coefficient of 0.50 between all interfaces - see Section 6.2.3 for further details on the finite element model. Good agreement between the predicted and experimentally obtained instantaneous slip was observed for all steel-reinforced resin-injected specimens: a consistent but small deviation (between 0.02-0.03 mm) between the experimental and numerical results was found. For the resin-injected specimens only good agreement was found for $\sigma_{b,nom} = 75$ and 125 MPa: for $175 \leq \sigma_{b,nom} \leq 275$ MPa the instantaneous slip was 33 - 66% larger than predicted by finite element analysis. It is hypothesised that this deviation occurred because of the viscoelastic/plastic behaviour of the resin during the load application: the load was not applied instantaneously but over a finite time period (approximately 2-10 minutes depending on the load level). The short-term material model for the resin developed in Chapter 3 can inherently not describe any time-dependent effects and it is thus sensible that this material model led to an underestimation of the slip.

Because of the discrepancy of the predicted and the experimentally obtained instantaneous slip for a selection of resin-injected specimens, it was chosen to only consider the results in terms of the instantaneous slip, the total slip during sustained loading, and the residual slip at zero imposed load. The difference between the total slip and the instantaneous slip is in theory the creep slip, but this measure was not considered to be appropriate because additional time-dependent slip might have developed during loading already which would not be accounted for in the creep slip definition.
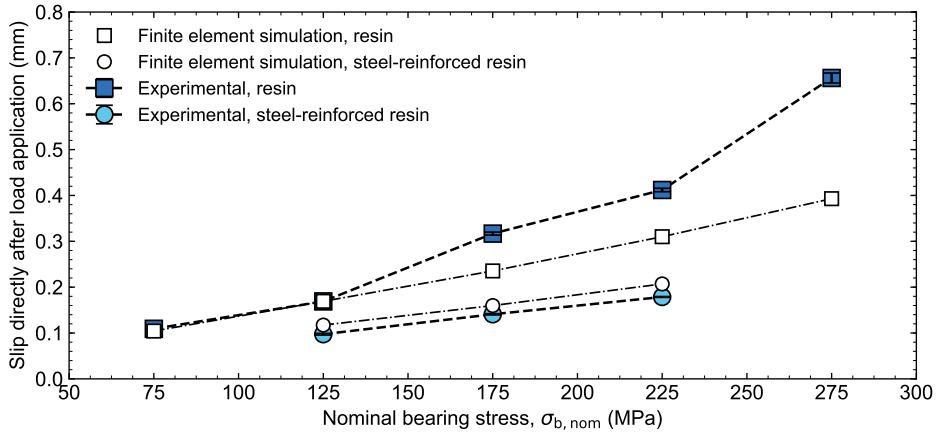
(a) Instantaneous, at $t = 0$ days.

6
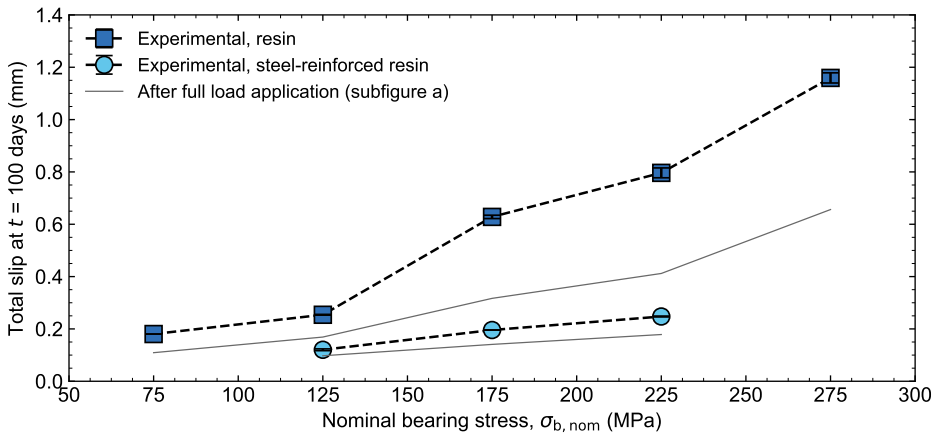
(b) At $t = 100$ days.

Figure 6.7 | Slip as a function of nominal bearing stress for the (steel-reinforced) resin-injected double lap shear connection specimens.

TOTAL SLIP

The relation between nominal bearing stress and total slip at $t = 100$ days is illustrated in Figure 6.7b. The total slip increased more rapidly for $\sigma_{b,nom} > 125$ MPa compared to lower nominal bearing stress levels for resin-injected connections. Such a difference was not observed for the steel-reinforced resin-injected specimen in the range of the nominal bearing stresses considered in the experimental programme. This implies that steel-reinforced resin is more suitable for use in applications with higher bearing stresses because of its more consistent and more favourable response over a wider range of $\sigma_{b,nom}$ from both short-term and long-term perspectives.

Figure 6.8 illustrates the development of the total slip over time on a linear-logarithmic diagram. A function in the form $s = a \cdot \ln(t) + b$ was fitted to each of the experimental curves over the interval $t = 1 \dots 100$ days to determine the *steady-state* creep sensitivity (governed by the magnitude of a) of the connections. This approach ignores any viscoelastic/plastic or primary creep effects that occurred during or immediately after loading. The coefficients a are summarised in Table 6.2, from which it was derived that the steady-state creep of the steel-reinforced resin-injected connections was only 20-25% that of the resin-injected connections for $125 \le \sigma_{b,nom} \le 225$ MPa over the considered time period. A slightly smaller value of a (-9%) for resin-injected specimens subject to a nominal bearing stresses of 125 MPa was observed compared to $\sigma_{b,nom} = 75$ MPa (40% reduction of $\sigma_{b,nom} = 75$) was observed, suggesting that the steady state creep rate could be (approximately) constant or could decrease as a result of larger instantaneous deformation for larger but relatively low bearing stresses. For resin-injected specimens subject to $\sigma_{b,nom} \ge 175$ MPa, a increased approximately linearly with the increase of the nominal bearing stress. For steel-reinforced resin-injected specimens, it was observed that a was slightly smaller (3%) for $\sigma_{b,nom} = 225$ MPa than for $\sigma_{b,nom} = 175$ MPa, suggesting there could be a maximum steady state creep rate for this injectant, although additional experiments at increased nominal bearing stresses are necessary to confirm this suggestion.

RESIDUAL SLIP AFTER RECOVERY

The residual slip fourteen days after unloading is illustrated in Figure 6.9 , alongside the instantaneous slip and the total slip at $t = 100$ days. It should be noted that the specimens for which $\sigma_{b,nom} = 125$ MPa were not unloaded at $t = 100$ days, but were briefly loaded to $\sigma_{b,nom} = 175$ MPa, after which the bearing stress was again reduced to $\sigma_{b,nom} = 125$ MPa which was sustained until $t = 118$ days. On average, this short-duration overload led to a permanent slip of 0.033 mm and 0.017 mm for the resin- and steel-reinforced resin-injected

Table 6.2 | Steady-state ($1 < t \le 100$ days) slip function coefficients for the (steel-reinforced) resin-injected double lap shear connection specimens, see Figure 6.8.

$\sigma_{b,nom}$ (MPa)	$\Delta s \propto a_i \cdot \ln(t)$ Resin-injected, a_R	R^2 (–)	Steel-reinforced resin-injected, a_{SRR}	R^2 (–)	a_{SRR}/a_R (–)
75	0.0134	0.931	-	-	-
125	0.0128	0.968	0.0032	0.865	0.254
175	0.0281	0.990	0.0069	0.936	0.245
225	0.0329	0.992	0.0067	0.978	0.205
275	0.0411	0.969	-	-	-
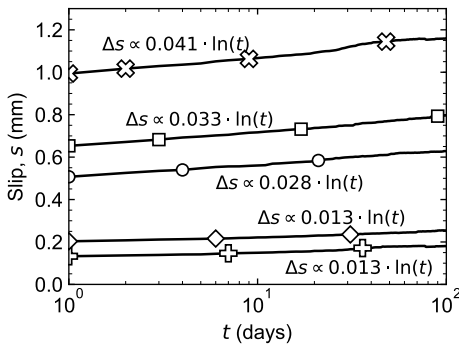
(a) Resin-injected connections.
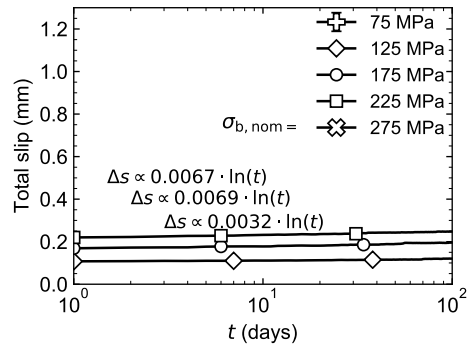
(b) Steel-reinforced resin-injected connections.

Figure 6.8 | Slip vs. log(time) diagrams of the long-term double lap shear connection specimens with curve-fitted function $\Delta s = a \cdot \ln(t) + b$ over the steady-state ($t = 1 \dots 100$ days) time interval, see also Table 6.2.
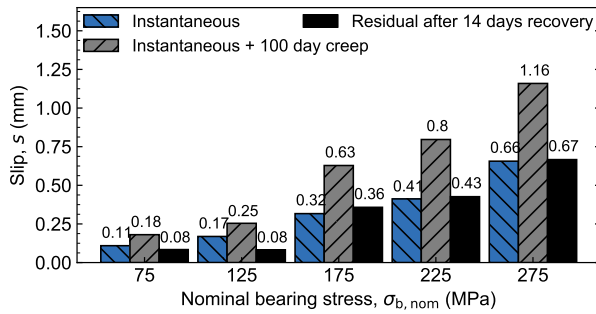
(a) Resin-injected specimens.
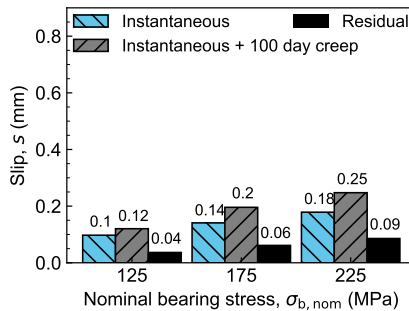
(b) Steel-reinforced resin-injected specimens.

Figure 6.9 | Instantaneous, creep and residual slip of the double-lap shear connection specimens.

specimens, respectively, which have been deducted from the residual slip in Figure 6.9 at the appropriate point in time for a fair comparison between the specimens subjected to different nominal bearing stress levels.

For the resin-injected specimens, the residual slip (14 days after unloading) was in the same order of magnitude as the instantaneous slip for nominal bearing stresses of 175, 225 and 275 MPa, indicating that either (i) the creep had not (yet) fully recovered, (ii) a time-independent plastic deformation occurred during loading or (iii) a combination of both. The latter is the most reasonable, because for the specimen subject to $\sigma_{b,nom}$ = 125 MPa the residual slip was considerably (47%) smaller than the instantaneous slip, indicating that plastic deformation played a comparatively smaller role at lower nominal bearing stresses. However, the residual slip was approximately equal for specimens subjected to $\sigma_{b,nom}$ = 75 MPa and 125 MPa, hindering any conclusive evidence that lower nominal bearing stresses lead to lower residual slip.

The results for the steel-reinforced resin-injected specimens indicated that the ratio of residual slip over instantaneous slip was substantially smaller (0.4-0.5) than for resin-injected specimens and within a consistent range for all three stress levels. Therefore the results suggest that permanent deformation plays a smaller role for steel-reinforced resin-injected connections than for the resin-injected connections, and is dominantly due to irreversible creep given the good agreement between the experimentally and numerically obtained instantaneous slip.

6.2.3. FINITE ELEMENT ANALYSIS OF TIME-DEPENDENT BEHAVIOUR

The material creep models for sustained uniaxial compression, developed in Chapter 4, were implemented in a finite element representation of the experimental double lap shear connections. This finite element model was briefly introduced in Section 6.2. A constant tensile force was instantaneously applied at the edge of the centre plate, with a magnitude that corresponds to one of the considered magnitudes of the nominal bearing stress $\sigma_{b,nom}$. Symmetry conditions were imposed on the cover plates to reduce computational time. A nominal friction coefficient of 0.5 was assumed at all interfaces. The loading was imposed for a seven-day period (600 000 s): the choice for this time frame avoided potential extrapolation effects of the material creep models, which were based on one-week tests, when comparing against the experimental results of the double lap shear connections.

RESIN-INJECTED SPECIMENS

Figure 6.10 illustrates the development of the slip over time for the resin-injected specimens and the finite element simulation. The results are summarised in Table 6.3 and in Figure 6.11. Good agreement between the experimental and numerical results was observed in terms of the the instantaneous slip for $\sigma_{b,nom}$ = 75 and 125 MPa: for larger nominal bearing stresses the finite element analysis underestimated the short-term slip. It is hypothesised that this deviation occurred because of viscoelastic/plastic behaviour of the resin during the load application, because the load was not applied instantaneously but over a finite time period (approximately 2-10 minutes depending on the load level). However, even if this could be accounted for, the observation remains that the incremental creep slip during the seven-day period was significantly (by a factor 3.7-8.3, see Table 6.3) under-predicted by the finite element model.

A possible cause for the underestimation of the creep slip by the finite element model

is that the material creep model does not reflect all possible creep mechanisms. For example[1], the influence of the first stress invariant I_1 (related to the hydrostatic pressure) is inherently neglected by the uniaxial creep model proposed in Chapter 4, although it is reported by Buckley [16], Buckley & Resen [17] and Zolochevsky et al. [18] to have a pronounced influence on polymer creep. Figure 6.12 illustrates the hydrostatic pressure at $t = 0$ and $t = 7$ days, demonstrating that the effects of the first invariant are expected to become dominant over time. This is because the creep strain components generate a higher hydrostatic pressure (due to the confined environment and the volume conservation of the material, see p. 94) and thereby reduce the Von Mises stress. A reduced Von Mises stress leads to smaller creep deformation because it is related to the effective creep stress $\overline{\sigma}_{cr}$ and the effective creep strain $\overline{\varepsilon}_{cr}$. The foregoing expresses the need for further investigation on material level to develop a creep model that describes both the pressure-dependent and pressure-independent creep deformation of the epoxy resin injectant under confined conditions. The implementation of such a material creep model is expected to lead to better agreement between finite element and experimental results for injected bolted connections subject to sustained loading.

STEEL-REINFORCED RESIN-INJECTED SPECIMENS

Figure 6.13 illustrates the development of the slip over time for the resin-injected specimens, and the results are summarised in Table 6.4 and in Figure 6.11. In all cases the instantaneous slip was overestimated (on average by 14%) compared to the experimental results, although the difference in absolute terms are small (in the order of 0.02-0.03 mm). Such small differences could potentially be caused by frictional effects, for example between the spherical steel particles and the cover plates. In contrast to the resin-injected specimens, the instantaneous slip was predicted consistently and accurately over the range of tested nominal bearing stresses, indicating that viscoelastic/plastic behaviour during load application plays a negligible role for the steel-reinforced resin-injected specimens.

In terms of the time-dependent behaviour, it was observed that the incremental creep slip during the seven-day period was significantly underpredicted by the finite element model. The experimentally obtained slip increments were a factor 2.8-4.9 larger than the numerical predictions, see Table 6.4, although these deviations are not evident from Figure 6.11 because the limited magnitude of the actual creep slip (in the range 0.012-0.05 mm). The error was less pronounced compared to the resin-injected double lap shear connec-

---

[1]Further creep slip could also be caused by for example local tensile and shear stresses in the injectant.

Table 6.3 | Experimentally (Exp.) and numerically (FEA) obtained slip at $t = 0$ days and slip increment between $t = 0$ and $t = 7$ days for nominal bearing stresses $\sigma_{b,nom}$ for **resin**-injected specimens.

Nominal bearing stress, $\sigma_{b,nom}$ (MPa)	Slip (mm) after $t = 0$ days (Instantaneous)			Slip increment (mm) between $t = 0$ days and $t = 7$ days		
	Exp.	FEA	Exp./FEA (-)	Exp.	FEA	Exp./FEA (-)
75	0.109	0.104	1.05	0.037	0.006	6.53
125	0.169	0.169	1.0	0.048	0.013	3.68
175	0.317	0.235	1.35	0.239	0.029	8.34
225	0.412	0.310	1.33	0.293	0.052	5.63
275	0.653	0.393	1.66	0.417	0.076	5.47
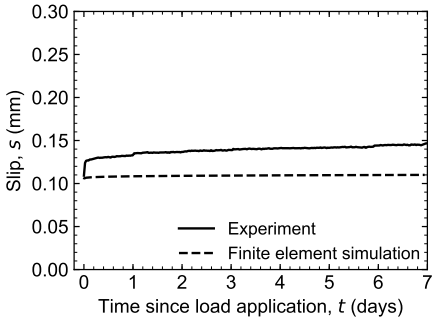
(a) $\sigma_{b,nom} = 75$ MPa.
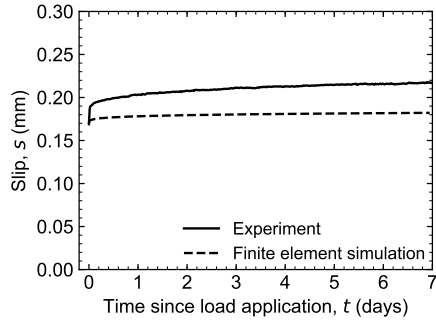
(b) $\sigma_{b,nom} = 125$ MPa.
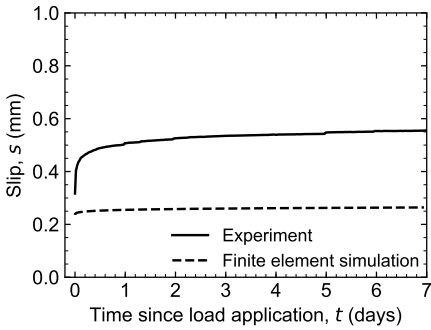
(c) $\sigma_{b,nom} = 175$ MPa.
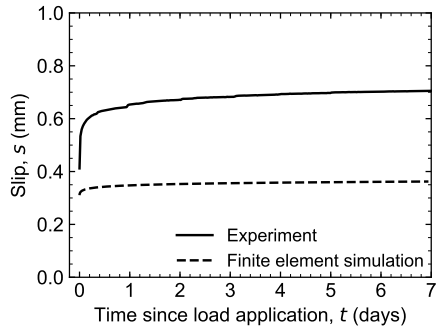
(d) $\sigma_{b,nom} = 225$ MPa.
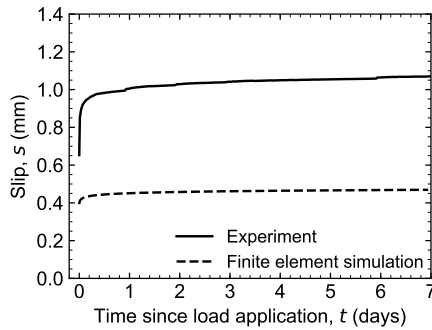
(e) $\sigma_{b,nom} = 275$ MPa.

Figure 6.10 | Experimentally and numerically obtained slip vs. time diagrams for the **resin**-injected double-lap shear connection specimens. The line between the origin and the first data point (resembling the instant where the load was first fully applied) has been omitted in favour of the figure's clarity.
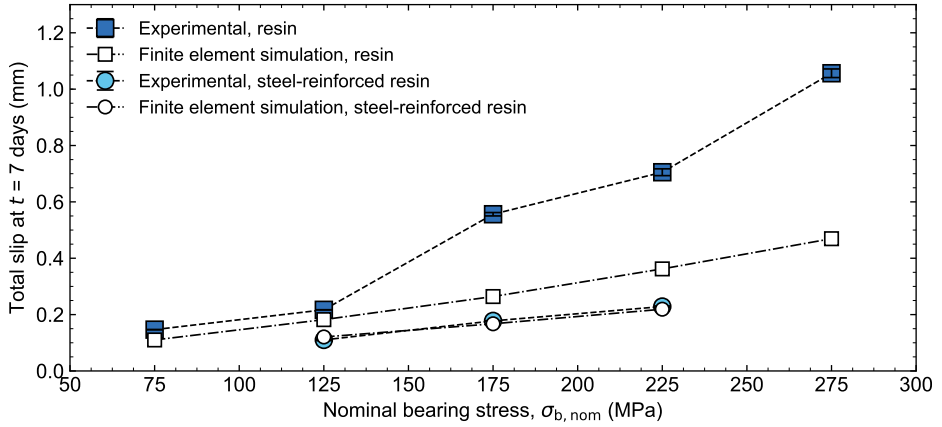
Figure 6.11 | Experimentally and numerically obtained slip after $t = 7$ days for the (steel-reinforced) resin-injected double lap shear connection specimens as a function of nominal bearing stress.

6

(a) At $t = 0$ days.

(b) At $t = 7$ days.
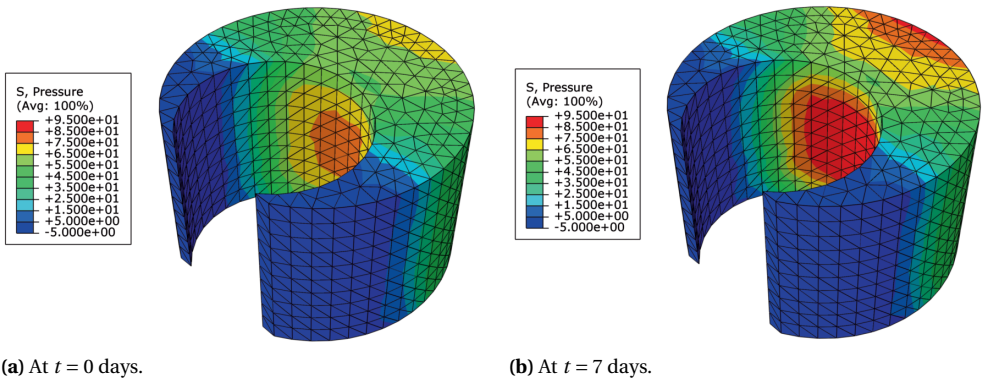
Figure 6.12 | Hydrostatic pressure (MPa) of the epoxy resin injectant in the double lap shear connection for $\sigma_{b,nom} = 175$ MPa. The injection bolt is located in the inner circle, the outer circle represents the edge of the bolt hole.

tions: it is reduced by 25%, 42% and 26% for nominal bearing stresses of 125, 175 and 225 MPa, respectively. This suggests that the hypothesised influence of the first stress invariant I_1 (related to the hydrostatic pressure) is comparatively smaller for steel-reinforced resin, which is supported by the fact that the volume of steel-reinforced resin partially consists of (pressure-independent) steel particles. However, the steel spherical particles provide additional local confinement to the resin matrix, which could counteract the beneficial influence of the reduced matrix volume. On this basis it is concluded that further investigation on material level is necessary to develop a creep model that describes both the pressure-dependent and pressure-independent creep deformation of the steel-reinforced resin. The implementation of such a material creep model is expected to lead to better agreement between finite element and experimental results for injected bolted connections subject to sustained loading.

6.3. RELATIVE CONTRIBUTIONS OF INJECTANT AND CONCRETE TO TIME-DEPENDENT SLIP

The aligned design of the long-term push-out and double-lap shear tests in terms of the nominal bearing stress enables the quantification of the relative contributions of injectant and concrete. This analysis relies on the assumption that the time-dependent behaviour of the concrete and the injectant can be superimposed. This assumption is considered to be valid because both materials are separated in space, and therefore their mutual time-dependent influence is expected to be negligible, although this shall be confirmed by future experiments. Based on the aforementioned assumption, the total time-dependent slip of the push-out test $\Delta s_{\mathrm{cr,POT}}$ can be written in the form

$$\Delta s_{\mathrm{cr,POT}} = \Delta s_{\mathrm{cr,POT,concrete}} + \Delta s_{\mathrm{cr,DLSC,SRR}} \tag{6.1}$$

where $\Delta s_{\mathrm{cr,POT,concrete}}$ is the contribution of the concrete element (as part of a push-out specimen) to the time-dependent slip and $\Delta s_{\mathrm{cr,DLSC,SRR}}$ is the time-dependent slip observed in the double-lap shear connection due to the steel-reinforced resin. From the experiments the development of $\Delta s_{\mathrm{cr,POT}}$ and $\Delta s_{\mathrm{DLSC,SRR}}$ over time are known, and therefore $\Delta s_{\mathrm{cr,POT,concrete}}$ can be determined.

The sudden slip for the long-term push-out tests for $t < 3$ days (see Section 6.1) impeded the correct evaluation of the contribution to the time-dependent slip since the load was first applied. To obtain a meaningful analysis of the contributions of the injectant and the concrete to the time-dependent behaviour, the incremental slip for $4 \leq t \leq 14$ days was used instead: the development of the slip since $t = 4$ days is illustrated in Figure 6.14 for $\sigma_{\mathrm{b,nom}} = 175$ and 225 MPa.

Figure 6.15 illustrates the accumulated slip at $t = 14$ days since $t = 4$ days for both the push-out specimens (POT) and the (steel-reinforced) resin-injected double-lap shear specimens (DLSC). These figures provide the fundament for the discussions in the following subsections.

6.3.1. LOAD PROPORTIONALITY OF CONCRETE ELEMENT

In the time interval $4 \leq t \leq 14$ days, the average accumulated creep slip for the push-out test specimens increased approximately linearly (+34%) with the increase in applied load from $0.37P_{\mathrm{u}}$ to $0.48P_{\mathrm{u}}$ (+29%). The time-dependent effect of the concrete was determined based

Table 6.4 | Experimentally (Exp.) and numerically (FEA) obtained slip at $t = 0$ days and slip increment between $t = 0$ and $t = 7$ days for nominal bearing stresses $\sigma_{b,nom}$ for **steel-reinforced resin**-injected specimens.

Nominal bearing stress, $\sigma_{b,nom}$ (MPa)	Slip (mm) after $t = 0$ days (Instantaneous)			Slip increment (mm) between $t = 0$ days and $t = 7$ days		
	Exp.	FEA	Exp./FEA (-)	Exp.	FEA	Exp./FEA (-)
125	0.097	0.117	0.84	0.011	0.004	2.78
175	0.141	0.160	0.88	0.037	0.008	4.9
225	0.179	0.207	0.86	0.05	0.012	4.15
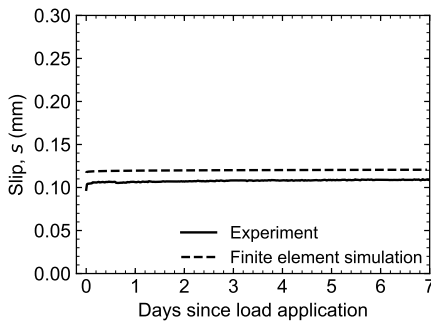
(a) $\sigma_{b,nom} = 125$ MPa.
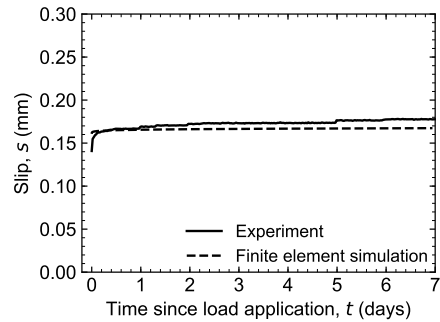
(b) $\sigma_{b,nom} = 175$ MPa.
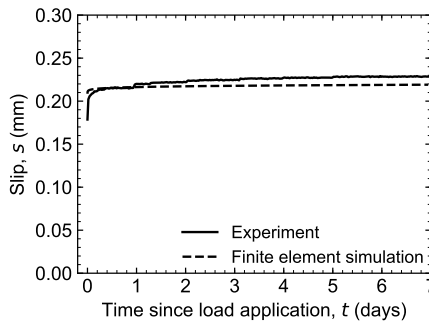
(c) $\sigma_{b,nom} = 225$ MPa.

Figure 6.13 | Experimentally and numerically obtained slip vs. time diagrams for the **steel-reinforced resin**-injected double-lap shear connection specimens. The line between the origin and the first data point (resembling the instant where the load was first fully applied) has been omitted in favour of the figure's clarity.
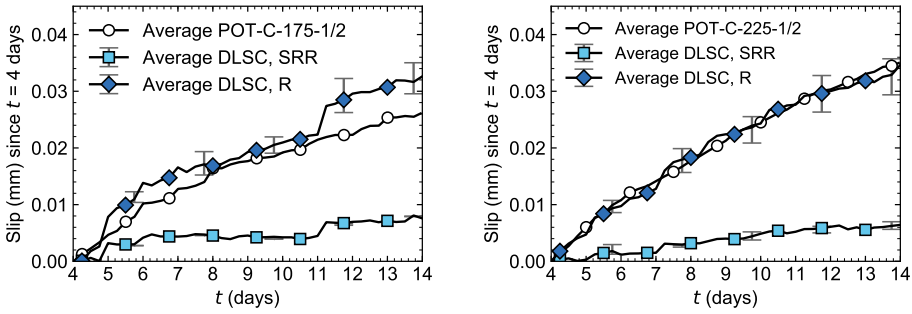
(a) $0.37P_u \equiv \sigma_{b,nom} = 175$ MPa.

(b) $0.48P_u \equiv \sigma_{b,nom} = 225$ MPa.

Figure 6.14 | Averaged incremental slip since $t = 4$ days vs. time diagrams of the long-term push-out (POT) and the double-lap shear connection (DLSC) specimens.
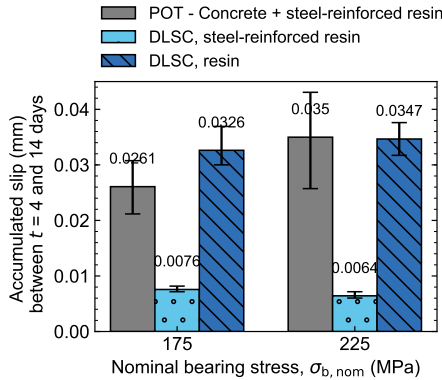
Figure 6.15 | Cumulative slip for push-out specimens (POT) and double lap shear connections (DLSC) between $t = 4$ and 14 days.
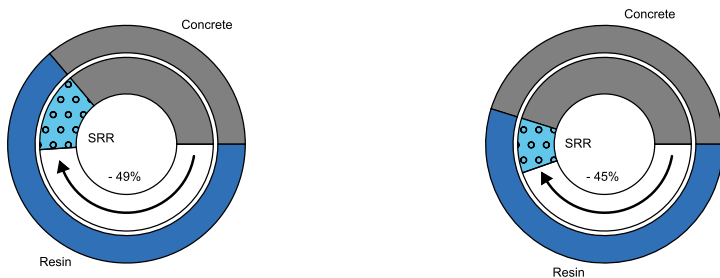
(a) $\sigma_{b,nom} = 175$ MPa $\equiv P = 0.37P_u$.

(b) $\sigma_{b,nom} = 225$ MPa $\equiv P = 0.48P_u$.

Figure 6.16 | Estimated relative contributions of (steel-reinforced) resin (SRR) and concrete to the time-dependent slip of the demountable shear connector system. The use of steel-reinforced resin is expected to reduce the slip increment in this time interval by 45-49% compared to a resin-injected connection.

on the principle of linear superposition conform Equation 6.1, i.e. the time-dependent slip due to concrete is the difference between the results of the push-out test and the double-lap shear test. It followed that the incremental slip due to the creep of the concrete increased by 48% for a 29% higher load. According to EN 1992-1-1 [5], this non-proportional increase implies that the stresses exceed 45% of the characteristic concrete compressive strength at one or both load levels. It should be noted, however, that this creep deformation occurs both directly in front of the coupler, as well as in the undisturbed zones of the specimens, and therefore the 41% increase is a homogenised measure for the entire push-out specimen.

6.3.2. RELATIVE CONTRIBUTIONS TO TIME-DEPENDENT SLIP

By superimposing the effects of concrete, resin, and steel-reinforced resin, it was found that the steel-reinforced resin contributed on average 29% and 18% to the time-dependent slip of the push-out specimen at sustained loads of 0.37 P_u ($\sigma_{b,nom}$ = 175 MPa) and 0.48 P_u ($\sigma_{b,nom}$ = 225 MPa), respectively. The contribution of the steel-reinforced resin can therefore not be neglected, although its relative influence will be less significant for smaller nominal hole clearances and for fresh concrete, e.g. 28 days old. According to EN 1992-1-1 [5], the concrete is approximately 70% more sensitive to creep at this age compared to the age of the push-out specimens (15 months). This reduces the (estimated) creep contribution of the steel-reinforced resin from 18-29% to 12-19%. It should be noted that, in practice, the bolts will be distributed more favourably in their bolts holes than in the laboratory tests, reducing the creep caused by the injectant. The attention of the reader is also drawn to the observation that absolute and relative time-dependent behaviour may be different for each life cycle of the demountable composite floor system. In subsequent life cycles the total magnitude of the accumulated creep slip will decrease due to ageing of the concrete, causing the creep of the injectant (which is replaced in every new life cycle) to become more dominant.

The principle of linear superposition was also used to evaluate the effects if the push-out specimens would have been injected with resin instead of steel-reinforced resin. For this purpose, the results presented in Section 6.2 for (steel-reinforced) resin-injected double lap shear connections were used. In this case, the epoxy resin would contribute 64% and 55% to the time-dependent slip of the push-out specimen at sustained loads of 37% and 48% of the short-term resistance, respectively. This implies that the time-dependent behaviour of the epoxy resin would be dominant for this particular case, although it contribution to the time-dependent slip was estimated [based on 5] to reduce to 51% and 42%, respectively, if the concrete age at first loading would be 28 days. Figure 6.16 illustrates the relative contributions of the (steel-reinforced) resin and concrete at both load levels considered in the experiments. Based on this diagram it can be derived that the time-dependent slip of the shear connection system would increase by a factor 1.8-2.0 in case of a resin-injected rather than a steel-reinforced resin-injected push-out specimen.

6.4. Conclusions

This chapter presented the long-term behaviour of demountable injected bolted shear connectors, and focused on the time-dependent behaviour of push-out specimens (consisting of concrete elements and an injectant) and of double lap shear connections (consisting of only an injectant). The main findings of the work are:

- Five fourteen-day push-out tests were performed at sustained load levels corresponding to nominal bearing stresses in the epoxy resin layer of 175 and 225 MPa. Sudden slip up to 0.6 mm was observed during load application and/or during early stages of the experiment ($t < 3$ days), unless the specimen was subject to 25 cycles between 5% and 40% of the short-term resistance prior to imposing the sustained load. Further experiments are necessary to confirm the need for cyclic loading prior to creep testing to obtain reliable long-term shear connector behaviour.

- The time-dependent behaviour of the push-out specimens was evaluated in terms of the incremental creep slip since $t = 4$ days to exclude influences of sudden slip. It was found that the average accumulated creep slip for the push-out test specimens increased approximately linearly (+34%) with the increase in applied load from $0.37P_u$ to $0.48P_u$ (+29%) for the specimens that were not subject to prior cyclic loading. The specimen subject to prior cyclic loading exhibited a 46% smaller creep increment than specimens tested at the same load level without cyclic loading.

- The fourteen-day period of sustained loading at 37%-48% of the short-term resistance did not influence the resistance and the failure mode compared to short-term push-out tests. However, an earlier onset of non-linearity was observed in the load-slip diagram.

- Long-term (100 day) creep tests on steel-to-steel (steel-reinforced) resin-injected bolted double-lap shear connections with significantly oversized holes in the centre plates ($d_0 - d = 12$ mm) were conducted at three to five nominal bearing stress levels. The instantaneous slip after load application was in good agreement with finite element predictions based on the injectants' short term material models for steel-reinforced resin-injected specimens (all stress levels) and for resin-injected specimens with $\sigma_{b,nom} = 75$ and 125 MPa. For resin-injected specimens subject to $175 \leq \sigma_{b,nom} \leq 275$ MPa the instantaneous slip was 33 - 66% larger than predicted by finite element analysis: this deviation was hypothesised to have occurred because of the viscoelastic/plastic behaviour of the resin during load application.

- A function in the form $s = a \cdot \ln(t) + b$ was fitted to each of the experimental curves over the interval $t = 1 \ldots 100$ days to determine the *steady-state* creep sensitivity (governed by a) of the double-lap shear connections connections. This approach ignored any viscoelastic/plastic or primary creep effects that occurred during or immediately after loading. Based on this analysis it was found that the steel-reinforced resin-injected connections only exhibited 20-25% of the time-dependent deformation of the resin-injected connections for $125 \leq \sigma_{b,nom} \leq 225$ MPa over the considered time period.

- No distinct difference in terms of a for resin-injected specimens subject to nominal bearing stresses of 75 and 125 MPa was observed. A similar observation was made

6

for steel-reinforced resin-injected specimens subject to $\sigma_{b,nom}$ = 175 and 225 MPa. Therefore the results suggested that for resin-injected connections the steady state creep rate was constant for relatively low bearing stresses, whereas for steel-reinforced resin-injected specimens a maximum steady state creep rate existed for high nominal bearing stresses. Additional experiments at lower and higher magnitudes of $\sigma_{b,nom}$ are necessary to confirm these suggestions.

• The long-term response of double lap shear connections with neither injectant could be accurately predicted using the long-term material models developed in Chapter 4: the slip increment during the first seven days was underestimated by a factor 3.7-8.3 and 2.8-4.9 for resin-injected and steel-reinforced resin-injected specimens, respectively. Based on literature review, this substantial difference was hypothesised to be caused by a pressure-dependent creep mechanism, which was not included in the definition of the material model based on the long-term uniaxial compression tests.

• The experimental results of the long-term push-out and double-lap shear connection tests were used to identify the relative contributions of the steel-reinforced resin injectant and the concrete to the time-dependent slip of the push-out specimens. This analysis required the assumption of linear superposition of the behaviour of the injectant and concrete. The accumulated slip between $t = 4\ldots14$ days was used as a measure because of sudden slip at earlier points in time. It was found that, over this time interval, the steel-reinforced epoxy resin was responsible for 29% and 18% of the time-dependent slip at nominal bearing stresses of 175 and 225 MPa, respectively. Adjusting for the age of concrete at testing (15 months), the contribution of the injectant was estimated to decrease to 19% and 12% for load application at 28 days after casting.

• If the steel-reinforced resin would be replaced by resin in the long-term push-out test, the injectant would have contributed 64% and 55% to the time-dependent slip at nominal bearing stresses of 175 and 225 MPa, respectively. The contribution of the resin to the time-dependent slip was estimated to decrease to 51% and 42% for load application at 28 days after casting. These values suggest that resin and concrete contribute an approximately equal share to the time-dependent deformation. The application of resin instead of steel-reinforced resin in the long-term specimens would have increased the time-dependent slip by a factor 1.8-2.0.

6

REFERENCES PART II

REFERENCES

[1] ISO, *ISO 898-1: Mechanical properties of fasteners made of carbon steel and alloy steel - Part 1: Bolts, screws and studs with specified property classes - Coarse thread and fine pitch thread* (ISO, 2013).

[2] ISO, *ISO 4017: Fasteners - Hexagon head screws - Product grades A and B* (ISO, 2014).

[3] NEN, *NEN-EN 1090-2: Execution of steel structures and aluminium structures - Part 2: Technical requirements for steel structures* (Nederlandse Norm (NEN), 2018).

[4] NEN, *NEN-EN 1994-1-1: Eurocode 4: Design of composite steel and concrete structures - Part 1-1: General rules and rules for buildings* (NEN, 2011).

[5] NEN, *NEN-EN 1992-1-1: Eurocode 2: Design of concrete structures - Part 1-1: General rules and rules for buildings* (NEN, 2011).

[6] NEN, *NEN 6008: Steel for the reinforcement of concrete* (NEN, 2020).

[7] A. Kozma, C. Odenbreit, M. Braun, M. Veljkovic, and M. Nijgh, *Push-out tests on demountable shear connectors of steel-concrete composite structures,* Structures **21**, 45 (2019).

[8] NEN, *NEN-EN 1990: Eurocode 0: Basis of structural design* (NEN, 2002).

[9] M. Pavlovic, *Resistance of bolted shear connectors in prefabricated steel-concrete composite decks,* Ph.D. thesis, University of Belgrade (2013).

[10] A. S. Kozma, *Demountable composite beams: Design procedure for non-conventional shear connections with multilinear load-slip behaviour,* Ph.D. thesis, University of Luxembourg (2020).

[11] B. Milosavljevic, I. Milicevic, M. Pavlovic, and M. Spremic, *Static behaviour of bolted shear connectors with mechanical coupler embedded in concrete,* Steel and Composite Structures **29** (2018).

[12] M. Pavlović, Z. Marković, M. Veljković, and D. Buđevac, *Bolted shear connectors vs. headed studs behaviour in push-out tests,* Journal of Constructional Steel Research **88**, 134 (2013).

[13] M. Spremic, M. Pavlovic, Z. Markovic, M. Veljkovic, and D. Budjevac, *FE validation of the equivalent diameter calculation model for grouped headed studs,* Steel and Composite Structures **26** (2018).

[14] A. Prakash, N. Anandavalli, C. K. Madheswaran, and N. Lakshmanan, *Modified push-out tests for determining shear strength and stiffness of HSS stud connector-experimental study,* International Journal of Composite Materials **2**, 22 (2012).

[15] M. P. Nijgh, *New Materials for Injected Bolted Connections: A Feasibility Study for Demountable Connections,* Master's thesis, Delft University of Technology (2017).

[16] C. P. Buckley, *Multiaxial nonlinear viscoelasticity of solid polymers,* Polymer Engineering and Science **27**, 155 (1987).

[17] C. P. Buckley and A. S. Resen, *Characterisation of creep of plastics under multiaxial stress,* in *Proceedings of the 48th Annual Technical Conference of the Society of Plastics Engineers* (1990) pp. 469–472.

[18] A. Zolochevsky, S. Sklepus, Y. Kozmin, A. Kozmin, D. Zolochevsky, and J. Betten, *Constitutive equations of creep under changing multiaxial stresses for materials with different behavior in tension and compression,* Forschung im Ingenieurwesen **68**, 182 (2004).

III

DEMOUNTABLE COMPOSITE FLOOR SYSTEMS

EXPERIMENTAL WORK: WEB-TAPERED STEEL-CONCRETE COMPOSITE FLOOR SYSTEM

To achieve great things, two things are needed: a plan, and not quite enough time.

Leonard Bernstein

INTRODUCTION

This chapter presents the design and the results of the first ever experimental work on a demountable and reusable web-tapered steel-concrete composite floor system. This chapter relates to Part II of this dissertation because it implements the proposed demountable shear connector in a composite floor system with a design representing a car park building. The work presented in this chapter is particularly novel because it is the first time experimental results for a non-prismatic composite floor system are presented: prior work in the literature only considered prismatic steel sections.

This chapter consists of three parts: Section 7.1 presents the design of the composite floor system and focuses on practical aspects related to execution, whereas Section 7.2 concentrates on the structural response of the composite floor system. In latter section the results of four-point bending experiments on a web-tapered steel-concrete composite floor system are evaluated at linear-elastic load levels for six different shear connector arrangements, with the aim to maximise the beneficial effects of composite action with as few connectors as possible. The chapter concludes with Section 7.3, summarising the main findings of this chapter.

Parts of this chapter have been published in Engineering Structures **183**, 366 [1].

7.1. FEASIBILITY STUDY

The objective of the feasibility study was to understand the influencing factors and their implication on the assembly and disassembly of demountable steel-concrete composite floor systems. For example, geometrical and dimensional imperfections and deformation of the structure during construction influence the alignment of the components of a composite floor system, and thus affect the probability of successful installation of a demountable shear connector system. Similarly, the time and processes required to assemble the floor system play an important role in the acceptance of demountable and reusable composite floor systems in the construction sector. To address the speed of execution, prefabricated floor concrete element with as large as practically possible dimensions (e.g. taking into account transportability) were considered in this work in combination with an unpropped construction method and significantly oversized bolt holes.

The feasibility study aimed to identify the required processes including potential risks, and to quantify the timespan and the magnitude of the nominal hole clearance for the execution of a full-scale demountable web-tapered composite floor system under laboratory conditions. The laboratory work hereby contributes to the implementation of demountable composite floor systems in engineering practice and is unique from a scientific perspective because it is the first ever non-prismatic composite floor system ever tested.

7.1.1. SPECIMEN DESIGN AND EXPERIMENTAL DETAILS

The experimental composite floor system was designed to replicate the typical layout of a multi-storey car park building[1], see Figure 7.1. The span of the composite floor system was reduced to 90% of the typical 16 m span to fit into the laboratory: the (nearly) full-scale work of presented in this chapter is therefore directly relevant for practical applications.

An overview of the experimental setup for the feasibility study is shown in Figures 7.2 and 7.3. The design consisted of three simply supported web-tapered steel beams, and four prefabricated concrete floor elements denoted by A, B, C and D. The tapered steel beams had a clear span of 14.4 m and a centre-to-centre distance of 2.6 m. One of the outer

---

[1]An overview of typical designs is given in Reference [2]
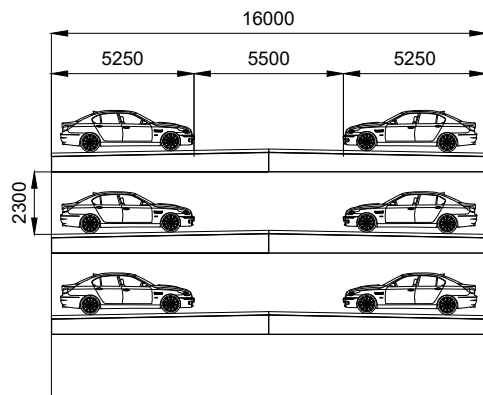
Figure 7.1 | Typical dimensions (mm) of a multi-storey car park building for one-way traffic circulation.

steel beams was supported at three additional points to represent the presence of facade columns. The steel beams were interconnected by cross-bracing at 3.6 m centre-to-centre to prevent their instability. It should be noted that in practical applications the use of bracing systems should be avoided in favour of the speed of (dis)assembly: Chapter 9 suggests design strategies to minimise the need for bracing to prevent lateral-torsional buckling.

DESIGN OF THE WEB-TAPERED STEEL BEAMS

The web-tapered steel beams were welded I-shaped profiles of steel grade S355 with single-sided fillet welds. The height of beams varied piecewise linearly over their 14.4 m length: at the supports it was $h|_{x=0,L} = 590$ mm, and at midspan it was $h|_{x=L/2} = 725$ mm. The bottom (tensile) flange was parallel to the span, whereas the top (compression) flange was inclined to provide drainage of water for the floor system. A second reason to consider web-tapered beams was to enable a reduction of material demand. In addition, built-up members offer more freedom for cross-sectional design compared to standard hot-rolled sections: in Chapter 9 it will be demonstrated which particular needs exist for the cross-section design to maximise both the in-plane and out-of-plane resistance of the steel beam and/or the composite floor system. The top and bottom flange width of the I-shaped section were $b_{f,t} = b_{f,b} = 300$ mm. The thickness of the web was $t_w = 4.5$ mm, and the thickness of the compression (top) and tensile (bottom) flanges were $t_{f,t} = 12$ mm and $t_{f,b} = 10$ mm, respectively.

DESIGN OF THE PREFABRICATED CONCRETE FLOOR ELEMENTS

The four prefabricated concrete floor elements of concrete strength class C30/37 were nominally 7.2 m long, 2.6 m wide and 120 mm thick. The dimensions of the floor elements minimised the number of parts to be assembled, but were still within typical transportation limits. The mass of each floor element was approximately 6 tonnes. The floor elements were reinforced by two reinforcement meshes #8-150 mm of grade B500B, at a cover of 25 mm from the top and bottom surfaces.

The floor elements were designed to be in direct contact in longitudinal direction to enable the transfer of compressive forces at midspan during the service life of the composite floor system. In transversal direction, account was taken of possible geometrical and/or dimensional imperfections by reducing the nominal width of the floor elements by 6 mm compared to the nominal spacing of the steel beams. This 6 mm clearance was based on the assumed 6 mm nominal hole clearance for the demountable shear connector (see next subsection), and ensured that all concrete floor elements could be positioned without constraints imposed by adjacent elements.

In line with the design of the push-out specimens, see Section 5.1, angle profiles were used to provide confinement to the concrete in the vicinity of the shear connectors, and prevented any damage to the floor element as a result of accidental collisions during execution. These angle profiles were $120 \times 120 \times 10$ mm and of steel grade S355. The floor elements and the push-out elements were cast from the same concrete batch, therefore the actual cube compressive strength was $f_{cm,cube} = 48.2$ MPa.

DESIGN OF THE DEMOUNTABLE SHEAR CONNECTORS

The epoxy resin-injected demountable shear connector that was proposed in Section 2.2.3 and experimentally tested in Section 5.1 was implemented in present study, see Figure 7.4. This demountable shear connector consisted of a bolt (M20, grade 8.8) and coupler (M20,
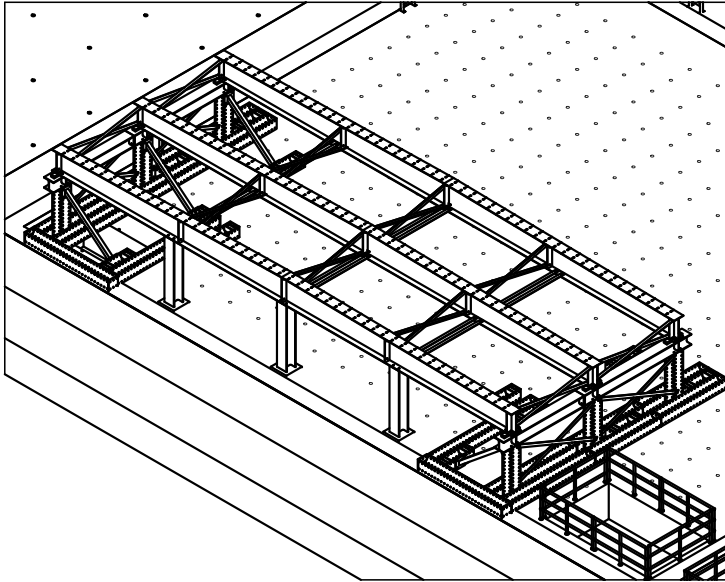
(a) Setup without floor elements.
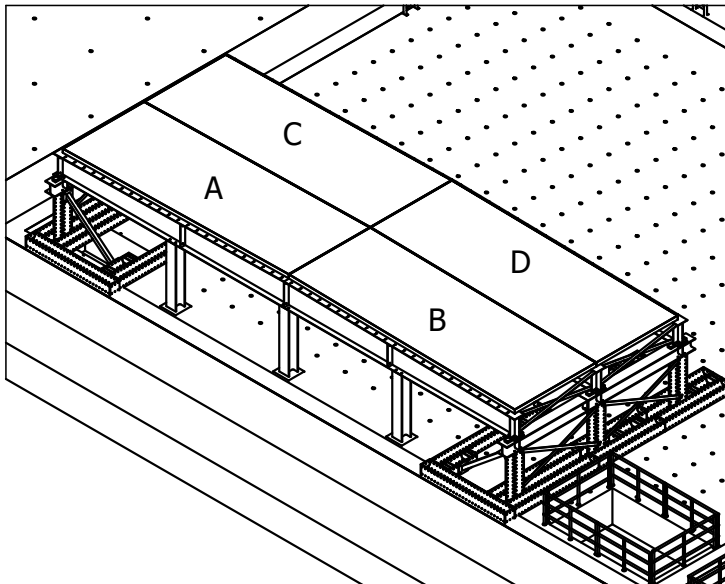
(b) Setup with four 7.2 × 2.6 × 0.12 m floor elements denoted by A, B, C, and D.

Figure 7.2 | Overview of the composite floor system during the feasibility phase. The bottom flanges are parallel to the span, whereas the top flanges are inclined (see Figure 7.3).
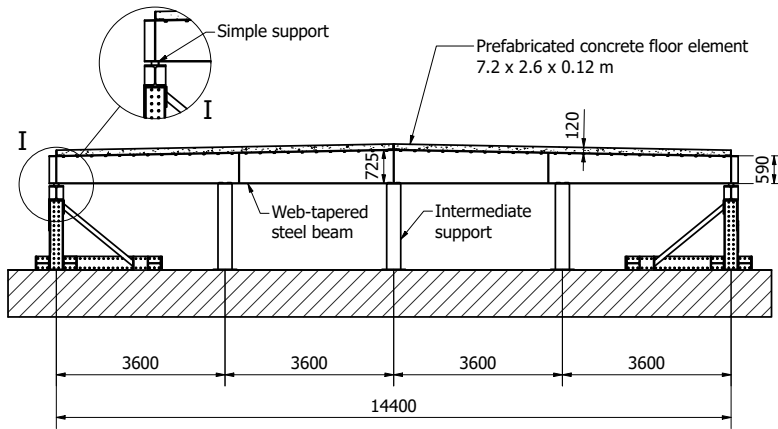
Figure 7.3 | Side view of the feasibility setup including key dimensions (in mm). The intermediate supports were only present under one outer beam: the other two beams were simply supported with span $L = 14.4$ m.

grade 10.9) which were both embedded in the prefabricated floor elements, and an external injection bolt (M20, grade 8.8). Both the epoxy systems RenGel SW 404 + HY 2404 and Ren-Gel SW 404 + HY 5159 (see Part I) were considered as injectants. Grooves in the top flange of the steel beam were made perpendicular to the breadth of the flange to avoid the formation of large air voids in the epoxy resin and to confirm the successful injection procedure. Adhesion between the connector components and the epoxy resin system was mitigated by a wax-based release agent to enable the demountability of the shear connection.

The concrete in the vicinity of the shear connectors was confined by a Ø8 mm reinforcing U-bar around each connector and by an angle profile, to replicate conditions of the push-out tests presented in Chapter 5, and to prevent damage to the concrete during transportation and assembly. Thirdly the confinement prevented splitting of the concrete in the vicinity of the connectors during the beam experiments introduced in Section 7.2. The centre-to-centre distance of the shear connectors was 300 mm, and the outer shear connectors were at 150 mm from the supports. This led to a total of 192 connectors for the setup shown in Figure 7.2. A 6 mm nominal hole clearance was initially assumed to lead to successful assembly of the composite floor system.

ASSEMBLY PROCESS AND PERFORMANCE INDICATORS
The novelty of the prefabricated steel-concrete composite floor system required a new approach to install the large prefabricated concrete floor elements on the steel beams. The construction method must ensure (i) a sufficiently safe working environment for the workers and machinery, (ii) be competitive in terms of execution speed and (iii) prevent any damage to the structural elements during the assembly.

To guarantee a safe working environment, the floor elements should be either connected to the crane or to the steel beam at all times. Once the floor element was hoisted above its intended position, the embedded couplers were progressively aligned with the bolt holes, starting from mid-span and moving towards the support. The alignment took
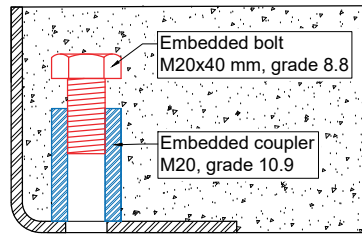
(a) Lifting the prefabricated concrete floor element over the steel beam.
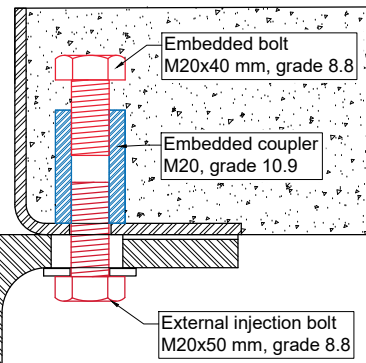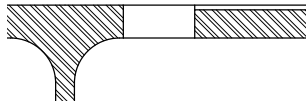
(b) Aligning the embedded coupler with the oversized holes in the steel beam (e.g. using handheld tools or long bolts), followed by the installation of an external injection bolt.
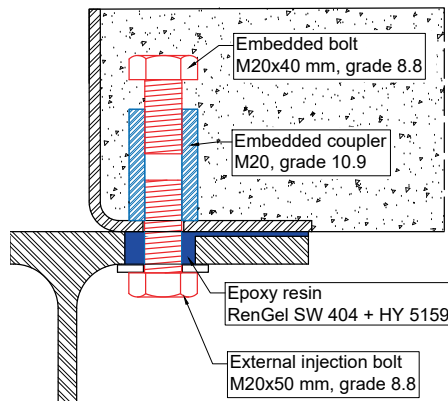
(c) Injecting the bolt-hole clearance with the epoxy resin system. The horizontal channel avoids large air voids and enables the verification of successful injection.

Figure 7.4 | Execution sequence of the demountable shear connector system during the feasibility experiments.

place by installing temporary long bolts through the bolt hole into each coupler[2]. After the long bolts were installed in every coupler, they were replaced by an external injection bolt and tightened until the gap between flange and floor element was closed. The execution sequence of the composite floor system is summarised by Figure 7.4. During the feasibility study, the required time to complete each step was timed to obtain performance indicators of the execution process of the floor system. In addition, any additional processes were identified and the tools and machinery for assembly were documented.

The prefabricated decks were placed in two different execution sequences on the tapered steel beams: either in the order A-B-C-D or in the order D-C-B-A, where the letters refer to the floor element designation presented in Figure 7.2. The latter installation sequence was expected to be the most onerous, because of the transversal inclination of A and B due to the larger deflection of the middle beam as a result of the self-weight of floor elements C and D. The deflections of the two simply supported beams were measured by `Sakae S13FLP50A` potentiometers installed at midspan and at 4.05 m from each support, see Figure 7.5. The deflection of the beam supported by the three facade columns was not measured.

7.1.2. FABRICATION

The fabrication of all structural components was subcontracted: one contractor was responsible for all steel components, and a second one focused on the realisation of the concrete floor elements.

Figure 7.6 gives an overview of the various fabrication stages. First, the steel beams and angle profile frames were collected in the laboratory and were used to execute a preliminary mock-up of the floor system, see Figure 7.6a. This mock-up revealed large bow imperfections of the angle profile frames, which were subsequently braced to mitigate the frames' geometrical and dimensional deviations.

After confirming the sizing of the structural elements through the mock-up, preparations for the fabrication of the floor elements began. The angle profile frame was placed on wooden formwork sheets. The shear connectors were installed through the holes in the angle profiles and were hand-tightened to the formwork. The two reinforcement meshes #8-150 mm were installed and reinforcing U-bars were positioned around each connector, see Figure 7.6c. Two plate anchors were placed along the centreline of the formwork to pro-

---

[2]Initially, threaded rods were pre-installed into the couplers, with the expectation that it would cause the floor element to self-align with the steel beams. However, this led to the situation where the weight of the floor element was partially supported by one of the threaded rods, causing punching shear failure of the connector.
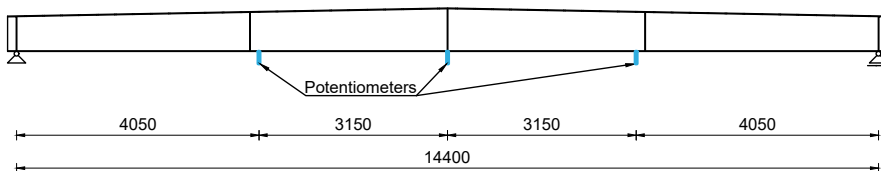
Figure 7.5 | Schematic overview of the locations where the deflection of the two simply supported beams was measured during the feasibility study. The potentiometers measured relative to the laboratory floor. Dimensions in mm.

vide support for the hoisting system, after which the concrete was cast. After two weeks of hardening, the prefabricated concrete floor elements were transported to the laboratory by truck to form the final assembly illustrated in Figure 7.6f.

7.1.3. RESULTS AND DISCUSSION

REQUIRED NOMINAL HOLE CLEARANCE

It was found that not all external injection bolts could be installed through the Ø26 mm bolt holes into the embedded coupler for neither of the two execution sequences A-B-C-D and D-C-B-A. The needs for an even larger nominal hole clearance than first assumed originated from geometrical and dimensional imperfections, for example related to the out-of-straightness of the steel beam, the scatter in the position of the shear connectors in the formwork, and the relative displacement between the beams and floor elements (slip) due to the self-weight of the floor elements. After quantifying the geometrical and dimensional deviations of the floor elements and computing the slip due to self-weight, the diameter of the bolt holes was enlarged to Ø32 mm. The quantification of this hole enlargement was one of the key tasks in the Master's thesis of Gîrbacea [3], where the reader is referred to for further details. In Chapter 8, a generic modelling method is developed to predict the required nominal hole clearance, and in that context the results of the model are compared to the required magnitude within the feasibility study.

After the hole enlargement, all external injection bolts (192 pieces) were successfully installed for both execution sequences. There was no visual evidence that the required hole clearance for floor element installation sequence D-C-B-A was larger compared to sequence A-B-C-D. Figure 7.7 illustrates the deflection along the length of middle beam for sequence A-B-C-D with $d_0 = 26$ mm and $d_0 = 32$ mm: the 12% smaller deflection for $d_0 = 26$ mm indicate that the 6 mm nominal hole clearance was indeed too small, which led to composite interaction during the execution stage caused by bearing by one of more connectors.

ASSEMBLY PROCESS AND PERFORMANCE INDICATORS

The experimental feasibility study identified the need for the following processes:

   i. Attaching the lifting beam / crane to the prefabricated concrete floor element;

   ii. Hoisting the floor element over the pre-executed steel beams;

   iii. Aligning the embedded part of the shear connector (coupler) with the bolt holes in the upper flange using temporary long bolts;

   iv. Lowering the prefabricated concrete floor element onto the steel beams;

   v. Disconnecting the floor element from the crane;

   vi. Replacing the temporary bolts with injection bolts;

   vii. Injecting the bolted connection with epoxy resin to obtain shear interaction,

which were all timed to obtain performance indicators.

Attaching and safely securing the lifting beam to the prefabricated concrete floor element took on average 2-3 minutes, and required the alignment of the floor anchors with holes in the lifting beam, and the installation of a nut to form a temporary connection.
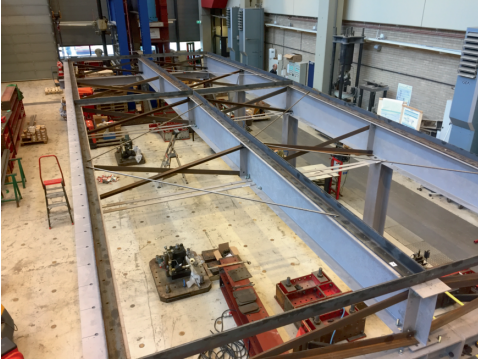
(a) Mock-up of steel beams, bracing system, and angle profile frames.

(b) Detail of angle profiles at midspan.
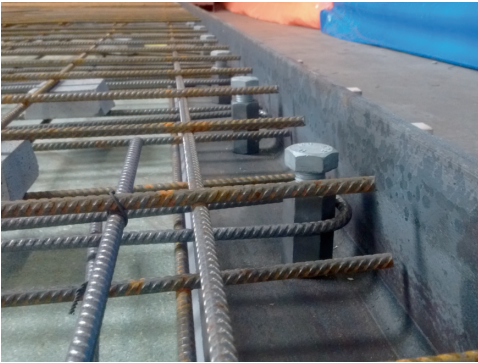
(c) Detail of shear connector system, reinforcement and angle profile, prior to casting.

(d) Concrete casting of the floor elements.

(e) Final assembly. The rods extending from the top surfaces of the floor elements were used for hoisting.

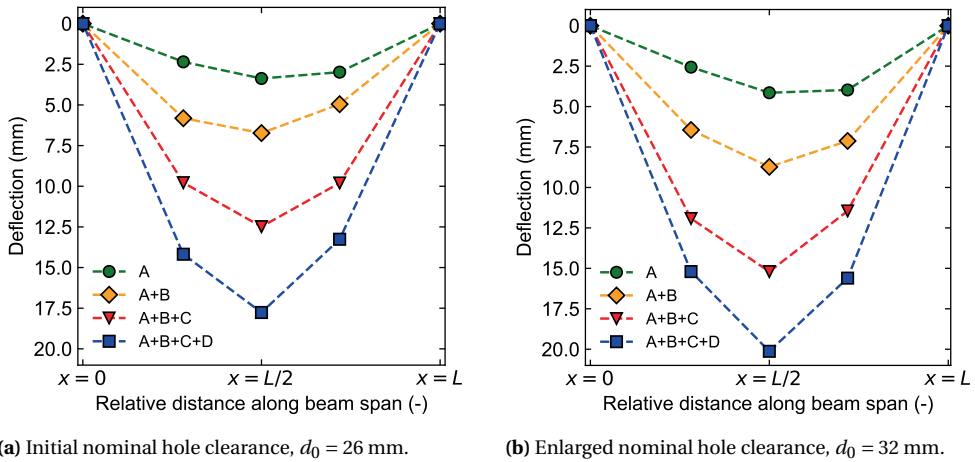**Figure 7.6 |** Pictures of the fabrication of the structural elements and of the assembled floor system.

(a) Initial nominal hole clearance, $d_0 = 26$ mm.   **(b)** Enlarged nominal hole clearance, $d_0 = 32$ mm.

Figure 7.7 | Deflection of the middle beam, installation sequence A-B-C-D.

The duration of the lifting process depends on the distance that needs to be travelled, but was on average 1.5 minutes for the laboratory test setup. A longer duration is expected for real applications. Alignment of the prefabricated concrete decks with the steel beams took on average 4-6 minutes, including installation of the temporary long bolts and lowering of the floor element onto the beams.

The replacement of the temporary bolts by injection bolts was determined to take on average 15-20 seconds per injection bolt. Handheld wrenches were used to generate a small pretension in the injection bolts. This small pretension force mitigated any gaps between the steel beam and concrete deck to prevent any leakage of the epoxy resin. Upon the first disassembly, it was found that significant amounts of resin leaked around the bolt hole at the steel-floor element interface, see Figure 7.8a, despite the minor pretension to mitigate visible gaps. This excessive resin consumption, see Figure 7.8b, occurred mainly due to imperfections regarding the flatness of the flanges (governed by the slenderness and single-sided fillet weld), and due to imperfections regarding the prefabricated concrete floor elements. These observations highlight that resin-injected bolted connections require a relatively flat, level, and even surface of the connected components.

The injection of the hole clearance took on average 30 seconds per bolt, including preparation of the epoxy resin. The epoxy resin system RenGel SW 404 + HY 5159 was considered more suitable than RenGel SW 404 + HY 2404 (see Chapter 3 for the mechanical properties of these epoxy systems), mainly because of its lower viscosity and longer pot time. The latter was particularly relevant because the feasibility study took place during the summer: the high ambient temperature led to impractical pot times (5-10 minutes) using hardener HY 2404, which was not sufficient to process a 0.5 kg batch. Using hardener HY 5159, the full 0.5 kg batch could be injected successfully.

All of the above time measurements are based on two persons working in parallel plus one designated crane operator. The total assembly time for one floor element of the composite floor system (48 connectors) therefore took approximately 23 minutes. The subsequent injection process took approximately 24 minutes per floor element, but was only

(a) Removal of the floor elements revealed substantial epoxy resin leakage at the steel-concrete interface.
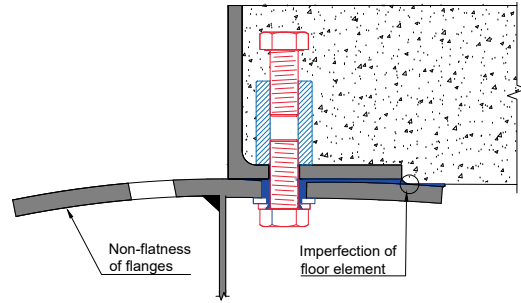
(b) Flatness imperfections of the flange and floor element, leading to epoxy resin leakage. Drawn after Gîrbacea [3].

Figure 7.8 | Resin leakage due to imperfections of steel beam and concrete floor element.

performed once all other floor elements were installed. This leads to an total execution time for one floor element of 47 minutes for two workers and one crane operator.

The presented time indication is partially conservative, because it is based laboratory experiments where shear connectors were installed at a 300 mm centre-to-centre distance and where temporary long bolts were installed and replaced at each of these locations. In a practical application, the number of temporary bolts may be reduced to for instance 6, four at the corners and two midway the length of the floor element, which still leads to safe working conditions and the alignment of the embedded couplers with the bolt holes[3]. Under the assumption of 24 shear connectors (12 pairs) per floor element, the total execution time per floor element reduces to approximately 30 minutes, or 1.6 min/m^2, for this particular composite floor system design, without considering any longer distance to be travelled by the crane and/or the installation of any safety equipment necessary for work at increased height.

MACHINERY AND ACCESSORIES
The following machinery and accessories were required for assembly and disassembly:

 i. An overhead crane (work load 6.5 tonnes);

 ii. HE300B lifting beam, see Figure 7.9;

 iii. Temporary alignment bolts (M20x200);

 iv. Handheld wrenches (M20);

 v. Injection gun including disposables.

The prefabricated concrete floor elements, each weighing 6 tonnes, were lifted using a lifting beam made of a HEB300 steel section, see Figure 7.9. Two holes were drilled through

---

[3]Given that the nominal hole clearance is sufficiently large, e.g. based on the prediction method presented in Chapter 8

the beam web. The location of these holes was chosen such that the hogging and sagging bending moment in the prefabricated concrete deck are of similar magnitude. Anchor plates below the prefabricated concrete decks were used to support the steel decks, and threaded pins connected the anchor plate to the HEB300 section through a channel in the prefabricated deck. After connecting the lifting points to a crane, the floor element could be hoisted and moved to its intended position. The vertical channels through the concrete decks were not (temporarily) closed after assembly, but this would be required in case of a real structure to prevent flow of liquids from one floor level to another. Alternatively, a tailor-made lifting system could be designed that does not require a full-depth opening in the prefabricated concrete deck.

The injection gun can either be manual, electric or pneumatic. Within the feasibility study, a manual gun was considered to be most practical, because the injection pressure was sufficient to inject, but was not too high to cause any leakage. In case of electric or pneumatic guns, care must be taken to limit the injection pressure, else components of the machine may get into direct contact with the (leaked) epoxy resin, which damaged the gun on a number of occasions.
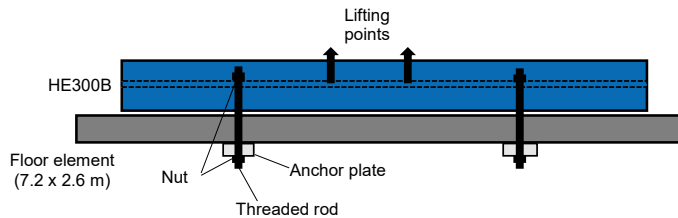
Figure 7.9 | Hoisting system for the prefabricated concrete floor elements.

MATERIAL, MANUFACTURING, EXECUTION AND TRANSPORT COSTS
Appendix E gives an overview of the actual and estimated costs for materials and execution related to the resin-injected demountable shear connector. It should be noted that cost data is highly location, volume, time and context dependent, and it is presented only as an indication.

7.2. STRUCTURAL TESTING

After completing the feasibility study, the experimental setup presented in Section 7.1 was modified to study the mechanical linear-elastic response of the demountable composite floor system. The justification for the limitation to elastic behaviour is that the focus is on demountable and reusable structures, and therefore plasticity in the beam, deck and shear connectors should be prevented in the design. The need for elastic design is further elaborated on in Appendix G. At the end of the experimental work, the composite floor system was loaded to failure. This additional experiment was carried out to observe the failure mechanism and to obtain information about the demountability after plastic deformation of the composite floor system.

7.2.1. SPECIMEN DESIGN AND EXPERIMENTAL DETAILS

The existing experimental setup used for the feasibility study was reduced from two to one bay, such that the two simply-supported steel beams and floor elements C and D remained. Two loading frames were installed at 4.05 m from each support. Figures 7.10 and 7.11 provide a schematic and detailed overview of the modified experimental setup, respectively. All details related to the design of the composite floor system were identical to those provided in Section 7.1, unless stated otherwise.

LOADING FRAMES, ACTUATORS, AND BRACING

The loading frames at 4.05 m from the supports were connected to individual hydraulic actuators, which could deliver a concentrated force up to $F = 550$ kN each. The surface of the floor elements at the location of the loading frames was levelled using self-compacting concrete to obtain a well-defined loading zone. Flat steel strips of 50 mm width were used to transfer the forces from the loading frames onto the floor elements. Torsional and/or out-of-plane deformation was prevented by the same bracing system as was used in the feasibility study, meaning that the beam was laterally restrained at 3.6 m intervals. This ensured that bending occurred only around the strong axis, in the direction of the applied load.

SHEAR CONNECTOR ARRANGEMENTS

The design of the steel beam and prefabricated concrete floor elements enabled to install demountable shear connectors at 300 mm intervals along the length of the floor system. This shear connector arrangement is referred to as U24, where "U" denotes a uniform distribution and where "24" represents the number of pairs of shear connectors from support to midspan.[4]

   The flexibility of the decision to install shear connectors or not enabled the investigation of the effects of different shear connector arrangements on the (vertical) deflection and the end-slip (the relative displacement at the steel-concrete interface at the supports). Based on theoretical findings presented in the literature [4–6], it was expected that fewer shear connectors are sufficient to fulfil deflection and end-slip criteria if they were concentrated near the supports, rather than uniformly distributed along the beam length. An overview of the six shear connector arrangements considered in the experimental programme is provided in Figure 7.12. For the arrangements in which the shear connectors are concentrated

---

[4]7200 mm / 300 mm/pair = 24 pairs of shear connectors from support to midspan.

(a) Schematic overview.

(b) Physical assembly.
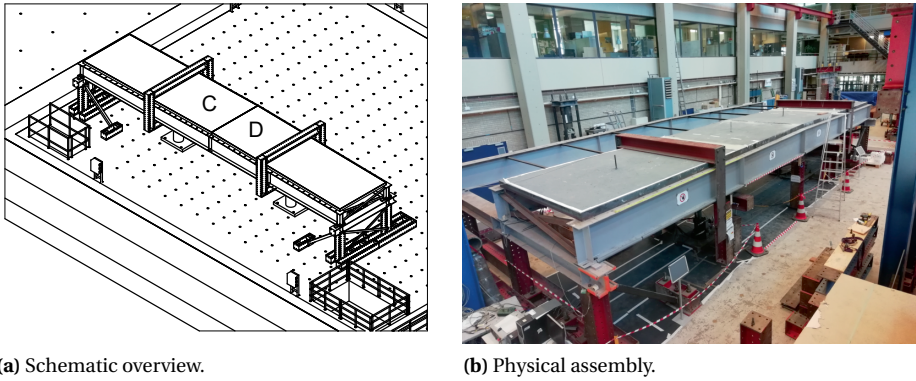
Figure 7.10 | Overview of the composite floor system during the structural testing phase.
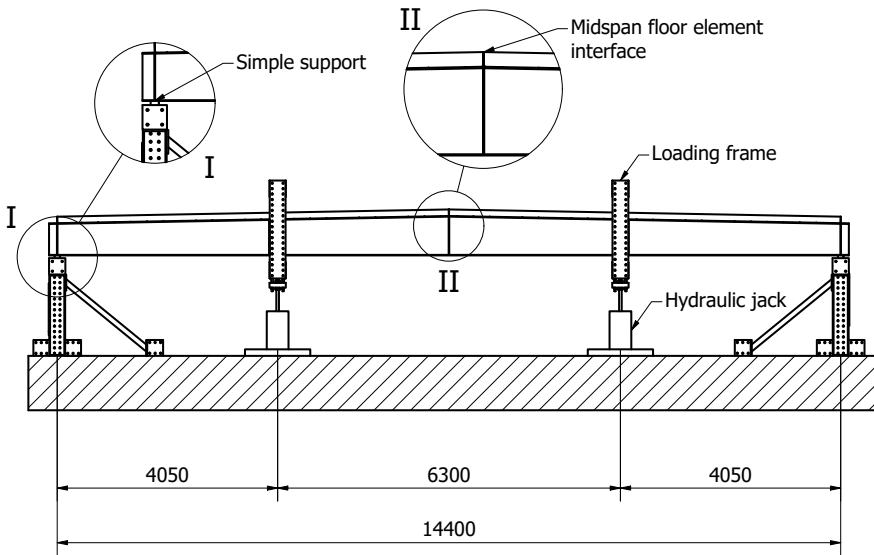

Figure 7.11 | Side view of the experimental setup including key dimensions (in mm).

near the supports, denoted by "C", additional bolts (drawn in black) are installed to prevent vertical separation of the steel beam and concrete deck, although the experimental results obtained by Naraine [7] suggested that this separation is negligible (≪ 0.5 mm) at linear-elastic load levels. These additional bolts did not act as shear connectors, because the bolt-hole clearances were intentionally not injected and therefore no significant shear force could be transferred by these bolts at the load levels imposed during the tests because these bolts were not sufficiently close to bearing.

It should be noted that none of the shear connector arrangements followed the elastic longitudinal shear flow distribution as required by EN 1994-1-1 [8]. Only arrangements U-24 and U-12 satisfied the Eurocode 4 spacing requirement of the connectors (no more than 800 mm or 6 times the height of the concrete element - in this case 720 mm). The other arrangements are outside the (current) application limits of EN 1994-1-1 [8].

The linear-elastic response of the composite floor system was guaranteed by preliminary finite element analysis, based on which the maximum actuator force was determined for each shear connector arrangement that would certainly not lead to inelastic behaviour of any of the structural components, including the shear connectors. This preliminary analysis was conducted using the load-slip curve of the shear connector obtained by finite element analysis (see Chapter 5) and by requiring the end slip to not exceed 0.6-0.8 mm.

DETAILING AT MID-SPAN
The midspan interface between the prefabricated concrete floor elements was designed as a dry joint, see Figure 7.13a. Compressive forces can, but bending moments cannot be transferred through such a joint. Given that the bending stiffness of the concrete deck is an order of magnitude lower than that of the steel beam, it is evident that the effects of this detailing on the deflection are insignificant.

Another type of midspan joint was investigated, see Figure 7.13(b), to reduce the differential deflection between two floor elements if either one would be subject to a concentrated force applied near midspan and at approximately mid-width of the floor element. The effects of this midspan joint, consisting of additional cover plates and bolts, was assessed by imposing a concentrated force at 300 mm from midspan on one of the floor elements at their mid-width (1300 mm from either steel beam), distributed on a 200 × 200 mm surface [as defined in 9]. The magnitude of the concentrated force was based on the maximum axle load defined by EN 1993-1-1 [9] (category G, 90 kN) corresponding to a wheel load of 45 kN. The deflection between the floor elements was measured for both floor elements at 300 mm from midspan at mid-width of the floor element: the differential deflection was taken as the difference between the maximum and minimum of the two measurements.

MEASUREMENTS
The relative horizontal displacement (slip) between the steel beam and the floor element interface was measured at each support by `ETI SYSTEMS LCP8` potentiometers. The deflection of the steel beam with respect to the laboratory floor was measured at midspan and directly below the point of load application, see Figure 7.5. Strain gauges of type `TML FLA-6-11` were used to monitor the stresses in the beam and to determine the beam curvature. The strains were measured on the outer tensile fibre of the steel beam, as well as on the web in the vicinity of both flanges. The strain gauges were installed at 5.0 m from the supports, because (i) the maximum longitudinal stresses resulting from self-weight and
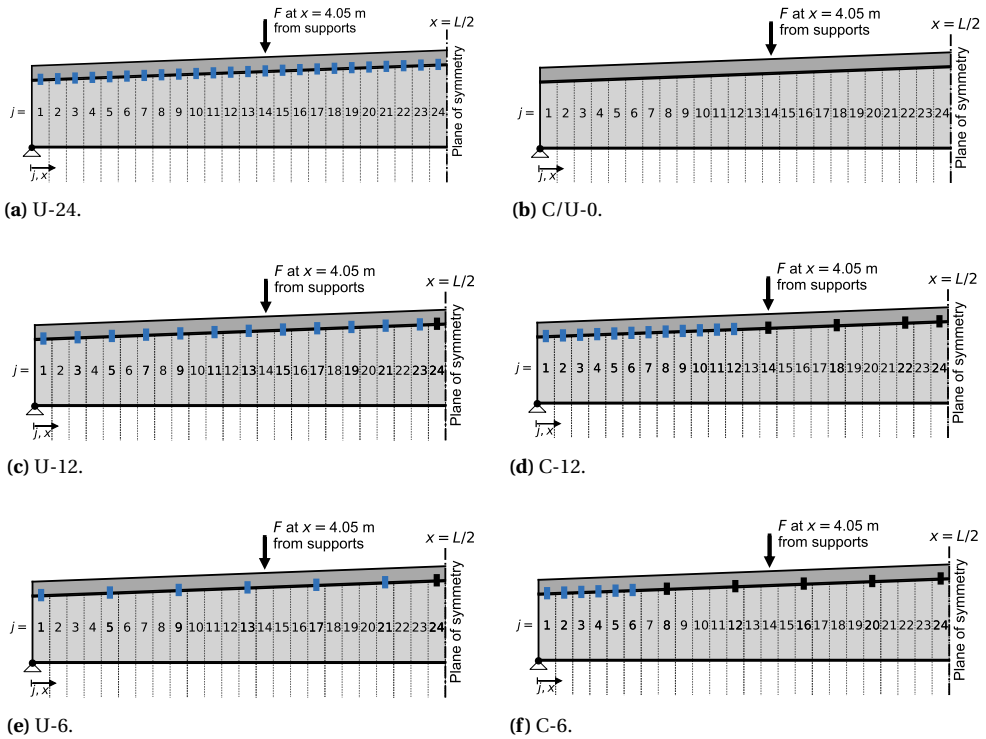
Figure 7.12 | Shear connector arrangements: each blue-coloured bar indicates a pair of shear connectors (one per steel beam). Normal bolts (represented by black bars) are placed only to prevent vertical separation of the deck and beam. "U" denotes uniform shear connector spacing, "C" denotes concentrated spacing near the supports. The number, e.g. "24", represents the number of pairs of resin-injected bolted shear connectors. The beam is symmetric in the plane at $x = L/2$.
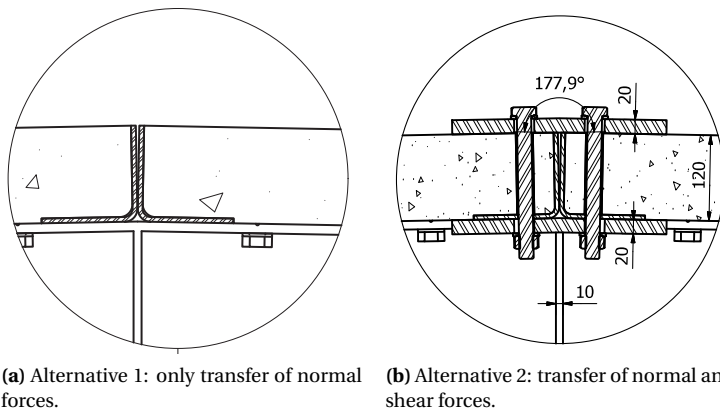

Figure 7.13 | Dry joints at midspan ($x = L/2$).

applied load were expected in this cross-section and (ii) because this was an undisturbed zone, meaning that no strain concentrations existed due to stiffeners and/or bolt holes.

LOADING SPEEDS AND REPETITIONS

The loads were applied by controlling the stroke of the hydraulic actuators. The loading and unloading speeds were set as 0.15 mm/s and 0.30 mm/s, respectively. The composite floor system was loaded and unloaded five times during experiment to check the consistency of the results in subsequent loading cycles.

7.2.2. RESULTS AND DISCUSSION

The experimental results regarding deflection and end-slip were evaluated for each of the shear connector arrangements in terms of the effective bending stiffness and the effective shear stiffness, respectively defined as

$$k_{b,eff} = \frac{\Delta F}{\Delta w(x = L/2)} \tag{7.1}$$

$$k_{s,eff} = \frac{\Delta F}{\Delta s(x = 0, L)} \tag{7.2}$$

where ΔF is the force increment, $\Delta w(x = L/2)$ is the deflection increment at midspan and $\Delta s(x = 0, L)$ is the slip increment at the supports. These parameters were evaluated at linear-elastic load levels in the 10-25 mm deflection range by fitting a linear regression line that minimises the sum of the squared errors. For arrangements C/U-0 and U-6, the midspan deflection did not reach 25 mm, and therefore the last 10 mm deflection increment was used to quantify the aforementioned effective stiffness parameters.

The strain gauge readings were converted to nominal normal stresses by the product of the longitudinal strain increment and the nominal Young's Modulus of steel, E = 210 GPa. The evaluation of the stresses was performed over the same interval as mentioned in the preceding, but the stresses were inter- or extrapolated to concentrated forces F = 100 kN to facilitate easy comparison between the results.

EFFECTIVE BENDING STIFFNESS

The effective bending stiffness $k_{b,eff}$ is summarised in Figure 7.14a, including the variation of the result over the five loading cycles. The results demonstrate that the effective bending stiffness increases by 42%-68% relative to the case of no shear connection (C/U-0) for the considered shear connector arrangements. Figure 7.15 shows the relation between the concentrated force F and the deflection at midspan for each of the shear connector arrangements. The results confirm the previous theoretical findings [4–6] that concentrating the (same number of) shear connectors leads to improved effective bending stiffness: in case of 6 and 12 pairs of connectors, the effective bending stiffness increased by 6% and 5.4%, respectively. This implies that the design of the composite floor system could be improved by reducing the number of shear connectors (to reduce costs and execution time) by optimising their location. Further benefits could be achieved by a reduced spacing of connectors in the support zone: in Chapter 5 it was demonstrated that no substantial difference exists between a spacing of $15d$ (present case, 300 mm c.t.c.) and $10d$ in terms of the shear connector stiffness k_{sc}. Their reduced spacing would improve the beneficial effect of the

composite interaction, without requiring additional work or resources if the less effective connectors in the midspan region were to be omitted.

Concentrated shear connector arrangements in the support regions could readily be implemented in practice if the only goal of the shear connection is to fulfil deflection and end-slip criteria under serviceability loads. The design load in the ultimate limit state should then be resisted by the steel beam alone: a suggestion for this design approach was made by Crisinel [10]. If composite action shall be required for the resistance, further experimental investigation is necessary to account for the potential influences of vertical separation of beam and floor element, although the work of Naraine [7] indicated that such effects are negligible in the linear-elastic stage.

Effective shear stiffness

The effective shear stiffness $k_{s,eff}$ is summarised in Figure 7.14b, including the variation of the results over the five loading cycles, which was significant (up to 30%) compared to the variation of the effective bending stiffness. Figure 7.16 shows the relation between the concentrated force F and the relative displacement (slip) at the steel-concrete interface at the supports for each of the shear connector arrangements. It was observed that the effective shear stiffness underwent larger relative changes in magnitude compared to the effective bending stiffness: this implies that the relation between the slip and deflection is non-linear, which is in line with the observations based on the prediction models presented in the literature review.

Comparison of the effective shear stiffness with expected values (based on the finite element model presented in Chapter 9) revealed that the experimental values of $k_{s,eff}$ were substantially ($\approx 45\%$) smaller, although the experimental and predicted effective bending stiffness were in good agreement. To investigate the cause for this observation, one of the two concrete decks was removed to inspect the beam-floor element interface. In line with the findings of the feasibility study, it was found that a resin layer had formed between the solid deck and the steel beam during the injection process, which was assumed to be intentionally broken during preliminary tests.

To investigate if adhesion was responsible for deviation in slip between experiments and prediction models, the beam-floor element interface in one half-span was thoroughly cleaned and greased to reduce the effect of adhesion and friction. The deck in the other half-span was left in the as-tested condition. An additional experiment was carried out with the C-6 shear connector arrangement. No significant difference in terms of the effective bending stiffness (+1.4%) was observed, but the effective shear stiffness increased substantially on both the greased and non-modified side by 17% and 62%, respectively, compared to the original experiment. The minor difference in effective bending stiffness indicates that adhesion and friction at the interface may only have had a small effect in the original test series. This hypothesis was later confirmed when testing the behaviour of the flooring system without any shear connectors (arrangement U-0) but with the same interface conditions: the effective bending stiffness of the beam approached that of the steel beam (see Chapter 9), indicating that no significant shear interaction due to adhesion or friction was present. The large variation of the end-slip (or effective shear connector stiffness) for nominally equal effective bending stiffness implies that further research is necessary to explain the seemingly complex relation between the experimentally obtained end-slip and the deflection.
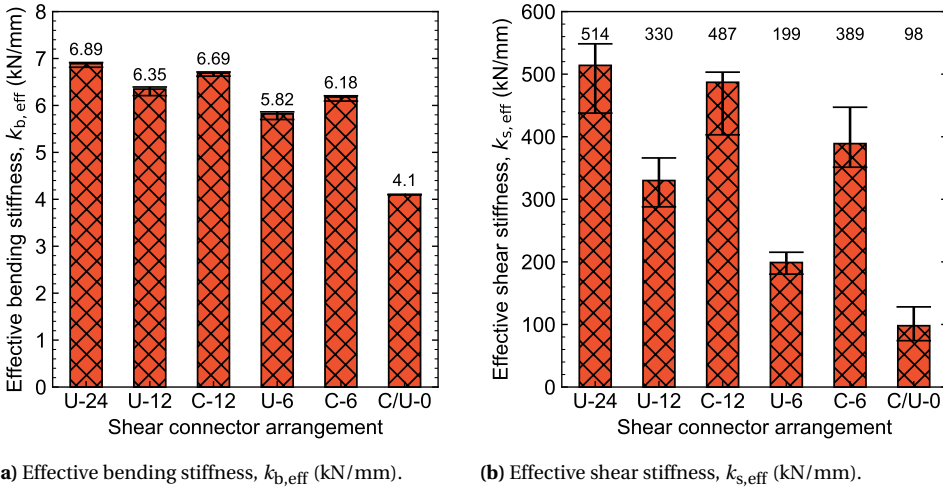
(a) Effective bending stiffness, $k_{b,eff}$ (kN/mm).

(b) Effective shear stiffness, $k_{s,eff}$ (kN/mm).

Figure 7.14 | Averaged effective stiffness parameters including their variations over the five loading cycles.

NORMAL STRESSES DUE TO BENDING

Figure 7.17 illustrates the averaged nominal bending stresses (based on $E = 210$ GPa) over the height of the cross-section at 5.0 m from the supports. The elastic neutral axis of the steel beam shifted upwards (towards the compression flange) as the number of shear connectors increased. This shift was caused by the stronger composite interaction and the corresponding larger tensile normal forces (and thus larger tensile stresses) in the steel beam. An exception to this trend occurred for C-6: the higher effective bending stiffness compared to U-6 led to a slightly larger distance $(+0.01h)$ of the elastic neutral axis to the outer compression fibre. This minor deviation from the general trend was considered to be the result of a local influence of the shear connector in this region for U-6, see Figure 7.12.

MIDSPAN DETAILING

Figure 7.18 illustrates the differential deflection between the two adjacent floor elements for the two alternative midspan joints presented in Figure 7.13 . The design where the prefabricated decks were not able to transfer vertical shear forces but were only capable to transfer compressive forces (alternative 1) led to a higher differential deflection (+175%) between the floor elements than the alternative with the cover plates (alternative 2). However, it must be noted that the differential deflection at the 45 kN wheel load level was rather small (2 mm for the solution without cover plates) and therefore would not significantly affect any comfort, well-being or other serviceability criterion. In addition, a 45 kN (or 4500 kg) wheel load is excessive for the intended application of a multi-storey car park building: it is double the weight of an average car. For a typical car ($m = 2000$ kg) the differential deflection reduces to approximately 0.2 mm: it is therefore recommended to not use cover plates, because the negative impact of omitting them is small but their application could have a negative effect on the speed of execution. It should be noted that this recommendation is only valid for present case: for larger centre-to-centre distances of the steel beams, the differential deflection could become more pronounced.
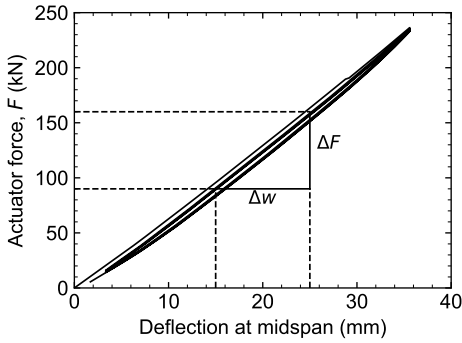
(a) Arrangement U-24.
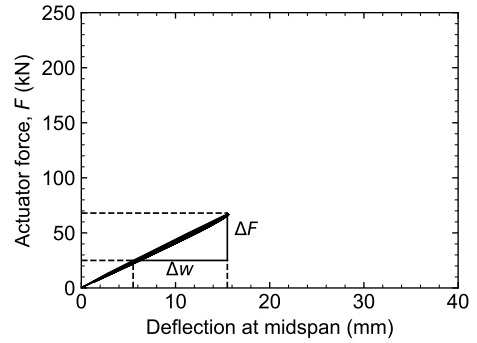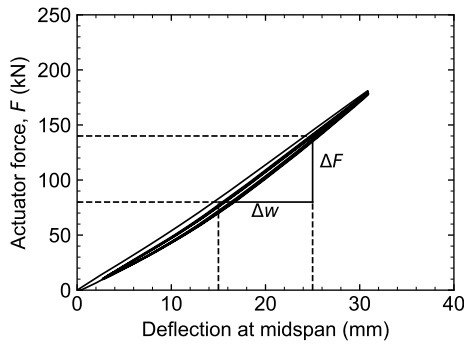
(b) Arrangement C/U-0.
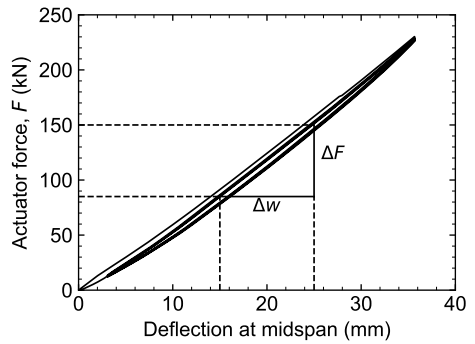
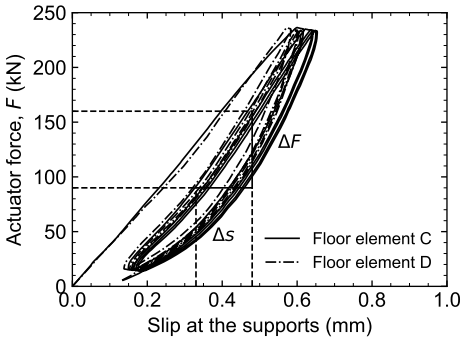**(c)** Arrangement U-12.
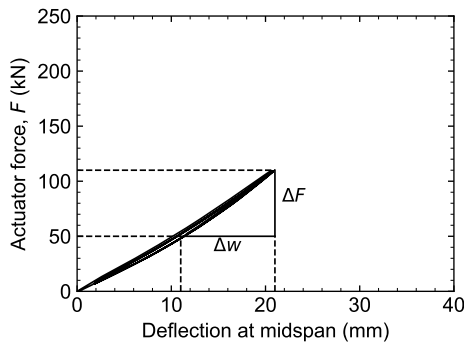
(d) Arrangement C-12.
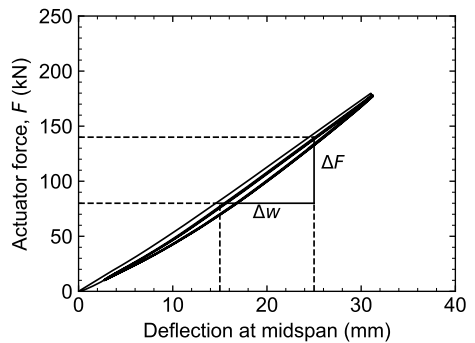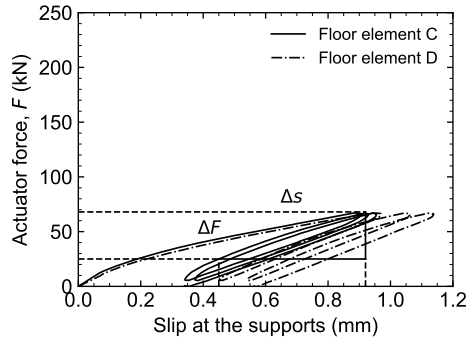
(e) Arrangement U-6.
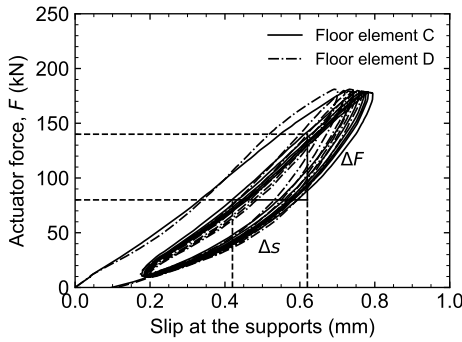
(f) Arrangement C-6.

Figure 7.15 | Force-displacement curves obtained for the various shear connector arrangements. The maximum actuator force F is variable to ensure linear-elastic response.
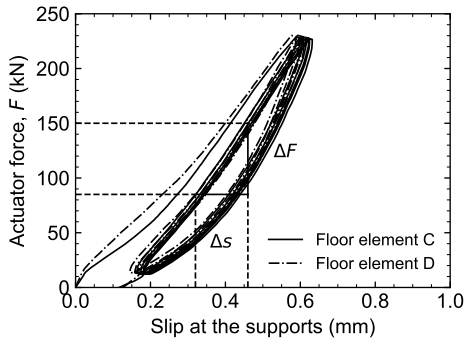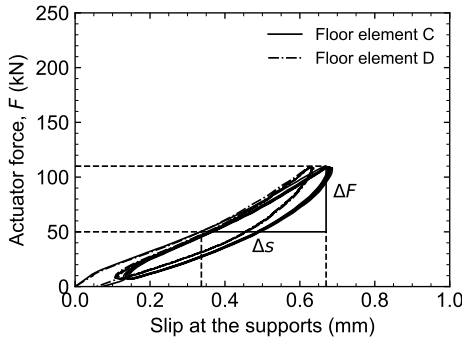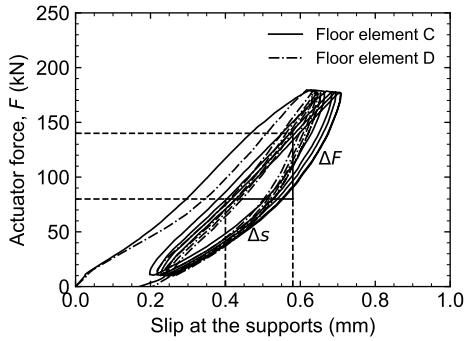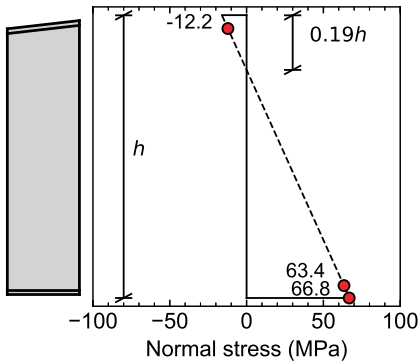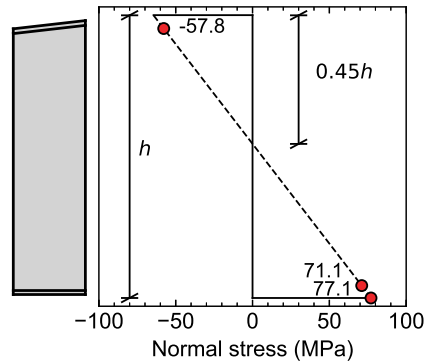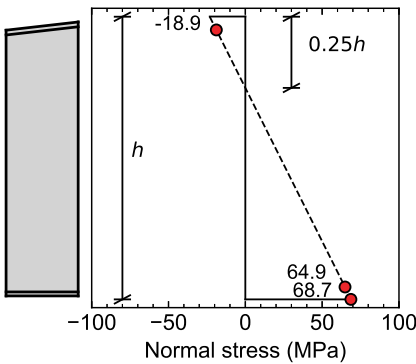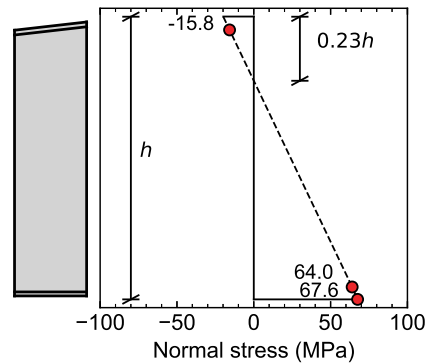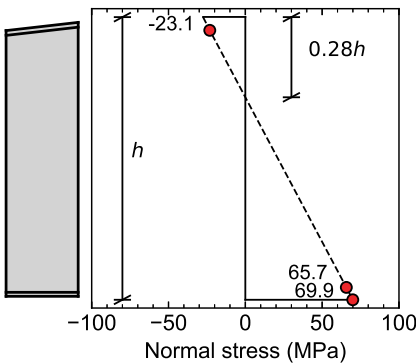
(a) Arrangement U-24.

(b) Arrangement C/U-0.

(c) Arrangement U-12.

(d) Arrangement C-12.

(e) Arrangement U-6.

(f) Arrangement C-6.

Figure 7.16 | Force-slip curves obtained for the various shear connector arrangements. The maximum actuator force F is variable to ensure linear-elastic response.

(a) Arrangement U-24.
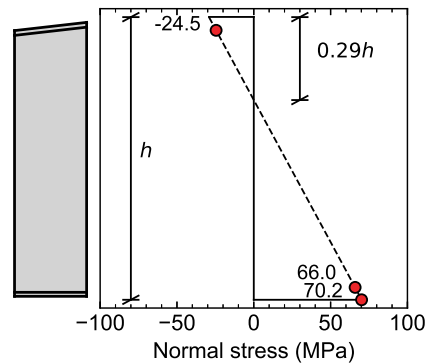

(b) Arrangement U-0.

(c) Arrangement U-12.

(d) Arrangement C-12.

(e) Arrangement U-6.

(f) Arrangement C-6.

Figure 7.17 | Normal stresses over the height of the steel beam for the cross-section at 5.0 m from the supports, inter- or extrapolated to nominal point loads $F = 100$ kN.

TESTING TO FAILURE

At the end of the linear-elastic experimental campaign, the composite floor system was loaded to failure using shear connector arrangement C-6. The injection of one of the sixth connectors from the supports was unsuccessful because the air escape channel was blocked: therefore it was decided to perform the experiment with 5 pairs of shear connectors concentrated in the support regions instead.

Figures 7.19a and -b illustrate the relation between the applied load, midspan deflection, and end slip. The relation between force and deformations is linear until $F = 300\text{-}350$ kN, followed by a non-linear branch due to tensile yielding of the steel beam and plastic deformation of the shear connectors. At $F \approx 550$ kN, the experiment was terminated because the nominal resistance of the hydraulic actuators was reached. No observable concrete damage initiated within this force range. A permanent deflection of 38 mm remained after unloading due to the plastic deformation of the steel beam. Figure 7.19c illustrates the development of the averaged strains on the beam web with the external load. The strain readings confirmed that partial tensile plastification of the cross-section occurred.

After the failure experiment, the composite floor system could be disassembled without any additional work or time compared to previous instances. This implies that demountability does not necessarily require linear-elastic response[5], which was attributed to the large nominal hole clearance which prevented the bolt from becoming immobile due to inclination of the bolt axis.

---

[5]However, from a reusability point of view, requiring a linear-elastic response is the most intuitive design approach. See also Appendix G for a discussion on plastic vs. elastic design approaches structural elements intended to be reused.
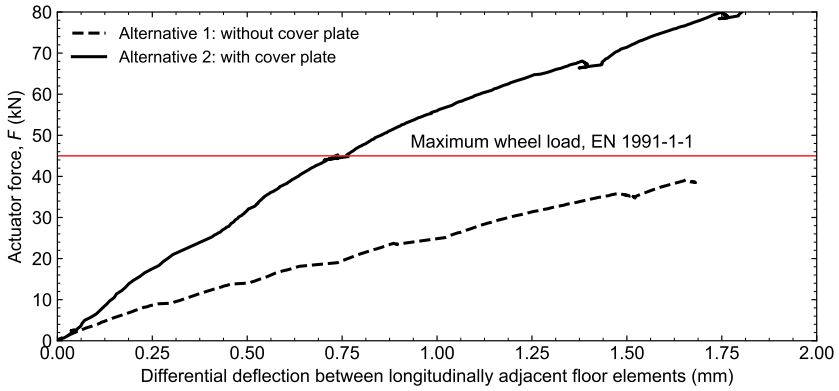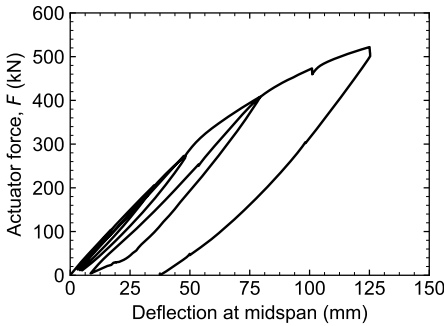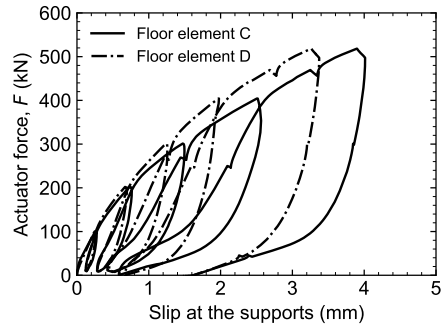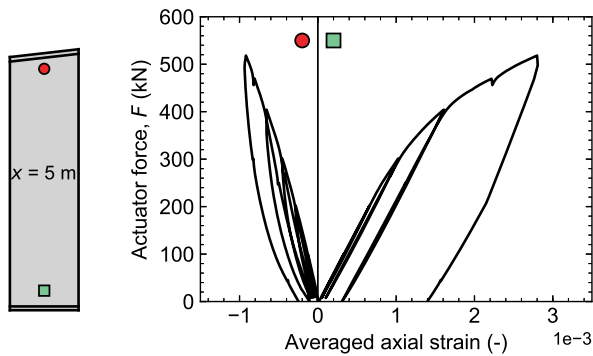
Figure 7.18 | Differential deflection between the adjacent floor elements C and D for both midspan detailing alternatives.

(a) Force vs. midspan deflection.

(b) Force vs. end-slip.

(c) Force vs. strain. The square and circle denote the readings of the strain gauges in the tensile and compressive part of the web, respectively.

Figure 7.19 | Experimental results of the test to failure, shear connector arrangement C-5.

7.3. CONCLUSIONS

This chapter presented the first ever experimental work on a demountable web-tapered steel-concrete composite floor system, and addressed both its feasibility of construction as well as its structural response during the service life. To this extent an experimental setup representing the composite floor system of a multi-story car park building was designed, and consisted of large (7.2 × 2.6 × 0.12 m) prefabricated floor elements, simply-supported web-tapered steel beams ($L = 14.4$ m) and resin-injected demountable shear connectors. The main findings of the work are:

- The feasibility of construction depended on the nominal hole clearance: the prefabricated concrete floor elements could only be connected to the steel beam in case of a 12 mm hole clearance. This magnitude was substantially larger than the typical 1-3 mm clearance for steel-to-steel connections and the initially assumed value of 6 mm. The needs for a larger nominal hole clearance originated from geometrical and dimensional imperfections, for example related to the out-of-straightness of the steel beam (although mitigated by the bracing system), the scatter in the position of the shear connectors in the floor element, and from slip due to self-weight of the floor elements.

- The injection of the epoxy resin system RenGel SW 404 + HY 5159 took on average 30 seconds per bolt, including preparations. The epoxy did not influence the demountability of the composite floor system, because all components were treated with a wax-based release agent. RenGel SW 404 + HY 5159 was preferred the injectant because of its lower viscosity and longer pot time compared to RenGel SW 404 + HY 2404.

- Four-point bending experiments were conducted on one bay of the composite floor system. Six shear connector arrangements were studied under linear-elastic conditions: in line with earlier theoretical observations, it was found that concentrating the shear connectors near the supports reduced the deflection by approximately 6% and thus led to increased composite interaction.

- Significant scatter (up to 30%) was observed in terms of the effective shear stiffness (related to the slip) over multiple load cycles, although the effective bending stiffness (related to the deflection) reproduced more accurately. Attempts to reduce the scatter by greasing the steel-concrete interface led to up to 64% higher effective shear stiffness while the effective bending stiffness remained almost identical: therefore further experimental research is necessary to understand the development of slip and its relation to the deflection.

- The composite floor system was loaded to failure for the case where five pairs of shear connectors were concentrated in the support regions. The resistance of the floor system could not be determined because of the limited capacity of the hydraulic actuators. However, inelastic deformation of the shear connectors and tensile yielding of the beam led to a permanent deflection of 38 mm after unloading. Despite the substantial plastic deformations, the floor system could be readily disassembled.

8

OVERSIZED HOLES TO FACILITATE RAPID EXECUTION AND EASY DEMOUNTING

We live on an island surrounded by a sea of ignorance.
As our island of knowledge grows, so does the shore of our ignorance.

John Archibald Wheeler

INTRODUCTION

This chapter presents a framework to quantify the magnitude of the oversized holes required to assemble and disassemble steel-concrete composite floor systems. In Chapter 7 it was experimentally demonstrated that larger (12 mm) than usual (1-3 mm) nominal hole clearances were necessary to install demountable shear connectors because of dimensional and geometrical deviations of the structural components. A sufficiently large nominal hole clearance contributes to the speed of execution and to the demountability of the composite floor system. This chapter quantifies the required nominal hole clearance based on statistical evaluation of geometrical and dimensional deviations and based on a performance criterion related to the executability of the connection.

This chapter is subdivided into five sections. Section 8.1 identifies dimensional and geometrical deviations relevant to the execution of steel-concrete composite floor systems. A statistical approach to solving the required nominal hole clearance is presented in Section 8.2, which is implemented for a case study example in Section 8.3. In Section 8.4 the required nominal hole clearance according to the proposed statistical approach is compared to the actual needs for the experimental composite floor system presented in Chapter 7. The chapter concludes with Section 8.5, summarising the main findings of this chapter.

Parts of this chapter have been published in Structures **24**, 489 [11].

8.1. Dimensional and geometrical deviations

All engineering structures contain a degree of uncertainty with respect to their geometry. The magnitude of the uncertainty is controlled by imposing limits related to dimensional or geometrical deviations. Dimensional deviations concern the variation of a given dimension at a fixed point in space, whereas geometrical deviations are related to the variation of positions. The magnitude of the dimensional and geometrical deviations affect the speed of execution, the appearance, and the load bearing resistance of a structure. An extensive list of tolerance limits for steel structures is specified in Annex B of EN 1090-2 [12], which distinguishes between essential and functional tolerances. Essential tolerances are specified to ensure the validity of the design assumptions concerning resistance and stability, whereas functional tolerances are imposed to ensure executability and/or appearance. In this chapter, tolerances are defined as the *maximum allowable* difference and deviations are defined as the *actual* difference of a certain dimension or geometry.

The functional tolerances specified in EN 1090-2 [12] provide sufficient certainty that the various structural elements of a typical steel structure can be assembled using the *nominal hole clearance* for normal round holes specified in EN 1090-2 [12]. The *nominal hole clearance* is defined as the difference between the nominal hole diameter and the nominal bolt diameter, i.e. $d_0 - d$. In case of a complex structural design characterised by potential execution challenges, the contractor could preassemble the structure in the factory. Alternatively, the structure could be designed with connections with oversized round holes or slotted holes to increase the probability of successful execution of the bolted connections. The latter is often the less expensive solution, because it saves the labour costs and time related to preassembly and because it can easily be implemented in the existing fabrication process.

The alignment of the demountable shear connectors embedded in a prefabricated concrete floor element and the bolt holes in a steel beam depends on the geometrical and dimensional deviations of both members, as well as on the deviations within the structural grid. EN 1090-2 [12] contains an extensive list of maximum dimensional and geometrical deviations for two tolerance classes, with stricter requirements for tolerance class 2 compared to tolerance class 1.

The geometrical and dimensional deviations relevant to demountable composite floor systems are presented and discussed in Sections 8.1.1-8.1.5. Distinction between deviations in various directions is made according to the global coordinate system shown in Figure 8.1. The x-coordinate along the beam span is always positive, i.e. the global yz-plane coincides with the support that causes the x-vector to point in the direction of the span.

8.1.1. Location of bolt holes

The distance between the intended and actual location of the centre of a bolt hole in a steel beam is limited by EN 1090–2 [12] as ±2 mm and ± 1 mm for tolerance class 1 and 2, respectively. The magnitude of the actual deviation is denoted by random variable R in Figure 8.2, whereas the direction in which this deviations occurs is controlled by random variable θ. The deviation along the axes of the coordinate system can then be expressed by

$$(\Delta x_{\text{hole}}, \Delta y_{\text{hole}}) = (R\cos\theta, R\sin\theta). \tag{8.1}$$
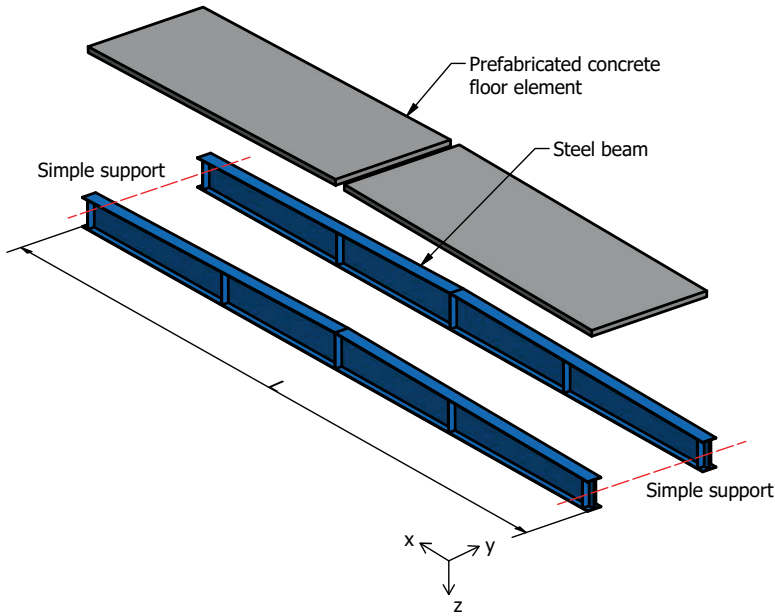
Figure 8.1 | Global coordinate system of the composite floor system, consisting of steel beams and prefabricated concrete floor elements.
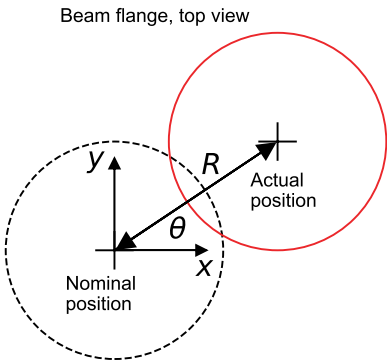

Figure 8.2 | Deviation of the actual hole position from the nominal hole position in the beam flange.
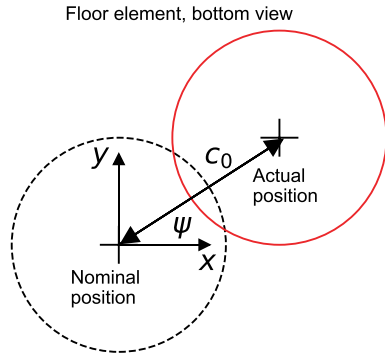

Figure 8.3 | Deviation of the actual connector position from the nominal connector position in the prefabricated floor element.

8.1.2. Shear connector position within floor element

It is assumed that a tailor-made and high-precision formwork is used to cast the prefabricated concrete floor elements. The demountable shear connectors are assumed to be fixed to the formwork with a nominal bolt-to-formwork clearance denoted by c_0. Due to the installation and tightening, the demountable shear connector will be in contact with the hole walls in nearly all cases and therefore c_0 can be regarded as a deterministic variable. The direction in which this occurs is assumed to be random and is represented by the angle ψ. The offset from the nominal position of the demountable shear connector along the axes of the coordinate system is then given by

$$(\Delta x_{sc}, \Delta y_{sc}) = (c_0 \cos \psi, c_0 \sin \psi), \tag{8.2}$$

which is illustrated in Figure 8.3.

8.1.3. Out-of-straightness of the beam

The initial out-of-straightness of the steel beams affects the probability of transversal alignment of the bolt holes in the top flange and the demountable shear connectors embedded in the prefabricated concrete floor elements. Generally, the out-of-straightness of beams and columns is represented by a half sine wave with imperfection amplitude $A_{0,u}$, expressed by

$$\Delta y_{str,u} = A_{0,u} \sin\left(\frac{\pi x}{L}\right), \tag{8.3}$$

where L is the beam span. The deviation $\Delta y_{str,u}$ is illustrated in Figure 8.4. Relatively long beam spans optimise the flexibility of the building: the combination of long spans and slender steel profiles may lead to the need of a bracing system at midspan to prevent lateral-torsional buckling of the steel beam due to the self-weight floor elements (see Chapter 9). Such a bracing system mitigates the out-of-straightness of the main girders, see Figure 8.4. An out-of-straightness function compatible with the restraints imposed by the bracing at midspan is given by

$$\Delta y_{str,b} = A_{0,b} \sin\left(\frac{2\pi x}{L}\right). \tag{8.4}$$
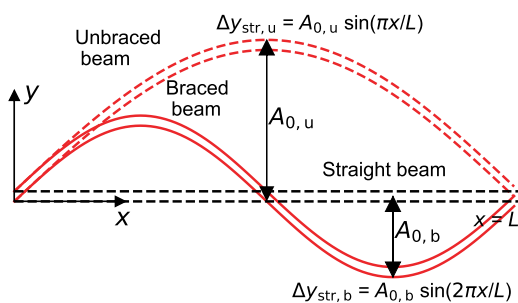

Figure 8.4 | Out-of-straightness of an unbraced beam and a beam braced at midspan compared to the nominal geometry.

The subscripts "u" and "b" denote the unbraced and braced case, respectively. The length of the steel beam is not influenced by the presence of a bracing system. Therefore, the arc length P, given by

$$P = \int_0^L \sqrt{1 + \left(\frac{\mathrm{d}y}{\mathrm{d}x}\right)^2}\,\mathrm{d}x,\tag{8.5}$$

remains constant at all times, which requires that the derivatives of Equations 8.3 and 8.4 must be equal. It follows that the amplitude of the out-of-straightness of the beam braced at midspan is one half of the amplitude of the out-of-straightness of the (original) unbraced beam, i.e. $A_{0,b} = 0.5A_{0,u}$. Similar derivations can be made for cases in which the beam is braced at other locations along its span.

The out-of-straightness is limited by EN 10034 [13] for hot rolled sections and by EN 1090-2 [12] for all other profiles. An overview of the maximum out-of-straightness according to these standards is given in Table 8.1.

The actual out-of-straightness of steel beams was extensively investigated in the context of establishing buckling curves in EN 1993-1-1 [14]. The average out-of-straightness of a large batch of various profiles (IPE, DIE, DIR, TB) determined by Beer & Schulz [15] is listed in Table 8.2 together with data reported by Strating & Vos [16], Tebedge et al. [17], Dux & Kitipornchait [18], Aoki & Fukumoto [19] and Essa & Kennedy [20]. The average out-of-straightness $A_{0,u}$ reported by these authors is $L/2800$ and the corresponding averaged standard deviation is $L/5700$. It is worth noticing that all experimentally obtained data originates from the 1970s to 1990s, and that technological advancements in the production process of steel beams may have decreased the magnitude of the out-of-straightness. Several mills and workshops have been consulted for more recent out-of-straightness measurements, but none actively registered the magnitude of this imperfection, and therefore the deviations found in the 1970s–1990s were adopted in this chapter.

8.1.4. RELATIVE DISPLACEMENT DUE TO SELF-WEIGHT

A relative longitudinal displacement (slip) between the concrete floor elements and the steel beam occurs due to sliding of the floor elements relative to the steel beam because of their self-weight. The slip along the beam length is assumed to be represented by a halve cosine wave [21] with amplitude s_0, expressed by

$$\Delta x_{\mathrm{slip}} = -s_0 \cos\left(\frac{\pi x}{L}\right),\tag{8.6}$$

Table 8.1 | Maximum out-of-straightness amplitude $A_{0,u}$ for hot-rolled I and H sections and for generic beams used in buildings.

Height h (mm)	Maximum out-of-straightness amplitude $A_{0,u}$ [L]			
	Hot rolled I/H sections, EN 10034 [13]	Beams in buildings, EN 1090-2 [12]		
		Essential tolerance	Functional Tolerance	
			Tolerance class 1	Tolerance class 2
$80 < h \leq 180$	$L/333$	$L/750$	$L/500$	$L/1000$
$180 < h \leq 360$	$L/667$	$L/750$	$L/500$	$L/1000$
$h > 360$	$L/1000$	$L/750$	$L/500$	$L/1000$

Table 8.2 | Out-of-straightness amplitude $A_{0,\mathrm{u}}$ around the weak (z-)axis for various types of profiles.

Author	Profile	Number of specimens	Length (m)	Origin	Out-of-straightness $A_{0,\mathrm{u}}$	
					Mean	Standard dev.
	IAP 150 (IPE 140/160)			BE/GE	$L/2100$	
	IPE 160			NL	$L/4400$	
	IPE 200			BE	$L/3800$	
Beer & Schulz [15]	DIE 20 (HEA 200)			BE	$L/3700$	
	DIR 20 (HEM 200)			BE	$L/5800$	
	Welded section			BE	$L/5500$	
Strating & Vos [16]	IPE 160		1.0-2.9	NL	$L/1200$	$L/5000$
Tebedge [17]	HEM 340	12	3.9-7.5	BE/DE/IT	$L/3600$	$L/5800$
Dux & Kitipornchait [18]	280UB37.3			AUS	$L/2500$	
Aoki & Fukumoto [19]	Welded H-section (100 x 100 mm)	85	1.4-2.9	JAP	$L/3300$	$L/6400$
Essa & Kennedy [20]	W360 x 39	11	9	CA	$L/2000$	
Average					$L/2800$	$L/5700$

which is illustrated in Figure 8.5. Its sign reflects the relative outward motion of the pre-fabricated floor elements along the steel beam with respect to midspan. It should be noted that, because of the sequential placement of the prefabricated concrete decks, the slip at both sides does not develop simultaneously. In fact, the slip generated by the first floor element (of two) is less than half the total slip because of the unsymmetrical loading. Hence, the assembly of the first deck requires the least nominal hole clearance. However, as will be shown later, the slip is typically not the most influential factor in the required nominal hole clearance, and for the sake of simplicity and symmetry the installation process is considered as if both prefabricated floor elements are installed simultaneously. This is the most conservative case, and is also applicable to floor systems with single floor elements, which could be relevant in case of smaller spans.

The slip amplitude s_0 for a generic simply-supported steel beam, symmetric with respect to midspan, on which prefabricated concrete floor elements with self-weight q_z per unit length are simultaneously installed is
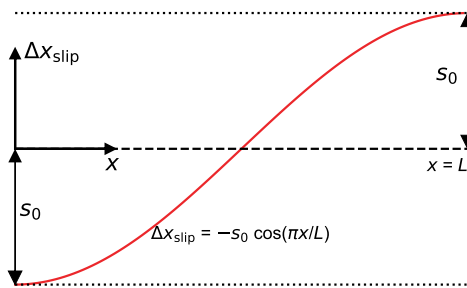
Figure 8.5 | Change in position of bolt hole occurring as a result of slip due to the self-weight of the prefabricated floor element.

$$s_0 = \int_0^{L/2} \frac{1}{2} \frac{q_z x (L-x) e}{EI_0} \, dx, \tag{8.7}$$

which can be derived based on Euler-Bernoulli beam theory. In Equation 8.7 e denotes the distance between the neutral axes of the steel beam and prefabricated concrete floor element, and EI_0 represents the bending stiffness without composite interaction. If the concrete floor elements are shorter than the beam span the bending stiffness EI_0 should be taken as the bending stiffness of the steel section. For prismatic steel beams, Equation 8.7 reduces to

$$s_0 = \frac{1}{24} \frac{q_z L^3}{EI_0} e. \tag{8.8}$$

For non-prismatic beams, the evaluation of Equation 8.7 is more complex. Therefore, a design formula to determine the slip amplitude of a simply-supported web-tapered steel beam, symmetrical with respect to the plane at midspan, is derived based on the exact Euler-Bernoulli results for a large database of cross-sections. The details regarding the derivation of the design formula can be found in Appendix F. The proposed design formula is expressed by

$$s_0 = \frac{1}{24} \frac{q_z L^3}{0.437 \cdot EI_0|_{x=0} + 0.563 \cdot EI_0|_{x=L/2}} \left(0.388 \cdot e|_{x=0} + 0.612 \cdot e|_{x=L/2}\right), \tag{8.9}$$

which becomes the exact solution given by Equation 8.8 for prismatic beams.

8.1.5. DIMENSIONAL AND GEOMETRICAL DEVIATIONS OF THE STRUCTURAL GRID

The alignment of the demountable shear connectors embedded in the prefabricated concrete floor element and the bolt holes in the steel beam partially depends on the deviations of the structural grid. During the installation of the main and secondary steel beams part of the geometrical and dimensional deviations in the columns are corrected. However, the centre-to-centre distance between two adjacent beams may still vary. An overview of this deviation perpendicular to the span is illustrated in Figure 8.6.

The magnitude of the deviation between the nominal distance between adjacent erected beams measured at the supports ($\Delta Y_{c,1} = \Delta y_{c,1,L} + \Delta y_{c,1,R}$, see Figure 8.6, and similarly for $\Delta Y_{c,2}$) is limited by EN 1090-2 [12] to ±10 mm and ±5 mm for tolerance class 1 and 2, respectively. The maximum deviation for each individual erected beam end is not specified , but could be approximated, for instance by an expression in the form

$$\Delta y_{c,1,L} = \eta_L \Delta Y_{c,1} \; ; \; \Delta y_{c,1,R} = (1 - \eta_L) \Delta Y_{c,1}, \tag{8.10}$$

where η_L is a random variable on the interval [0,1] and subscripts "L" and "R" denote the left and right beam, respectively. The deviation for the beams at $x = L$ can be modelled similarly. The deviation of the nominal position of the left beam in Figure 8.6 is a function of position along the beam length, described by the relation

$$\Delta y_{c,L} = \eta_{L,1} \Delta Y_{c,1} + (\eta_{L,2} \Delta Y_{c,2} - \eta_{L,1} \Delta Y_{c,1}) \frac{x}{L}, \tag{8.11}$$
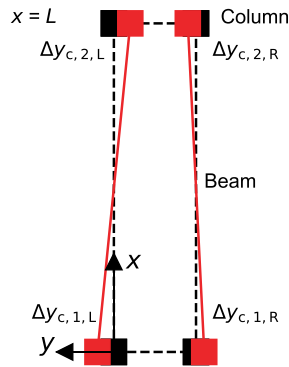
Figure 8.6 | Nominal and actual position of the beams due to imperfections in the structural grid perpendicular to the span.

which is a linear interpolation function between the beam supports. It should be noted that η_L was replaced by $\eta_{L,1}$ and $\eta_{L,2}$ to reflect the independence of the deviations of the structural grid at both beam ends. This function implicitly assumes that the prefabricated floor elements remain parallel to the nominal span direction. A similar expression is derived for the right beam by replacing $\eta_{L,i}$ by $1 - \eta_{L,i}$ ($i = 1, 2$) in Equation 8.11.

The structural grid is also subject to geometrical and dimensional deviations in longitudinal direction, resulting in a staggered pattern of beams. For the two adjacent beams these random deviations are denoted as $\Delta X_{c,L}$ and $\Delta X_{c,R}$ for the left and right beam, respectively. In this case, the floor elements could be translated longitudinally to mitigate the effects of the offset of one of the beams. However, it was assumed that no attempt would be made to find the most suitable installation position, and that the prefabricated concrete decks would be installed on their nominal locations, which leads to the most conservative result for the nominal hole clearance and is best suited to be implemented in a non-iterative prediction model. For both tolerance classes the magnitude of the maximum longitudinal deviation is taken equal to that in transversal direction. Due to the axial rigidity of the steel beams the deviations are constant along their length, thus equally affecting the required nominal hole clearance of all demountable shear connectors, i.e. $\Delta x_{c,L} = \Delta X_{c,L}$ and $\Delta x_{c,R} = \Delta X_{c,R}$.

8.1.6. TOTAL DEVIATION AND THE REQUIRED NOMINAL HOLE CLEARANCE
The total deviation from nominal positions in x and y directions of the centre of the bolt holes and the centreline of the demountable shear connectors embedded in the concrete floor elements are the cumulative effects of the contributions made by Equations 8.1-8.11. For the left beam in Figure 8.6, the total deviation is given by

$$(\Delta x_{beam}, \Delta y_{beam}) = \left(R\cos\theta + \Delta x_{c,L}, R\sin\theta + A_{0,u/b}\sin\left(\frac{n_{u/b}\pi x}{L}\right) \right.$$
$$\left. + \eta_{L,1}\Delta Y_{c,1} + (\eta_{L,2}\Delta Y_{c,2} - \eta_{L,1}\Delta Y_{c,1})\frac{x}{L} \right) \tag{8.12}$$

and for the left side of the prefabricated concrete floor elements

$$(\Delta x_{floor}, \Delta y_{floor}) = \left(-s_0\cos\left(\frac{\pi x}{L}\right) + c_0\cos\psi, c_0\sin\psi \right) \tag{8.13}$$

The deviations are derived similarly for the right beam. The magnitude of the distance between the actual centreline of the bolt hole and the actual centreline of the demountable shear connector, denoted by r, can be calculated using Pythagoras' theorem according to

$$r = \sqrt{(\Delta x_{\text{beam}} - \Delta x_{\text{floor}})^2 + (\Delta y_{\text{beam}} - \Delta y_{\text{floor}})^2} \tag{8.14}$$

The demountable shear connector can be installed if

$$r + \frac{d}{2} < \frac{d_0}{2} \tag{8.15}$$

where d represents the nominal bolt diameter and d_0 denotes the hole diameter. The required nominal hole clearance, defined as $d_0 - d$, is therefore equal to $2r$.

8.2. Statistical evaluation of required nominal hole clearance

Although EN 1090-2 [12] provides a list of geometrical and dimensional tolerances, it does not provide any details regarding their probability distributions. Kala [22] assumed that deviations related to the out-of-straightness of beams could be represented by a Gaussian (normal) distribution, and that 95% of all realisations fall within the imposed tolerance limitations. According to this approach, the tolerance limit represents a certain number of standard deviations, expressed by

$$n \cdot \sigma = |\pm \text{tolerance}|, \tag{8.16}$$

where n is any positive number and equal to 1.96 for Kala's assumption. A smaller value of n implies that more observations outside the tolerances limits are expected. Kala's assumption is valid for all deviations, as long as the deviations are bilateral. In this dissertation, n is taken as 1.96, corresponding to 95% of the realisations complying to the tolerance limits.

Table 8.3 contains the statistical parameters that are assumed based on EN 1090-2 [12], Kala [22] and Table 8.2 for the normal-distributed basic variables included in Equation 8.15. Tables 8.4 and 8.5 contain the uniformly distributed parameters and the deterministic variables, respectively.

The combination of different stochastic distributions is considered using the Monte Carlo method. Random realisations of each of the basic variables as well as random positions along the length of the composite floor system are generated to evaluate the required nominal hole clearance ($d_0 - d$) based on Equation 8.15. The aggregated results of the simulations are used to obtain the statistical distribution of the required nominal hole clearance.

Table 8.3 | Normal-distributed basic variables.

Basic variable	Distribution	Mean	Tolerance Class 1 - Standard deviation	Tolerance class 2 - Standard deviation	Unit
R	Normal	0	1.02	0.510	mm
$\Delta Y_{\text{c},i}$	Normal	0	5.10	2.55	mm
$\Delta X_{\text{c},i}$	Normal	0	5.10	2.55	mm
$A_{0,\text{u}}$	Normal	$L/2800$	$L/5700$	$L/5700$	mm

8

Table 8.4 | Uniformly distributed basic variables.

Basic variable	Distribution	Interval	Unit
θ	Uniform	$[0, 2\pi]$	rad
ψ	Uniform	$[0, 2\pi]$	rad
η_i	Uniform	$[0, 1]$	-

Table 8.5 | Deterministic basic variables.

Basic variable	Distribution	Magnitude	Unit
s_0	Deterministic	Equation 8.9	mm
c_0	Deterministic	1	mm
d	Deterministic	e.g. 20	mm

It is assumed that no correction of any deviations occurs during execution except for the installation of the bracing at midspan.

The successful application of demountable and reusable composite floor systems in engineering practice is influenced by the speed of execution, which is characterised by the ability to connect the prefabricated floor elements through the demountable shear connectors to the steel beams. It should be noted that the demountable shear connectors embedded in a prefabricated concrete floor element should simultaneously align with the bolt holes in two beams, and therefore the probability P of successful alignment of one floor element is

$$P(\text{L} \cap \text{R}) = P(\text{L}) P(\text{R}), \tag{8.17}$$

where $P(\text{L})$ and $P(\text{R})$ denote the probability of individual alignment of the demountable shear connectors for the left and right beam, respectively. The probability of successful installation of the demountable shear connectors must be sufficiently high to obtain an acceptable high speed of execution, and depends on the risk the contractor is willing to take. For instance, it could be considered acceptable if 5 out of 100 prefabricated floor elements cannot be installed at the first attempted position. The 'failure' probability of 5% can then be used to determine the required nominal hole clearance by determining its 95th percentile value based on the aggregated simulation results.

8.3. CASE-STUDY EXAMPLE

The required nominal hole clearance was quantified for the case study of a main girder of a multi-storey car park building, with a design similar as in the experimental work presented in Chapter 7. The composite floor system consisted of web-tapered steel beams with a clear span of 16 m at a centre-to-centre distance of 2.7 m, and prefabricated concrete floor elements with a length of 8 m, a width of 2.7 m and a thickness of 0.12 m. The weight per unit length q_z of the prefabricated concrete floor elements was 8.1 kN/m. The steel beams and the prefabricated concrete floor elements were connected by demountable shear connectors embedded in the floor elements.

The height of the tapered steel beam varied linearly between the supports, $h|_{x=0,L} = 590$ mm, and midspan, $h|_{x=L/2} = 740$ mm. The thickness and width of the flanges, as well as the thickness of the web, were constant along the beam length and are provided in Figure 8.7.

Tolerance classes 1 and 2 were considered in combination with the possible presence of a bracing system at midspan to prevent lateral-torsional buckling during execution. The out-of-straightness of the beam was assumed independent of the tolerance class because the statistical parameters originate from actual measurements (see Table 8.2) instead of

from EN 1090-2 [12]. The slip amplitude $s_0 = 2.96$ mm was determined based on Equation 8.9.

The (stochastic) variables in Equations 8.13 and 8.14 were generated according to their distributions (see Tables 8.3–8.5) followed by a deterministic evaluation of the performance function expressed by Equation 8.15. The convergence of the statistical characteristics of the aggregated results was an indicator that sufficient number of simulations had been considered. For this case study the number of simulations was $N = 75000$ based on a maximum deviation of 0.05 mm of the 95th percentile of the aggregated results between ten subsequent simulation runs.

The nominal hole clearance as a function of the probability of successful installation of the demountable shear connectors upon the first attempt is illustrated in Figure 8.8. The required nominal hole clearance for a given probability of successful alignment was smallest in case of tolerance class 2 in combination with a brace at midspan. In case of an unbraced span, the magnitude of the nominal hole clearance increased significantly for the same probability of successful installation of the demountable shear connectors. For a 95% probability of successful connector installation, a nominal hole clearance of 16.5 mm and 22.7 mm was required for tolerance class 1 in case of a braced and unbraced span, respectively. For the stricter tolerance class 2, these values decreased to 12.6 mm and 20.2 mm, respectively, but still demonstrate a pronounced sensitivity to the midspan restraint.

Figure 8.9 shows a 'heat map' of the required nominal hole clearance for the successful installation of demountable shear connectors for the case study flooring system with and without a bracing system. It was observed that the critical locations to connect the demountable shear connectors were located at a quarter and at three-quarters of the span for a braced beam, which is in line with the out-of-straightness shape illustrated in Figure 8.4. A similar agreement between the out-of-straightness shape and the shape of the heatmap was observed for the unbraced beam and indicated that the out-of-straightness had a pronounced influence on the required nominal hole clearances.

It should be noted that the determination of the required nominal hole clearances was carried out under the assumption that it must be possible to connect the demountable shear connectors along the full length of the composite floor system. However, in Chapter 7 it has been shown that concentrating the shear connectors near the supports is the most effective strategy to optimise the structural response of the composite beam. Figure 8.9 illustrates that at these locations the required nominal hole clearance was not maximum, implying that the current findings provided a lower bound probability of successful installation of the demountable shear connectors if they were concentrated in the support regions.
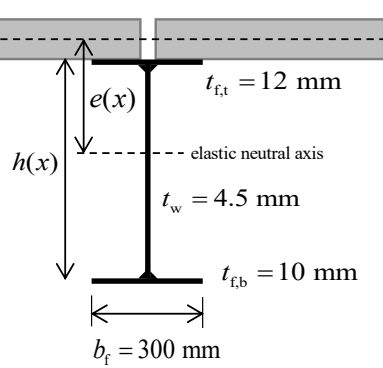
8

Figure 8.7 | Cross-section of the steel web-tapered beam, including prefabricated concrete floor element, considered in the case study.
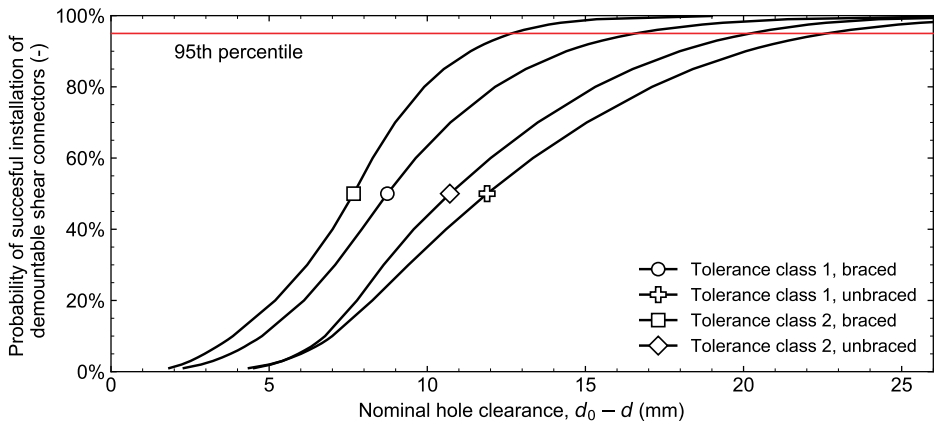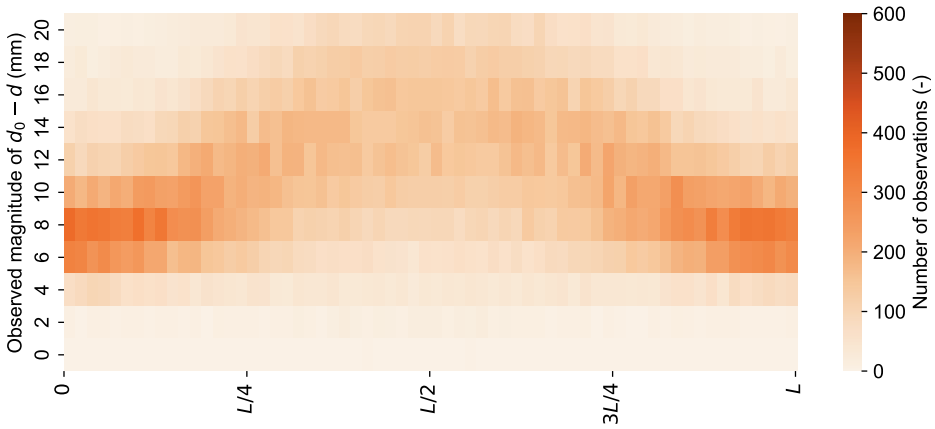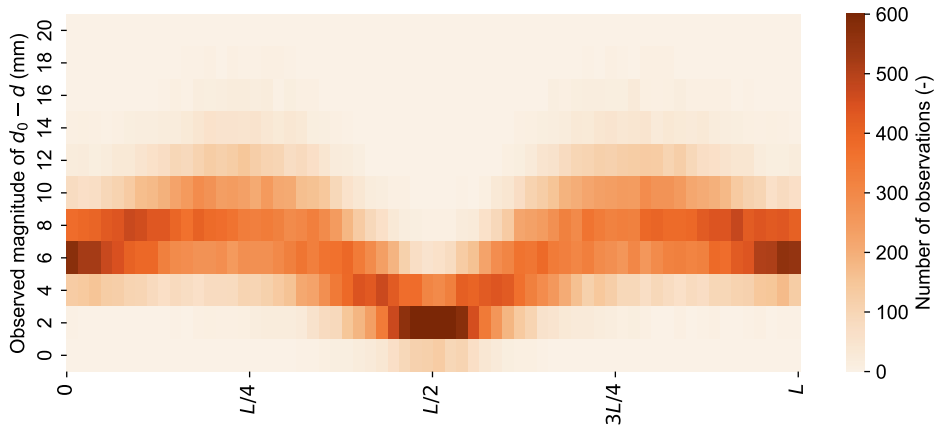

Figure 8.8 | Probability of successful installation of composite floor system as function of the nominal hole clearance for the case study example.

(a) Unbraced beam.

(b) Beam braced at $L/2$.

Figure 8.9 | Heat map identifying the need for nominal hole clearances along the beam length for the case study composite floor system.

8.4. COMPARISON OF MODEL TO FINDINGS OF CHAPTER 7

In Chapter 7, a steel-concrete composite floor system with similar specifications as in the case study example (see Section 8.3) was successfully assembled and disassembled using a 12 mm nominal hole clearance. These steel beams were braced at 5 locations during execution and were not subject to support offset due to deviations in the structural grid. The free span of this experimental composite floor system beam was $L = 14.4$ m. In this section, a comparison between the predicted and experimentally required nominal hole clearance is made, and the source for the variation is discussed.

To reflect the experimental conditions for the experimental composite floor system presented in Chapter 7, the formulation for the out-of-straightness function was modified to

$$\Delta y_{\text{str,b}} = \frac{1}{4} A_{0,\text{u}} \sin\left(\frac{4\pi x}{L}\right) \tag{8.18}$$

which reflects braced conditions at the supports and at $L/4$, $L/2$ and $3L/4$. In addition, the structural grid was modelled without any imperfections by setting $\Delta X_{\text{c},i} = \Delta Y_{\text{c},i} = 0$, and the free span length was set to $L = 14.4$ m (instead of $L = 16$ m as in Section 8.3). The slip amplitude s_0 was determined as 2.18 mm based on Equation 8.9.

The nominal hole clearance as a function of the probability of successful installation of the demountable shear connectors upon the first attempt is illustrated in Figure 8.10, and a heat map of the required nominal hole clearance is shown in Figure 8.11. The latter illustrates a pronounced interaction between the magnitude of $d_0 - d$ due to slip and out-of-straightness. The results in Figure 8.10 clearly demonstrate that the theoretically required nominal hole clearance to successfully execute the composite floor system is larger than the 6 mm initially assumed in Chapter 7. The experimentally required nominal hole clearance (12 mm) exceeds the predicted value for all probabilities for both tolerance class and 2. Therefore, according to the prediction model, the hole diameter during the experiments was larger than theoretically necessary.

However, the results of the Monte Carlo analysis are based on the assumption that the floor elements did not exhibit significant geometrical and dimensional deviations, which were observed in the physical specimens. For example, the maximum transversal deviations of the spacing of the demountable shear connectors were +2.6 and -2.8 mm. In longitudinal direction of the prefabricated concrete floor elements, the maximum deviations of the connector spacing were +1.4 and -0.9 mm, and the floor elements were 4.8 mm too long on average. The quantification of these deviations was one of the key tasks in the Master's thesis of Gîrbacea [3], where the reader is referred to for further details.

The observed deviations of the geometry and dimensions of the prefabricated concrete floor elements were significant and need to be taken into account when predicting the required nominal hole clearance. However, these deviations arose due to a non-standardised production process and the use of steel angle profiles as formwork, and are not expected to be of great significance in practical applications. A tighter control over the dimensional and geometrical deviations of the prefabricated concrete floor elements could have mitigated the experimentally required nominal hole clearances, and could be achieved by using high-precision moulds and established techniques of the prefabricated concrete sector. A coarse-scale measure for the influence of these additional deviations is the difference between the actual required nominal hole clearance (12 mm) and the predicted nominal hole clearance, for instance for 90% and 99% probability of successful installation of the shear
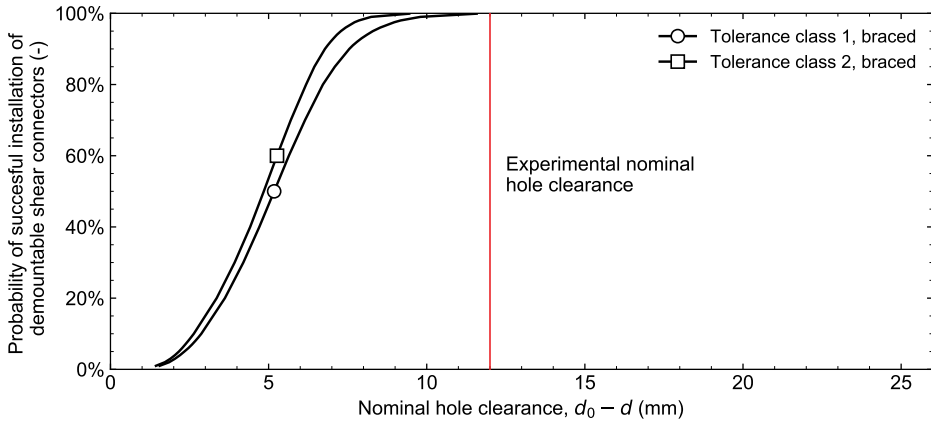
Figure 8.10 | Probability of successful installation as a function of the nominal hole clearance for the experimental composite floor system presented in Chapter 7.
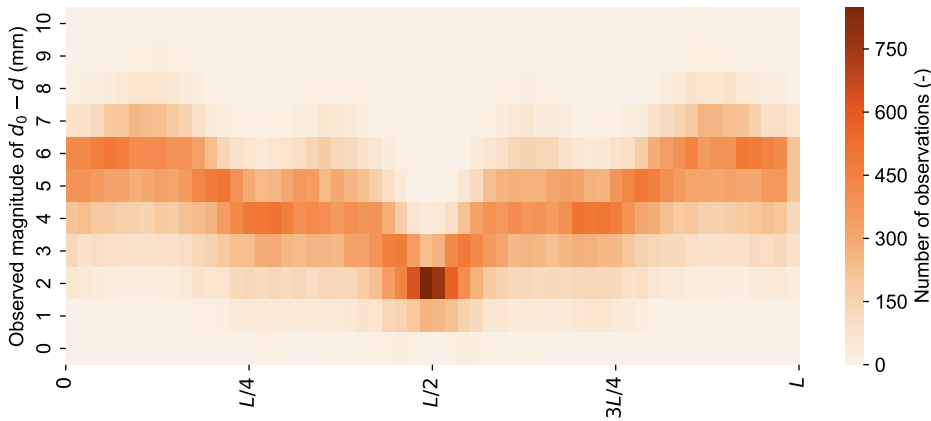

Figure 8.11 | Heat map identifying the need for nominal hole clearances along the beam length for the experimental composite floor system.

connectors, which leads to a need for 2.2-4.4 mm additional nominal hole clearance that arises due to imperfections (currently) unaccounted for in the prediction model.

8.5. Conclusions

This chapter identified the relevant geometrical and dimensional deviations that impact the assembly and disassembly of reusable composite floor systems. The considered deviations included equations derived for column offset (imperfection of the structural grid), bolt hole offset, shear connector offset, out-of-straightness, and relative displacement (slip) between the steel beam and the prefabricated concrete floor elements due to their self-weight. The magnitude of the deviations was been identified based on EN 1090-2 [12] and literature. An approximate formula to quantify the slip amplitude for a composite floor system consisting of prefabricated floor elements and a web-tapered steel beam was derived based on regression analysis. A generic prediction model to integrate the various sources of deviations and to quantify the required nominal hole clearance was developed, which relies on Monte Carlo Simulation for statistical evaluation.

The work of this chapter was mainly of generic nature. The complex relation between input and output variables hinders the formulation of generic conclusions. Nonetheless, the main findings of the work include:

- The magnitude of the required nominal hole clearance mainly depended on span length, specified probability of successful installation of the demountable shear connectors, tolerance class and the presence of bracing systems. The prediction model was applied to a tapered composite floor system, representing the main girder of a multi-storey car park building with a span of 16 m. For this case study example, a nominal hole clearance between 12.7 and 22.6 mm was required to achieve a 95% probability of successful installation of the prefabricated concrete floor elements, depending on the tolerance class and the presence of a bracing system at midspan.

- The outcome of the prediction model was compared to the needs for oversized holes reported in Chapter 7 related to the experimental composite floor system. The prediction model underpredicted the required nominal hole clearance, mainly due to deviations that originate from a non-standardised production process of the prefabricated concrete floor element, which were not included in the model. These deviations were estimated to amount to a need for 2.2-4.4 mm additional nominal hole clearance. A tighter control over the dimensional and geometrical deviations of these elements could have mitigated the additionally required nominal hole clearance, and could be achieved by using high-precision moulds and established techniques of the prefabricated concrete sector.

9

MECHANICAL RESPONSE: PREDICTION MODELS AND DESIGN OPTIMISATION STRATEGIES

Two roads diverged in a wood, and I took the one less travelled by,
and that has made all the difference.

Robert Frost

INTRODUCTION

This chapter presents prediction models and design optimisation strategies for non-prismatic demountable steel-concrete composite floor systems with non-uniform shear connection. Prediction models for deflection, in-plane resistance and fundamental frequency are derived and aim to optimise the performance during the service life. The execution phase is considered by deriving prediction models for lateral-torsional buckling of non-prismatic beams. The findings related to in-plane and out-of-plane behaviour are integrated to suggest cross-section design optimisation strategies.

This chapter is subdivided into five sections. Section 9.1 presents prediction models for deflection and elastic in-plane resistance of non-prismatic steel-concrete composite floor systems with non-uniform shear connection, which are validated against the experimental results obtained in Chapter 7. A prediction model for the fundamental frequency is proposed in Section 9.2. Section 9.3 focuses on the out-of-plane resistance. The implications of the in-plane and out-of-plane prediction models are integrated in Section 9.4 to derive cross-section design recommendations. The chapter concludes with Section 9.5, summarising the main findings of this chapter.

9.1. DEFLECTION AND ELASTIC IN-PLANE RESISTANCE

According to the SCI guidelines [25], the reusability of the composite floor system implies that the structural elements should not have plastically deformed[1]. Therefore a linear-elastic design approach is most suited for the design of reusable steel-concrete composite flooring systems, because it inherently prevents plastic deformation of the structural elements. The choice for an elastic or plastic design approach is further elaborated on in Appendix G.

Although in the majority of cases EN 1994-1-1 [8] allows to neglect the flexibility of the shear connection, see Section 2.5, it is considered more appropriate to account in all cases for such effects to obtain more accurate values of the stresses (related to the reusability condition) and deformations (e.g. vertical deflection and slip of the connector). The starting point for the analytical model for the in-plane linear-elastic mechanical behaviour of non-prismatic composite beams with non-uniform flexible shear connection is the differential equation

$$\frac{\mathrm{d}^6 w(x)}{\mathrm{d}x^6} - \alpha^2 \frac{\mathrm{d}^4 w(x)}{\mathrm{d}x^4} = -\frac{\alpha^2}{EI_\infty} q(x) + \frac{1}{EI_0} \frac{\mathrm{d}^2 q(x)}{\mathrm{d}x^2}, \tag{9.1}$$

also known as the Newmark model [27]. This equation is valid for prismatic composite beams with uniformly distributed flexible shear connectors subject to bending deformation due a uniformly distributed load $q(x)$. The shear deformation originating from the transversal load is not included in the analysis, because deflection due to bending is dominant for composite beams with typical span over depth ratios. For the derivation of Equation 9.1, the reader is referred to the Appendix H.

In Equation 9.1, $w(x)$ is the deflection function along the span and $q(x)$ represents the distributed load (force per unit length) acting on the beam. EI_∞ and EI_0 denote the bending stiffness in case of rigid and no shear connection, respectively, between the steel and concrete members. α^2 is a shear connection parameters defined as

$$\alpha^2 = K\left(\frac{1}{E_1 A_1} + \frac{1}{E_2 A_2} + \frac{e^2}{EI_0}\right) = \frac{Ke^2}{EI_0\left(1 - \frac{EI_0}{EI_\infty}\right)}, \tag{9.2}$$

where e denotes the distance between the elastic neutral axes of the connected members under the assumption of no shear interaction, and where K denotes the smeared shear connection stiffness, defined as the shear connector stiffness k_{sc} divided by the (uniform) connector spacing c_{sc}. The axial stiffness of the two cross-sectional elements is denoted by $E_i A_i$ ($i = 1, 2$), with subscript 1 referring to the concrete floor element and subscript 2 to the steel beam. The convention of internal and external actions is defined in Figure 9.1, which is discussed in further detail in Appendix H.

---

[1]In addition, economical considerations dictate that testing of individual elements is not required [26]. However, it could be argued that not only 'testing' but also 'thorough inspection' should be avoided.
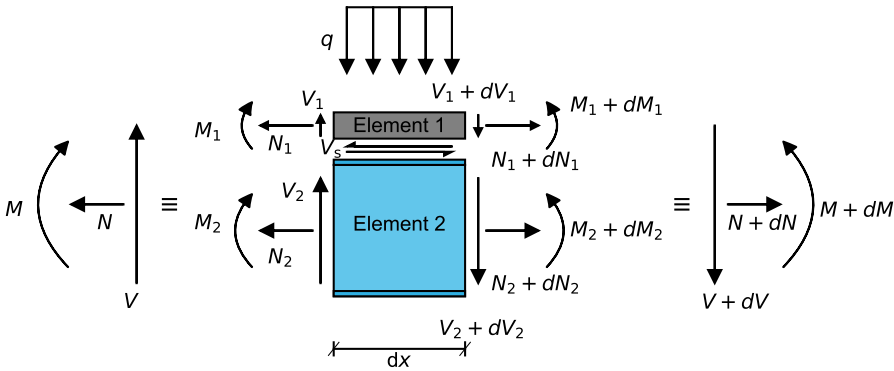
Figure 9.1 | Differential element of composite floor system with flexible shear connection subject to distributed transverse load $q(x)$. The resultant of the normal force is zero, $N = N + dN = 0$, if no external axial load is applied. The distance between the centroid of elements 1 and 2, denoted by e, is not shown in favour of the clarity of the figure.

9.1.1. BEYOND THE NEWMARK MODEL: NON-PRISMATIC COMPOSITE FLOOR SYSTEMS WITH NON-UNIFORM SHEAR CONNECTION

The experimental work in Chapter 7 demonstrated the benefits of concentrating shear connectors near the supports of simply supported floor systems to maximise the effective bending stiffness and to minimise end slip. In addition, the experimental work focused on a non-prismatic, web-tapered steel beam. The Newmark model cannot predict behaviour of composite floor systems with non-uniform shear connection and/or non-prismatic members, and can therefore not be used to understand the experimental observations.

A discretisation of the composite floor system into J equally sized segments was performed along the length of the composite beam to account for the non-uniform shear connector arrangements and varying geometry[2]. The discretisation process generates a stepped beam with different geometrical and mechanical properties in each equally sized segment, as illustrated in Figure 9.2. The geometrical and mechanical properties of the j-th segment are determined based on the magnitudes of the influencing variables at the x-coordinate corresponding to its centroid, and are reflected by the subscript j, e.g. $EI_{\infty, j}$. In each segment, the shear connection is assumed continuous (smeared) over the segment length. It is assumed that all materials behave linear-elastically and that the curvature of the constituent members is equal in each cross-section. Therefore, each beam segment fulfils the basic assumptions of the Newmark model. The validity of the overall modelling approach is confirmed later in this chapter by comparing the analytical results to the experimentally obtained results presented in Chapter 7.

Discretising the beam into J segments of equal length (see Figure 9.2), and assuming that the applied load per unit length q is constant in each beam segment, Equation 9.1 can be rewritten in the form

---

[2]Such a discretisation process was first adopted by Taleb & Suppiger [28] to model the free vibrations of non-composite beams.
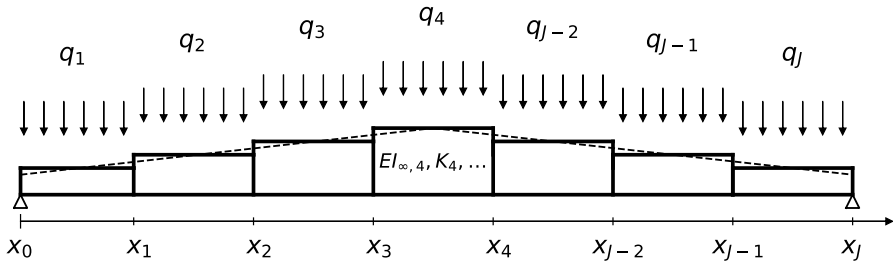
Figure 9.2 | Discretisation of a web-tapered composite floor system (dashed line) into J prismatic segments of equal length, subject to uniformly distributed loads q_j ($j = 1 \ldots J$). The cross-sectional parameters are evaluated midway between the segment boundaries.

$$\frac{\mathrm{d}^6 w_j(x)}{\mathrm{d}x^6} - \alpha_j^2 \frac{\mathrm{d}^4 w_j(x)}{\mathrm{d}x^4} = -\frac{\alpha_j^2}{EI_{\infty,j}} q_j, \tag{9.3}$$

with $1 \le j \le J$. The solution to this sixth-order linear differential equation is given by

$$w_j(x) = C_{1,j} \frac{\mathrm{e}^{a_j x}}{a_j^4} + C_{2,j} \frac{\mathrm{e}^{-a_j x}}{a_j^4} + C_{3,j} x^3 + C_{4,j} x^2 + C_{5,j} x + C_{6,j} + \frac{1}{24} \frac{q_j x^4}{EI_{\infty,j}}, \tag{9.4}$$

where $C_{m,j}$ ($m = 1, 2 \ldots 6$) are integration constants corresponding to the j-th segment. The expressions for the bending moment M, vertical shear force V, normal force N_1, longitudinal shear flow V_s, and interface slip s are given by

$$M_j = \frac{EI_{\infty,j}}{\alpha_j^2} \left[\frac{\mathrm{d}^4 w_j}{\mathrm{d}x^4} - \alpha_j^2 \frac{\mathrm{d}^2 w_j}{\mathrm{d}x^2} - \frac{q_j}{EI_{0,j}} \right], \tag{9.5}$$

$$V_j = \frac{\mathrm{d}M_j}{\mathrm{d}x} = \frac{EI_{\infty,j}}{\alpha_j^2} \left[\frac{\mathrm{d}^5 w_j}{\mathrm{d}x^5} - \alpha_j^2 \frac{\mathrm{d}^3 w_j}{\mathrm{d}x^3} \right], \tag{9.6}$$

$$N_{1,j} = \frac{\kappa_j EI_{0,j} - M_j}{e_j}, \tag{9.7}$$

$$V_{\mathrm{s},j} = -\frac{\mathrm{d}N_{1,j}}{\mathrm{d}x}, \tag{9.8}$$

$$s_j = \frac{V_{\mathrm{s},j}}{K_j}, \tag{9.9}$$

respectively. Their derivations are presented in Appendix H.

The $6J$ integration constants $(C_{1,1}, C_{2,1} \ldots C_{5,J}, C_{6,J})$, resulting from the J segments in which Equation 9.4 is defined, can be solved by imposing boundary conditions at x_0 and x_J, and interface conditions at $x_1 \ldots x_{J-1}$. For a beam simply supported at $x_0 = 0$ and $x_J = L$, the six boundary conditions are $w_1(0) = w_J(L) = 0$, $M_1(0) = M_J(L) = 0$ and $N_1(0) = N_J(L) = 0$. Other types of supporting conditions could be included by modifying the boundary conditions accordingly. The equilibrium of shear force, bending moment and normal force, as well as the continuity of deflection, slope and slip are enforced at the interface of neighbouring segments. These six interface conditions are expressed as $w_j(x_j) = w_{j+1}(x_j)$, $w'_j(x_j) = w'_{j+1}(x_j)$, $M_j(x_j) = M_{j+1}(x_j)$, $s_j(x_j) = s_{j+1}(x_j)$, $V_j(x_j) = V_{j+1}(x_j)$ and $N_{1,j}(x_j) = N_{1,j+1}(x_j)$, for $1 \le j \le J - 1$.

The collection of boundary and interface conditions leads to a set of $6J$ equations for $6J$ unknowns, which can solved analytically.

9.1.2. EXPERIMENTAL VALIDATION OF PREDICTION MODEL
The analytical method presented in Section 9.1 was validated against the experimental results presented in Section 7.2. The simply-supported composite floor system (see Figures 7.10 and 7.11) consisted of two prefabricated concrete floor elements of 7.2×2.6 m, connected to two web-tapered steel beams, symmetrical with respect to midspan, using various arrangements of demountable shear connectors, see Figure 7.12. The composite floor system spanned $L = 14.4$ m and was subjected to bending by applied point loads at 4.05 m from the supports.

The shear connector stiffness k_{sc} was iteratively calibrated to match the experimental results. The experimental and predicted results were compared in terms of the effective bending stiffness and the effective shear stiffness of the composite floor system, previously defined by Equations 7.1 and 7.2, respectively, and in terms of the bending stresses.

FINITE ELEMENT MODEL
To strengthen the validation of the analytical prediction model, the results were not only compared to experimental data but also to solutions obtained by finite element analysis. The finite element model is illustrated in Figure 9.3 and replicated the actual test conditions presented in Section 7.2. To limit the calculation time, the model was reduced to a quarter of its actual size by utilising the symmetry of the experimental set-up.

The prefabricated concrete floor element was modelled as a solid part using eight node brick elements with reduced integration (C3D8R) following a linear-elastic stress-strain relation with nominal Young's Modulus $E_{cm} = 33$ GPa [29]. The steel angle profiles were modelled as part of the prefabricated concrete deck. The tapered steel beam was modelled using four-node shell elements with reduced integration (S4R). The steel braces were modelled with 2-node linear beam elements (B31) and were *tied* to the steel beam. All steel elements had a linear relation between stresses and strains, with Young's Modulus $E = 210$ GPa. The mesh of the steel beam was such that the nodal stresses at exactly 5.0 m from the supports could be obtained, which is where the strain gauges were located during the experiments.

The discrete longitudinal shear connectors were modelled using mesh-independent, point-based fasteners with a linear spring stiffness k_{sc} that was kept constant durnig the simulation. Rigid springs prevented the vertical separation of the concrete slab and steel beam at the locations where either an injected or non-injected external bolt was present
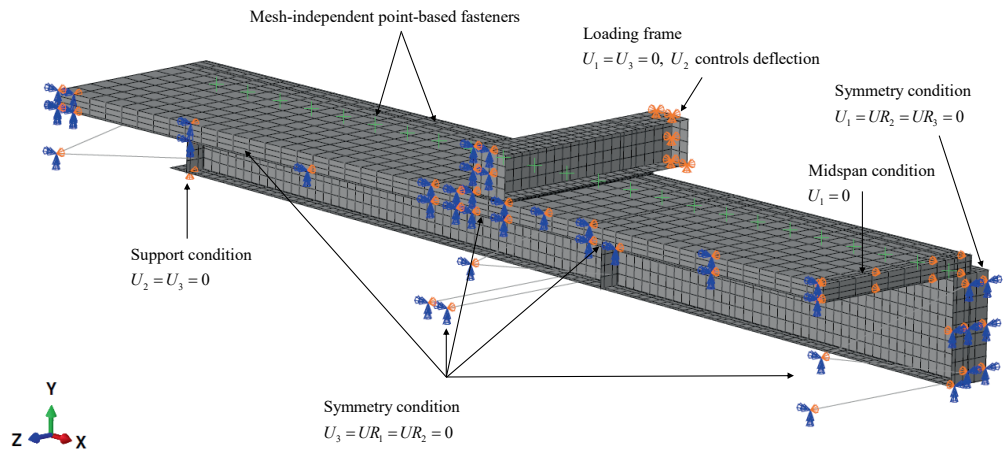
Figure 9.3 | Finite element model of the experimental composite floor system, including the point-based fasteners and the boundary and symmetry conditions.

conform Figure 7.12. Normal contact was defined as *hard* and tangential behaviour was assumed to be represented by a *penalty* formulation with a friction coefficient of 0.30.

ANALYTICAL MODEL

The experimental composite floor system was modelled using the analytical method presented in Section 9.1.1. The symmetry with respect to the plane at midspan was used to reduce the computational time. The floor system was subdivided into $J = 24$ segments to reflect the possible patterns of shear connectors in the experimental beam. The analytical model used the same elastic material properties as the finite element model.

RESULTS AND DISCUSSION

The shear connector stiffness was calibrated as $k_{sc} = 55$ kN/mm to match the analytical and numerical results to the experimentally obtained effective bending stiffness. Figure 9.4 demonstrates the good agreement between the models and experimental results in terms of the effective bending stiffness for all the considered shear connector arrangements. The numerical and analytical predictions closely match the experimental results regarding $k_{b,eff}$, with maximum deviations of +4.0% and -0.7%, and +3.7% and -5.1%, respectively. The average error in terms of the effective bending stiffness of the numerical and analytical predictions compared to the experimental results was +1.6% and +0.1%, respectively. Appendix I presents the deflection, slip, bending moment, normal stresses, normal force and shear force flow distributions along the length of the composite floor system according to the analytical model.

The calibrated magnitude of k_{sc} is 33% smaller than the magnitude presented in Chapter 5, where a secant connector stiffness at $0.4P_u$ of 82.1 kN/mm was determined based on finite element simulation of push-out specimens.[3] The discrepancy between shear connec-

---

[3]The calibrated finite element push-out model presented in Chapter 5 was modified to account for the leaked resin layer, see Figure 7.8, to check whether the partial contact between flange and angle profile could lead to substantially lower values of k_{sc} in the push-out tests. It was found that the difference was 2% and thus it was concluded that such an imperfection had negligible effects.
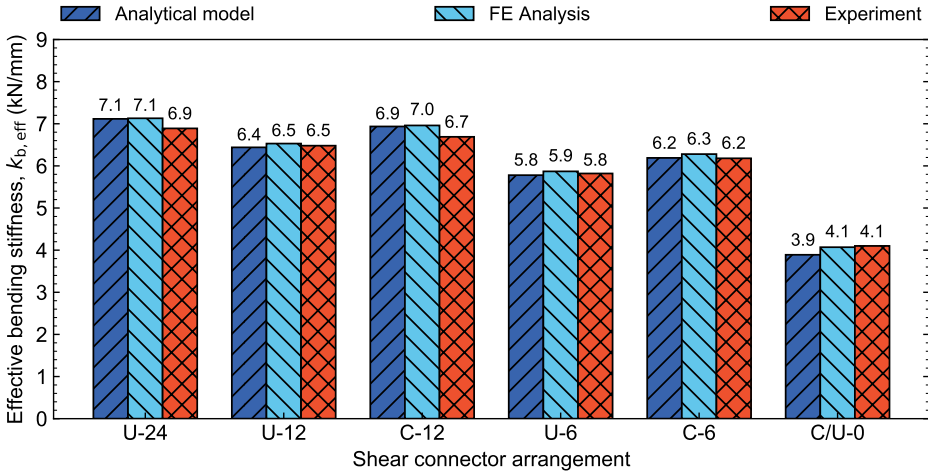
(a) Effective bending stiffness, $k_{b,eff}$(kN/mm).
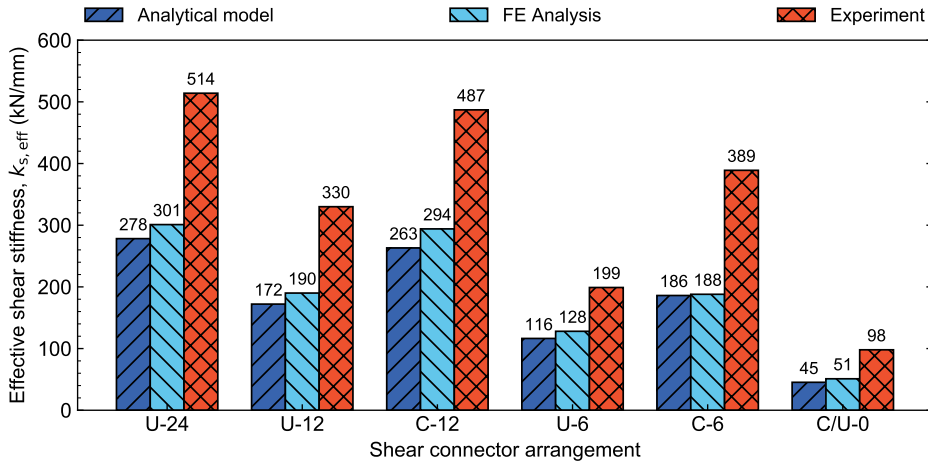
(b) Effective shear stiffness, $k_{s,eff}$ (kN/mm).

Figure 9.4 | Effective bending and shear stiffness for the different shear connector arrangements, according to the experiments and the numerical and analytical models.

tor stiffness observed in push-out tests and beam tests was also found by other authors. For example, Aribert [30] reported that the observed shear connector stiffness in beam experiments was 45% higher compared to push-out tests. According to Ernst et al. [31] good agreement in terms of shear connector stiffness between push-out and beam tests was found in their experiments, however, inspection of the published force-slip diagrams suggests that this match is more qualitative than quantitative, particularly because no relative differences were given, the diagrams were on a relatively coarse slip scale (0-12 mm), and no force-deflection curves were presented. The difference between the shear connector stiffness in push-out and beam tests was also observed by Mele [32], who stated that only beam experiments can give reliable information regarding the influence of slips on the defection. Aribert [30] expressed the same line of thought more strongly by stating "*any push-out testing procedure should be criticised thoroughly*" and "*in some cases of composite floors, push-out tests are unable to supply correct evaluation of the real connection behaviour in beams*". These statements and observations indicated that further research is necessary to determine the general suitability of push-out tests to predict the elastic response of composite floor systems.[4]

Large deviations between the models and experiments existed regarding the effective shear stiffness, see Figure 9.4b. On average, the actual effective shear stiffness was 48% smaller than predicted using the proposed analytical model. The proposed analytical model, however, showed better agreement with the finite element model with an average deviation of 9%. This indicated that the large deviation between analytical model and experimental results was likely related to the experiments and not to the present analytical model nor to the finite element analysis. This hypothesis is supported by previous observations in the literature: for example, Kamalanandan & Patnaikuni [34] and Lawson et al. [21] reported an underestimation of the slip (equivalent to an overestimation of the effective shear stiffness) although their models did accurately reproduce the experimentally obtained deflection. Leskelä [33] made a similar observation when modelling the beam experiments of Hanswille et al. [35]: also here the slip was underestimated although the prediction of the deflection was in good agreement with the experimental results. A similar agreement in terms of effective bending stiffness and disagreement in terms of effective shear stiffness can be found in the work of Kozma [36] and Gogoi [37]: the latter performed experiments on nominally identical (prismatic) composite beams, whilst only varying the condition (e.g. surface roughness) of the steel-concrete interface. The experimental load-deflection curves were almost identical for all beams, whereas the relation between applied load and end-slip differed significantly, which is in line with the findings presented in this dissertation. All the above suggests that the end slip is not readily defined for a given deflection, and thus that it cannot be considered as a representative measure. Further research is necessary to explain a seemingly complex relation between theoretically predicted and experimentally observed end-slips and their relation to the deflection.

Reasonably good agreement was observed between the analytically, numerically and experimentally obtained stresses at 5.0 m from the supports was observed for the composite floor system presented in Chapter 7. Figure 9.5 illustrates the longitudinal stresses over the height of the steel beam. The error of the finite element model in terms of tensile stresses

---

[4]Also differences between push-out and beam tests are observed in terms of the resistance, particularly for floor elements with trapezoidal sheeting. The reader is referred to Leskelä [33] (p. 80) for a literature overview focusing on the resistance discrepancies.

was between +1.1 MPa (1.6%) and +1.4 MPa (2.1%), and in compression the error was between -2.1 MPa (-10.6%) and +3.6 MPa (+12.9%) compared to the experimental results with shear interaction. The error of the analytical model in terms of tensile stresses was between +5.2 MPa (+7.6%) and +6.2 MPa (+8.9%), and in compression the error was between -0.3 MPa (-1.5%) and +5.4 MPa (+20%) compared to the experimental results with shear interaction. The finite element model predicted on average 8% lower compressive stresses and 6% lower tensile stresses than the analytical model. This discrepancy was attributed to the frictional effects at the beam-floor element interface taken into account in the FE model, reducing the bending stresses, which was confirmed by the observation that the largest errors for the analytical model to both the experimentally and numerically obtained results occurred for the case with no shear connection (C/U-0). The larger maximum relative errors for the compressive stresses are due to their limited magnitude: the steel beam is dominantly in tension due to the composite interaction, which causes any deviation of compressive stresses to be more pronounced in relative terms.

On the basis of the comparisons to the finite element and experimental results, it was concluded that the analytical model is suitable to predict the deflection and the stresses of composite floor systems consisting of web-tapered steel beams with non-uniformly distributed shear connectors.

9.1.3. COMPARISON TO SIMPLIFIED MODEL OF LAWSON ET AL.

The analytical model proposed in Section 9.1.1 has the ability to capture both effects related to varying geometry over the beam length and to non-uniform shear connection. This makes the model more versatile in its application, but also more exact compared to simplified models, such of that of Lawson et al. [21].

Lawson et al. [21] derived a simplified prediction model for the deflection of prismatic composite floor system with (quasi-)uniform shear connection. This model was based on approximating the slip curve by a cosine shape function, the reader is referred to the original publication for further details. In this section, results obtained by Lawson et al. [21] are compared to the solution according to the more refined model proposed in present work.

In the following subsections, five examples are presented which are based on the simplified model of Lawson et al. [21]. Four of these originate from their original publication, and the fifth originates from the work of Kozma [36]. The comparison is followed by a brief discussion and conclusion of the findings.

COMPARISON TO EXAMPLES PRESENTED BY LAWSON ET AL.

Lawson et al. [21] presented four examples for prismatic composite floor systems with spans $L = 6, 9, 12$, and 15 m. The corresponding steel sections were IPE270, IPE400, IPE500 and IPE600, respectively. The floor element was a 130 mm deep composite slab with a profiled sheeting height of 60 mm. The width of the floor elements was $L/4$. Single shear connectors with stiffness $k_{sc} = 70$ kN/mm were at 300 mm centre-to-centre. The Young's Modulus of the concrete was taken as 10% of that of the steel. The results have been normalised to correspond to a line load $q_z = 10$ kN/mm to facilitate easy comparison.
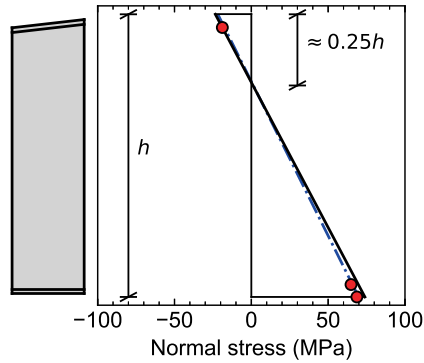
Tables 9.1 and 9.2 summarise the results in terms of midspan deflection and end slip as presented by Lawson et al. [21] and the corresponding solution according to the model proposed in this dissertation. In addition, Figure 9.6 illustrates the slip along the beam length based on both models.
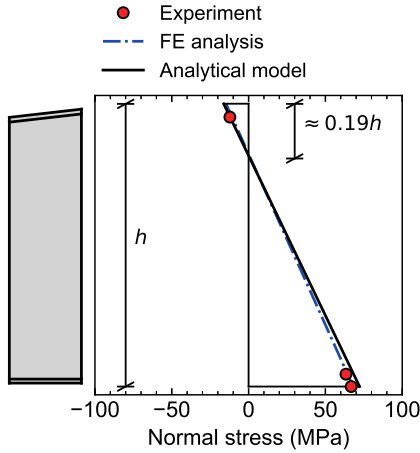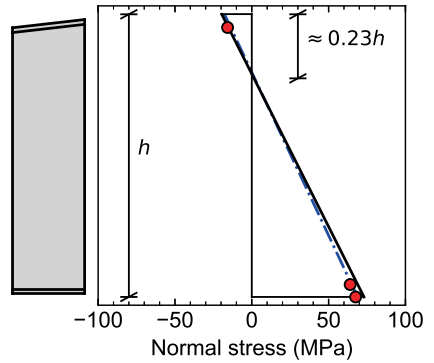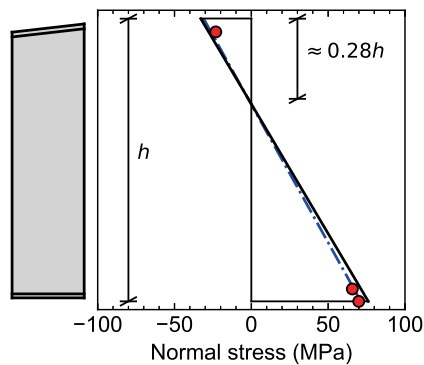
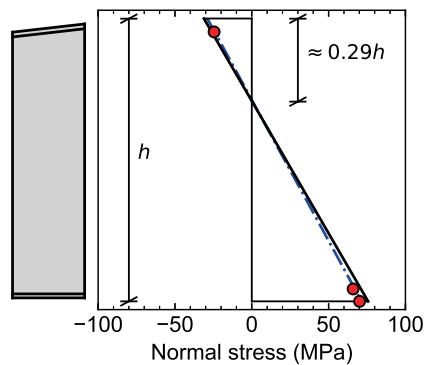**(a)** Arrangement U-24.
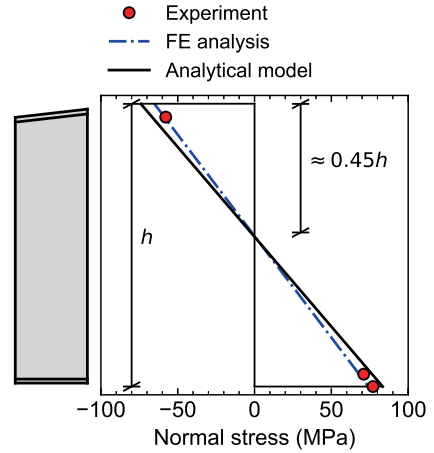
(b) Arrangement C/U-0.

(c) Arrangement U-12.

(d) Arrangement C-12.

(e) Arrangement U-6.

(f) Arrangement C-6.

Figure 9.5 | Normal stresses over the height of the steel beam for the cross-section at 5.0 m from the supports, inter- or extrapolated to nominal point loads $F = 100$ kN.

Table 9.1 | Midspan deflection(mm) for examples presented by Lawson et al. [21] for $q_z = 10$ kN/m.

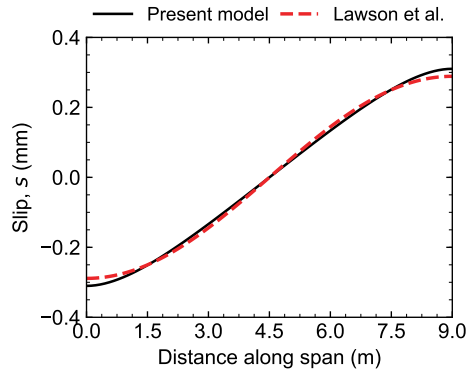| Beam size	Lawson et al. [21]	Present model	Lawson / Present
IPE270	5.14	5.15	0.998
IPE400	7.58	7.65	0.990
IPE500	11.30	11.77	0.960
IPE600	15.08	15.53	0.971

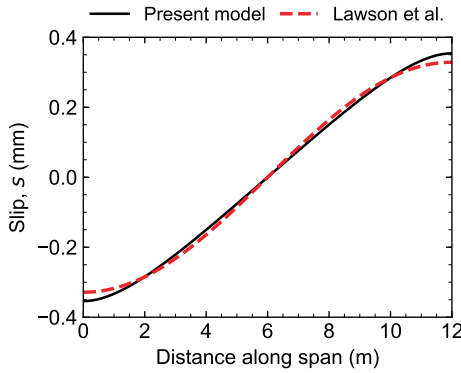**Table 9.2 |** End slip (mm) for examples presented by Lawson et al. [21] for $q_z = 10$ kN/m.

Beam size	Lawson et al. [21]	Present model	Lawson / Present
IPE270	0.26	0.29	0.897
IPE400	0.29	0.31	0.933
IPE500	0.33	0.35	0.930
IPE600	0.35	0.38	0.918
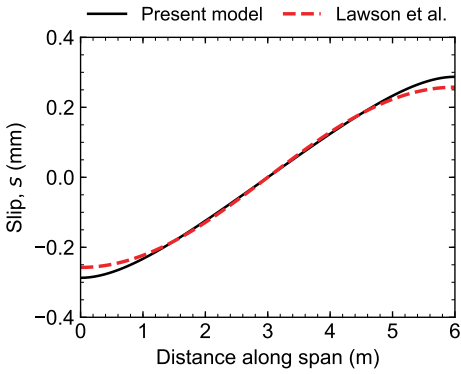
(a) Beam size IPE270, $L = 6$ m.

(b) Beam size IPE400, $L = 9$ m.

(c) Beam size IPE500, $L = 12$ m.
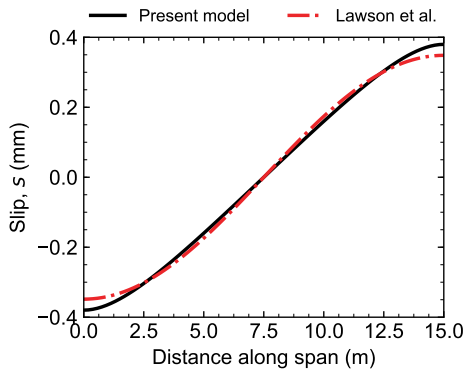
(d) Beam size IPE600, $L = 15$ m.

Figure 9.6 | Slip as a function of position along beam span for the composite floor system examples presented by Lawson et al. [21] for $q_z = 10$ kN/m.

COMPARISON TO EXAMPLE PRESENTED BY KOZMA

Kozma [36] presented one example for a prismatic composite floor system with span $L =$ 16.2 m and steel section IPE600. The solid floor element was 150 mm deep and 4050 mm wide. Pairs of shear connectors with stiffness $k_{sc} = 15.9$ kN/mm were at 600 mm centre-to-centre. The Young's Moduli of the steel and concrete were 210 GPa and 40.1 GPa, respectively. The results have been normalised to correspond to a line load $q_z = 10$ kN/mm.

The midspan deflection according to Kozma [36], who obtained his results based on the model of Lawson et al. [21], is 24.85 mm. This is 2% smaller than the 25.36 mm deflection based on the method proposed in present work. The end slips according to the simplified method and the present method were 1.16 mm and 1.27 mm, respectively, implying an underprediction of the simplified method of 8.7%. Figure 9.7 illustrates the slip along the beam length based on both models.
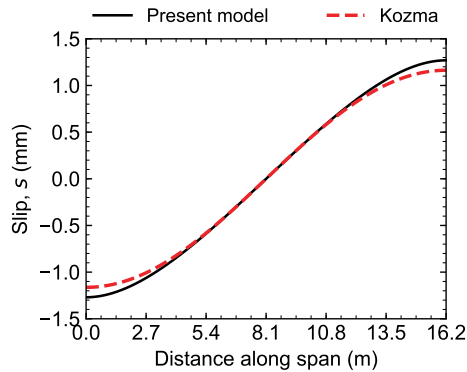

Figure 9.7 | Slip as a function of position along beam span for the composite floor system example presented by Kozma [36] for $q_z = 10$ kN/m.

DISCUSSION AND CONCLUSION

The results demonstrated that in all presented cases the simplified model of Lawson et al. [21] led to an underestimation of the deflection and the end slip. The deviation ranged between 0.2% to 2.9% for the deflection and between 8.2% and 10.3% for the slip. This indicated that there is a systematic error with the simplified method: Figures 9.6 and 9.7 suggest that the cosine shape function does not adequately represent the actual slip distribution. The simplified model is therefore regarded to be suitable for preliminary design only. It is not recommended to use the simplified method of Lawson et al. [21] for non-prismatic composite floor systems with non-uniform shear connection: in Chapter 10 it will be demonstrated that in such cases the slip distribution can no longer be approximated by a cosine shape function.

9.2. FUNDAMENTAL FREQUENCY

The fundamental frequency of a floor system is relevant to consider because it affects the perception of human comfort when the floor system is excited by for example pedestrian traffic. This section proposes a prediction model for the fundamental frequency of non-prismatic composite floor systems with non-uniform shear connection. First the well-known expression for the fundamental frequency of prismatic beams is presented, based on which a prediction model is proposed, which is validated against results obtained by finite element simulation.

9.2.1. PRISMATIC BEAMS

The well-known relation for the n-th eigenfrequency of a prismatic beam with a span L, a uniformly distributed mass m and constant bending stiffness EI is given by

$$f_n = \frac{K_n}{2\pi}\sqrt{\frac{EI}{mL^4}}, \tag{9.10}$$

where K_n is a constant depending on the boundary conditions. The most important observation of the previous equation is that $f_n \propto \sqrt{EI}$: the implications of this relation are illustrated using an example for two fictitious beams, denoted A and B. If the bending stiffness of beam A with n-th eigenfrequency $f_{n,A}$ is EI_A, and that the mass per unit length m and the span L of beams A and B are identical, it follows that the n-th eigenfrequency of beam B equals

$$f_{n,B} = f_{n,A}\sqrt{\frac{EI_B}{EI_A}}. \tag{9.11}$$

Therefore the fundamental frequency of prismatic beams with identical span and mass per unit length is proportional to the square root of the their bending stiffness.

9.2.2. HYPOTHESIS AND SOLUTION STRATEGY FOR NON-PRISMATIC COMPOSITE FLOOR SYSTEMS

For non-prismatic beams, Equation 9.11 cannot be used because EI is not constant along the beam length. However, the deflection $w(x)$ can be regarded as a proxy for the homogenised (or effective) bending stiffness of an equivalent prismatic beam. This relationship is used to develop a hypothesis to predict the eigenfrequency of web-tapered composite floor systems, symmetrical with respect to midspan.

HYPOTHESIS

It is given that a web-tapered composite floor system with rigid shear connection ($K \to \infty$) leads to a deflection at midspan $w_{m,\infty}$ under the its self-weight, and has eigenfrequencies $f_{n,\infty}$. The hypothesis is that the fundamental frequency of the same beam but with flexible shear connection can then be predicted by

$$f_{1,K} = f_{1,\infty}\sqrt{\frac{w_{m,\infty}}{w_{m,K}}}, \tag{9.12}$$

where $w_{\mathrm{m},K}$ is the deflection at midspan for the beam with flexible shear connection due to the self-weight, which can be determined using the method developed in Section 9.1[5]. The attention of the reader is drawn to the observation that only the first eigenfrequency (or fundamental frequency) is predictable using the proposed method: the shape of the assumed deflection curve and the shape of the eigenmodes do not match for $n > 1$.

EULER-BERNOULLI PARTIAL DIFFERENTIAL EQUATION FOR FREE VIBRATION

The rigid composite interaction reference case in Equation 9.12 enables the use of comparatively simple beam theory to determine $f_{1,\infty}$. The choice for Euler-Bernoulli beam theory is justified because no significant difference exists between lower order eigenfrequencies compared to Timoshenko beam theory, although for higher-order ($n > 10$) modes the effect of shear deformation cannot be neglected [38]. The rotational inertia is also disregarded because its influence on the lower eigenfrequencies is negligible for $n = 1$ [39].

The governing partial differential equation (PDE) for the free vibration of a prismatic Euler-Bernoulli beam is

$$EI_\infty \frac{\partial^4 w(x,t)}{\partial x^4} = m \frac{\partial^2 w(x,t)}{\partial t^2}. \tag{9.13}$$

Using the principle of separation of variables, an expression $w(x,t) = \widetilde{w}(x) \exp(i\omega_{1,\infty} t)$ is substituted in the PDE, resulting in a normal fourth-order differential equation in the form

$$\frac{\mathrm{d}^4 \widetilde{w}(x)}{\mathrm{d}x^4} - \zeta^4 \widetilde{w}(x), \tag{9.14}$$

where

$$\zeta^4 = \frac{m\omega_{1,\infty}^2}{EI_\infty}. \tag{9.15}$$

In the previous equation, $\omega_{1,\infty}$ is a trial solution for the angular eigenfrequency of the composite floor system with rigid shear connection. The angular eigenfrequency $\omega_{1,\infty}$ and the eigenfrequency $f_{1,\infty}$ are related to each other by $f_{1,\infty} = \omega_{1,\infty}/(2\pi)$.

The general solution to Equation 9.14 is given by

$$\widetilde{w}(x) = C_1 \sin(\zeta x) + C_2 \cos(\zeta x) + C_3 \sinh(\zeta x) + C_4 \cosh(\zeta x) \tag{9.16}$$

where C_i ($i = 1, 2 \ldots 4$) are integration constants that follow from the boundary conditions. It should be noted that this solution is only suitable for prismatic composite floor systems. In the following subsection, the theory introduced in the preceding is combined with a discretisation method to determine the eigenfrequencies of non-prismatic composite floor systems.

---

[5]It should be noted that, only in this case, the self-weight of the prefabricated concrete floor elements is assumed to be carried by composite interaction. In a real situation, no composite interaction exists during the assembly phase. However, the adopted definition of w_{m} in the current framework enables the prediction of the eigenfrequencies *after* assembly, i.e. in the use-phase.

DISCRETISING THE EULER BERNOULLI BEAM TO ANALYSE NON-PRISMATIC BEAMS

To account for the variation of the geometry along the length, the discretisation processed presented in Section 9.1.1 is used. The floor system is divided into J equally sized segments (see Figure 9.2), with the general solution to Equation 9.14 in the j-th ($1 \leq j \leq J$) segment given by

$$\widetilde{w}(x) = C_{1,j} \sin(\zeta_j x) + C_{2,j} \cos(\zeta_j x) + C_{3,j} \sinh(\zeta_j x) + C_{4,j} \cosh(\zeta_j x), \qquad (9.17)$$

where

$$\zeta_j^4 = \frac{m_j \omega_{1,\infty}^2}{EI_{\infty,j}} \qquad (9.18)$$

In Equation 9.17 $C_{i,j}$ ($i = 1,2\ldots4$, $j = 1..J$) are integration constants that follow from the boundary and interface conditions, and m_j is the average mass per unit length in segment j.

The corresponding bending moment and vertical shear force in the beam segments are given by

$$M_j = -EI_{\infty,j} \frac{\mathrm{d}^2 \widetilde{w}(x)}{\mathrm{d}x^2} \text{ and} \qquad (9.19)$$

$$V_j = \frac{\mathrm{d}M_j}{\mathrm{d}x}, \qquad (9.20)$$

respectively.

BOUNDARY AND INTERFACE CONDITIONS

The $4J$ integration constants ($C_{1,1}, C_{2,1} \ldots C_{3,J}, C_{4,J}$), resulting from the J segments in which Equation 9.17 is defined, can be solved by imposing boundary conditions at x_0 and x_J, and interface conditions at $x_1 \ldots x_{J-1}$. For a beam simply supported at $x_0 = 0$ and $x_J = L$, the four boundary conditions are $w_1(0) = w_J(L) = 0$ and $M_1(0) = M_J(L) = 0$. Other types of supporting conditions could be included by modifying the boundary conditions accordingly. The interface conditions are expressed as $\widetilde{w}_j(x_j) = \widetilde{w}_{j+1}(x_j)$, $\widetilde{w}'_j(x_j) = \widetilde{w}'_{j+1}(x_j)$, $M_j(x_j) = M_{j+1}(x_j)$ and $V_j(x_j) = V_{j+1}(x_j)$, where $'$ denotes the spatial derivative. It should be noted that the full beam must be modelled to find all eigenfrequencies and –modes: if symmetry conditions are used, only results corresponding to $n = 1,3,5\ldots$ can be found. For this method, which is focused solely on $n = 1$, the use of symmetry conditions is justified.

By inserting the boundary conditions into the general solutions, a system of $4J$ homogeneous equations is obtained. The system of equations can be written as $\mathbf{Ac} = 0$, where $\mathbf{c} = [C_{1,1}, C_{2,1} \ldots C_{3,J}, C_{4,J}]^\mathrm{T}$ and $\mathbf{A}$ is the coefficient matrix.

SOLUTION STRATEGY TO OBTAIN $f_{1,\infty}$ AND f_1

The solution to the system of equations is non-trivial only if the determinant of the coefficient matrix is zero, i.e. $\det(\mathbf{A}) = 0$, which is the case if the angular eigenfrequency $\omega_{1,\infty}$ was assumed correctly in Equation 9.18. In case $\det(\mathbf{A}) \neq 0$, another trial solution for $\omega_{1,\infty}$ must be adopted to find the angular eigenfrequency. Wu et al. [40] proposed to find the angular eigenfrequency by stepping through a sequence of small increments of $\omega_{1,\infty}$ and computing the sign for the determinant of $\mathbf{A}$. If the sign of the determinant of $\mathbf{A}$ changes,

an approximation for the angular eigenfrequency is obtained, which can be further refined using the bisection method. This strategy was implemented in present work.

After determining $\omega_{1,\infty}$ such that $\det(\mathbf{A}) = 0$, the eigenfrequency of the composite floor system with rigid shear connection can be determined by $f_{1,\infty} = \omega_{1,\infty}/(2\pi)$. The eigenfrequency for the composite floor system with flexible shear connection can then be determined using the proposed expression in Equation 9.12.

9.2.3. NUMERICAL VALIDATION OF PREDICTION MODEL

VALIDATION FOR PRISMATIC COMPOSITE FLOOR SYSTEMS

The fundamental eigenfrequency of a prismatic composite floor system according to the hypothesised expression, Equation 9.12, is compared against results of Xu & Wu [39], which were obtained using the method of Wu et al. [40]. The latter derived that the natural frequency of a prismatic composite floor system, with uniformly distributed flexible shear connection and without an external axial force, is given by the equation

$$f_n^2 = \left(1 - \frac{\beta^2 - 1}{\beta^2 + \dfrac{\alpha^2}{\xi^2}} \right) f_{n,\infty}^2, \tag{9.21}$$

where $\xi = n\pi/L$, $\beta^2 = EI_\infty/EI_0$, and where $f_{n,\infty}^2$ is the n-th eigenfrequency of the composite floor system with rigid shear connection ($K \rightarrow \infty$), which can be determined by Equation 9.10 with $K_1 = 9.87$. The parameter α^2 reflects the influence of the uniformly distributed shear connection, and has been defined in Equation 9.2.

Xu & Wu [39] presented results for the fundamental frequency of the four meter span simply supported composite floor system illustrated in Figure 9.8, which is characterised by $EI_0 = 1.5 \times 10^6$ Nm^2, $EI_\infty = 1.5 \times 10^6$ Nm^2, $\beta^2 = 4$ and $m = 39.75$ kg/m. Parameter α^2, reflecting the influence of the shear connection, was varied between 10^{-3} and 10^3 m^{-2}.

The results obtained from the literature are illustrated in Figure 9.8 together with the fundamental frequencies according to Equation 9.12. Excellent agreement between the two methods is found for a wide range of α^2, which demonstrates that the proposed equation is suitable to be used for prismatic composite floor systems.

VALIDATION FOR NON-PRISMATIC COMPOSITE FLOOR SYSTEMS

To the author's knowledge, no results for the fundamental frequencies of non-prismatic composite floor systems have ever been published. Therefore, the proposed expression, represented by Equation 9.12, is validated against results obtained using the commercial finite element package ABAQUS.

The first eigenfrequency of the web-tapered composite floor system presented in Section 7.2 is determined for the shear connector arrangements U-24, U-12, U-6, C-12, C-6 and C/U-0 (illustrated in Figure 7.12). Three different magnitudes of the shear connector stiffness k_{sc} (25, 55 and 100 kN/mm) were considered. In this analysis, the composite beam was regarded as part of a larger structure and therefore the representative part of the composite floor system effectively consisted of one web-tapered steel beam and two prefabricated concrete floor elements, see Figure 9.9.

A sensitivity study was carried out to determine the minimum number of beam segments per half-span (J) that were necessary to be modelled, such that the first eigenfre-
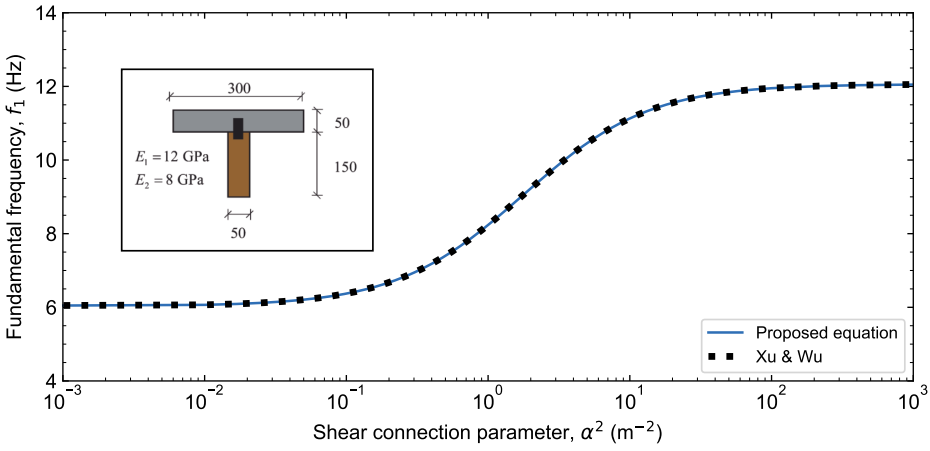
Figure 9.8 | Simply supported prismatic composite beam ($L = 4$ m) studied by Xu & Wu [39] and comparison of the results in terms of the fundamental frequency f_1 over a wide range of α^2. Dimensions in mm.
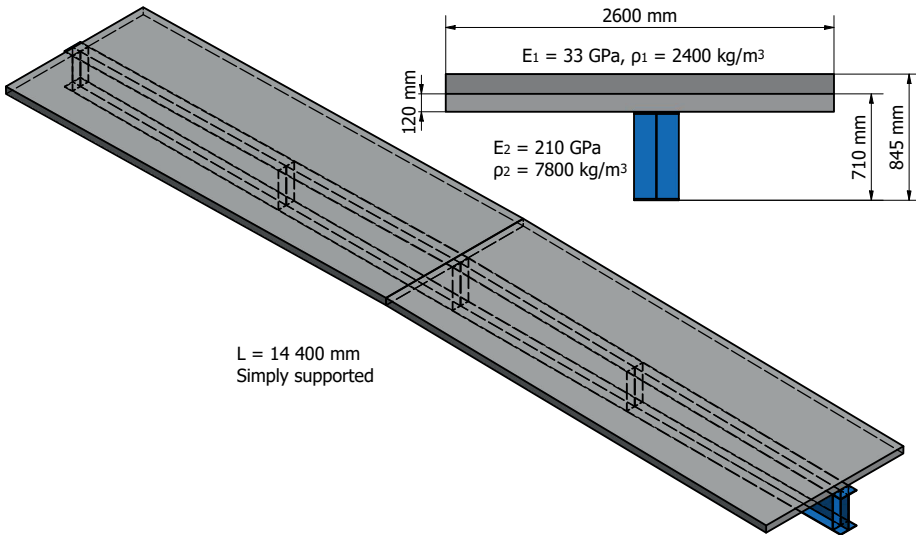

Figure 9.9 | Overview of the repetitive representative part of the web-tapered composite floor system used for validation of Equation 9.12. Pairs of shear connectors connect the steel beam to the concrete floor elements, the shear connector arrangements are presented in Section 7.2.

quency based on J segments converged to the value obtained for $J \to \infty$. This analysis was performed under the assumption of a uniformly distributed load q and a uniformly distributed shear connection with $K = 367$ kN/mm^2, equivalent to shear connector arrangement U-24 with $k_{sc} = 55$ kN/mm and $c_{sc} = 300$ mm. The results of the sensitivity study demonstrated that for $J \geq 3$ the convergence error in terms of the first eigenfrequency is smaller than 1%. It was therefore considered to be appropriate to subdivide the beam into $J = 24$ segments per half-span to match the segmentation used in Section 7.2.

The simply supported composite beam was modelled in `ABAQUS/Standard` using four-node shell elements (S4) for the tapered steel beam and concrete floor elements. The shear connectors were modelled using mesh-independent, point-based fasteners with a spring stiffness k_{sc}.

The results obtained using the analytical and numerical models are presented in Table 9.3. On average, the first eigenfrequency obtained by the proposed analytical model was 0.3% lower than predicted by the finite element model, and $R^2 = 0.973$, which implies that the proposed equation accounts for 97.3% of the observed variation. The fundamental frequency is slightly underestimated (up to 4.3%) in case of a compliant shear connection and slightly overestimated (up to 3.1%) in case of a stiff shear connection. The proposed analytical model is therefore considered suitable to predict the first eigenfrequency of web-tapered composite floor systems with non-uniform shear connector arrangements, with sufficient accuracy for engineering applications.

9.3. LATERAL-TORSIONAL BUCKLING

During execution, global instability modes may arise in laterally unrestrained steel beams. At a critical load, the compression flange tends to buckle out-of-plane, while the tension flange attempts to maintain the laterally undeformed state of the beam. This causes lateral bending and rotation of the cross-section. This instability phenomenon is known as *lateral-torsional* or *flexural-torsional buckling*, and was first theoretically analysed by Prandtl [41] and Michell [42].

The lateral-torsional buckling resistance of a steel beam does not only depend on its cross-sectional properties and support conditions, but also on the detailing of the floor system. Snijder et al. [43] observed that lateral-torsional buckling was prevented by a monolithic concrete floor without mechanical connection to the steel beam, except for a rubber strip ($t = 20$ mm) at the steel-concrete interface. The prevention of lateral-torsional buckling was attributed to the partially restrained rotation of the cross-section [43, 44] due to the rigidity of the floor element.

The rotation constraint is caused by a shift of the point of load application from the centre to the tip of the flange, which the only point of contact with the monolithic concrete floor. For a demountable composite floor system, characterised by large discontinuous prefabricated concrete elements, no rotation constraint emerges. The prefabricated floor elements are supported by only one side of the compression flange. The absence of a prefabricated floor element on the other side of the compression flange implies that the cross-section is free to rotate, see Figure 9.10. The lateral displacement of the compression flange is unrestrained because the shear connectors have not been installed yet. De-

Table 9.3 | Fundamental frequencies of the tapered composite beam based on Equation 9.12 and according to finite element analysis. The geometry and shear connector arrangements can be found in Section 7.2.

Arrangement	$f_{1,\infty,\text{FEA}}$ (Hz)	$f_{1,\infty,\text{Eq. 9.12}}$ (Hz)	k_{sc} (kN/mm)	$w_{\text{m},\infty}/w_{\text{m}}$ (-)	$f_{1,\text{Eq. 9.12}}$ (Hz)	$f_{1,\text{FEA}}$ (Hz)	$f_{1,\text{Eq. 9.12}}/f_{1,\text{FEA}}$ (-)
			25	0.820	4.99	5.00	0.998
U-24			55	0.902	5.23	5.17	1.012
			100	0.941	5.34	5.25	1.017
			25	0.786	4.88	4.92	0.992
C-12			55	0.871	5.14	5.10	1.007
			100	0.917	5.27	5.20	1.031
			25	0.695	4.59	4.71	0.975
C-6			55	0.785	4.88	4.89	0.997
			100	0.836	5.03	5.00	1.007
	5.39	5.51	25	0.730	4.71	4.81	0.978
U-12			55	0.836	5.04	5.02	1.002
			100	0.897	5.22	5.15	1.013
			25	0.642	4.41	4.61	0.957
U-6			55	0.755	4.78	4.85	0.987
			100	0.832	5.02	5.00	1.004
C/U-0			0	0.439	3.65	3.67	0.995
Average			-	-	-	-	0.997

9

mountable steel-concrete composite floor systems with discontinuous floor elements are therefore sensitive to lateral-torsional buckling.[6]

This section presents a prediction model for the critical bending moment, which can be used to determine the resistance against lateral-torsional buckling. The distinguishing feature of the prediction model is that it focuses on web-tapered steel beams with monosymmetrical cross-sections - rather than on standard hot-rolled sections. The prediction model is validated against results extracted from the literature and it is explained how the proposed model integrates with the existing EN 1993-1-1 [14] design verification for combined in-plane and out-of-plane resistance of non-prismatic beams.

9.3.1. COORDINATE SYSTEMS AND CONVENTIONS

The coordinate systems and cross-sectional dimensions for a monosymmetrical I-shaped cross-section are illustrated in Figure 9.11. The $y - z$ coordinate system is used to define the cross-sectional properties with respect to the elastic neutral axis for bending around the strong y axis, while the $v - w$ coordinate system is adopted to describe the out-of-plane and in-plane deflections. Th x-axis is perpendicular to the yz-plane and parallel to the beam span. The cross-sectional dimensions are denoted by b (width), t (thickness) and h (height); the subscripts "f" and "w" refer to the flange and web, respectively. Distinction between the top and bottom flanges is made by the subscripts "t" and "b", respectively. The total cross-sectional area is denoted by A.

The cross-sectional parameters (i.e. area, area moment of inertia, torsion rigidity and warping rigidity) depend on the slope α_{w} of the web and are proportional to $\cos(\alpha_{\mathrm{w}})^3$ [45]. The effects of the web-tapering on these cross-sectional parameters are not included in present work because the error for practical web slopes ($\alpha_{\mathrm{w}} < 10\%$) is limited (<1.5%).

ELASTIC NEUTRAL AXIS, SHEAR CENTRE, AND TWIST CENTRE

The steel beam is assumed to be symmetrical in the xz-plane and to be subject to loads in positive z-direction. Hence, the beam is subject to uniaxial bending around its strong y-axis prior to the onset of lateral-torsional buckling, with compressive stresses developing above the elastic neutral axis. The y-axis coincides with the elastic neutral axis, and is located at an absolute distance

$$\overline{z}_{\mathrm{c}} = \frac{b_{\mathrm{f,t}} t_{\mathrm{f,t}} \left(\frac{t_{\mathrm{f,t}}}{2}\right) + h_{\mathrm{w}} t_{\mathrm{w}} \left(t_{\mathrm{f,t}} + \frac{h_{\mathrm{w}}}{2}\right) + b_{\mathrm{f,b}} t_{\mathrm{f,b}} \left(t_{\mathrm{f,t}} + h_{\mathrm{w}} + \frac{t_{\mathrm{f,b}}}{2}\right)}{A}, \tag{9.22}$$

from the outer compressive fibre.

Upon reaching a critical load, the cross-section starts to deflect in v-direction and rotates around its twist centre (TC), which has been proven to coincide with the shear centre (SC) [46, 47]. The ordinate of the twist and shear centre is given by

$$z_{\mathrm{s}} = \frac{I_{z,\mathrm{b}}}{I_{z,\mathrm{t}} + I_{z,\mathrm{t}}} \left(h - \frac{t_{\mathrm{f,t}}}{2} - \frac{t_{\mathrm{f,b}}}{2}\right) + \frac{t_{\mathrm{f,t}}}{2} - \overline{z}_{\mathrm{c}}, \tag{9.23}$$

---

[6]It should be noted that lateral-torsional buckling is only critical during execution; in the persistent design situation the beam is laterally supported by the concrete floor elements through the demountable shear connectors. Also it should be noted that once only one floor element is in place during (dis)assembly, the beam is also subject to torsion because of the eccentricity of the (reduced) self-weight with respect to the beam web. The latter phenomenon is not further addressed in this dissertation.
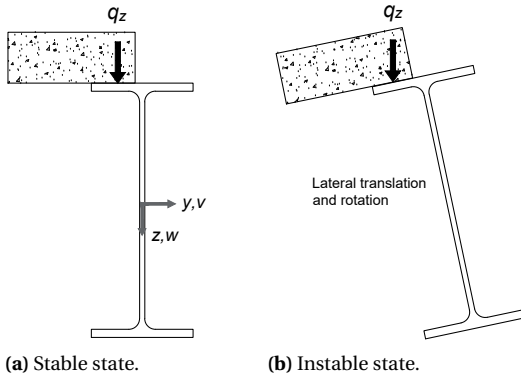
(a) Stable state.   **(b)** Instable state.

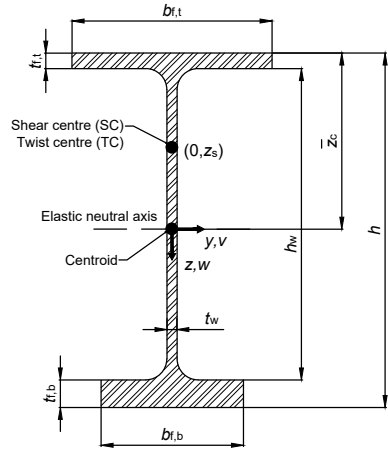**Figure 9.10 |** Lateral-torsional buckling of a steel beam loaded by a prefabricated concrete floor element.

Figure 9.11 | Axes convention and dimensional parameters for a monosymmetrical I-shaped cross-section.

where $I_{z,\mathrm{b}}$ and $I_{z,\mathrm{t}}$ denote the area moment of inertia around the z-axis of the bottom and top flanges, respectively. The abscissa of the twist and shear centres is at $y_\mathrm{c} = 0$.

9.3.2. SOLUTION STRATEGY AND APPROACH

Lateral-torsional buckling can be analysed analytically using equilibrium, energy, and numerical methods [48], although the energy method is most commonly used. The Energy Method is based on the (linear) strain energy of the beam and the work done by the external loads, which are used to evaluate the critical load based on an instability criterion. This method has been used for bisymmetrical cross-sections [e.g. in 45, 49], for prismatic monosymmetrical cross-sections [e.g. in 50–52], and for web-tapered monosymmetrical cross-sections [e.g. in 53–56], and solved using solution strategies based on the finite element method, finite difference method and Rayleigh-Ritz method.

The Rayleigh-Ritz method is based on the assumption that the unknown deformation functions can be approximated by a linear combination of a number of independent assumed linear functions. These independent functions must satisfy the boundary conditions and any intermediate restraints.

The model derived in this chapter combines the Energy Method approach for web-tapered bisymmetrical cross-sections, augmenting it with the effects of monosymmetry and solving it using the Rayleigh-Ritz method. A similar approach was used by Asgarian et al. [54], but in present work trigonometric instead of power series are used and the opportunities for design optimisation are extensively discussed. The output of the proposed model is the critical bending moment, which is the lateral-torsional buckling resistance in absence of any geometrical and material imperfections. The effects of imperfections are included in Section 9.3.6 through the EN 1993-1-1 [14] design verification for lateral-torsional buckling.

9

9.3.3. STRAIN ENERGY AND VIRTUAL WORK

The prediction of the critical bending moment using the Energy Method requires the determination of the internal strain energy and the virtual work generated by the loads. Relevant contributions to the strain energy originate from [45, 52–56]:

   i. Normal stresses due to lateral bending around the z-axis

   ii. Shear stresses due to uniform torsion

   iii. Normal stresses due to warping (non-uniform) torsion

The strain energy contributions are superimposed to determine the total internal strain energy U. The effects of the pre-buckling deflection along the w-axis are not included in the analysis, because their effects are negligible for typical beam designs ($h/b > 2$) [57, 58]. The individual contributions to the internal strain energy are introduced separately in the following subsections.

STRAIN ENERGY DUE TO LATERAL BENDING

Lateral bending (i.e. in v-direction) induces compressive and tensile stresses in the flanges and web. It is assumed that the end of an infinitesimal beam segment with length dx rotates relative to its other end by a small angle dθ around the z-axis. This rotation is accompanied by a bending moment

$$M_z = EI_z \frac{\mathrm{d}\theta}{\mathrm{d}x}, \tag{9.24}$$

where EI_z denotes the bending stiffness of the steel beam around the weaker z-axis. The corresponding virtual work of magnitude $\mathrm{d}U = 0.5 M_z \mathrm{d}\theta$ is stored as strain energy in the beam segment, which can be simplified to

$$\mathrm{d}U = \frac{1}{2} \frac{M_z^2}{EI_z} \mathrm{d}x. \tag{9.25}$$

This can be rewritten in terms of lateral deflection and integrated over the beam length to obtain the total strain energy due to lateral bending, given by

$$U_{\mathrm{bending},z} = \frac{1}{2} \int_0^L EI_z \left(\frac{\mathrm{d}^2 v}{\mathrm{d}x^2} \right)^2 \mathrm{d}x. \tag{9.26}$$

STRAIN ENERGY DUE TO UNIFORM TORSION

Shear stresses τ_{yz} develop as a result of uniform torsion. It is assumed that the end of an infinitesimal beam segment with length dx rotates relative to its other end by a small angle dφ. This rotation is accompanied by a torque

$$T = GJ_{\mathrm{eff}} \frac{\mathrm{d}\varphi}{\mathrm{d}x}, \tag{9.27}$$

where GJ_{eff} denotes the effective torsional rigidity, defined as the sum of the torsional rigidity GJ and the Wagner torsional rigidity β_y. The virtual work of magnitude $\mathrm{d}U = 0.5 T\varphi$ is stored as strain energy in the beam segment, which can be simplified to

$$dU = \frac{1}{2}\frac{T^2}{GJ_{\text{eff}}}\,dx. \tag{9.28}$$

This can be rewritten in terms of the cross-sectional rotation and integrated over the beam length to obtain the total strain energy due to uniform torsion, given by

$$U_{\text{uniform torsion}} = \frac{1}{2}\int_0^L GJ_{\text{eff}}\left(\frac{d^2\varphi}{dx^2}\right)^2 dx. \tag{9.29}$$

Torsional rigidity The torsional rigidity is the product of the shear modulus G and the torsional constant J, the latter being defined as

$$J = \xi_{\text{f,t}}b_{\text{f,t}}t_{\text{f,t}}^3 + \xi_{\text{w}}h_{\text{w}}t_{\text{w}}^3 + \xi_{\text{f,b}}b_{\text{f,b}}t_{\text{f,b}}^3, \tag{9.30}$$

where ξ is a correction factor depending on the aspect ratio of the flange or web. For thin-walled parts ($b/t > 10$) ξ may be taken as $1/3$. For hot-rolled sections, the web-flange transition may further contribute to the torsional rigidity of the cross-section.

Wagner torsional rigidity The Wagner torsional rigidity β_y originates from compressive and tensile bending stresses which form a resulting torque in case of monosymmetrical cross-sections.

The Wagner torsional rigidity has a significant influence on the critical bending moment; its effect was first recognised in the 1960s by Timoshenko & Gere [59], Vlasov [60] and Galambos [61]. The expression for the Wagner torsional rigidity,

$$\beta_y = \frac{M_y}{I_y}\left(\int_A y^2 z\,dA + \int_A z^3\,dA\right) + 2z_{\text{s}}, \tag{9.31}$$

is often included in the modern literature, without identifying its true source. Its derivation is included in present work, see Appendix J, to illustrate the background to the potential benefits in terms of the critical bending moment for a given cross-sectional area.

STRAIN ENERGY DUE TO WARPING TORSION
Zhang & Tong [45] derived the linear strain energy related to warping torsion of a web-tapered I beam undergoing lateral torsional buckling as

$$U_{\text{warping torsion}} = \frac{1}{2}\int_0^L\left[EI_\omega\left(\frac{d^2\varphi}{dx^2}\right)^2 + 2\frac{d^2 EI_\omega}{dx^2}\left(\frac{d\varphi}{dx}\right)^2 + 2\frac{dEI_\omega}{dx}\frac{d\varphi}{dx}\frac{d^2\varphi}{dx^2}\right]dx. \tag{9.32}$$

The latter two terms represent the effects originating from the non-prismatic (tapered) geometry of the beam. The warping rigidity I_ω is expressed as

$$I_\omega = \frac{I_{z,\text{b}}I_{z,\text{t}}}{I_{z,\text{b}} + I_{z,\text{t}}}\left(h - \frac{t_{\text{f,t}}}{2} - \frac{t_{\text{f,b}}}{2}\right)^2, \tag{9.33}$$

where $I_{z,\text{b}}$ and $I_{z,\text{t}}$ denote the area moment of inertia around the z-axis of the bottom and top flanges, respectively.

VIRTUAL WORK BY THE LOADS

Possible loads in z-direction include uniformly distributed loads q_z and concentrated loads P_z, which are applied in the cross-sectional plane of symmetry at ordinates z_q and z_P, respectively.

The vertical displacement of the external loads due to the rotation of the cross-section generates virtual work. The loads and vertical displacement act in the same direction if the loads are applied above the shear centre. This leads to positive virtual work, reducing the critical lateral-torsional buckling load. Applying the loads below the level of the shear centre increases the critical lateral-torsional buckling load. Additional virtual work is generated by the bending moment M_y, resulting from q_z and P_z, because the rotation φ of the cross-section of the beam generates a torque component φM_y.

The total virtual work done by the loads is expressed by[7]

$$V = \int_0^L \left[\varphi M_y \frac{\mathrm{d}^2 v}{\mathrm{d}x^2} - \frac{1}{2} q_z \left(z_\mathrm{s} - z_\mathrm{q} \right) \varphi^2 \right] \mathrm{d}x - \frac{1}{2} \sum P_z \left(z_\mathrm{s} - z_\mathrm{P} \right) \varphi \big|_{x=x_P}^2. \qquad (9.34)$$

9.3.4. EQUILIBRIUM CONDITION AND RAYLEIGH-RITZ FUNCTIONS

By the principle of conservation of energy, the total work done by the loads must be balanced by the internal strain energy. The total potential energy Π of the beam equals

$$\Pi = U - V. \qquad (9.35)$$

The conservative elastic system is in a state of stable equilibrium if, and only if, the value of the potential energy is a relative minimum. This means that the onset of lateral-torsional buckling is characterised by a stationary condition of the total energy function, such that the derivative of Equation 9.35 must be zero.

The deformation functions $v(x)$ and $\varphi(x)$ in the equations of Section 9.3.3 are yet unknown, but are necessary to evaluate the stationary condition of the total energy function. The lateral-torsional eigenmodes of the beam can be approximated by the Rayleigh-Ritz method. This method is based on the assumption that the deformation functions can be approximated by a linear combination of a number of independent linear functions. The independent functions must satisfy the boundary conditions and any intermediate restraints.

For a simply-supported beam without any intermediate lateral restraints, the lateral deflection $v(x)$ can be approximated by the function [53]

$$v = \sum_{m=1}^{n} c_{v,m} \sin\left(m \frac{\pi x}{L} \right), \qquad (9.36)$$

where $c_{v,m}$ is a weighing factor of lateral deflection mode m. Similarly, the rotation field $\varphi(x)$ of a simply-supported beam with fork supports (restraining motion along the y-axis and rotation around the x-axis) can be approximated by

$$\varphi = \sum_{m=1}^{n} c_{\varphi,m} \sin\left(m \frac{\pi x}{L} \right). \qquad (9.37)$$

These assumed lateral deflection and rotation fields discretise the problem in $2(n - m + 1)$ degrees of freedom. In case other supports or restraints are present, the two functions must

---

[7]The reader is referred to Vesko [62] for an extensive derivation.

be modified accordingly. For example, $m = 2$ for a simply-supported beam with a lateral and torsional restraint at mid-span.

The number of modes n must (i) be as small as possible to minimise the computational time and (ii) be as large as required to obtain satisfactory results. The number of modes n can be determined based on a sensitivity study; the results obtained with n modes must convergence to the result for $n \rightarrow \infty$ modes.

The assumed expressions for the lateral deflection and the cross-sectional rotation are substituted in the total potential energy function given by Equation 9.35. The onset of lateral-torsional buckling is characterised by a stationary condition of the total energy function, implying that

$$\frac{\partial \Pi}{\partial c_{v,m}} = \frac{\partial \Pi}{\partial c_{\varphi,m}} = 0. \tag{9.38}$$

These conditions imply a local minimum for the potential energy function for each of the degrees of freedom, and lead to a linear system of $2(n - m + 1)$ equations with equally many unknowns. This system of equations can be represented in matrix form as $\mathbf{Ac} = 0$, where $\mathbf{c}$ is a column vector containing all variables and $\mathbf{A}$ is the coefficient matrix, which contains the unknown critical load $q_{z,\mathrm{cr}}$ and/or $P_{z,\mathrm{cr}}$. Non-trivial solutions only exist for $\det(\mathbf{A}) = 0$. Solving this equation gives the eigenvalues of the coefficient matrix. The critical load can be determined by multiplying the magnitude of the imposed loads q_z and/or P_z by the smallest positive eigenvalue; the larger eigenvalues represent higher-order lateral-torsional buckling modes.

9.3.5. VALIDATION OF PREDICTION MODEL
The method outlined above is validated by comparing its results against outcomes reported in literature. The work of Andrade et al. [53] and Asgarian et al. [54] was selected for the validation of the prediction model.

ANDRADE ET AL. [53]
Andrade et al. [53] investigated the lateral-torsional buckling of simply-supported bisymmetrical web-tapered beams subject to concentrated loads P_z at midspan using the finite element method. The span ranged from $L = 6$ - 12 m and the beams were symmetric with respect to the yz-plane at midspan. The external load was either applied on the top flange ($z_P = -\overline{z}_c$) or at the shear centre ($z_P = z_s$).

The tapering of the web was introduced through parameter α, indicating the relative beam height at the support $h_{\min}$ compared to the larger beam height at midspan $h_{\max}$. The cross-section considered had the following dimensional properties: $h_{\max} = 600$ mm, $h_{\min} = \alpha h_{\max}$, $b_{\mathrm{f,t}} = b_{\mathrm{f,b}} = 150$ mm, $t_{\mathrm{f,t}} = t_{\mathrm{f,b}} = 12.7$ mm, and $t_{\mathrm{w}} = 9.5$ mm.

The results of the proposed method are compared to the finite element results reported by Andrade et al. [53] in terms of the critical bending moment $M_{\mathrm{cr}} = 0.25P_{z,\mathrm{cr}}$. The number of Rayleigh-Ritz modes $n = 7$ was based on a sensitivity study. The critical bending moments are presented in Table 9.4. Good agreement between the analytical and finite element modelling strategies was observed, particularly for longer span beams. Substantial tapering and short beam spans led to slightly larger differences, which Andrade et al. [53] attributed to web distortion and compression flange distortion. The former is characterised by lateral bending of the web, the latter by in-plane bending of the compression flange and the associated non-perpendicularity of the flange with respect to the web.

9

Table 9.4 | Comparison between results obtained using present method and finite element results by Andrade et al. [53].

L (m)	α (-)	Load on top flange			Load at shear centre		
		M_{cr} (kNm)		Deviation (%)	M_{cr} (kNm)		Deviation (%)
		Present method	Andrade et al. [53]		Present method	Andrade et al. [53]	
	0.6	108.1	103.8	+4.14	176.8	168.5	+4.90
6	0.8	124.8	124.9	-0.08	196.7	190.1	+3.47
	1.0	147.8	149.0	-0.74	223.3	211.9	+5.40
	0.6	56.33	56.25	+0.14	76.06	75.96	+0.13
12	0.8	60.10	60.60	-0.83	80.30	80.61	-0.38
	1.0	65.06	65.76	-1.06	85.76	86.01	-0.29

ASGARIAN ET AL. [54]

Asgarian et al. [54] investigated the lateral-torsional buckling of simply-supported mono- and bisymmetrical tapered beams subject to uniformly distributed loads q_z using the finite element method. The span ranged from L = 6 - 10 m and the beams were symmetric with respect to the yz-plane at midspan. The external load was either applied on the top flange ($z_P = -\overline{z}_c$) or at the shear centre ($z_P = z_s$).

The tapering of the web was introduced through parameter α, indicating the relative beam height at the support h_{min} compared to the larger beam height at midspan h_{max}. The monosymmetrical cross-section considered had the following dimensional properties: h_{max} = 300 mm, $h_{min} = \alpha h_{max}$, $b_{f,t}$ = 150 mm, $b_{f,b}$ = 75 mm, $t_{f,t} = t_{f,b}$ = 10.7 mm, and t_w = 7.1 mm. For the bisymmetrical cross-section the same dimensions applied, but in this case $b_{f,t} = b_{f,b}$ = 150 mm.

The results of the proposed method are compared to the finite element results reported by Asgiarian et al. [54] in terms of the critical bending moment $M_{cr} = 0.125 q_{z,cr} L^2$. The number of Rayleigh-Ritz modes n = 7 was based on a sensitivity study. The critical bending moments are presented in Table 9.5. Good agreement between the analytical and finite element modelling strategies is observed, again the deviations were larger for more pronounced tapering ratios and shorter beam spans because of the reasons previously mentioned.

9.3.6. INTEGRATION OF THE PREDICTION METHOD IN THE EN 1993-1-1 DESIGN VERIFICATION

EN 1993-1-1 [14] contains a generic method that should be applied to determine the lateral torsional buckling design resistance of non-prismatic members. It must be verified that

$$\frac{\chi_{op} \alpha_{ult,k}}{\gamma_{M1}} \geq 1.0, \tag{9.39}$$

where χ_{op} is a reduction factor related to lateral torsional buckling and $\alpha_{ult,k}$ is the minimum load amplifier of the design loads such that the characteristic in-plane resistance of the cross section is attained.

A load amplification factor $\alpha_{cr,op}$ is introduced, which is the ratio of the critical bending moment M_{cr} over the design bending moment $M_{y,Rd}$. According to the Dutch National

Table 9.5 | Comparison between results obtained using present method and finite element results by Asgarian et al. [54].

(a) Monosymmetrical cross-section

L (m)	α (-)	Load on top flange			Load at shear centre		
		M_{cr} (kNm)		Deviation (%)	M_{cr} (kNm)		Deviation (%)
		Present method	Asgarian et al. [54]		Present method	Asgarian et al. [54]	
	0.6	55.11	54.01	+2.04	58.98	60.23	-2.08
6	0.8	58.53	57.14	+2.43	62.72	65.85	-4.75
	1.0	62.68	62.73	-0.08	67.17	66.23	+1.42
	0.6	39.94	41.06	-2.73	42.06	43.37	-3.02
8	0.8	41.88	41.80	+0.19	44.17	43.30	+2.01
	1.0	44.14	44.31	-0.38	46.58	46.34	+0.52
	0.6	31.31	31.68	-1.17	32.64	32.21	+1.33
10	0.8	32.61	31.95	+2.07	34.04	34.83	-2.27
	1.0	34.07	34.31	-0.70	35.59	35.47	+0.34

(b) Bisymmetrical cross-section

L (m)	α (-)	Load on top flange			Load at shear centre		
		M_{cr} (kNm)		Deviation (%)	M_{cr} (kNm)		Deviation (%)
		Present method	Asgarian et al. [54]		Present method	Asgarian et al. [54]	
	0.6	61.04	58.40	+4.52	81.71	79.64	+2.60
6	0.8	64.53	62.50	+3.25	86.41	85.21	+1.41
	1.0	70.61	70.58	+0.04	94.02	92.32	+1.84
	0.6	46.55	45.40	+2.53	58.54	57.86	+1.18
8	0.8	48.16	47.46	+1.47	60.84	60.65	+0.31
	1.0	51.06	51.31	-0.49	64.43	63.90	+0.83
	0.6	37.90	37.30	+1.61	45.72	45.46	+0.57
10	0.8	38.82	38.40	+1.09	47.11	47.01	+0.08
	1.0	40.48	40.77	-0.71	49.20	48.98	+0.45

9

Annex [63] to EN 1993-1-1 [14], $\alpha_{\mathrm{cr,op}}$ should be determined based on the effective critical bending moment $M_{\mathrm{cr}}^* = k_{\mathrm{red}} M_{\mathrm{cr}}$ to account for the effects of web distortion. The reduction factor k_{red} is defined as

$$k_{\mathrm{red}} = \begin{cases} 1 & h/t_{\mathrm{w}} \leq 75 \\ \min\left(1.03 - 5.4 \cdot 10^{-5}\alpha,\ 1\right) & h/t_{\mathrm{w}} > 75,\ \alpha \leq 5000, \end{cases} \tag{9.40}$$

with

$$\alpha = \frac{h t_{\mathrm{f}}}{t_{\mathrm{w}}^3 L_{\mathrm{g}}^2} \cdot 10^{12}. \tag{9.41}$$

The latter equation requires the quantities to be expressed in millimetres.

Based on the load amplification factors, the global non-dimensional slenderness for the beam is defined as

$$\overline{\lambda}_{\mathrm{op}} = \sqrt{\frac{\alpha_{\mathrm{ult,k}}}{\alpha_{\mathrm{cr,op}}}}. \tag{9.42}$$

The reduction factor for lateral-torsional buckling is expressed by

$$\chi_{\mathrm{op}} = \min\left(\frac{1}{\Phi_{\mathrm{op}} + \sqrt{\Phi_{\mathrm{op}}^2 - \overline{\lambda}_{\mathrm{op}}^2}},\ 1\right), \tag{9.43}$$

where $\Phi_{\mathrm{op}} = 0.5\left[1 + \alpha_{\mathrm{LT}}\left(\overline{\lambda}_{\mathrm{op}} - 0.2\right) + \overline{\lambda}_{\mathrm{op}}^2\right]$, with α_{LT} representing an imperfection factor for lateral torsional buckling, which depends on the height over width ratio and the type of cross section.

After determining the reduction factor χ_{op} the design verification for lateral torsional buckling can be carried out through Equation 9.39.

9.4. DESIGN OPTIMISATION

9.4.1. OPTIMISING THE IN-PLANE AND OUT-OF-PLANE BEHAVIOUR

In Section 9.3.6, the link between the in- and out-of-plane design verification for non-prismatic beams was identified based on EN 1993-1-1 [14] through Equation 9.39.

Designing a cross-section that maximises the in-plane and out-of-plane resistances contributes to the efficient material use and minimises assembly time. In this section, a strategy for the optimisation of the in-plane and out-of-plane resistance is presented, followed by the integration of both strategies to obtain the most efficient cross-section design.

OPTIMISATION OF THE OUT-OF-PLANE RESISTANCE

The out-of-plane resistance of a demountable composite floor system is only relevant during the execution of the demountable composite floor system. The prefabricated concrete floor elements must be positioned on the top flange to ensure an even and continuous surface of the floor system.

It was shown that the position of the shear centre has a significant effect on the effective torsional rigidity because of the contribution of the Wagner torsional rigidity β_y; the effect is beneficial if the compression flange is closest to the shear centre.

According to Equation 9.23, the location of the shear centre is closest to the compression flange if

$$\frac{I_{z,\mathrm{b}}}{I_{z,\mathrm{b}} + I_{z,\mathrm{t}}} = 0, \tag{9.44}$$

implying that a T-shaped cross-section maximises the Wagner torsional rigidity. A T-shaped section implies that the warping rigidity I_ω is zero. However, the effects of the increased effective torsional rigidity are generally dominant over the reduction of the warping rigidity, resulting in an increase of the critical bending moment for the same cross-sectional area A.

OPTIMISATION OF THE IN-PLANE RESISTANCE

The in-plane resistance of a demountable composite floor system is relevant both during execution and in the persistent design situation. The reuse of the steel beam is only possible if no plastification of any part of the cross-section has occurred [25], implying that nowhere in the cross-section the yield strength f_y should be exceeded.

Normal stresses in the beam originate from the self-weight of the beam and the floor elements (imposed during execution) and the live-load, carried through composite interaction in the persistent design situation. The magnitude of the normal stresses must be approximately equal in tension and compression to optimise the in-plane resistance. This implies that the elastic neutral axis of the steel beam must be located at or below mid-height of the cross-section, depending on the relative contribution of the loads imposed during the execution and the persistent design situation.

The beneficial effect of composite interaction in the persistent design situation depends, among other parameters, on the square of the distance between the elastic neutral axes of the steel beam and the prefabricated concrete floor elements. Therefore the needs for the location of the elastic neutral axis (at or below mid-height of the cross-section) are aligned both during construction and during the persistent design situation.

CONCURRENT OPTIMISATION OF THE IN-PLANE AND OUT-OF-PLANE RESISTANCE

Based on the previous considerations, the optimal design to maximise the in-plane and out-of-plane resistance minimises $I_{z,\mathrm{b}}$, locates the elastic neutral axis at approximately mid-height of the cross-section and leads to a sufficiently high area moment of inertia I_y. These demands can be accomplished by designing a monosymmetrical cross-section subject to the following two constraints:

$$I_{z,\mathrm{b}} \ll I_{z,\mathrm{t}} \implies b_{\mathrm{f,b}} \ll \sqrt[3]{\frac{t_{\mathrm{f,t}} b_{\mathrm{f,t}}^3}{t_{\mathrm{f,b}}}} \tag{9.45a}$$

$$t_{\mathrm{f,t}} b_{\mathrm{f,t}} \approx t_{\mathrm{f,b}} b_{\mathrm{f,b}} \tag{9.45b}$$

Fulfilling the above constraints ensures (i) maximisation of the out-of-plane resistance during execution, (ii) an optimal stress distribution over the height of the cross-section during execution and in the persistent design situation, and (iii) a significant effect of the shear interaction in the persistent design situation.

The dimensions of the top flange can be determined first, e.g. based on cross-section classification limits or based on practical considerations, for example the minimum width needed to support the prefabricated concrete floor elements. The area of the bottom flange

must be approximately equal to that of the top flange whilst minimising the bottom flange width within practical limitations, such as the availability of thick plate material.[8]

Illustrative example   The benefits of the proposed cross-section design optimisation strategy are illustrated through an example for a web-tapered composite floor system with a span $L = 16$ m. The I-shaped cross-section of the laterally unrestrained steel beam had dimensions $t_w = 4.5$ mm, $h|_{x=0,L} = 590$ mm and $h|_{x=L/2} = 740$ mm. The area of the flanges was assumed to be equal, i.e. $t_{f,t}b_{f,t} = t_{f,b}b_{f,b}$ and to amount to 3600 mm^2. Either the dimensions of the top flange were fixed as $t_{f,t} = 12$ mm and $b_{f,t} = 300$ mm and the dimensions of the bottom flange were varied, or $t_{f,b} = 12$ mm and $b_{f,b} = 300$ mm and the tensile flange dimensions were varied. The critical bending moment for each case was calculated using the method proposed in Section 9.3, and the deflection is obtained by solving the Euler-Bernoulli differential equation for a beam in bending.

Figure 9.12 illustrates the critical bending moment and the in-plane deflection due to the self-weight of the web-tapered steel beam. Conform the theoretical analysis of the presented theory, cross-sections with $b_{f,b}/b_{f,t} < 1$ generate the highest critical bending moment. For example, for a ratio 0.30 ($b_{f,b} = 90$ mm, $t_{f,b} = 40$ mm), the critical bending moment increases by 93% compared to the bisymmetrical cross-section. The 5% increase in deflection is insignificant compared to the substantially larger increase of the critical bending moment for the same cross-sectional area A, implying that the proposed design strategy indeed contributes to efficient material use. Secondly, the design strategy reduces the number of (or need for) bracing systems.

For $b_{f,b}/b_{f,t} > 1$ the lateral-torsional buckling resistance decreases. For large ratios a reverse trend is observed, because the comparatively large positive influence of the term $t_{f,t}^3$ on GJ starts to become dominant compared to the negative influence of the Wagner effect.

9.4.2. Barriers to hybrid beams
The material efficiency of steel beams could be further considered by the use of high-strength steel (HSS) in the bottom flange [64], also known as a *hybrid beam*. A potential advantage of such a hybrid beam is that the width of the bottom flange (in tension) could be reduced proportionally to the relative increase of its yield strength to obtain material and cost savings.

However, local yielding of the web is necessary to utilise the benefits of the high-strength steel bottom flange, which may impair the reusability of the beam due to the associated plastic strain [25]. The reduced area of the bottom flange decreases the distance between the elastic neutral axes of the steel beam and the prefabricated concrete floor elements, leading to a reduced benefit of composite interaction. These considerations indicate that the application of high-strength steel is more challenging in case of reusable steel-concrete composite floor systems compared to the traditional composite floor systems, which are based on plastic design.

---

[8]It should also be noted that the fabrication process of the optimised cross-section requires the availability of equipment to align both flanges with the centreline of the web.
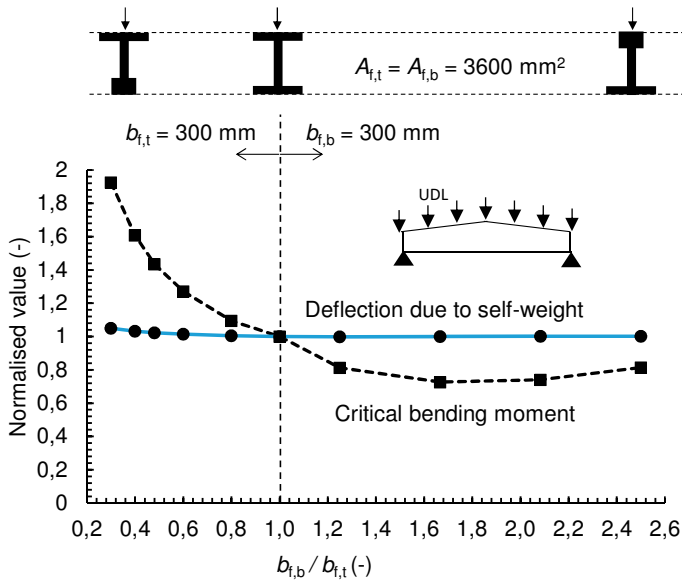
Figure 9.12 | Normalised critical bending moment and deflection due to self-weight for the L = 16 m span web-tapered steel beam.

9.5. CONCLUSIONS

This chapter presented prediction models for the deflection and elastic in-plane resistance, the fundamental frequency, and the lateral-torsional buckling resistance of non-prismatic steel-concrete composite floor systems with non-uniform shear connection.

Related to the prediction model for deflection and elastic in-plane resistance, the following conclusions are made:

• The proposed analytical method accurately predicted the deflection of the experimental web-tapered composite floor system for a calibrated shear connector stiffness k_{sc} = 55 kN/mm. On average, the deviation of the analytical method regarding midspan deflection was 0.1% compared to the experimental results presented in Chapter 7 and -1.6% compared to results obtained by finite element analysis. The calibrated magnitude of k_{sc} = 55 kN/mm was smaller than presented in Chapter 5, where a secant connector stiffness at $0.4P_u$ of 82.1 kN/mm was determined based on finite element simulation of push-out specimens. Therefore present work confirmed the discrepancy between shear connector stiffness observed in push-out tests and shear connector stiffness in beam tests, which is reported in the literature.

• Predictions regarding end slip obtained using the proposed analytical method (for k_{sc} = 55 kN/mm) were in approximately line with finite element analysis, with an average deviation of 9%. The analytical and numerical model did not reproduce the experimental end slip presented in Chapter 7: this type of discrepancy is widely reported in literature and led to an average underestimation of the end slip by 48%. Therefore the experiments suggested that the end slip is not uniquely defined for a

given deflection, and thus that it cannot be considered as a representative measure. Further research is necessary to explain the seemingly complex relation between theoretically predicted and experimentally observed end-slips and their link to the deflection.

- The shape of the slip distribution along the length of a non-prismatic composite beam is not necessarily cosinusoidal, particularly for non- uniform shear connector arrangements. This limits the validity of the Lawson model [21]. Therefore it is recommended to use the method proposed in Section 9.1 to determine the actual slip distribution and the corresponding internal actions.

Related to the prediction model for the fundamental eigenfrequencies, the following conclusion is made:

- Based on analysis of the formulae valid for fundamental frequencies of prismatic and homogeneous beams, the present work proposed an equation that is suitable to predict the fundamental frequency of non-prismatic composite floor systems with non-uniform shear connection. Very good agreement was found between the eigenfrequencies obtained using finite element analysis and the proposed analytical model: on average, the analytical model underestimated the first eigenfrequency by 0.3% for the web-tapered composite beams considered.

Related to the lateral-torsional buckling resistance, the following conclusions are made:

- Demountable steel-concrete composite floor systems are more sensitive to lateral-torsional buckling compared to monolithic cast in-situ steel-concrete floor systems, mostly because of unsymmetrical loading and the absence of rotational constraints in the execution phase. Lateral-torsional buckling is only relevant during execution: it is prevented by demountable shear connectors during the use-phase.

- The Energy method and Rayleigh-Ritz approach were used to develop an analytical prediction model for the critical bending moment of monosymmetrical web-tapered steel beams. The Wagner torsional rigidity was included in the formulation of the internal strain energy, this led to good agreement between the analytical prediction model and finite element results available in literature (max. deviation ±5%) in terms of the critical bending moment.

9

The work on lateral-torsional buckling, deflection, and elastic in-plane resistance highlighted the potential to optimise the cross-section design for all three design aspects. An optimisation strategy was derived, based on which the following conclusions are drawn:

- An overarching strategy to optimise the in-plane and out-of-plane resistance of monosymmetrical web-tapered steel beams was derived. This strategy calls for (i) a comparatively narrow tensile flange compared to the compression flange and (ii) approximately equal area of both flanges. The proposed strategy contributes to efficient material use because the out-of-plane resistance increases for the same cross-sectional area, without the need for a higher cross-section to fulfil in-plane resistance requirements.

- The optimisation strategy was demonstrated through a case study composite floor system, consisting of a 16 m span simply-supported web-tapered beam and large prefabricated concrete floor elements, connected by demountable shear connectors and loaded by a uniformly distributed load. An initially bisymmetrical cross-section of steel grade S355 was optimised by modifying the bottom flange dimensions from $300 \times 12 \ \mathrm{mm}^2$ to $90 \times 40 \ \mathrm{mm}^2$. The critical bending moment increased by 93%: the 5% increase of the deflection is considered as insignificant compared to the substantially larger relative increase of M_{cr}.

9

10

DESIGN EXAMPLE: NON-PRISMATIC COMPOSITE FLOOR SYSTEM WITH NON-UNIFORM SHEAR CONNECTION

The bitterness of poor quality remains long after the sweetness of low price is forgotten.

Benjamin Franklin

INTRODUCTION

This chapter presents a design example of a non-prismatic demountable composite floor system with non-uniform shear connection, and uses the prediction models developed in Chapters 8 and 9. The relevance of the other levels of scale, discussed in Parts I and II, is discussed where appropriate. The design example focuses on the design of a demountable composite floor system for a multi-storey car park building.

This chapter is subdivided into five subsections. Section 10.1 presents the basis of design of the floor system. The required nominal hole clearance is determined in Section 10.2 based on the statistical model developed in Chapter 8. Section 10.3 presents the design verification for the persistent (in-use) design situation based on the prediction models developed in Chapter 9. The design verification for the transient (execution) design situation is performed in Section 10.4. The chapter concludes with Section 10.5, summarising the steps taken in the design verification of the demountable composite floor system considered in the design example.

10.1. Basis of design

The design example focuses on the design of a demountable composite floor system for a multi-storey car park building, see Figure 10.1, consisting of prefabricated floor elements and web-tapered steel beams. At midspan there is a cross-bracing system that connects adjacent beams to reduce geometrical and dimensional deviations of the floor system and to increase the lateral-torsional buckling resistance.

The car park is designed without outer walls or façade elements, because car park structures with openings of equal or more than one third of the total surface area of outer walls generally do not have to fulfil any or only minimum fire-resistance requirements because of the natural ventilation[1].

The hypothetical structure is located in The Netherlands and is verified in accordance with the Eurocodes, the Dutch National Annexes and the Dutch Nationally Determined Parameters. The details of the design and the corresponding design verifications are presented in the following sections. It should be noted that only the most relevant design verifications to this dissertation are shown in this chapter.

The hypothetical steel frame structure is on a 1.35 m grid: the columns are at 2.70 m and 16.2 m centre-to-centre in perpendicular directions, see Figure 10.1. Web-tapered steel beams span between opposite columns and have nominal length $L = 16.2$ m. The actual span of the composite floor system is assumed as $L = 16.0$ m to account for the physical dimensions of the columns and of the connections. The focus of this design example is the demountable composite floor system which is designed with pinned connections at the supports. This long span floor system provides a user-friendly layout compared to more traditional designs with internal columns, see Figure 10.2, and offers a broader field of applications in a second life cycle because of the unobstructed floor plan.

10.1.1. Geometry and strength classes

WEB-TAPERED STEEL BEAMS

The web-tapered steel beams are symmetrical with respect to midspan: its height at the supports equals $h|_{x=0,L} = 560$ mm and increases to $h|_{x=L/2} = 710$ mm at midspan. The cross-sectional dimensions are illustrated in Figure 10.3. All parts of the welded profile are of strength grade S355 conform EN 1993-1-1 [14], therefore the characteristic yield strength equals $f_y = 355$ MPa.

FLOOR ELEMENTS

The prefabricated concrete floor elements have a nominal size of $8.0 \times 2.7 \times 0.12$ m (l×w×h, see Figure 10.3) and are of strength class C30/37 according to EN 1992-1-1 [29]. This strength class corresponds to a characteristic compressive strength of $f_{c,k} = 30$ MPa and Young's Modulus $E_{cm} = 33$ GPa. The effective Young's Modulus that may be used to reflect both the short- and long-term response of the concrete is determined according to EN 1994-1-1 [8] as

$$E_{c,eff} = \frac{E_{cm}}{2} = \frac{33}{2} = 16.5 \text{ GPa.} \tag{10.1}$$

---

[1] More requirements apply, see NEN 2443 [65]. See also references [66–68] for further background information on fire in naturally ventilated car park buildings.
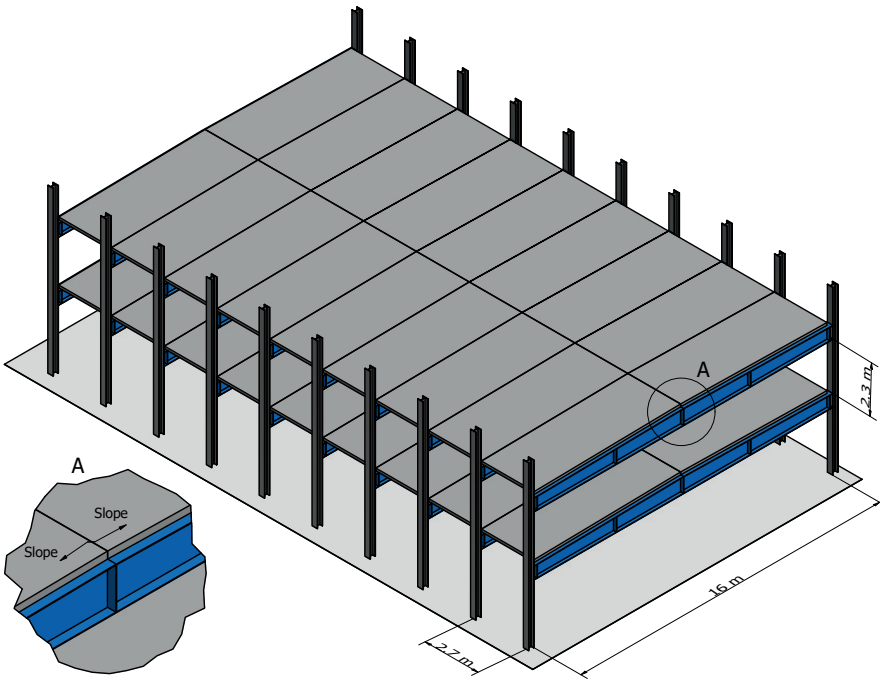
Figure 10.1 | Schematic overview of a representative part of the case study multi-storey car park building. The extended columns provide the opportunity to mount safety barriers and to vertically extend the structure.
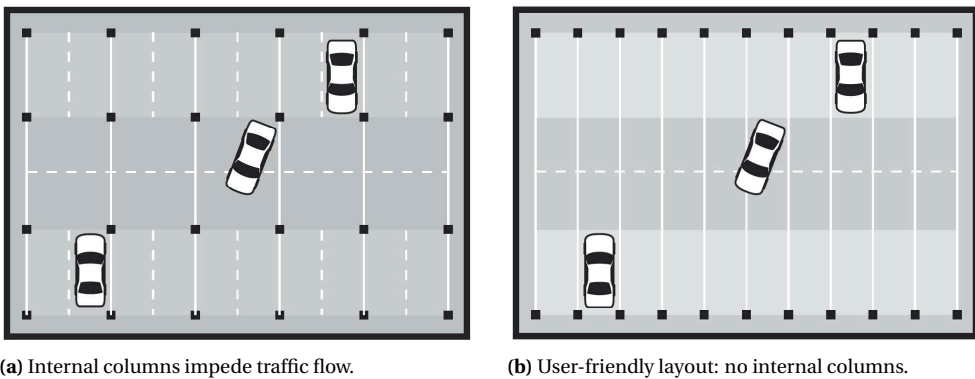
(a) Internal columns impede traffic flow. **(b)** User-friendly layout: no internal columns.

Figure 10.2 | Alternative floor plans for car park buildings, extracted from [69].

10
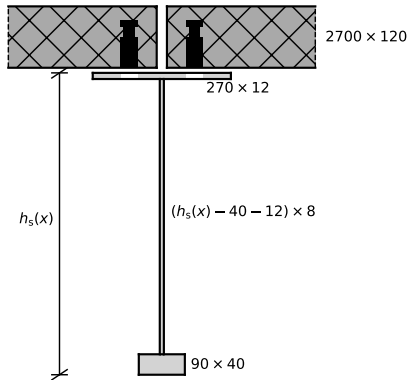
Figure 10.3 | Cross-sectional dimensions (in mm) of case study composite floor system. The prefabricated floor elements are 8000 mm long.

Embedded couplers and bolts are cast in the floor elements to form a horizontal shear connection similar to the design subjected to push-out tests in Chapter 5, but without the angle profiles confining the concrete at the elements' edges. The floor elements are assumed to be fabricated by an experienced fabricator of precast components, such that any dimensional and geometrical deviations regarding their exterior dimensions are insignificant. However, in practice this assumption must be checked based on the actual dimensions of the floor elements to include any geometrical and/or dimensional deviations in the prediction model presented in Chapter 8. The floor elements are not sensitive to shear lag effects because their width is smaller than $L/4$ therefore they fully contribute to the load-bearing.

SHEAR CONNECTION
The demountable shear connector system is similar to the one tested in Chapter 7 for which a shear connector stiffness $k_{sc} = 55$ kN/mm was calibrated. However, the angle profile does no longer form part of the shear connection: according to the finite element analysis this leads to 35% increase of the connector stiffness, see Section 5.3.3 and Figure 5.20, hence[2] $k_{sc} = 74$ kN/mm. This connector stiffness is based on a 12 mm nominal hole clearance, which will be proven to be sufficient to guarantee successful assembly of the composite floor system. It is assumed that the quasi-elastic limit of the shear connector corresponds to a slip of 0.60 mm (based on short term concrete properties, see Figure 5.4 for justification of the 0.60 mm criterion), and that the long-term connector stiffness equals $0.5 \times k_{sc}$ in absence of more accurate data.

The shear connectors are concentrated in the support region, see Figure 10.4, based on the experience gained from the experimental work presented in Chapter 7. Eight pairs of shear connectors are located near both supports, spaced at 200 mm ($10d$) centre-to-centre based on the recommendations made in Section 5.3.4 to maximise the beneficial effects of composite interaction and to prevent negative mutual influences of neighbouring connectors. The beam is conveniently subdivided into $J = 40$ segments in the appropriate pre-

---

[2]This is a simplification which is appropriate for a design example. However, it was previously shown that a discrepancy exists between connector stiffness according to push-out and beam tests, meaning that this is merely an approximation.

diction models derived in Chapter 9 to match the spacing of the shear connectors and to adequately capture the varying geometry of the steel beam along its length.

10.1.2. LOADS AND LOAD COMBINATIONS

ULTIMATE LIMIT STATE

Two load combinations are considered in the ultimate limit state (ULS) in accordance with EN 1990 [70] and its Dutch National Annex [71], which are represented by

$$1.35 \times G + \sum_{j \geq 1} 1.5 \times \psi_{0,i} Q_{k,i} \text{ and} \tag{10.2}$$

$$1.2 \times G + 1.5 \times Q_{k,1} + \sum_{i > 1} 1.5 \times \psi_{0,i} Q_{k,i}, \tag{10.3}$$

where G represents the total unfavourable self-weight[3] and Q denotes variable loads. Variable $\psi_{0,i}$ represents a combination value defined in EN 1990 [70] or its National Annexes.

In the transient design situation (assembly) only the self-weight of the structural components are taken into account in the ultimate limit state (ULS) design verification, and therefore the load combination is $1.35 \times G$. For the proposed design, see Section 10.1.1, the characteristic self-weight equals[4] $q_G = 8.5$ kN/m. Therefore the design value of the self-weight in the transient design situation equals $q_{G,d} = 1.35 \times 8.5 = 11.5$ kN/m.

In the persistent design situation only one variable load is accounted for in the ULS. Therefore Equation 10.3 is the most onerous of the two load combinations and thus the design verification will be based on $1.2 \times G + 1.5 \times Q$. Car park buildings (gross vehicle weight < 30 kN) belong to Category F in EN 1991-1-1 [9], which corresponds to a characteristic variable load of 2.5 kN/m^2. However, to enable a wider field of applications during the technical lifetime of the structural components, a higher characteristic variable load of 3.5 kN/m^2 is assumed. One representative part of the floor system is 2.7 m wide and thus it follows that $q_Q = 3.5 \times 2.7 = 9.5$ kN/m.

---

[3]The factor 1.35 and 1.20 must be replaced by 0.90 if the self-weight acts favourably
[4]$q_G = \left(\rho_c A_c + \rho_s A_{s,mean} \right) \times g = 8.5$ kN/m.
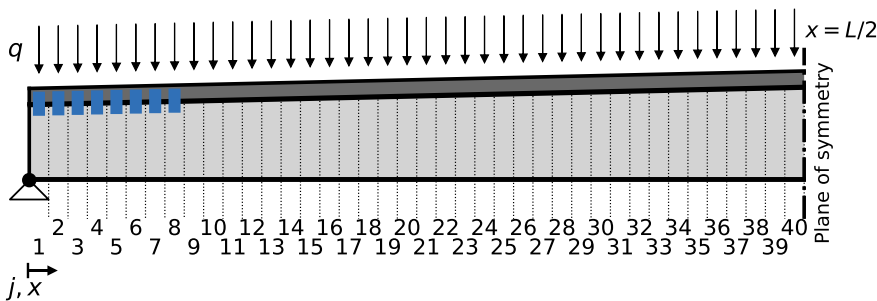
Figure 10.4 | Shear connector arrangement of the case study composite floor system: a blue line indicates a pair of shear connectors.

SERVICEABILITY LIMIT STATE

In the serviceability limit state (SLS) the characteristic load combination, $G + Q$, is used to verify compliance to a deflection limit of $L/250 = 64$ mm. And the fundamental frequency of the composite floor system is determined based on the combination $G + 0.1 \times Q$ as suggested by the Steel Construction Institute [72]. The effects of the slip on the deflection and eigenfrequency are taken into account because the shear connector arrangement (see 10.4) does not comply to the EN 1994-1-1 [8] requirements that may allow to ignore such effects.

10.2. NOMINAL HOLE CLEARANCE

The nominal hole clearance required for the successful assembly of the demountable composite floor system is determined by the model derived in Chapter 8. The deviations considered include support offset (imperfection of the structural grid), bolt hole offset, shear connector offset, out-of-straightness, and relative displacement (slip) between the steel beam and the prefabricated concrete floor elements due to their self-weight. The geometrical and dimensional deviations of the structural elements are based on Tolerance Class 2 of EN 1090-2 [12], with 95% of the observations being within the tolerance limits.

The normal, uniformly and deterministically distributed basic variables are summarised in Tables 10.1 - 10.3, respectively. The slip amplitude s_0 is determined as 3.10 mm based on the proposed design formula, expressed by Equation 8.9/F.8[5].

The number of Monte Carlo Simulations equals $N = 75000$ based on a sensitivity study on the convergence of the aggregated results. Figure 10.5 illustrates the probability of successful assembly as a function of the nominal hole clearance. Distinction is made between the probability based on shear connectors along the full length, and the probability based on the actual positions of the shear connectors, see Figures 10.4 and 10.6. It is considered most relevant to base the probability based on the actual positions of the connectors: it follows that a 12 mm nominal hole clearance leads to a 97% probability of successful installation. Therefore the assumption of the shear connector stiffness k_{sc} in Section 10.1.1 is justified.

Figure 10.6 shows a heat map of the required nominal hole clearances as a function of position along the beam axis. The figure illustrates the influence of the bracing system at midspan and demonstrates that the reduced magnitude of the nominal hole clearance based on the actual connector positions is due to the comparatively smaller effects of the geometrical and dimensional imperfections in the support regions.

---

[5]The value obtained by the design formula is 5.6% smaller than the exact solution given by Equation 8.7/F.3, although the error is negligible in absolute terms (0.18 mm).

10

Table 10.1 | Normal-distributed basic variables based on Tolerance Class 2 of EN 1090-2 [12] and 95% of the observations falling within the tolerance limits. The input for the out-of-straightness is based on literature review, see Section 8.1.3.

Basic variable	Physical meaning	Distribution	Mean	Standard deviation	Unit
R	Bolt hole offset amplitude	Normal	0	0.510	mm
$\Delta Y_{c,i}$	Lateral support offset	Normal	0	2.55	mm
$\Delta X_{c,i}$	Longitudinal support offset	Normal	0	2.55	mm
$A_{0,u}$	Out-of-straightness amplitude	Normal	$L/2800$	$L/5700$	mm

Table 10.2 | Uniformly distributed basic variables.

Basic variable	Physical meaning	Distribution	Interval	Unit
θ	Angle for R	Uniform	$[0, 2\pi]$	rad
ψ	Angle for c_0	Uniform	$[0, 2\pi]$	rad
η_i	Proportionality factor for $\Delta Y_{c,i}$	Uniform	$[0, 1]$	-

Table 10.3 | Deterministic basic variables.

Basic variable	Physical meaning	Distribution	Magnitude	Unit
s_0	Slip amplitude	Deterministic	3.28	mm
c_0	Shear connector offset amplitude	Deterministic	0.5	mm
d	Bolt diameter	Deterministic	20	mm
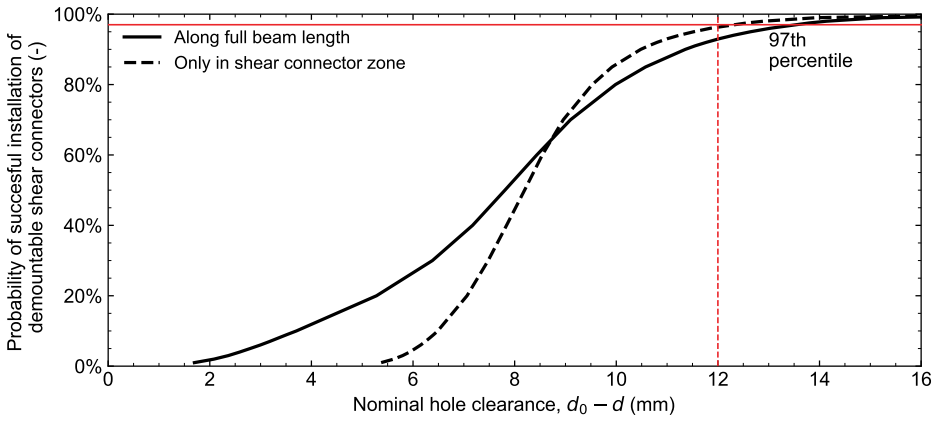
Figure 10.5 | Probability of successful assembly as a function of the nominal hole clearance $(d_0 - d)$.
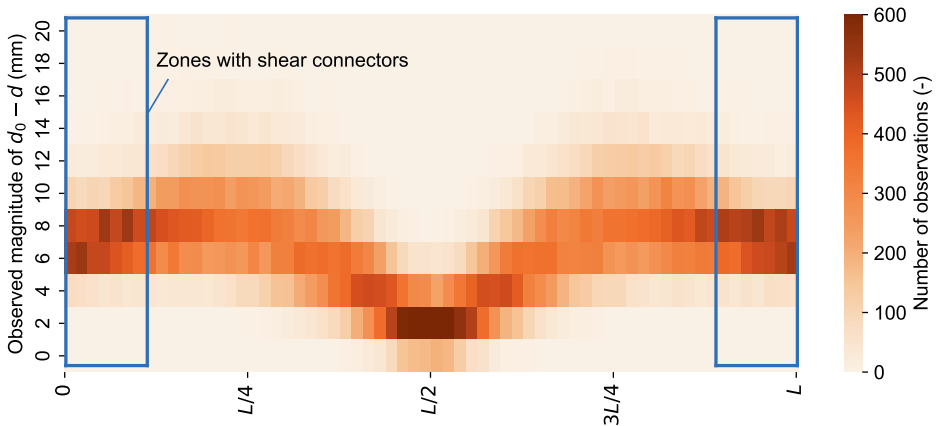
Figure 10.6 | Heat map of required nominal hole clearance $(d_0 - d)$ for successful assembly. A bracing system is located at $x = L/2$.

10.3. DESIGN VERIFICATION: PERSISTENT DESIGN SITUATION

10.3.1. ULTIMATE LIMIT STATE

An elastic design verification is performed in the Ultimate Limit State. Not only the steel beam and the concrete floor elements must remain within their elastic range, but so must the shear connectors. The latter can be verified by verifying that the slip at the locations of the connectors does not exceed the assumed quasi-elastic slip limit of 0.60 mm. The short-term properties of the concrete (E_{cm} = 33 GPa) and connector (k_{sc} = 74 kN/mm) are used: the implications of their time-dependency are discussed at the end of this section based on pseudo-elastic analysis.

In the persistent design situation (use-stage) only the in-plane resistance of the composite floor system must be verified. As discussed in Section 10.1.2, the governing ULS design load combination is $1.2 \times G + 1.5 \times Q$.

CROSS-SECTION CLASSIFICATION

The cross-section classification is carried out in accordance with EN 1993-1-1 [14], neglecting the beneficial influence of the welds. For the compression flange it follows that

$$\frac{c_{f,t}}{t_{f,t}} = \frac{0.5 \cdot \left(b_{f,t} - t_w\right)}{t_{f,t}} = \frac{0.5 \cdot (270 - 8)}{12} = 10.9 \leq 14\varepsilon = 11.3, \tag{10.4}$$

which corresponds to cross-section class 3.

The web is analysed at midspan, which is the most unfavourable location for the width-to-thickness ratio. The cross-section design is such that the elastic neutral axis is at mid-height of the web conform the recommendations made in Section 9.4.1. It follows that

$$\frac{c_w}{t_w} = \frac{h - t_{f,t} - t_{f,b}}{t_w} = \frac{710 - 12 - 40}{8} = 82.3 \leq 124\varepsilon = 100.4, \tag{10.5}$$

which corresponds to cross-section class 3.

Based on the classifications, it is concluded that all elastic design verifications can be based on a fully effective cross-section. It should be noted that the web is sensitive to shear buckling, but that it was verified according to EN 1993-1-5 that the shear buckling resistance is sufficient if non-rigid end posts are located at the supports.

NORMAL STRESSES IN STEEL AND CONCRETE

The normal stresses in the steel beam according to the design load combination of the self-weight G and the variable load Q are illustrated in Figure 10.7c. Nowhere in a cross-section is the design yield stress f_{yd} = 355 MPa exceeded. Although not shown in the diagram, the design bending stresses also do not exceed f_{yd} in absence of the shear connection. Therefore, the shear connection is not necessary from a bending resistance point of view: its main purpose is to limit deflection.

The absolute magnitude of the normal force in the concrete represents only 8% of the concrete design compressive strength f_{cd} = 30/1.5 = 20 MPa, see Figure 10.7d . This (nominal) stress level is sufficiently low for the concrete to remain in its linear-elastic branch. It is outside the scope of this example to verify the resistance of the floor element: shear forces and transversal bending of the floor element need to be checked as well.
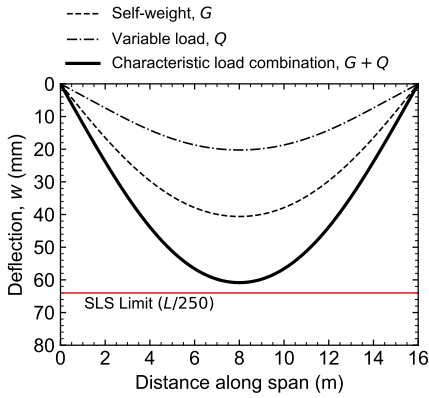
(a) Deflection.
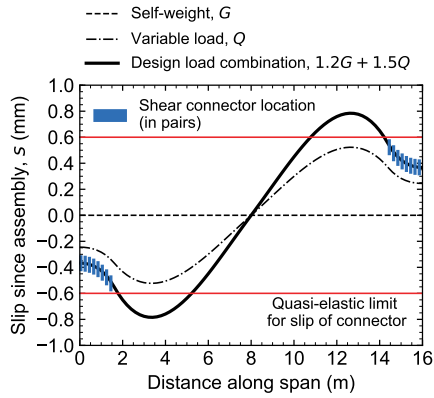
(b) Slip.
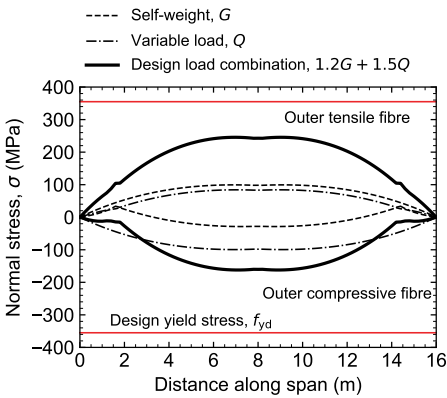
(c) Normal stresses in steel beam.
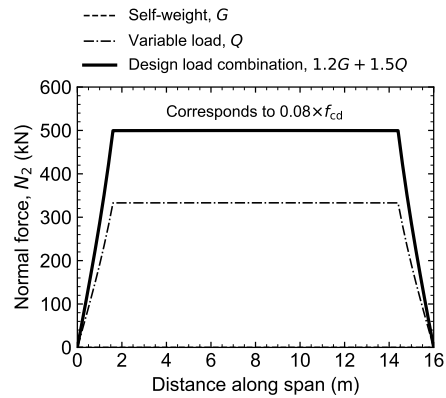
(d) Normal force in steel beam ($N_1 = -N_2$).

Figure 10.7 | Deflection, slip, normal stresses and normal force as a result of self-weight (G) and imposed variable loads (Q) based on the short-term properties of the concrete and shear connectors.

10

CONNECTOR SLIP

Figure 10.7b presents the connector slip since assembly as a function of the position along the beam axis. Nowhere along the beam axis is the quasi-elastic slip limit exceeded at a shear connector location under the design load combination.

Lawson et al.[21] suggested that for a uniformly distributed load the slip diagram could be represented by a cosine shape function: the results, however, demonstrate that this assumption is certainly not valid for this composite floor system. This implies that the method of Lawson et al. [21] leads to wrong results in terms of deflection and internal actions. The most particular difference is that it are not the shear connectors closest to the support, but the shear connectors furthest from the support that are most heavily loaded.

TIME-DEPENDENT EFFECTS

The long-term behaviour of the composite floor system depends on the time-dependent deformation of the concrete and the shear connectors. Both cause the composite interaction to be less pronounced over time. However, it has already been shown that the steel beam can support the loads without the presence of shear connectors at all. Therefore the time-dependent effects do not influence the conclusion regarding the resistance.

The time-dependent behaviour leads to increased slip deformations because (i) the effective concrete Young's Modulus reduces to $0.5 \times E_{cm}$ and (ii) the effective shear connector stiffness reduces to $0.5 \times k_{sc}$. However, the reduced stiffness of the shear connector and concrete leads to reduced connector shear forces. Therefore the time-dependent response does not lead to the risk of exceeding the quasi-elastic limit, although it will influence the deflection, which is discussed in the following section.

10.3.2. SERVICEABILITY LIMIT STATE

DEFLECTION

The deflection under the characteristic load combination is illustrated in Figure 10.7a based on the short-term properties of the concrete and shear connector. The imposed deflection limit of $L/250 = 64$ mm is exceeded nowhere along the beam: the deflection at midspan equals 60.8 mm. Based on the long-term properties of the concrete ($E_{c,eff} = 0.5 \times E_{cm}$) and the assumed degradation of the shear connector stiffness to $0.5 \times k_{sc}$, the deflection increases to 64.1 mm. This 3.3 mm deflection increase is equivalent to a 16% increase of the short-term deflection due to the variable load Q.

It is questionable whether such an increase of the deflection is realistic, because the composite floor system is not constantly loaded by the characteristic load combination. In part this is already accounted for in the definition of $E_{c,eff}$, which is more favourable compared to the unconditional concrete creep formulation of EN 1992-1-1 [29]. This remains a crude, engineering approach to estimate the influence of creep on the long-term deflection: the development of the shear connector stiffness as a function of applied load and time can be combined with existing creep models for concrete to make more comprehensive predictions. Once such relationships have been derived based on experiments, the theoretical models reviewed within Section 2.6.2 can be employed for more fundamental analysis.

It should be noted that, because the deflection due to self-weight is governing, pre-cambering of the steel beams could reduce the magnitude of total deflection considerably. However, in line with the experimental work presented in Chapter 7, no pre-cambering is

10

used in this design example, because there is no experimental evidence yet that the large straight floor elements can be readily installed on a curved beam.

Fundamental frequency
The fundamental frequency is obtained based on the load combination $G + 0.1 \times Q$. The prediction model proposed in Section 9.2 is used, expressed by

$$f_{1,K} = f_{1,\infty}\sqrt{\frac{w_{\mathrm{m},\infty}}{w_{\mathrm{m},K}}} \tag{10.6}$$

where $w_{\mathrm{m},K}$ and $w_{\mathrm{m},\infty}$ are the deflections at midspan due the load combination for the floor systems with flexible and rigid shear connection, respectively. These are derived using the prediction model presented in Section 9.1 as $w_{\mathrm{m},K} = 20.3$ mm and $w_{\mathrm{m},\infty} = 16.1$ mm.

The fundamental frequency $f_{1,\infty}$ of the composite beam with rigid shear connection is determined for this load combination based on the method presented in Section 9.2 as $f_{1,\infty} = 4.35$ Hz. This gives $f_{1,K} = 3.9$ Hz, which is substantially higher than the recommended value of 3 Hz for car park buildings [69, 72].

10.4. Design verification: transient design situation
In the transient design situation (execution) the in-plane and out-of-plane resistance of the beam must be verified. As discussed in Section 10.1.2, the governing load combination is $1.35 \times G$, which leads to a uniformly distributed load of $q_{\mathrm{G,d}} = 11.5$ kN/m.

10.4.1. Out-of-plane resistance
According to EN 1993-1-1 [14], the lateral torsional buckling design resistance of non-prismatic members must be verified by

$$\frac{\chi_{\mathrm{op}}\alpha_{\mathrm{ult,k}}}{\gamma_{\mathrm{M1}}} \geq 1.0 \tag{10.7}$$

where χ_{op} is a reduction factor related to lateral torsional buckling and $\alpha_{\mathrm{ult,k}}$ is the minimum load amplifier of the design loads such that the characteristic in-plane resistance of the cross section is attained. According to Section 10.3 the maximum bending stress due to the characteristic value of the self-weight (G) equals 99.4 MPa. This leads to $\alpha_{\mathrm{ult,k}} = 355/99.4 = 3.57$ (−).

The critical bending moment is obtained through the method presented in Section 9.3 as $M_{\mathrm{cr}} = 707$ kNm. In the Dutch National Annex [63] to EN 1993-1-1 [14], the reduction factor k_{red}, see Equations 9.40 and 9.41, accounts for web distortion. For this design $k_{\mathrm{red}} = 0.939$ (−) and thus $M_{\mathrm{cr}}^* = k_{\mathrm{red}}M_{\mathrm{cr}} = 664$ kNm. It follows that the ratio of the effective critical bending moment over the design bending moment[6] equals $\alpha_{\mathrm{cr,op}} = 664/368 = 1.81$ (−).

Based on the load amplification factors, the global non-dimensional slenderness for the beam is defined as

$$\overline{\lambda}_{\mathrm{op}} = \sqrt{\frac{\alpha_{\mathrm{ult,k}}}{\alpha_{\mathrm{cr,op}}}} = \sqrt{\frac{3.57}{1.81}} = 1.41 \; (-) \tag{10.8}$$

10

---
[6]$M_{y,\mathrm{G,Rd}} = 1/8\, q_{\mathrm{G,d}}L^2 = 368$ kNm with $q_{\mathrm{G,d}} = 11.5$ kN/m.

The reduction factor for lateral-torsional buckling is expressed by

$$\chi_{\text{op}} = \min\left(\frac{1}{\Phi_{\text{op}} + \sqrt{\Phi_{\text{op}}^2 - \overline{\lambda}_{\text{op}}^2}}, \ 1\right) = 0.304 \ (-) \tag{10.9}$$

where $\Phi_{\text{op}} = 0.5\left[1 + \alpha_{\text{LT}}\left(\overline{\lambda}_{\text{op}} - 0.2\right) + \overline{\lambda}_{\text{op}}^2\right] = 1.95 \ (-)$, with α_{LT} representing an imperfection factor equal to 0.76 for welded sections.

All input variables for the design verification are now known. It follows that

$$\frac{\chi_{\text{op}} \alpha_{\text{ult,k}}}{\gamma_{\text{M1}}} = \frac{0.304 \times 3.57}{1.00} = 1.08 \geq 1 \tag{10.10}$$

and thus the lateral-torsional buckling resistance is sufficient.

10.4.2. IN-PLANE RESISTANCE
The in-plane resistance during the transient design situation is also based on the design load combination $1.35 \times G$. In Sections 10.3 and 10.4.1 it was determined that the characteristic value of the self-weight (G) led to a maximum bending stress of 99.4 MPa. Therefore the normal stress-based unity check at the design load combination equals

$$\frac{1.35 \times 99.4}{355} = 0.38 \leq 1 \tag{10.11}$$

and thus the in-plane resistance during execution is sufficient.

10.5. SUMMARY
This chapter presented a design example for a non-prismatic demountable steel-concrete composite floor system with non-uniform shear connection. The required nominal hole clearance was quantified as 12 mm based on the statistical model presented in Chapter 8 for a probability of successful assembly of the shear connection of 97%. Design verifications for deflection, in-plane resistance, fundamental frequency and out-of-plane resistance were performed using the prediction models developed in Chapter 9. The long-term effects on the resistance and deflection were evaluated based on pseudo-elastic analysis.

10

REFERENCES PART III

REFERENCES

[1] M. P. Nijgh, I. A. Gîrbacea, and M. Veljkovic, *Elastic behaviour of a tapered steel-concrete composite beam optimized for reuse,* Engineering Structures **183**, 366 (2019).

[2] ArcelorMittal, *Car parks in steel,* Tech. Rep. (ArcelorMittal, 2014).

[3] I. A. Gîrbacea, *Assessment of demountable steel-concrete composite flooring systems,* Master's thesis, Delft University of Technology (2018).

[4] T. M. Roberts, *Finite difference analysis of composite beams with partial interaction,* Computers & Structures **21**, 469 (1985).

[5] J.-P. Lin, G. Wang, G. Bao, and R. Xu, *Stiffness matrix for the analysis and design of partial-interaction composite beams,* Construction and Building Materials **156**, 761 (2017).

[6] X. Zeng, S.-F. Jiang, and D. Zhou, *Effect of shear connector layout on the behavior of steel-concrete composite beams with interface slip,* Applied Sciences **9**, 207 (2019).

[7] K. S. Naraine, *Slip and uplift effects in composite beams,* Master's thesis, McMaster University (1984).

[8] NEN, *NEN-EN 1994-1-1: Eurocode 4: Design of composite steel and concrete structures - Part 1-1: General rules and rules for buildings* (NEN, 2011).

[9] NEN, *NEN-EN 1991: Eurocode 1: Actions on Structures - Part 1-1: General actions, Densities, self-weight, imposed loads for buildings* (NEN, 2019).

[10] M. Crisinel, *Partial-interaction analysis of composite beams with profiled sheeting and non-welded shear connectors,* Journal of Constructional Steel Research **15**, 65 (1990).

[11] M. P. Nijgh and M. Veljkovic, *Requirements for oversized holes for reusable steel-concrete composite floor systems,* Structures **24**, 489 (2020).

[12] NEN, *NEN-EN 1090-2: Execution of steel structures and aluminium structures - Part 2: Technical requirements for steel structures* (Nederlandse Norm (NEN), 2018).

[13] NEN, *NEN-EN 10034: Structural steel I and H sections - Tolerances on shape and dimensions* (Nederlandse Norm (NEN), 1994).

[14] NEN, *NEN-EN 1993-1-1: Eurocode 3: Design of steel structures - Part 1-1: General rules and rules for buildings* (NEN, 2006).

[15] H. Beer and G. Schulz, *The European column curves,* IABSE reports of the working commissions **23**, 385 (1975).

[16] J. Strating and H. Vos, *Computer simulation of the ECCS buckling curve using a Monte-Carlo method,* Heron **19** (1973).

[17] N. Tebedge, W.-F. Chen, and L. Tall, *Experimental studies on column strenght of European heavy shapes,* Laboratory report (LeHigh University - Fritz Engineering Laboratory, 1972).

[18] P. F. Dux and S. Kitipornchai, *Inelastic beam buckling experiments,* Journal of Constructional Steel Research **3**, 3 (1983).

[19] T. Aoki and Y. Fukumoto, *On the buckling strength distribution of welded h-columns,* in *Proceedings of the Japan Society of Civil Engineers,* Vol. 1974 (Japan Society of Civil Engineers, 1974) pp. 37–48.

[20] H. S. Essa and D. J. L. Kennedy, *Distortional buckling of steel beams,* Structural engineering report 185 (University of Alberta - Department of Civil Engineering, 1993).

[21] R. M. Lawson, D. Lam, E. S. Aggelopoulos, and S. Nellinger, *Serviceability performance of steel–concrete composite beams,* Proceedings of the Institution of Civil Engineers - Structures and Buildings **170**, 98 (2017).

[22] Z. Kala, *Sensitivity analysis of steel plane frames with initial imperfections,* Engineering Structures **33**, 2342 (2011).

[23] M. P. Nijgh and M. Veljkovic, *A static and free vibration analysis method for non-prismatic composite beams with a non-uniform flexible shear connection,* International Journal of Mechanical Sciences **159**, 398 (2019).

[24] M. P. Nijgh and M. Veljkovic, *An optimisation strategy for the (in- and out-of-plane) resistance of steel beams in demountable composite floor systems,* Structures **24**, 880 (2020).

[25] Steel Construction Institute (SCI), *Protocol for reusing structural steel,* Tech. Rep. (SCI, 2019).

[26] C. F. Dunant, M. P. Drewniok, M. Sansom, S. Corbey, J. M. Cullen, and J. M. Allwood, *Options to make steel reuse profitable: An analysis of cost and risk distribution across the UK construction value chain,* Journal of Cleaner Production **183**, 102 (2018).

[27] N. M. Newmark, *Test and analysis of composite beams with incomplete interaction,* Proceedings of the Society for Experimental Stress Analysis **9**, 75 (1951).

[28] N. J. Taleb and E. W. Suppiger, *Vibration of stepped beams,* Journal of the Aerospace Sciences **28**, 295 (1961).

[29] NEN, *NEN-EN 1992-1-1: Eurocode 2: Design of concrete structures - Part 1-1: General rules and rules for buildings* (NEN, 2011).

[30] J. M. Aribert, *Slip and uplift measurements along the steel and concrete interface of various types of composite beams,* in *Testing of Metals for Structures: Proceedings of the International RILEM Workshop,* edited by F. M. Mazzolani (1990) pp. 395–410.

[31] S. Ernst, R. Q. Bridge, and A. Wheeler, *Correlation of beam tests with pushout tests in steel-concrete composite beams,* Journal of Structural Engineering **136**, 183 (2010).

[32] M. Mele, *Experimental controls on shear connectors in composite steel-concrete structures,* in *Testing of Metals for Structures: Proceedings of the International RILEM Workshop,* edited by F. M. Mazzolani (1990) pp. 428–434.

[33] M. Leskelä, *Shear connections in composite flexural members of steel and concrete* (ECCS - European Convention for Constructional Steelwork, 2017).

[34] S. Kamalanandan and I. Patnaikuni, *Computer modeling of simply supported composite beam.* in *Proceedings of the First International Structural Engineering and Construction Conference: Creative Systems in Structural and Construction Engineering,* edited by A. Singh (2001) pp. 629–634.

[35] G. Hanswille, M. Porsch, and C. Ustundag, *Studies of the lifetime of cyclically loaded steel-concrete composite bridges,* Steel Construction **3**, 140 (2010).

[36] A. S. Kozma, *Demountable composite beams: Design procedure for non-conventional shear connections with multilinear load-slip behaviour,* Ph.D. thesis, University of Luxembourg (2020).

[37] S. Gogoi, *Interaction phenomena in composite beams and plates,* Ph.D. thesis, University of London (1964).

[38] J. F. Wang, J. T. Zhang, R. Q. Xu, and Z. X. Yang, *A numerically stable dynamic coefficient method and its application in free vibration of partial-interaction continuous composite beams,* Journal of Sound and Vibration **457**, 314 (2019).

[39] R. Xu and Y. Wu, *Static, dynamic, and buckling analysis of partial interaction composite members using Timoshenko's beam theory,* International Journal of Mechanical Sciences **49**, 1139 (2007).

[40] Y.-F. Wu, R. Xu, and W. Chen, *Free vibrations of the partial-interaction composite members with axial force,* Journal of Sound and Vibration **299**, 1074 (2007).

[41] L. Prandtl, *Kipperscheinungen,* Ph.D. thesis, Universität München (1899).

[42] A. G. M. Michell, *Elastic stability of long beams under transverse forces,* The London, Edinburgh, and Dublin Philosophical Magazine and Journal of Science **48**, 298 (1899).

[43] H. H. Snijder, J. C. D. Hoenderkamp, and J. Maljaars, *Influence of concrete slabs on lateral torsional buckling of steel beams,* in *Proceedings of the Third International Conference on Structural Engineering, Mechanics and Computation* (Milpress Science Publishers, 2007) pp. 001–006.

[44] T. Höglund, *Att konstruera med stål, Läromedel för konstruktörer: Modul 6, Stabilitet för balkar och stänger* (Stålbyggnadsinstitutet, 2006).

[45] L. Zhang and G. S. Tong, *Lateral buckling of web-tapered I-beams: A new theory,* Journal of Constructional Steel Research **64**, 1379 (2008).

[46] A. Weinstein, *The center of shear and the center of twist,* Quarterly of Applied Mathematics **5**, 97 (1947).

[47] I. Ecsedi, *A formulation of the centre of twist and shear for nonhomogeneous beam,* Mechanics Research Communications **27**, 407 (2000).

[48] M. T. M. Nemir, *Finite element stability analysis of thin-walled steel structures*, Ph.D. thesis, University of Salford (1985).

[49] A. B. Benyamina, S. A. Meftah, F. Mohri, and E. M. Daya, *Analytical solutions attempt for lateral torsional buckling of doubly symmetric web-tapered I-beams,* Engineering Structures **56**, 1207 (2013).

[50] S. Kitipornchai and N. S. Trahair, *Buckling properties of monosymmetric i-beams,* Journal of the Structural Division **106** (1980).

[51] C. M. Wang and S. Kitipornchai, *On stability of monosymmetric cantilevers,* Engineering Structures **8**, 169 (1986).

[52] W. bin Yuan, B. Kim, and C. yi Chen, *Lateral–torsional buckling of steel web tapered tee-section cantilevers,* Journal of Constructional Steel Research **87**, 31 (2013).

[53] A. Andrade, D. Camotim, and P. B. Dinis, *Lateral-torsional buckling of singly symmetric web-tapered thin-walled i-beams: 1d model vs. shell FEA,* Computers & Structures **85**, 1343 (2007).

[54] B. Asgarian, M. Soltani, and F. Mohri, *Lateral-torsional buckling of tapered thin-walled beams with arbitrary cross-sections,* Thin-Walled Structures **62**, 96 (2013).

[55] N. S. Trahair, *Lateral buckling of tapered members,* Engineering Structures **151**, 518 (2017).

[56] M. Soltani and B. Asgarian, *Determination of lateral-torsional buckling load of simply supported prismatic thin-walled beams with mono-symmetric cross-sections using the finite difference method,* Amirkabir Journal of Civil Engineering **50**, 23 (2018).

[57] T. M. Roberts and Z. G. Azizian, *Instability of thin walled bars,* Journal of Engineering Mechanics **109**, 781 (1983).

[58] R. E. Erkmen and M. M. Attard, *Lateral–torsional buckling analysis of thin-walled beams including shear and pre-buckling deformation effects,* International Journal of Mechanical Sciences **53**, 918 (2011).

[59] S. P. Timoshenko and J. M. Gere, *Theory of Elastic Stability* (McGraw-Hill, 1961).

[60] V. Z. Vlasov, *Thin-walled elastic beams,,* Israel Program for Scientific Translation (1961).

[61] T. V. Galambos, *Structural members and frames* (Prentice-Hall, 1968).

[62] M. J. Vesko, *Lateral-torsional buckling of structures with monosymmetric cross-sections,* Master's thesis, Swanson School of Engineering (2008).

[63] NEN, *NEN-EN 1993-1-1+C2/NB: Dutch National Annex to Eurocode 3: Design of steel structures - Part 1-1: General rules and rules for buildings* (NEN, 2016).

[64] M. Veljkovic and B. Johansson, *Design of hybrid steel girders,* Journal of Constructional Steel Research **60**, 535 (2004).

[65] NEN, *NEN 2443: Parkeren en stallen van personenauto's op terreinen en in garages* (Nederlandse Norm (NEN), 2013).

[66] ECCS, *Fire Safety in Open Car Parks*, 75 (ECCS, 1993).

[67] C. Haremza, A. Santiago, and L. Silva, *Design of open steel and composite car parks under fire,* Advanced Steel Construction **9**, 321 (2013).

[68] B. Fettah, *Fire analysis of car park building structures,* Master's thesis, Polytechnic Institute of Bragança (2016).

[69] Corus Construction & Industrial, *Steel-framed car parks*, Tech. Rep. (Corus, 2004).

[70] NEN, *NEN-EN 1990: Eurocode 0: Basis of structural design* (NEN, 2002).

[71] NEN, *NEN-EN 1990-1-1/NB: Dutch National Annex to Eurocode 0: Basis of Structural Design* (NEN, 2019).

[72] Steel Construction Institute (SCI), *Design of Floors for Vibration: A New Approach*, Tech. Rep. (SCI, 2007).

IV

CLOSURE

11

CONCLUSIONS AND PERSPECTIVES FOR FUTURE WORK

If I have seen further it is by standing on the shoulders of giants.

Isaac Newton

11.1. CONCLUSIONS

The research presented in this dissertation contributes to the development of demountable and reusable steel-concrete composite floor systems to enable the transition to a more sustainable construction sector. An important step towards this goal was the development of a novel (steel-reinforced) resin-injected demountable bolted shear connector. This shear connector is unique because of the oversized holes in the beam flange that enable the connection to be realised despite dimensional and geometrical deviations of the structural elements. During the service life, all demountable shear connectors contribute instantaneously and simultaneously to the shear interaction because the bolt-to-hole clearance is filled with a load-bearing (steel-reinforced) epoxy resin system.

This dissertation provides new knowledge on the (steel-reinforced) epoxy resin injectants as part of the demountable shear connector by devoting Part I to investigate the short- and long-term material properties of the materials. The application of the injectant in a bolted shear connection was considered in Part II based on the material models developed in Part I. Part III focused (amongst other aspects) on the effects of the shear connectors on a generic composite floor system and relied on the findings of Part II. This multi-scale approach enabled the evaluation of the behaviour or response for every level of scale. The main advantage was that only key characteristics obtained at a given level of scale (e.g. short- and long-term material models, shear connector stiffness) were necessary to predict the behaviour at a larger scale. This approach therefore simplified the design of a demountable and reusable steel-concrete composite floor system without compromising on accuracy.

The material-level research focused on the short- and long-term properties of the most commonly used epoxy resin systems in injected bolted connections in The Netherlands,

RenGel SW 404 + HY 2404/5159. Short term uniaxial compression tests indicated the beneficial effects of increasing the Young's Modulus of epoxy resin systems by adding spherical steel particles. This novel material, steel-reinforced resin, had a 180% higher Young's Modulus at a (typical) 60% particle volume fraction, and a similar uniaxial compressive strength. Unique outcomes of Chapter 3 are the development of a hybrid homogenisation method that could accurately predict Young's Modulus of the novel composite material, and the derivation of material constants and a hardening law for Drucker-Prager material models for the (steel-reinforced) epoxy resin injectants. One of the specific challenges was to obtain the tensile resistance of the composite material: a numerical homogenisation method was used to overcome a lack of reliable experiments. The short-term material models were complemented with deviatoric creep models based on the first ever long-term uniaxial compression tests on these specific materials. The material models for the (steel-reinforced) epoxy resin systems contribute to the literature by providing a scientific base to predict the response of injected bolted connections. The hybrid homogenisation method developed in this dissertation contributes to the literature by providing an approach to determine the Young's Modulus of generic composite materials based on known properties of the constituents.

Push-out tests on the proposed (steel-reinforced) resin-injected demountable shear connector system demonstrated their advantages in terms of connector stiffness compared to non-injected specimens. The main benefit is that all shear connectors engaged instantaneously and simultaneously in the shear force transfer. No statistical difference was found between the resistance of injected and non-injected connections ($p = 0.403$). Good agreement was observed between experimentally and numerically obtained results in terms of the connector resistance. A remarkable finding was that the secant stiffness could not be numerically reproduced because of hypothesised frictional and adhesive effects the components' interface due to the (steel-reinforced) epoxy resin. Based on finite element analysis, it was found that the secant shear connector stiffness at $0.4P_u$ was 80 kN/mm and 100 kN/mm (+25%) for resin-injected and steel-reinforced resin-injected specimens, respectively. The experimental push-out test results were compared to those obtained by Kozma for a similar shear connector type, which was only pretensioned to 70% of the bolt tensile resistance (but not injected). It was found that the pretensioned connector exhibited a 21% higher resistance due to additional force transfer by friction, but that substantial slip occurred once the friction resistance was overcome at $0.3 - 0.4P_u$. Such substantial slip did not occur in case of injected shear connectors because of the injectant fixated the location of the bolt: therefore injected shear connectors are more suitable than pretensioned shear connectors to develop significant composite interaction in a floor system under serviceability conditions. A finite element parameter study revealed that regardless of nominal hole clearance (varied in the range 6-20 mm), injected bolted shear connectors led to higher secant stiffness (+134% to +255%) compared to the experimental non-injected specimens (30 kN/mm). Another key finding was that the angle profile (120×120×10 mm) around the perimeter of the prefabricated concrete element did not contribute at all to the resistance if the concrete around the embedded coupler was adequately confined by a reinforcing Ø8 mm U-bar. Omitting the angle profile led to a significant (35-45%) increase of the secant stiffness because of reduced bolt bending, and would lead to lower costs in a practical application. Therefore omitting the U-bar around the embedded coupler was considered to

be the recommended design approach, although the omission causes the floor element to be more vulnerable to damage during its transportation and (dis)assembly.

Long-term push-out tests on steel-reinforced resin-injected specimens at 37%-48% of the short-term resistance revealed the sudden development of slip during load application or within the first two days after load application. It was reasoned that this sudden slip originates from material imperfections in either the injectant or concrete, which were mitigated for one of the specimens by 25 loading cycles between 5% and 40% of the short-term resistance prior to the start of the creep test. These loading cycles did not only prevent sudden slip, but also reduced the subsequent creep deformation by 46% in the time interval $4 \leq t \leq 14$ days. Companion steel-to-steel (steel-reinforced) resin-injected double lap shear connection tests were carried out at identical nominal bearing stresses to quantify the relative contributions of the injectant and concrete to the time-dependent slip. It was concluded based on the tests that if the steel-reinforced resin would be replaced by the epoxy resin system, the time-dependent slip would increase by a factor 1.8-2.0.

Material models for short- and long-term behaviour of the injectants were used to numerically predict the (time-dependent) response of the double lap steel-to-steel shear connections. Good agreement in terms of the instantaneous slip was found for all steel-reinforced resin-injected specimens, but only for resin-injected connections in case of relatively low nominal bearing stresses (75 and 125 MPa). The numerical prediction underestimated the deformation for larger nominal bearing stresses (175, 225 and 275 MPa) by 33-66%. The double-lap shear connection experiments demonstrated that the steel-reinforced resin-injected connections only exhibited 20-25% of the time dependent deformation of the resin-injected connections for the stress range $125 \leq \sigma_{\mathrm{b,nom}} \leq 225$ MPa over the time interval $1 \leq t \leq 100$ days. The long-term response of double lap shear connections with neither injectant could be accurately predicted using the developed short- and long-term material models: the slip increment was underestimated by a factor 3.7-8.3 for resin-injected specimens and by a factor 2.8-4.9 for steel-reinforced resin-injected specimens. Based on literature review, this substantial difference was hypothesised to be caused by a pressure-dependent creep mechanism, which was not included in the definition of the material model based on short- and long-term uniaxial compression tests.

Unique to this dissertation is the full-scale experimental work on a non-prismatic steel-concrete composite floor system with non-uniform shear connection. Prior work in the literature focused on floor systems with constant cross-section and with constant *uniform) spacing of the shear connectors. The requirement for reusability and demountability suggested a linear-elastic design approach for engineering practice to minimise the need for inspection of the structural components prior to reuse. The design of the experimental composite floor system addressed optimisation of resources by distributing the shear connectors in the most influential zone. The web of the steel beam was tapered to reduce deflection, to increase the (elastic) bending resistance, and to provide functional advantages (drainage) for a car park application. The experimental work on the composite floor system confirmed the need for significantly oversized holes (bolt diameter + 12 mm) necessary for the installation of large prefabricated concrete floor elements (7.2×2.6 m). A major contribution of this dissertation is the development of a statistical method to quantify the required magnitude of the oversized hole for a generic composite floor system design based on a user-defined probability of successful assembly. The experimental work on the composite floor system identified assembly processes and associated performance indicators

11

that could contribute to the implementation of demountable floor systems in engineering practice. Further experiments demonstrated the well-predicted structural response of the simply supported floor system for six different shear connector arrangements. The results confirmed the benefits (reduced deflection and slip) of concentrating the shear connectors near the supports that were reported based on theoretical linear-elastic considerations in the literature.

To enable the design of generic composite floor systems, this dissertation presented the first analytical prediction model for the linear-elastic response of non-prismatic steel-concrete composite floor systems with non-uniform shear connection. The prediction model was validated against the experimental results, and good agreement between experimentally and analytically obtained deflection and bending stresses was observed for all shear connector arrangements considered. In line with observations in the literature, disagreement was found in terms of the experimentally and analytically obtained magnitude of the interface slip. Additional experiments with highly lubricated steel-concrete interfaces did not lead to better agreement. Finite element analysis revealed consistency between the analytically and numerically obtained results in terms of both slip, deflection, and bending stresses. Therefore the discrepancy between experimentally and analytically obtained slip was hypothesised to originate from the experiments. Similar observations were also reported in prior literature. The shear connector stiffness k_{sc} used in the analytical and numerical prediction models was calibrated to a value of 55 kN/mm based on the experimental results on the composite floor system. This magnitude of k_{sc} was not in agreement with the shear connector stiffness based on push-out tests (80 kN/mm). The discrepancy between shear connector stiffness based on beam tests and push-out tests was also previously reported in the literature and present work confirms the disagreement without providing an explanation. This finding implies that push-out tests are not suitable to obtain a shear connector stiffness that is similar to that observed in beam experiments. Prediction models for the first eigenfrequency (relevant during service life for perception of human comfort) and out-of-plane resistance (relevant during execution) were derived and validated against results from the literature and/or results obtained by finite element analysis. The implications of the in-plane and out-of-plane prediction models were combined to derive a cross-section design optimisation strategy to maximise its resistance for equal cross-sectional area. The optimised cross-section design of an I-shaped section consists of equal area flanges, where the tensile flange is narrower but thicker (e.g 90×40 mm) compared to the compression flange (e.g 300×12 mm). This design strategy increases the critical bending moment (related to out-of-plane instability) significantly because of favourable influence of the inherently present bending stresses, whereas it only leads to negligible increases of the in-plane deflection. The increased critical bending moment may increase the speed of assembly and disassembly because no or fewer braces are required to stabilise the steel beam during execution.

11.2. PERSPECTIVES FOR FUTURE WORK

The research presented in this dissertation contributed to a better understanding of the three levels of scale (injectant, connector, and floor system) relevant to demountable and reusable steel-concrete floor systems. Further improvement to understand and predict the behaviour on each level of scale and to understand the relation between various scales is possible by conducting additional research.

On the material level, further experiments on (steel-reinforced) epoxy resin system Ren-Gel SW 404 + HY 5159 are recommended. Such investigations should particularly focus on understanding the time-dependent behaviour of the injectants to a greater extent. Particularly the pressure-dependent creep of the injectants, which was hypothesised in this dissertation to play an important role in the time-dependent deformation of injected bolted connections, should be investigated. In addition, the viscoelastic/plastic response of the epoxy resin system should be further addressed to improve the capability of the material model to predict the instantaneous slip of resin-injected bolted connections at nominal bearing stresses larger than 125 MPa.

On the connector level, further investigation on the time-dependent response of the demountable shear connector is suggested because this dissertation considered only five specimens subject to a sustained load for a fourteen-day period. Also long-term push-out tests on nominally identical but non-injected specimens should be performed to accurately (without the need for assumptions) quantify the contributions of the concrete and injectant to the time-dependent slip. In addition, the short-term response of push-out specimens without angle profiles could be experimentally addressed, to confirm that the omission does not decrease the resistance but does increase the shear connector stiffness as long as the concrete is sufficiently well confined. The hand-calculation model of Pavlovic for the concrete bearing resistance of bolted shear connectors with single embedded nut could be modified to account for the comparatively larger height of the coupler.

On the level of the composite floor system, it would be relevant to quantify geometrical and dimensional deviations of prefabricated floor elements to prevent execution problems. Such data could be used to improve the prediction model for the required nominal hole clearance presented in Chapter 8. Also of particular importance is to investigate the cause for the discrepancy between the shear connector stiffness observed in beam tests and push-out tests. The experimental work on the large-scale composite floor system only considered resin-injected bolted shear connectors: further experiments could determine the practical feasibility of injecting steel-reinforced resin and could quantify its beneficial effects on the structural response of the floor system. It is suggested to experimentally investigate the lateral-torsional buckling behaviour of composite floor systems with large discrete prefabricated floor elements to confirm the theoretically derived sensitivity to out-of-plane instability. To enable practitioners to design demountable and reusable composite floor systems, it would be useful to derive design equations for the resistance and deformation of generic designs based on the 'exact' solutions proposed in this dissertation.

The aforementioned research recommendations pertain to the scope of this dissertation. However, expanding the focus to include infrastructure and cyclically loaded structures (e.g. bridges, viaducts) would further increase the sustainability potential within the construction sector.

11

APPENDICES

A

INPUT DATA FOR SHORT-TERM (STEEL-REINFORCED) RESIN MATERIAL MODELS

INTRODUCTION

This Appendix presents the input data for the short-term (steel-reinforced) resin material models for use in ABAQUS based on the work performed in Chapter 3. The basic units are Newton, millimetres and degrees. Hardening is defined in compression.

A

A.1. RENGEL SW 404 + HY 2404
A.1.1. RESIN

Associative flow

```
*Material, name=R-2404-Assoc
*Density
1.8e-06,
*Drucker Prager
10.33,  0.93, 10.33
*Drucker Prager Hardening
80.,         0.
85., 0.00120146
90., 0.00257954
95., 0.00409868
100., 0.00571089
105., 0.00774785
110.,  0.0102398
115.,  0.0133859
120.,  0.0185948
125.,  0.0351337
130.,  0.0732029
135.,   0.106261
140.,   0.156484
*Elastic
5640., 0.315
```

Non-dilatant flow

```
*Material, name=R-2404-NonDil
*Density
1.8e-06,
*Drucker Prager
10.70,  1., 0.
*Drucker Prager Hardening
80.,         0.
85., 0.00120146
90., 0.00257954
95., 0.00409868
100., 0.00571089
105., 0.00774785
110.,  0.0102398
115.,  0.0133859
120.,  0.0185948
125.,  0.0351337
130.,  0.0732029
135.,   0.106261
140.,   0.156484
*Elastic
5640., 0.315
```

A.1.2. STEEL-REINFORCED RESIN

Associative flow

```
*Material, name=SRR-2404-Assoc
*Drucker Prager
38.3, 0.78, 38.3
*Drucker Prager Hardening
115.,         0.
120., 0.00267516
95.,  0.0126752
20.,  0.0326752
*Elastic
15700., 0.22
**
```

Non-dilatant flow

```
*Material, name=SRR-2404-NonDil
*Drucker Prager
39.44,1.,0.
*Drucker Prager Hardening
115.,         0.
120., 0.00267516
95.,  0.0126752
20.,  0.0326752
*Elastic
15700., 0.22
**
```

A.2. RENGEL SW 404 + HY 5159

A.2.1. RESIN

Associative flow

```
*Material, name=R-5159-Assoc
*Drucker Prager
10.33,  0.93, 10.33
*Drucker Prager Hardening
80.,     0.
100.,  0.004
120., 0.0115
115., 0.0395
110., 0.0895
106., 0.1895
*Elastic
7818., 0.315
```

Non-dilatant flow

```
*Material, name=R-5159-NonDil
*Drucker Prager
10.7,1.,0.
*Drucker Prager Hardening
80.,     0.
100.,  0.004
120., 0.0115
115., 0.0395
110., 0.0895
106., 0.1895
*Elastic
7818., 0.315
```

A.2.2. STEEL-REINFORCED RESIN

Associative flow

```
*Material, name=SRR-5159-Assoc
*Drucker Prager
35.74,  0.78, 35.74
*Drucker Prager Hardening
100.,       0.
135., 0.003871
130., 0.007371
100., 0.015434
20., 0.035434
*Elastic
21900., 0.22
```

Non-dilatant flow

```
*Material, name=SRR-5159-NonDil
*Drucker Prager
36.54,1.,0.
*Drucker Prager Hardening
100.,        0.
135., 0.003871
130., 0.007371
100., 0.015434
20., 0.035434
*Elastic
21900., 0.22
```

B

DUCTILE DAMAGE MODEL FOR BOLTS USED IN PUSH-OUT TESTS

INTRODUCTION

This Appendix contains the experimentally obtained stress-strain curves and the corresponding ductile damage model for the injection bolts used in the *push-out* tests presented in Chapter 5. Attention is drawn to the shear-dominated failure mode of the bolt in the push-out tests: initiation and evolution of shear damage is discussed on page 114.

EXPERIMENTAL WORK

The uniaxial tensile stress-strain relation of the injection bolts used in the *push-out* tests was determined by coupon tests. The as-received bolts were milled to a reduced diameter of 5 mm over a length L_c = 22 mm, which was less than the 27.5 mm required by ISO 6892-1 [1] due to the limited physical length of the bolts. The transition radius between the original and reduced cross-section was 8 mm, and the thread engagement was 10 mm: see the insert to Figure B.2 for a schematic overview of the specimens.

The specimens were installed in a fixture, see Figure B.1, and loaded by monotonically increasing the displacement of the hydraulic actuator at 0.025 mm/s. The elongation of the bolt within the parallel section of the specimen could not be determined due to the limited length of the bolt and the physical constraints imposed by the fixture. Instead, the relative displacement between the fixture elements was measured by two LVDTs, see Figure B.1.

The experimentally obtained data in the linear-elastic branch of the load-elongation curve was fitted to match the theoretical behaviour of a bar element in uniaxial tension. It was assumed from pre-knowledge that E = 210 GPa, whereas the area A and the length of the reduced section L_c were based on the actual dimensions of the specimens.

The strain at the onset of yielding is given by

$$\varepsilon_y = \frac{F_y}{EA},$$ (B.1)

where F_y is the force to initiate plastic deformation, corresponding to a nominal stress of

Figure B.1 | Fixture to apply a tensile load to the coupon specimens with two external LVDTs to measure the elongation.

$\sigma_y = F_y / A$. The first non-zero point on the stress-strain curve is then $(\varepsilon_y, \sigma_y)$. This approach implicitly assumes that all elastic deformation occurred in the reduced section length L_c, which is justified because (i) the cross-sectional area is substantially larger in all other parts of the specimen and (ii) those other parts are comparatively short.

All elongation beyond the elastic limit was assumed to occur within the reduced section, which in addition to previous arguments (i) and (ii) is justified because (iii) the development of plastic strains outside the reduced section zone is negligible. The elongation increment was converted to a plastic strain increment by division through L_c. The sum of the cumulative plastic strain ε_p and the elastic strain at first yield ε_y is the total strain ε.

The engineering stress-strain curves of the specimens are illustrated in Figure B.2. Yielding initiated at an average nominal tensile stress $\sigma_{y,mean} = 812$ MPa, and the average ultimate tensile strength was $\sigma_{u,mean} = 879$ MPa. These values were regarded as representative of the whole batch, such that the yield strength and the ultimate strength of the bolts could also be denoted by $f_{yb} = \sigma_{y,mean} = 812$ MPa and $f_{ub} = \sigma_{u,mean} = 879$ MPa. The ratio f_{yb} / $f_{ub} = 0.92$ was substantially larger than the nominal ratio 0.8 [2]. The mean nominal strain at fracture $\varepsilon_{r,mean}$ was 16%.

DERIVATION OF DUCTILE DAMAGE MODEL PARAMETERS

A finite element representation of the reduced section of the specimens was developed in ABAQUS. The elastic material parameters were set as $E = 210$ GPa and $\nu = 0.30$. Progressive damage models were iteratively calibrated to match the numerical to the experimental results using the dynamic explicit solver and variable, non-uniform mass scaling.
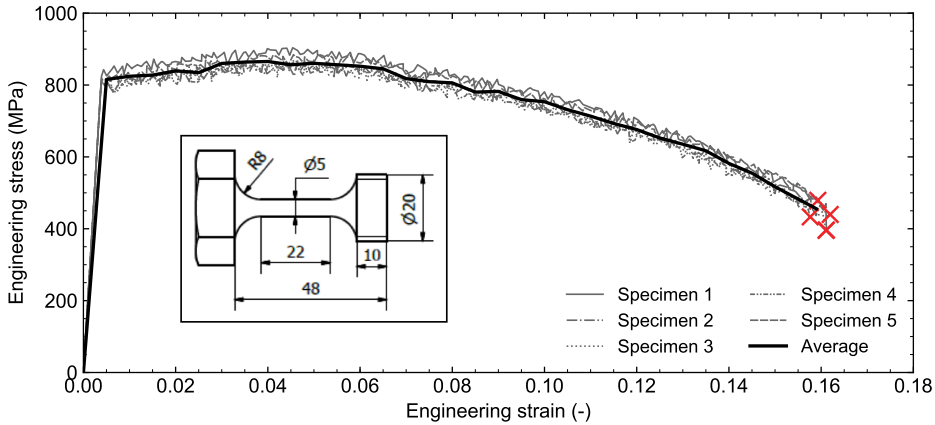
Figure B.2 | Engineering stress-strain curves for the coupon specimens of the injection bolts used in the *push-out* tests.

DAMAGE INITIATION

The damage initiation criterion for the external injection bolts was defined in terms of the equivalent plastic strain at the onset of damage, denoted by $\bar{\varepsilon}_0^{\text{pl}}$, as a function of the stress triaxiality θ (the ratio of hydrostatic stress over equivalent stress). Pavlovic [3] proposed to define the relation between stress triaxiality θ and $\bar{\varepsilon}_0^{\text{pl}}$ analogously to the relation between θ and the equivalent plastic strain at fracture $\bar{\varepsilon}_f^{\text{pl}}$, for which Trattnig et al. [4] and Rice & Tracy [5] proposed an exponential dependency given by

$$\bar{\varepsilon}_f^{\text{pl}} = \alpha \exp\{-\beta\theta\}, \tag{B.2}$$

where α and β are model parameters.

For the uniaxial conditions in present experiments $\theta = 1/3$, and the equivalent plastic strain at fracture $\bar{\varepsilon}_f^{\text{pl}}$ equalled the uniaxial plastic strain at fracture $\varepsilon_f^{\text{pl}}$. Pavlovic [3] proposed to assume that the ratio of equivalent plastic strain at fracture over the uniaxial plastic strain at fracture is a proxy for the ratio of equivalent plastic strain at the onset of damage over the uniaxial plastic strain at the onset of damage, which is expressed by

$$\frac{\bar{\varepsilon}_f^{\text{pl}}}{\varepsilon_f^{\text{pl}}} = \frac{\bar{\varepsilon}_0^{\text{pl}}}{\varepsilon_0^{\text{pl}}}, \tag{B.3}$$

and which was solved in terms of the equivalent plastic strain at the onset of damage as

$$\bar{\varepsilon}_0^{\text{pl}} = \varepsilon_0^{\text{pl}} \exp\left\{-\beta\left(\theta - \frac{1}{3}\right)\right\}. \tag{B.4}$$

Trattnig et al. [4] and Rice & Tracy [5] proposed $\beta = 1.88$ and $\beta = 1.5$, respectively. Myers et al. [6] proved that the latter value is adequate for all steel, and Pavlovic [3] successfully used it to model the fracture of steel bolts and plates. On this basis $\beta = 1.5$ was adopted in present work. Damage was assumed to occur after the initiation of necking, therefore $\varepsilon_0^{\text{pl}} = \varepsilon_n^{\text{pl}}$, where the subscript "n" represents necking.

B

DAMAGE EVOLUTION

Once the damage initiation criterion was met, the localisation of strains during necking was accounted for by fictitiously reducing the initial reduced section length L_c (assumed equal to the gauge length) to $L_{c,i}$, where i is a variable describing the relative position on the strain axis, see Figure B.3(a). The strain localisation was implemented by a power law [3] as

$$L_{c,i} = \begin{cases} L_c & \text{if } i < n, \\ L_c + (L_{loc} - L_c)\left[\dfrac{\Delta L_i - \Delta L_n}{\Delta L_r - \Delta L_n}\right]^{\alpha_L} & \text{if } i \geq n, \end{cases} \tag{B.5}$$

where ΔL_n, ΔL_i and ΔL_r represent the elongation of the specimen at the onset of necking, at point i, and at rupture, respectively. The fitting parameters of the model are L_{loc} (strain localisation length) and α_L (localisation rate factor), whereas ΔL_n and ΔL_r followed from the experimental results. The localised engineering strain was determined based on the assumption that all additional elongation after the onset of necking occurred within the strain localisation length $L_{c,i}$, following the relation

$$\varepsilon_i = \begin{cases} \Delta L_i / L_{c,i} & \text{if } i < n, \\ \varepsilon_{i-1} + (\Delta L_i - \Delta L_{i-1}) / L_{c,i} & \text{if } i \geq n. \end{cases} \tag{B.6}$$

This relationship originates from the work of Pavlovic [3].

The undamaged response was assumed to follow the engineering stress-strain curve until the onset of necking, followed by a horizontal plateau. The undamaged true stress-strain curve was determined using the localised strain, see Figure B.3(a). The damaged response was based on the full engineering stress-strain curve (including post-necking branch), and was also converted to a true stress-strain curve based on the localised strain, see Figure B.3(a). The damage variable D was introduced as the difference between unity and the ratio of undamaged true stress $\overline{\sigma}'$ over damaged true stress σ', multiplied by a damage eccentricity factor α_D. This approach was proposed by Pavlovic [3], and is expressed by

$$D_i = \begin{cases} \left(1 - \dfrac{\sigma'_i}{\overline{\sigma}'_i}\right)\alpha_D & \text{if } n \leq i \leq r, \\ 1 & \text{if } i = f. \end{cases} \tag{B.7}$$

In case $D_i = 1$ the element under consideration is removed from the mesh because its mechanical properties are fully degraded.

The equivalent plastic displacement $\overline{u}_i^{pl}$, corresponding to the state of the damage variable D_i, was derived based on the proportionality of $\overline{u}_i^{pl}$ to the localised strains in the necking region following the proposed by Pavlovic [3]. This proportionality is given by

$$\overline{u}_i^{pl} = \overline{u}_f^{pl}\left[\dfrac{\varepsilon_i^{pl} - \varepsilon_n^{pl}}{\varepsilon_f^{pl} - \varepsilon_n^{pl}}\right], \tag{B.8}$$

where $\overline{u}_f^{pl}$ is the mesh-dependent equivalent plastic displacement accumulated in the necking stage, given by

$$\overline{u}_f^{pl} = \lambda_S \lambda_E L_E \left(\varepsilon_f^{pl} - \varepsilon_n^{pl}\right), \tag{B.9}$$

where λ_S and λ_E are a finite element size and finite element type factor, respectively. For C3D4 tetrahedral elements, $\lambda_S = 0.79$ and $\lambda_E = 1.00$ based on Pavlovic [3]. The finite element size is denoted by L_E and should be kept constant in the localisation zone. In present work $L_E = 1.2$ mm.

Figure B.3 illustrates the principles behind the derivation of the damage parameters, as well as the damage initiation criterion and the damage evolution law.

CALIBRATION

The parameters α_D, L_{loc} and α_L are fitting parameters and have been iteratively calibrated to match the experimental results. The damage eccentricity factor α_D was calibrated as 1.85, which is similar to the value 1.7 reported by Pavlovic [3]. The localisation length was fitted as $L_{loc} = 3.4$ mm. The strain localisation factor α_L was evaluated as 0.85, larger than the range 0.3 - 0.5 reported by Pavlovic [3]. Potentially such discrepancy occurred because the magnitudes of α_D, L_{loc} and α_D may not be necessarily material constants but, for instance, also depend on size effects: in present work the diameter was 5 mm, compared to 8 mm for Pavlovic [3].

The experimentally obtained stress-strain curves are shown together with the numerical results in Figure B.4. Good agreement was observed in the elastic, strain hardening, necking and fracture phases.

B
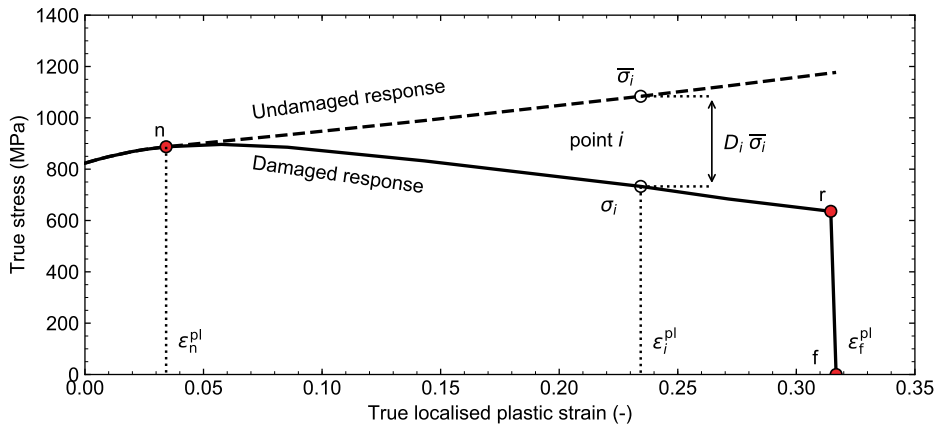
(a) Plasticity curve and damage variable.
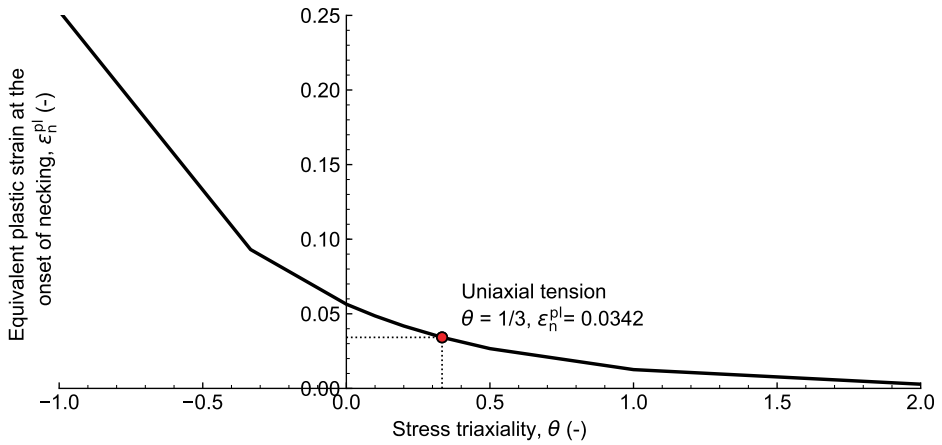
(b) Damage initiation criterion.
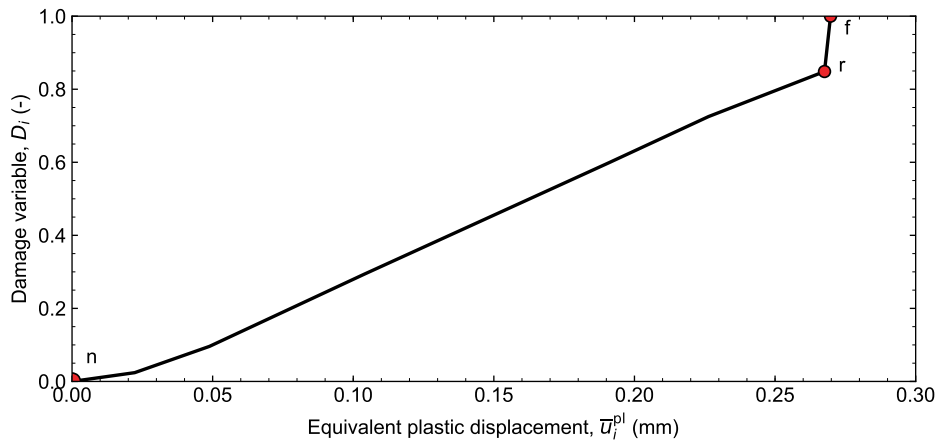
(c) Damage evolution law.

Figure B.3 | Overview of the ductile damage model for the coupon specimens of the injection bolts used in the *push-out* tests.
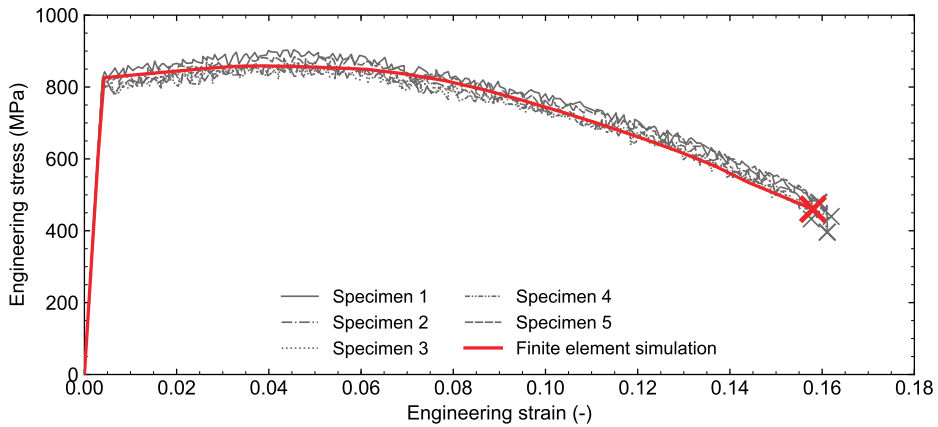
Figure B.4 | Experimental stress-strain curve of the injection bolts used in the *push-out* tests, complemented with the results of finite element simulation based on the calibrated ductile damage model.

References

[1] ISO, *ISO 6892-1: Metallic materials , tensile testing - Part 1: Method of test at room temperature* (ISO, 2009).

[2] ISO, *ISO 898-1: Mechanical properties of fasteners made of carbon steel and alloy steel - Part 1: Bolts, screws and studs with specified property classes - Coarse thread and fine pitch thread* (ISO, 2013).

[3] M. Pavlović, Z. Marković, M. Veljković, and D. Buđevac, *Bolted shear connectors vs. headed studs behaviour in push-out tests,* Journal of Constructional Steel Research **88**, 134 (2013).

[4] G. Trattnig, T. Antretter, and R. Pippan, *Fracture of austenitic steel subject to a wide range of stress triaxiality ratios and crack deformation modes,* Engineering Fracture Mechanics **75**, 223 (2008).

[5] J. R. Rice and D. M. Tracey, *On the ductile enlargement of voids in triaxial stress fields,* Journal of the Mechanics and Physics of Solids **17**, 201 (1969).

[6] A. T. Myers, A. M. Kanvinde, and G. G. Deierlein, *Calibration of the SMCS criterion for ductile fracture in steels: Specimen size dependence and parameter assessment,* Journal of Engineering Mechanics **136**, 1401 (2010).

C

CONCRETE DAMAGE MODEL FOR PUSH-OUT ELEMENTS

INTRODUCTION

This Appendix contains the Concrete Damage Plasticity (CDP) material model parameters used to describe the tensile and compressive behaviour of the concrete *push-out* elements. Distinction is made between parameters related to the actual material properties (to predict/validate experimental behaviour) and nominal material properties (to be used for the parametric study).

C.1. ACTUAL MATERIAL PROPERTIES

The average uniaxial cube compressive strength of the concrete *push-out* elements, see Section 5.1.1, was determined as $f_{cm,cube} = 48.2$ MPa. The cube compressive strength was converted to the cylinder compressive strength through $f_{cm} = 0.8 f_{cm,cube} = 38.6$ MPa [1]. The tensile strength of the concrete was not experimentally obtained, but was been derived based on EN 1992-1-1 [1] as $f_{ctm} = 0.30 f_{ck}^{(2/3)} = 2.9$ MPa with $f_{ck} = f_{cm} - 8$ MPa.

COMPRESSIVE STRESS-STRAIN RELATION

The EN 1992-1-1 [1] relation between uniaxial compressive stress and strain was used[1], given by

$$\sigma_c = f_{cm} \frac{k\eta - \eta^2}{1 + (k-2)\eta} \quad \text{for } 0 < |\varepsilon_c| < |\varepsilon_D|, \tag{C.1}$$

where $\eta = \varepsilon_c / \varepsilon_C$ represents the ratio of the actual strain over the strain at f_{cm}, and $k = 1.05 E_{cm} |\varepsilon_C| / f_{cm}$, with E_{cm} the mean Young's Modulus of the concrete. The EN 1992-1-1 compressive stress-strain relation is illustrated in Figure C.1, where point A represents the zero-stress state, point B denotes the nominal onset of non-linearity, point C denotes the compressive strength and point D represents nominal material failure. The subscripts C

---

[1] It should be noted that alternatives similar to the EN 1992-1-1 formulation exist, e.g. in References [2, 3]

and D in Equation C.1 refer to points C and D in Figure C.1, respectively. Magnitudes of ε_C, ε_D, f_{cm} and E_{cm} are specified in EN 1992-1-1 [1].

The softening branch of the compressive stress-strain curve is only defined until $\varepsilon_D = 0.35\%$, which is comparatively small to the potential strain. Pavlovic[2] [5] modelled the softening branch by extending the EN 1992-1-1 formulation by a sinusoidal part D-E and a linear part E-F, see Figure C.1, which was successfully used by Milosavljevic et al. [6] and Spremic et al. [7] to model push-out experiments. These extensions are expressed by

$$
\sigma_c = \left\{
\begin{array}{ll}
f_{cm}\left[\dfrac{1}{\beta} - \dfrac{\sin\left(\mu^{\alpha_{tD}}\alpha_{tE}\frac{\pi}{2}\right)}{\beta\sin\left(\alpha_{tE}\frac{\pi}{2}\right)} + \dfrac{\mu}{\alpha}\right] & \text{if } \varepsilon_D < \varepsilon_c \leq \varepsilon_E, \\
\dfrac{\sigma_E\left(\varepsilon_F - \varepsilon_c\right) + \sigma_F\left(\varepsilon_c - \varepsilon_E\right)}{\varepsilon_F - \varepsilon_E} & \text{if } \varepsilon_c > \varepsilon_E,
\end{array}
\right.
\tag{C.2}
$$

where μ is the relative coordinate between points D and E, $\beta = f_{cm}/\sigma_D$, and where capital subscripts denote the value at the respective point. The stress σ_D follows from Equation C.1, while $\sigma_E = \alpha f_{cm}$ and $\sigma_F = 0.4$ MPa. The remaining variables are taken from Pavlovic [5] as $\varepsilon_E = 0.03$, $\varepsilon_F = 0.10$, $\alpha = 20$, $\alpha_{tD} = 0.5$ and $\alpha_{tE} = 0.9$. The latter two parameters ensure a smooth transition between the three distinct parts of the stress-strain curve.

TENSILE STRESS-STRAIN RELATION

The uniaxial tensile stress-strain curve consists of two parts, (i) a linear-elastic region until the ultimate tensile strength f_{ctm} and (ii) a subsequent softening branch. The ultimate tensile strength was determined as $f_{ctm} = 0.30\left(f_{cm} - 8\right)^{2/3}$ [1]. During softening, the stress reduces from f_{ctm} to $\sigma_t = 0.05 f_{ctm}$ at a cracking strain $\varepsilon_t = 0.00108$ in a sinusoidal manner [5], as shown in Figure C.2.

CONCRETE DAMAGE PLASTICITY (CDP) MODEL

The compressive and tensile behaviour of the concrete are implemented in ABAQUS using the embedded Concrete Damage Plasticity (CDP) model, which is based on the work of Lubliner et al. [8] and Lee & Fenves [9], and which is a modification of the Drucker Prager model introduced in Section 3.4.1. The ratio of biaxial to uniaxial compressive strength was set as 1.20 [5, 6, 10], which is also supported by a three-dimensional mesostructure study by Huang et al. [11]. The dilatation angle was taken as $\psi = 36°$ [5, 7, 12] and the flow potential eccentricity as 0.1 [5, 6, 12]. The Young's Modulus was set as $E_{cm} = 34.7$ GPa and $\nu = 0.20$ [1].

The damage variables in tension and compression evolve based on the uniaxial response as $D_t = 1 - \sigma_t/f_{ctm}$ and $D_c = 1 - \sigma_c/f_{cm}$, respectively, on the softening branch. No damage develops on the ascending branch of the uniaxial stress-strain curves.

---

[2]Alternative formulations for the softening branch can be found in Chinese Code GB50010 and in References [3, 4]
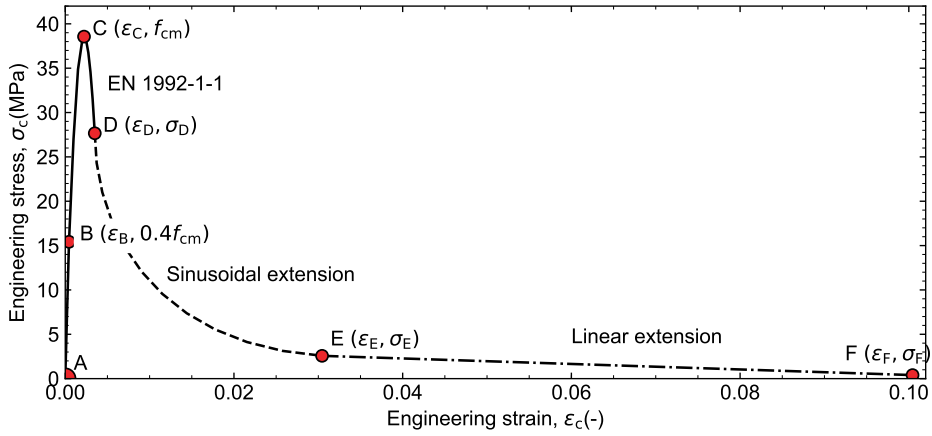
(a) Stress versus strain.
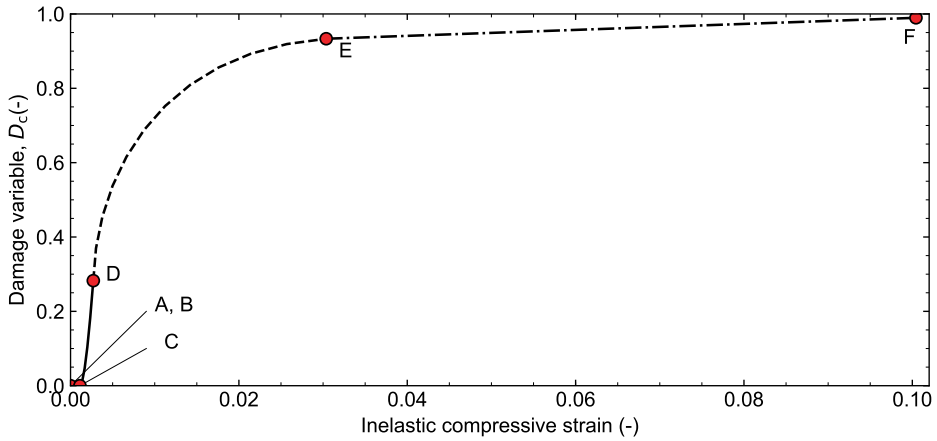
(b) Damage variable versus inelastic strain.

Figure C.1 | Concrete compression material model for the experimentally obtained $f_{cm,cube} = 48.2$ MPa.

C

C
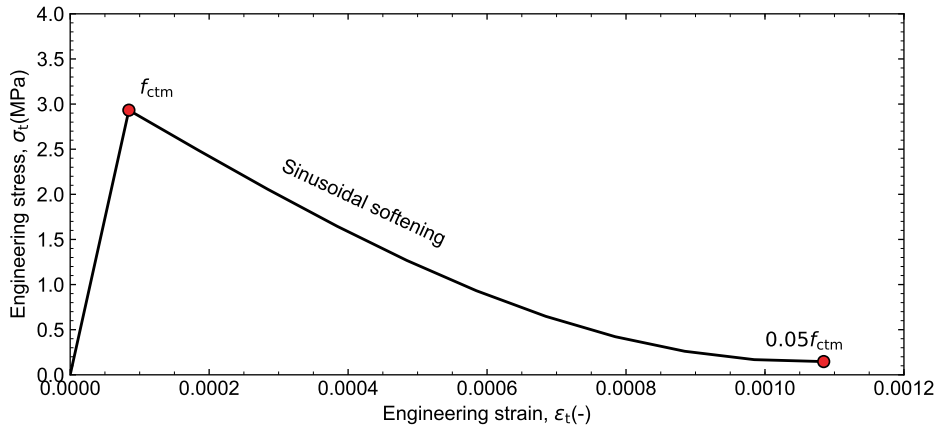
(a) Stress versus strain.
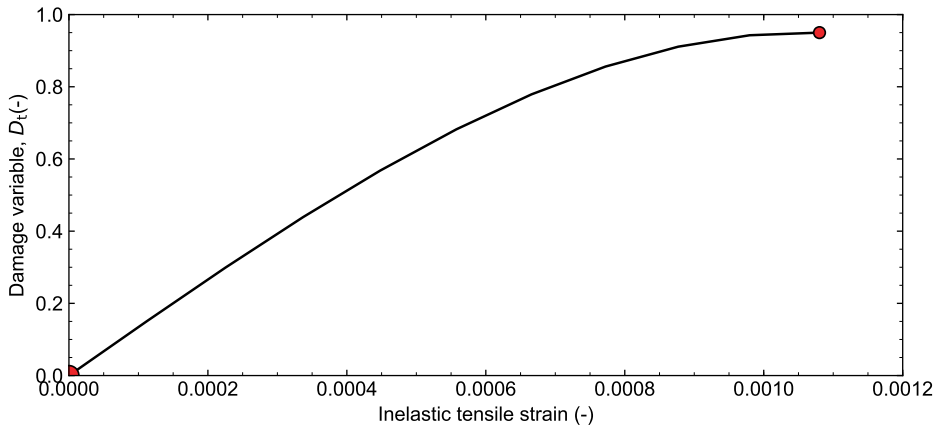
(b) Damage variable versus inelastic strain.

Figure C.2 | Concrete tension material model for the experimentally obtained f_{cm} = 48.2 MPa.

C.2. NOMINAL MATERIAL PROPERTIES

Nominal (mean) concrete material properties were used in the parameter study described in Section 5.3, and are based on EN 1992-1-1[1]. The stress-strain curves and concrete damage plasticity models for strength classes C20/25, C30/37 and C40/50 [1] were derived based on the same approach as outlined in Section C.1, and are illustrated in Figure C.3 .

C
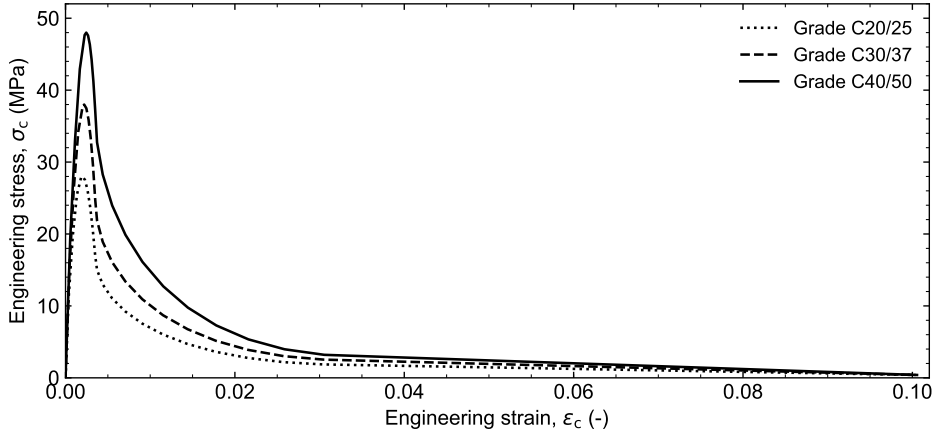
(a) Compression.
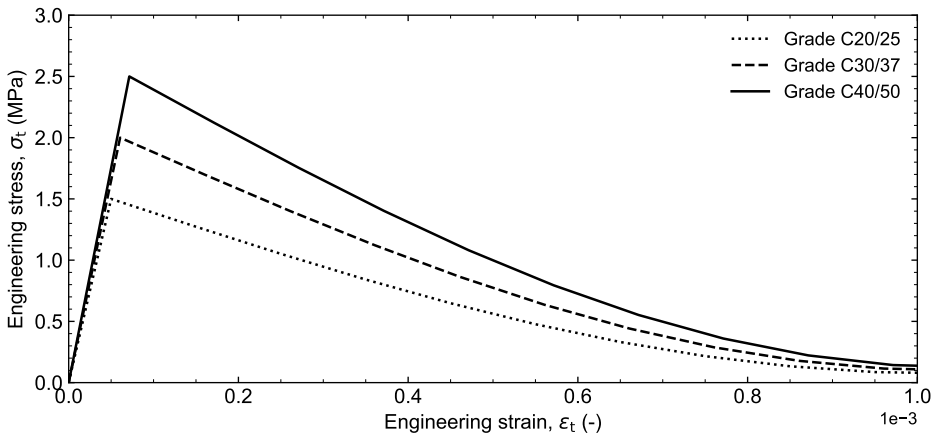
(b) Tension.

Figure C.3 | Nominal concrete model for strength grades C20/25, C30/37 and C40/50.

REFERENCES

[1] NEN, *NEN-EN 1992-1-1: Eurocode 2: Design of concrete structures - Part 1-1: General rules and rules for buildings* (NEN, 2011).

[2] D. J. Carreira and K. han Chu, *Stress-strain relationship for plain concrete in compression,* Journal of the American Concrete Institute (1985).

[3] F. Ding, X. Ying, L. Zhou, and Z. Yu, *Unified calculation method and its application in determining the uniaxial mechanical properties of concrete,* Frontiers of Architecture and Civil Engineering in China **5**, 381 (2011).

[4] S. W. Pathirana, B. Uy, O. Mirza, and X. Zhu, *Bolted and welded connectors for the rehabilitation of composite beams,* Journal of Constructional Steel Research **125**, 61 (2016).

[5] M. Pavlović, Z. Marković, M. Veljković, and D. Buđevac, *Bolted shear connectors vs. headed studs behaviour in push-out tests,* Journal of Constructional Steel Research **88**, 134 (2013).

[6] B. Milosavljevic, I. Milicevic, M. Pavlovic, and M. Spremic, *Static behaviour of bolted shear connectors with mechanical coupler embedded in concrete,* Steel and Composite Structures **29** (2018).

[7] M. Spremic, M. Pavlovic, Z. Markovic, M. Veljkovic, and D. Budjevac, *FE validation of the equivalent diameter calculation model for grouped headed studs,* Steel and Composite Structures **26** (2018).

[8] J. Lubliner, J. Oliver, S. Oller, and E. Oñate, *A plastic-damage model for concrete,* International Journal of Solids and Structures **25**, 299 (1989).

[9] J. Lee and G. L. Fenves, *Plastic-damage model for cyclic loading of concrete structures,* Journal of Engineering Mechanics **124**, 892 (1998).

[10] CEB-FIP, *CEB-FIP MODEL CODE 1990* (Thomas Telford Publishing, 1993) pp. 1–32.

[11] Y.-Q. Huang, S.-W. Hu, and Y.-Y. Sun, *The Effect of Inner Friction on Concrete Fracture Behavior under Biaxial Compression: A 3D Mesostructure Study,* Materials **12**, 3880 (2019).

[12] K. Śledziewski, *Selection of appropriate concrete model in numerical calculation,* ITM Web of Conferences **15**, 07012 (2017).

C

D

LOAD-SLIP DIAGRAMS FOR PUSH-OUT TEST PARAMETER STUDY

INTRODUCTION

This Appendix contains the load-slip curves for the parameter study, in which geometrical and material properties of the demountable shear connector were varied with respect to a reference design. The details of this reference connector design can be found in Section 5.3.

Figures D.1-D.6 illustrate the load-slip curves for variations in connector spacing, bolt diameter, bolt grade, confinement of the concrete around the connector, concrete strength class and nominal hole clearance, respectively. A summary of the results is given in Section 5.3.3 in terms of connector stiffness and resistance.

D
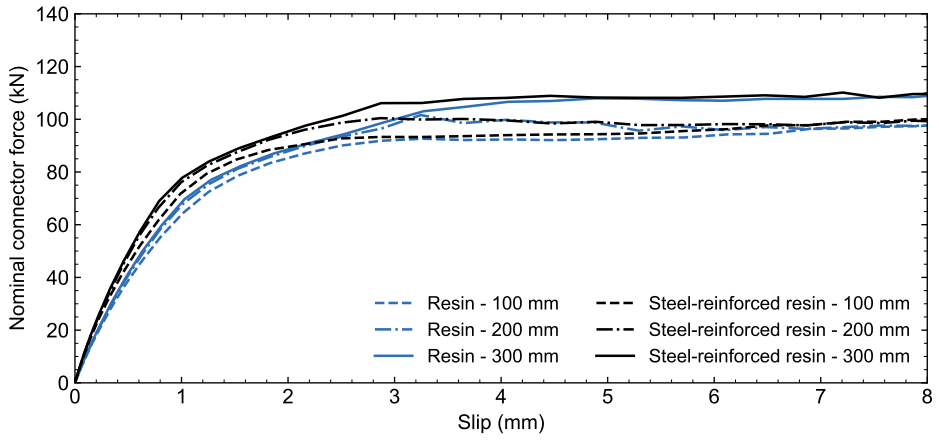
Figure D.1 | Load-slip diagram for variations in connector spacing.
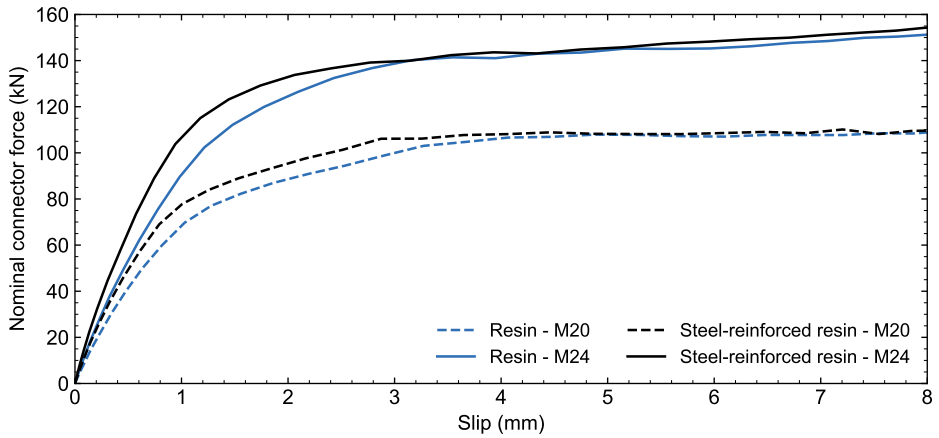
Figure D.2 | Load-slip diagram for variations in bolt diameter.
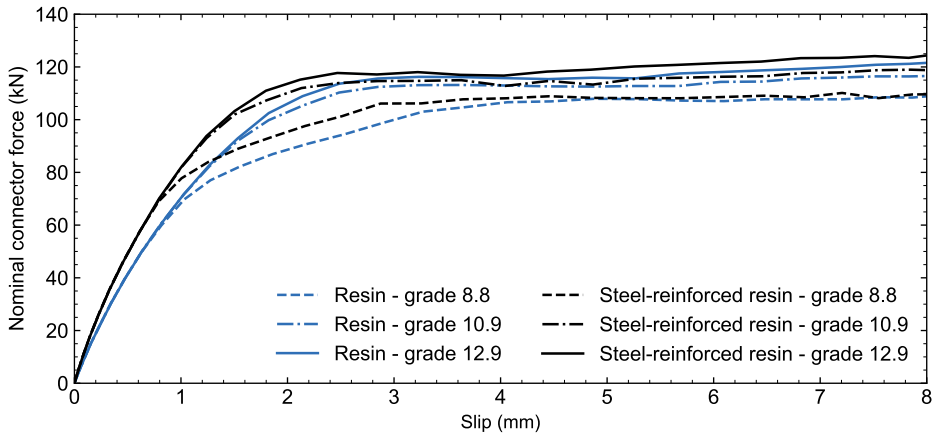
Figure D.3 | Load-slip diagram for variations in bolt grade.
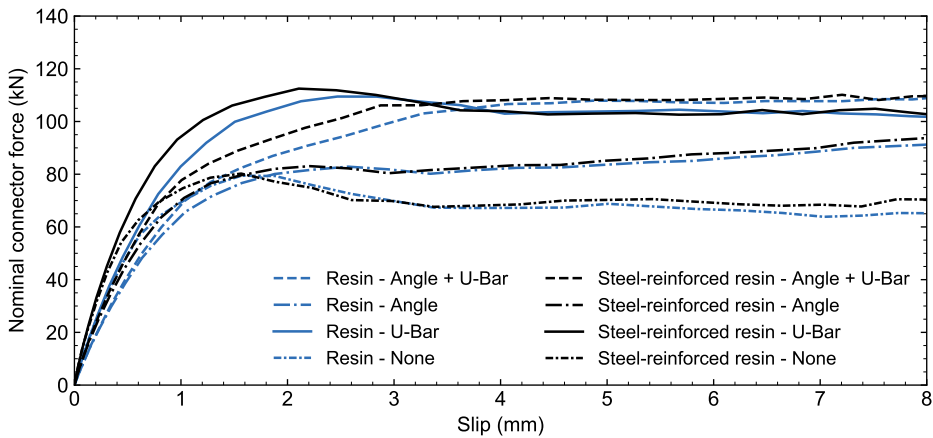
Figure D.4 | Load-slip diagram for variations in confinement of the concrete around the shear connector.
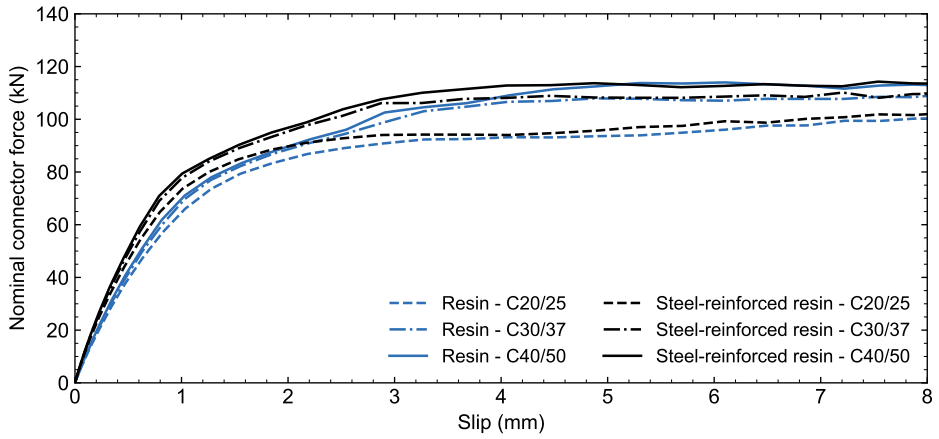
Figure D.5 | Load-slip diagram for variations in concrete strength class.
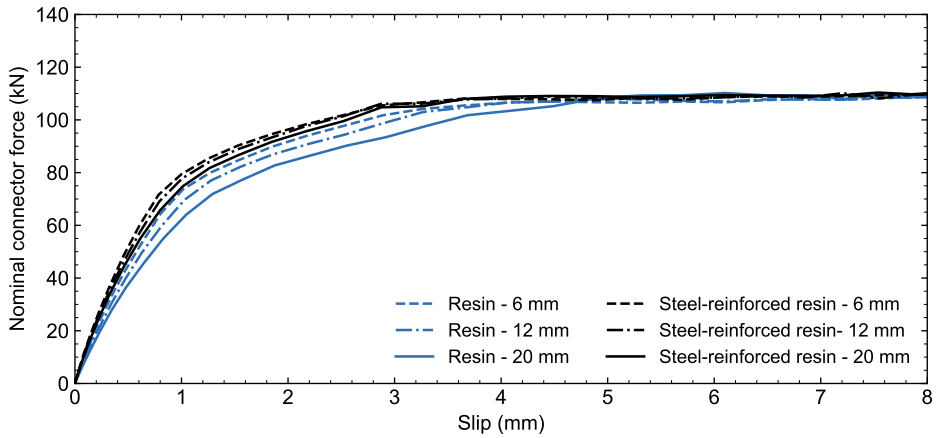
Figure D.6 | Load-slip diagram for variations in nominal hole clearance.

E

MATERIAL AND EXECUTION COSTS

Actual and estimated costs related to materials and execution of the resin-injected demountable shear connector are summarised in Tables E.1 and E.2. It should be noted that cost data is highly location, volume, time and context dependent, and it is presented only as an indication and for the sake of comparison.

Table E.1 | Shear connector material costs (all galvanised).

Item/material/process	Price (€)	Price per	Source
Injection bolt, M20×50 mm, grade 8.8	3,-	piece	experiment costs
Coupler, M20, grade 10.9	3.10	piece	experiment costs
Bolt, M20×50 mm, grade 8.8	0.75	piece	experiment costs
Injection washer, M20	0.75	piece	experiment costs

Table E.2 | Execution costs.

Item/material/process	Price (€)	Price per	Source
Resin injection, including	2.50	shear connector	experiment cost

- Resin and consumables

- Release agent (ACMOS 82-2404)

- Labour

F

DESIGN FORMULAE FOR DEFLECTION AND SLIP OF WEB-TAPERED STEEL BEAMS DURING EXECUTION

To develop design formulae for the deflection and end-slip for simply-supported web-tapered composite floor systems during execution, regression analysis is performed on results obtained by solving the Euler-Bernoulli differential equation for beams subject to bending around their strong y-axis.[1] The objective is to find suitable modifications to the well-known deflection and slip solutions to generalise their applicability to web-tapered sections.

EXACT SOLUTION FOR DEFLECTION

The midspan deflection w_m for a generic simply supported steel beam, symmetric with respect to midspan, on which prefabricated concrete floor elements with self-weight per unit length q_z are simultaneously installed is

$$w_\mathrm{m} = \int_0^{L/2} \frac{M}{EI_0} x \, \mathrm{d}x = \int_0^{L/2} \frac{1}{2} \frac{q_z x (L-x)}{EI_0} x \, \mathrm{d}x, \tag{F.1}$$

according to Euler-Bernoulli beam theory, where EI_0 is the bending stiffness of the steel beam without composite interaction. For prismatic beams the solution to the former expression is

$$w_\mathrm{m} = \frac{5}{384} \frac{q_z L^4}{EI_0}. \tag{F.2}$$

---

[1]See Figure 8.1 for the axes convention.

EXACT SOLUTION FOR SLIP

The slip at the supports s_0 for a generic simply supported steel beam, symmetric with respect to midspan, on which prefabricated concrete floor elements with self-weight per unit length q_z are simultaneously installed is

$$s_0 = \int_0^{L/2} \frac{Me}{EI_0} \, \mathrm{d}x = \int_0^{L/2} \frac{1}{2} \frac{q_z x(L-x)e}{EI_0} \, \mathrm{d}x, \tag{F.3}$$

according to Euler-Bernoulli beam theory, where e denotes the distance between the elastic neutral axes of the beam and floor element. For prismatic beams the solution to the former expression is

$$s_0 = \frac{1}{24} \frac{q_z L^3}{EI_0} e. \tag{F.4}$$

MODIFICATIONS TO CLOSED-FORM EXPRESSIONS

The closed-form expressions for midspan deflection and end slip, given by Equations F.2 and F.4, respectively, are only valid for prismatic floor systems. The closed-form expression for the deflection is modified to

$$w_\mathrm{m} = \frac{5}{384} \frac{q_z L^4}{C_1 \cdot EI_0|_{x=0} + (1-C_1) \cdot EI_0|_{x=L/2}}, \tag{F.5}$$

to capture the effects of a symmetrically tapered web with respect to midspan on the deflection. In Equation F.5 the bending stiffness of the steel beam without composite interaction EI_0 is evaluated at $x = 0$ and $x = L/2$. The bending stiffnesses at these locations are predictors for the midspan deflection and their relative influences are expressed through the fitting parameter C_1.

The closed-form expression for the end slip is modified to

$$s_0 = \frac{1}{24} \frac{q_z L^3}{C_1 \cdot EI_0|_{x=0} + (1-C_1) \cdot EI_0|_{x=L/2}} \left(C_2 \cdot e|_{x=0} + (1-C_2) \cdot e|_{x=L/2}\right), \tag{F.6}$$

to capture the effects of a symmetrically tapered web with respect to midspan on the end slip. In Equation F.6 the bending stiffness of the steel beam without composite interaction EI_0 is evaluated at $x = 0$ and $x = L/2$. The bending stiffnesses at these locations are predictors for the midspan deflection and their relative influences are expressed through the fitting parameter C_1. Also the distance between the elastic neutral axes e at $x = 0$ and $x = L/2$ are considered as predictors, and their relative influences are expressed through the fitting parameter C_2.

In the following section, the procedure to obtain the magnitudes for C_i ($i = 1, 2$) in Equations F.5 and F.6 is presented.

DESIGN VARIATIONS

The database of cross-sections that is considered to fit parameters C_i ($i = 1, 2$) in Equations F.5 and F.6 consists of simply-supported web-tapered steel beams, symmetrical with respect to the plane at midspan, loaded by a uniformly distributed load q_z. It was assumed that the prefabricated concrete floor elements do not contribute to the bending resistance. The dimensional parameters considered in the database are listed in Table F.1 and represent

a wide range of bisymmetrical and monosymmetrical web-tapered steel beam designs, and therefore the design formulae are considered to be generically applicable for this type of beam designs. Combining the parameters in Table F.1 led to 78 500 beam designs which were used as input for the regression analysis. The fitting parameters C_i ($i = 1, 2$) Equations F.5 and F.6 were derived by minimising the sum of the squared errors between the simplified formula and the 'exact' solution based on Euler-Bernoulli beam theory.

Table F.1 | Dimensional parameters considered in the derivation of design formulae for the deflection and end-slip of bi- and monosymmetrical non-prismatic beams.

Parameter	Physical meaning	Magnitude	Unit
L	Span	6, 8, 10, 12, 14, 16, 20	m
$h\|_{x=0,L}$	Beam height at supports	$L/20$, $L/25$, $L/30$	m
$\Delta h'$	Change in beam height per unit length	1.0%, 1.5%, 2.0%, 2.5%, 3.0%	-
b_f	Flange width	100, 150, 200, 250, 300	mm
$t_{f,t}$	Thickness of top (compression) flange	10, 12, 14, 16, 18	mm
$t_{f,b}$	Thickness of bottom (tensile) flange	10, 12, 14, 16, 18	mm
t_w	Web thickness	4, 6, 8, 10, 12	mm

RESULTS AND DISCUSSION

The design formula to determine the midspan deflection of a simply-supported web-tapered steel beam, symmetrical with respect to the plane at midspan, is determined based on the results obtained for the database of cross-sections as

$$w_m = \frac{5}{384} \frac{q_z L^4}{\frac{1}{3} \cdot EI_0|_{x=0} + \frac{2}{3} \cdot EI_0|_{x=L/2}}. \tag{F.7}$$

Figure F.1a illustrates the results obtained by the 'exact' solution based on Euler-Bernoulli beam theory and by the proposed design equation for the midspan deflection. The proposed design formula has a coefficient of determination $R^2 = 0.99998$. The maximum deviations between the approximate formula and the exact solution are +0.8% and -3.44%. In case of a prismatic beam, the approximation given by Equation F.7 becomes the exact solution given by Equation F.2.

The design formula to determine the end slip of a simply-supported web-tapered steel beam, symmetrical with respect to the plane at midspan, is determined based on the results obtained for the database of cross-sections as[2]

$$s_0 = \frac{1}{24} \frac{q_z L^3}{0.437 \cdot EI_0|_{x=0} + 0.563 \cdot EI_0|_{x=L/2}} \left(0.388 \cdot e|_{x=0} + 0.612 \cdot e|_{x=L/2}\right). \tag{F.8}$$

Figure F.1b illustrates the results obtained by the 'exact' solution based on Euler-Bernoulli beam theory and by the proposed design equation for the end slip. The proposed design

---

[2]In previous work the design formula has also been reported as

$$s_0 = \frac{1}{24} \frac{q_z L^3}{0.35 EI_0|_{x=0} + 0.65 EI_0|_{x=L/2}} \left(0.2 e|_{x=0} + 0.8 e|_{x=L/2}\right),$$

but the numerical coefficients have been revised to obtain a better match between the design model and the exact solution.

formula has a coefficient of determination $R^2 = 0.9997$. The maximum deviations between the approximate formula and the exact solution are +1.00% and -3.16%. In case of a prismatic beam, the approximation given by Equation F.8 becomes the exact solution given by Equation F.4.
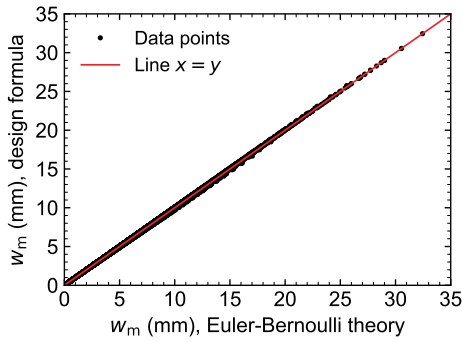
(a) Deflection.   **(b)** Slip.
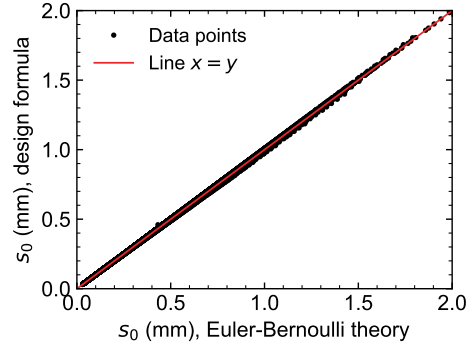
Figure F.1 | Results obtained by proposed design formulae versus the 'exact' analytical solutions based on Euler-Bernoulli beam theory.

F

G

AN INDICATION OF THE PROBABILITY OF REUSABILITY: ELASTIC VS. PLASTIC DESIGN

Traditionally, composite floor systems are designed according to theory of plasticity. Plastic design may impair the reuse or reselling of composite beams due to the perceived risks associated to damaged elements. In the past, this was not an issue, because it was physically impossible to demount the shear connection to retrieve the individual structural elements.

In case of demountable composite floor systems, the reusability of the structural elements plays an important role. According to the SCI guidelines [1], any evidence of plastic deformations leads to disapproval for reuse. Therefore any plasticity and/or damage must be prevented to ensure a sufficiently high probability of reusability of the structural elements, to prevent the formation of waste (discarded elements) and to maintain the economic value of the structural members.

The probability of encountering plasticity depends on the age of the structure and the type of analysis (elastic/plastic). At equal age and loading history, plastic design inherently leads to a higher probability of plasticity compared to elastic design. This appendix quantifies the probability of plasticity for both elastic and plastic design.

PLASTIC DESIGN

EN 1990 [2] specifies a target reliability index β related to irreversible behaviour in the serviceability limit state (SLS). This reliability index was used to quantify the probability of plastic deformations for a generic consequence class 2 composite floor system designed according to plastic theory (which fulfils the ultimate limit state (ULS) requirements). The target reliability index for a one-year reference period is $\beta_1 = 2.9$ [2], which corresponds to the characteristic (unfactored) load combination. For a reference period of n years, the corresponding reliability index β_n can be calculated by

$$\Phi\left(\beta_n\right) = \left[\Phi\left(\beta_1\right)\right]^n \tag{G.1}$$

where Φ is the cumulative distribution function of the standardised Normal distribution. The equation is valid assuming that the actions have statistically independent maxima in each year.

The probability of failure, i.e. having exceeded the irreversibility limit, after n years is then given by

$$p_{f,n} = 1 - \left[\Phi \left(\beta_1 \right) \right]^n \tag{G.2}$$

Figure G.1 illustrates the probability of exceeding the irreversibility limit as a function of time. The relation between the probability and time is quasi-linear. After 25 years, the probability of having exceeded the irreversibility limit is 4.6%. When reusing a composite floor system after 25 years of service, approximately the same proportion of its components may be assumed to have undergone plastic deformation, and should therefore be discarded based on the SCI guidelines [1]. Replacing a relatively small number of structural elements might not be a major issue in terms of sustainability, but it could be the need for thorough inspection of all beam elements to identify the rejectables that may lead to significant costs and delays.

ELASTIC DESIGN

An elastic design verification at the ultimate limit state (ULS) leads to a significantly smaller probability of exceeding the irreversibility limit compared to plastic design. In this case the probability of reusability is governed by $\beta_1 = 4.7$ [2]. Again, Equation G.2 can be used to determine the probability of failure (i.e. plastic deformation) over time, which is illustrated in Figure G.1. After 25 years, the probability of plasticity equals 0.0033%, which is negligible compared to the 4.6% obtained for plastic design. The elastic design verification at the ULS implies that all SLS conditions related to reversibility are automatically fulfilled as well.

It should be noted that not only the steel beams, but also the prefabricated concrete floor elements are designed for reuse. The largest potential for irreversible (plastic) deformation exists in the vicinity of the demountable shear connectors: substantial forces are locally introduced at their locations, which are not readily inspectable for any signs of damage. This suggests the shear connector should be limited to its (quasi-)elastic response to prevent irreversible behaviour, which could be achieved by limiting the maximum slip or connector force in the design verification.

The elastic design verification may lead to a comparatively higher initial cost due to the increase in material use, but may generate cost savings when the structure is demounted and subsequently reused. The phenomenon of requiring a greater initial investment, e.g. due to increased material use or energy consumption, is typical for reusable structures. Such design strategies are potentially competitive to traditional (non-demountable and non-reusable) designs if the total life-cycle costs are considered.

CONCLUDING REMARKS

The most sustainable structure is a structure that fully utilises its technical lifespan (e.g. 50 or 100 years) without the need for it to be demounted and relocated. However, because of inherent future changes in terms of functional needs, it is appropriate to design for demountability and reusability to prevent the need for demolition once the structure becomes functionally obsolete by enabling changes to the lay-out and location of the existing structure. The reuse of structural components requires, according to the SCI guidelines [1], that
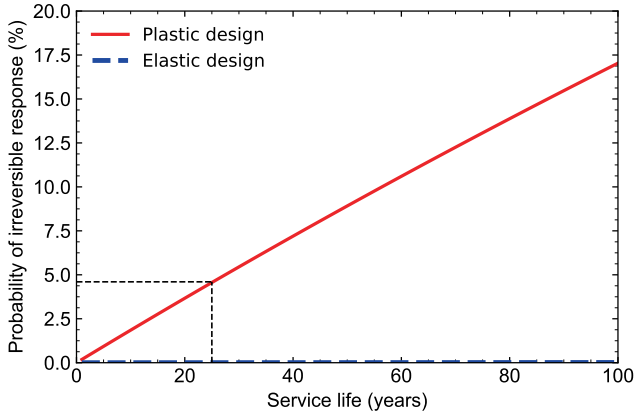
Figure G.1 | Probability of irreversible behaviour as a function of time.

there should not be any evidence of plastic deformations. This appendix demonstrated that an elastic design approach is the most appropriate method to avoid plasticity and to avoid the need for thorough inspections.

REFERENCES

[1]   Steel Construction Institute (SCI), *Protocol for reusing structural steel*, Tech. Rep. (SCI, 2019).

[2]   NEN, *NEN-EN 1990: Eurocode 0: Basis of structural design* (NEN, 2002).

G

H

DERIVATION OF DIFFERENTIAL EQUATION FOR COMPOSITE FLOOR SYSTEMS WITH PARTIAL SHEAR INTERACTION

Figure H.1 illustrates an infinitesimal segment with length dx of a composite floor system with partial shear interaction, and includes all internal and external forces. Element 1 represents the concrete floor and element 2 represents the steel beam. The bending moment around the strong axis, the vertical shear force and thee normal force in each element are denoted by M_i, V_i and N_i ($i = 1, 2$), respectively. The global internal actions are denoted without subscripts.

In the absence of an external axial force, it follows that $N = N + dN = 0$ and thus $dN_1 = -dN_2$. This condition implies that a interlayer shear force V_s exists, with magnitude

$$V_\mathrm{s} = -\frac{\mathrm{d}N_1}{\mathrm{d}x} = \frac{\mathrm{d}N_2}{\mathrm{d}x}. \tag{H.1}$$

If the interlayer shear force is assumed to be linearly related to the relative displacement of the elements' interfaces (slip, s), then $V_\mathrm{s} = Ks$, where K denotes the smeared shear connection stiffness, defined as the shear connector stiffness k_sc divided by the (uniform) connector spacing c_sc.

Bending moment equilibrium requires that $M = M_1 + M_2 - N_1 e$, where e is the distance between the centroids of elements 1 and 2. The interface slip can be expressed by

$$s = u_2 - u_1 - \varphi e, \tag{H.2}$$

where u_i ($i = 1, 2$) is the horizontal translation of the centroid of the i-th element, and where $\varphi = -\frac{\mathrm{d}w}{\mathrm{d}x}$ is the inclination of the cross-section of the composite floor system. The derivative of Equation H.2 is given by
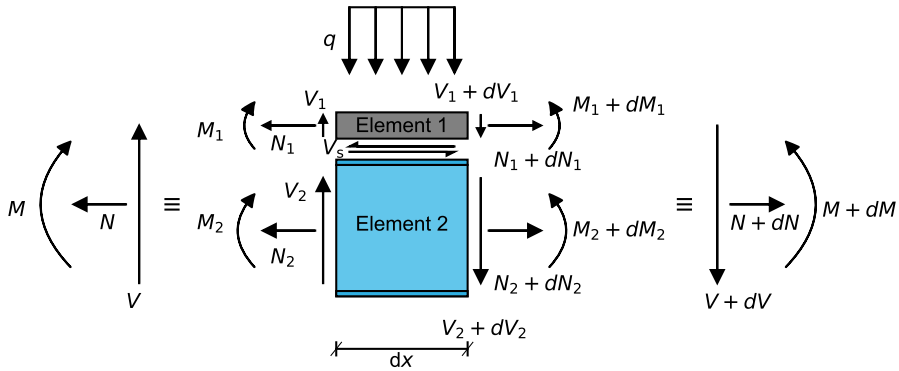
Figure H.1 | Differential element of composite floor system with flexible shear connection subject to distributed transverse load $q(x)$. The resultant of the normal force is zero, $N = N + dN = 0$, if no external axial load is applied. The distance between the centroid of elements 1 and 2, denoted by e, is not shown in favour of the clarity of the figure.

$$\frac{\mathrm{d}s}{\mathrm{d}x} = \varepsilon_2 - \varepsilon_1 - \kappa e, \tag{H.3}$$

where $\varepsilon_i = N_i/E_i A_i (i = 1,2)$ is the axial strain in the $i-$th element. The curvature of the composite floor system is defined as $\kappa = \varphi'$, with φ' denoting the derivative of the cross-sectional inclination with respect to x. The Young's Modulus and area of each element of the composite floor system are represented by E_i and A_i, respectively.

According to Euler-Bernoulli beam theory, the bending moment and curvature of each element ($i = 1,2$) are related by

$$M_i = E_i I_i \kappa. \tag{H.4}$$

Based on this equation and the moment equilibrium condition, the following expression for the curvature κ is derived

$$\kappa = \frac{M + N_1 e}{EI_0}, \tag{H.5}$$

where $EI_0 = E_1 I_1 + E_2 I_2$ is the bending stiffness under the absence of shear interaction. Substituting Equation H.5 into H.3 and simplifying gives

$$\frac{\mathrm{d}^2 N_1}{\mathrm{d}x^2} - \alpha^2 N_1 = \frac{Ke}{EI_0} M, \tag{H.6}$$

with α^2 defined as

$$\alpha^2 = K\left(\frac{1}{E_1 A_1} + \frac{1}{E_2 A_2} + \frac{e^2}{EI_0}\right) = \frac{Ke^2}{EI_0\left(1 - \frac{EI_0}{EI_\infty}\right)}, \tag{H.7}$$

where EI_∞ is the bending stiffness in case of rigid composite interaction.

According to the Euler-Bernoulli beam theory and the previously derived expressions,

$$V = \frac{dM}{dx} = \frac{d\kappa}{dx}EI_0 - \frac{dN_1}{dx}e. \tag{H.8}$$

Vertical force equilibrium for the system shown in Figure H.1 demands that $V' = -q$. Therefore, Equation H.8 can be differentiated once more to obtain

$$\frac{dV}{dx} = -q = \frac{d^2\kappa}{dx^2}EI_0 - \frac{d^2N_1}{dx^2}e, \tag{H.9}$$

and it follows that

$$\frac{d^2N_1}{dx^2} = \frac{q + \frac{d^2\kappa}{dx^2}EI_0}{e}. \tag{H.10}$$

The former expression is substituted into Equation H.6 to obtain

$$q + \frac{d^2\kappa}{dx^2}EI_0 - \alpha^2\kappa EI_0 + \alpha^2 M = \frac{Ke^2}{EI_0}M. \tag{H.11}$$

The curvature κ can be eliminated in favour of the deflection w, because according to the Euler-Bernoulli beam theory it holds that $\kappa = -w''$. It follows that

$$\frac{d^4w}{dx^4} - \alpha^2\frac{d^2w}{dx^2} = \frac{\alpha^2}{EI_\infty}M + \frac{q}{EI_0}. \tag{H.12}$$

Finally, the differential equation for a composite floor system with flexible shear connection is obtained, by differentiating the previous equation twice with respect to x to eliminate the immediate dependency on M because $M'' = -q$. The governing differential equation is then given by

$$\frac{d^6w}{dx^6} - \alpha^2\frac{d^4w}{dx^4} = -\frac{\alpha^2}{EI_\infty}q + \frac{1}{EI_0}\frac{d^2q}{dx^2}, \tag{H.13}$$

which has also been obtained by Girhammar & Gopu [1], Girhammar & Pan [2] and Xu & Wu [3], and which is also known as the Newmark model [4]. For beams subject to a uniform distribution load q, the differential equation reduces to

$$\frac{d^6w}{dx^6} - \alpha^2\frac{d^4w}{dx^4} = -\frac{\alpha^2}{EI_\infty}q, \tag{H.14}$$

The solution to this sixth-order differential equation is expressed by

$$w(x) = C_1\frac{e^{\alpha x}}{\alpha^4} + C_2\frac{e^{-\alpha x}}{\alpha^4} + C_3x^3 + C_4x^2 + C_5x + C_6 + \frac{1}{24}\frac{qx^4}{EI_\infty}, \tag{H.15}$$

where C_m ($m = 1, 2 \ldots 6$) are integration constants that follow from the boundary conditions.

The expression for the bending moment M can be derived based on Equation H.12 as

$$M = \frac{EI_\infty}{\alpha^2}\left[\frac{d^4w}{dx^4} - \alpha^2\frac{d^2w}{dx^2} - \frac{q}{EI_0}\right], \tag{H.16}$$

from which the shear force V follows directly as

H

$$V = \frac{\mathrm{d}M}{\mathrm{d}x} = \frac{EI_\infty}{\alpha^2}\left[\frac{\mathrm{d}^5 w}{\mathrm{d}x^5} - \alpha^2 \frac{\mathrm{d}^3 w}{\mathrm{d}x^3}\right]. \tag{H.17}$$

The normal force N_1 can be expressed in the form

$$N_1 = \frac{\kappa EI_0 - M}{e}, \tag{H.18}$$

from which expressions for the interlayer shear force V_s and the interlayer slip s logically follow as

$$V_\mathrm{s} = -\frac{\mathrm{d}N_1}{\mathrm{d}x}, \tag{H.19}$$

$$s = \frac{V_\mathrm{s}}{K}. \tag{H.20}$$

The relative contribution of elements 1 and 2 to the load bearing is proportional to their stiffness and to the magnitude of the composite interaction. The contribution of each element ($i = 1, 2$) to the total bending moment M is given by

$$|M_i| = \frac{E_i I_i}{EI_0}\left(|M| - |N_i e|\right). \tag{H.21}$$

Practically, however, it holds that $E_2 I_2 \gg E_1 I_1$ and thus the majority of the bending moment not carried by composite interaction will be carried by the steel beam alone.

REFERENCES

[1] U. A. Girhammar and V. K. A. Gopu, *Composite beam-columns with interlayer slip—exact analysis,* Journal of Structural Engineering **119**, 1265 (1993).

[2] U. A. Girhammar and D. H. Pan, *Exact static analysis of partially composite beams and beam-columns,* International Journal of Mechanical Sciences **49**, 239 (2007).

[3] R. Xu and Y. Wu, *Static, dynamic, and buckling analysis of partial interaction composite members using Timoshenko's beam theory,* International Journal of Mechanical Sciences **49**, 1139 (2007).

[4] N. M. Newmark, *Test and analysis of composite beams with incomplete interaction,* Proceedings of the Society for Experimental Stress Analysis **9**, 75 (1951).

H

I

ANALYTICAL RESULTS FOR EXPERIMENTAL COMPOSITE FLOOR SYSTEM

Figures I.1 - I.6 illustrate the analytical predictions related to the experimental composite floor system (see Sections 7.2 and 9.1.2) for the six studied shear connector arrangements. The diagrams reflect the deflection, slip, bending moment, normal stresses, normal force and longitudinal shear force flow distributions along the length of the composite floor system. Each plot contains two vertical dashed lines that represent the points of load application. All results correspond to concentrated forces $F = 100$ kN. In each subplots (b) the location of the shear connectors is marked to reflect the shear connector arrangement.
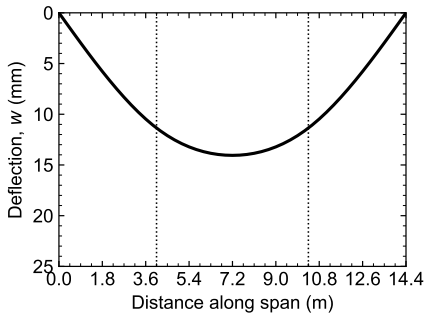
(a) Deflection.
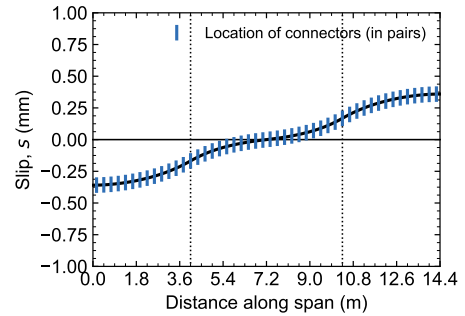
(b) Slip.
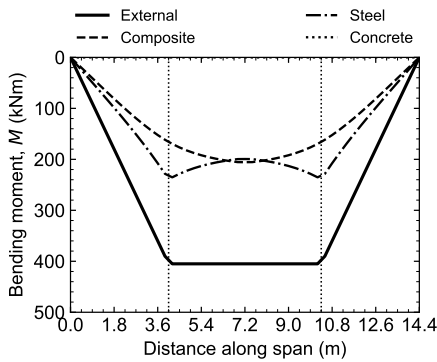
(c) Bending moment.
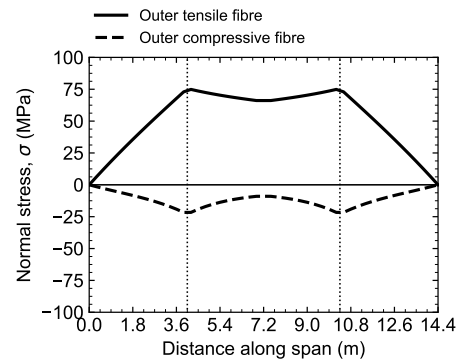
(d) Normal stresses in the steel beam.
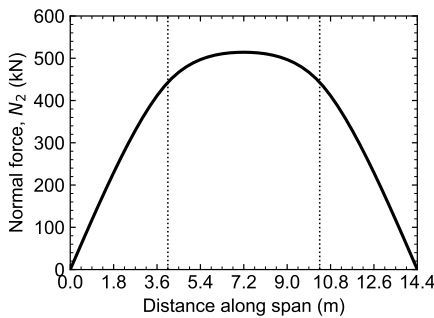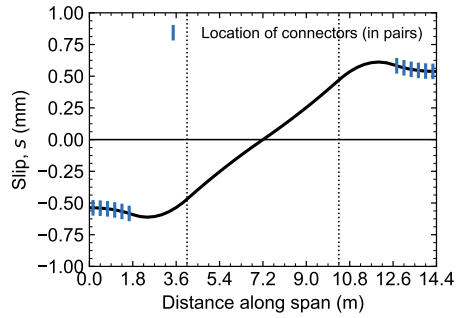

(e) Normal force.
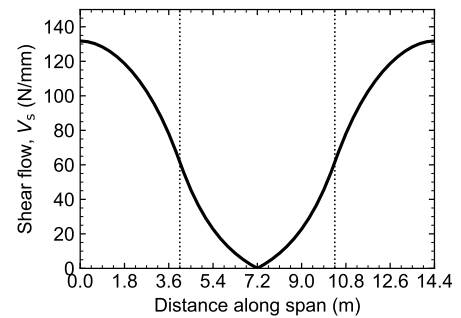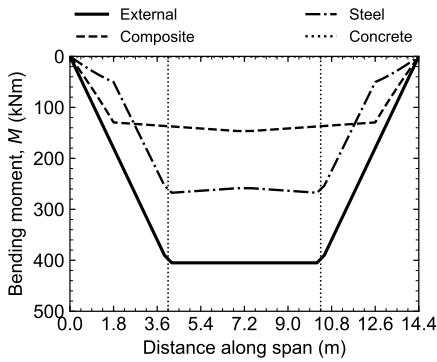

(f) Shear force flow.

Figure I.1 | Analytical results for shear connector arrangement U-24 (see subfigure b) for concentrated forces $F =$ 100 kN applied at the locations indicated by vertical dashed lines.
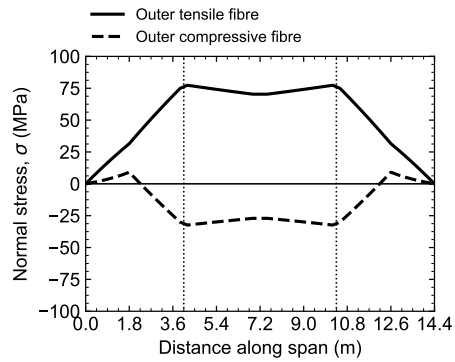
(a) Deflection.

(b) Slip.

(c) Bending moment.

(d) Normal stresses in the steel beam.

(e) Normal force.

(f) Shear force flow.
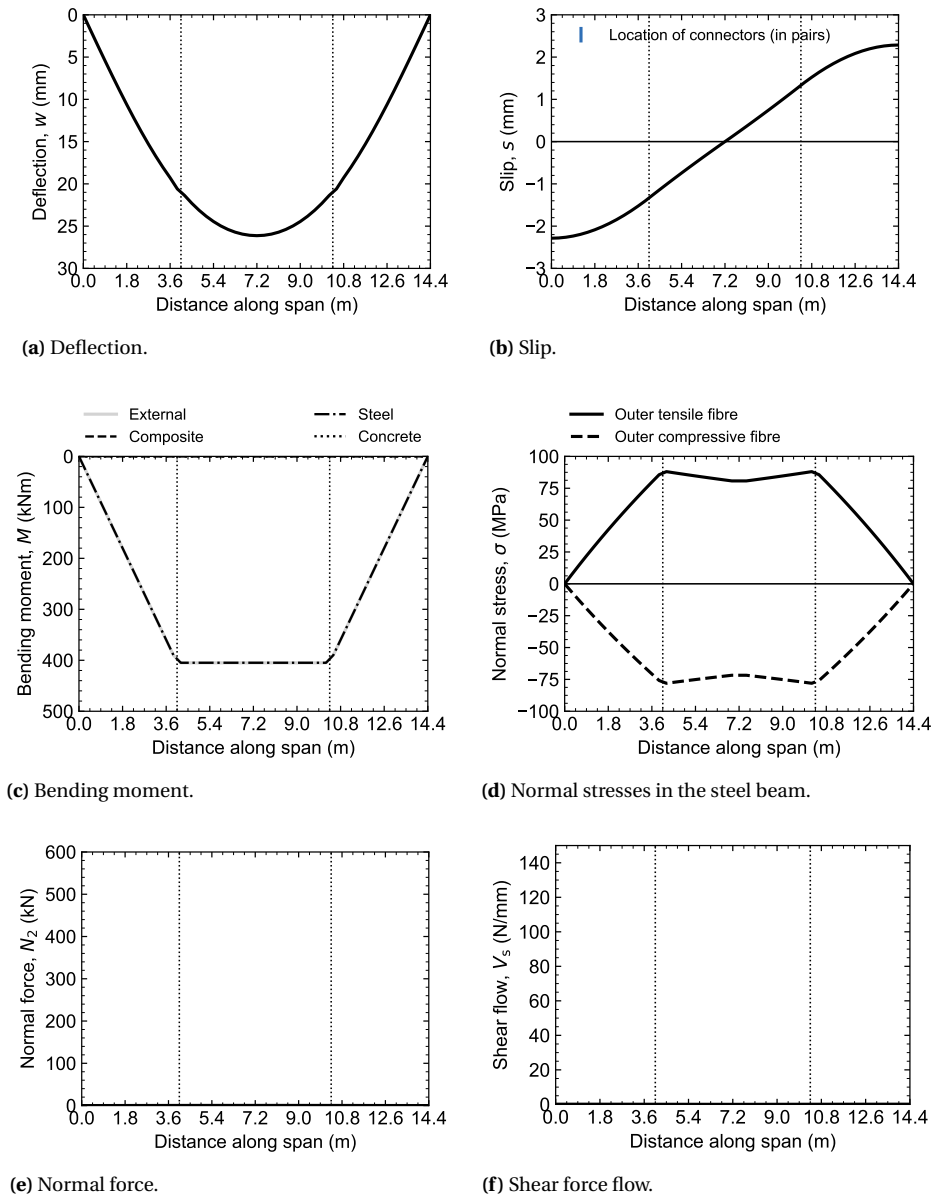
Figure I.2 | Analytical results for shear connector arrangement C/U-0 (see subfigure b) for concentrated forces $F = 100$ kN applied at the locations indicated by vertical dashed lines.
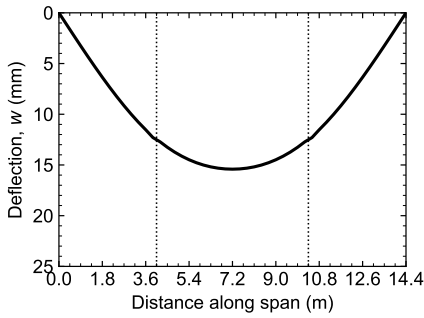
(a) Deflection.
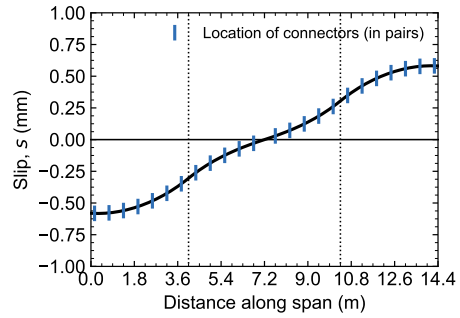
(b) Slip.
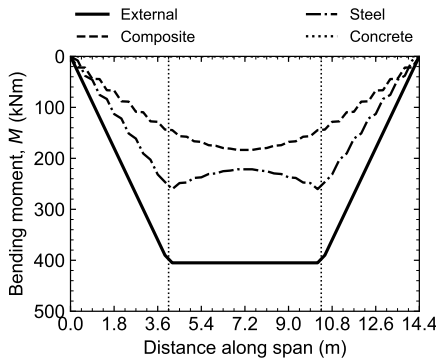
(c) Bending moment.
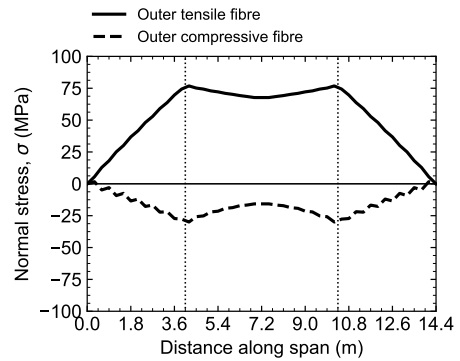
(d) Normal stresses in the steel beam.
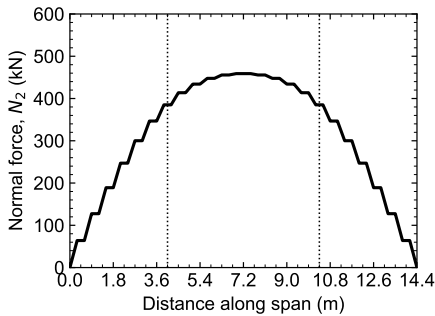
(e) Normal force.
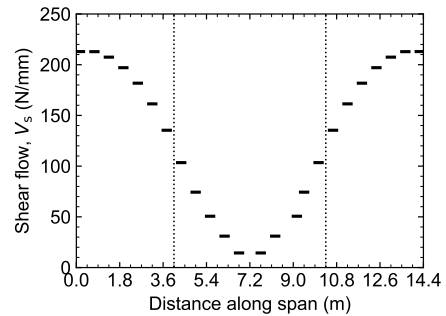
(f) Shear force flow.

Figure I.3 | Analytical results for shear connector arrangement U-12 (see subfigure b) for concentrated forces $F = 100$ kN applied at the locations indicated by vertical dashed lines.
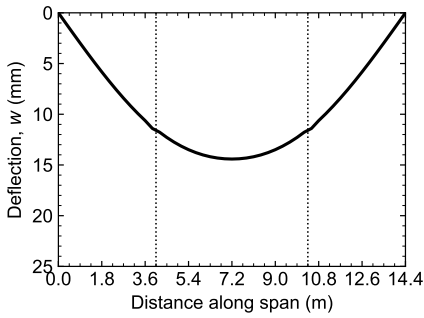
(a) Deflection.
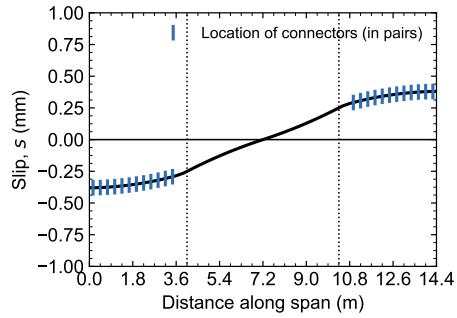
(b) Slip.
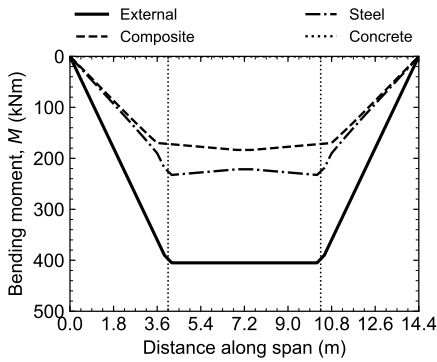
(c) Bending moment.
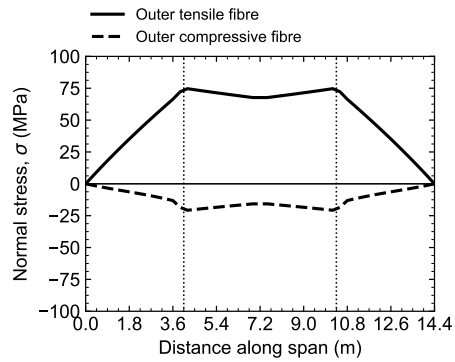
(d) Normal stresses in the steel beam.
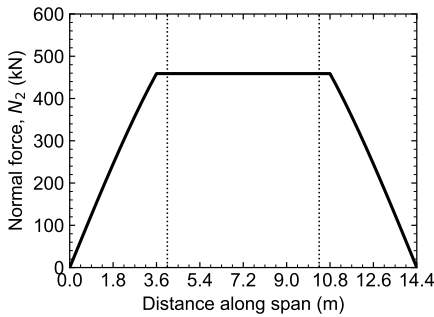
(e) Normal force.
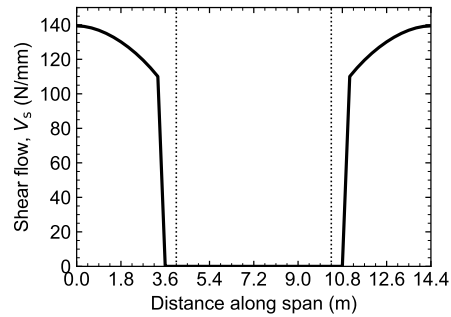
(f) Shear force flow.

Figure I.4 | Analytical results for shear connector arrangement C-12 (see subfigure b) for concentrated forces $F = 100$ kN applied at the locations indicated by vertical dashed lines.

I
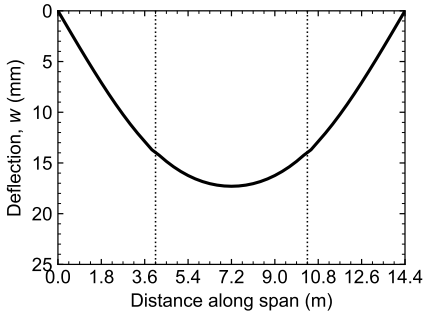
(a) Deflection.
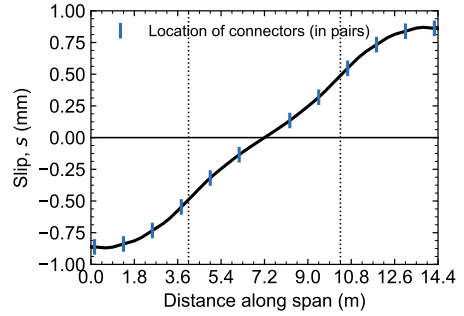
(b) Slip.
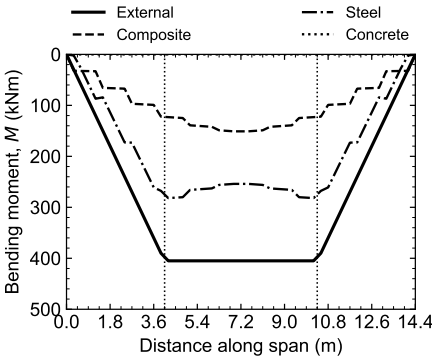
(c) Bending moment.
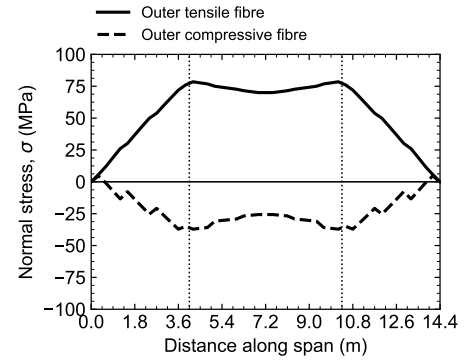
(d) Normal stresses in the steel beam.
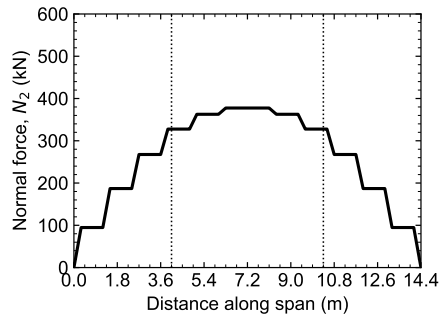
(e) Normal force.
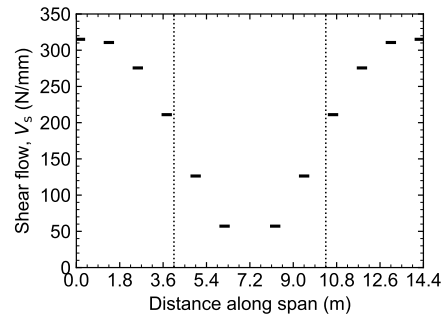
(f) Shear force flow.

Figure I.5 | Analytical results for shear connector arrangement U-6 (see subfigure b) for concentrated forces $F =$ 100 kN applied at the locations indicated by vertical dashed lines.
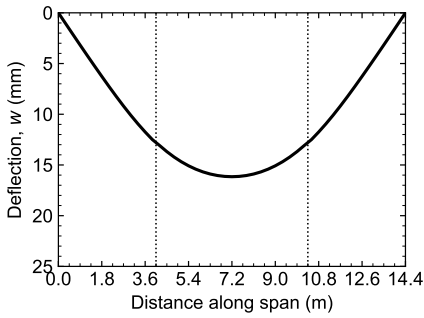
(a) Deflection.

(b) Slip.

(c) Bending moment.

(d) Normal stresses in the steel beam.
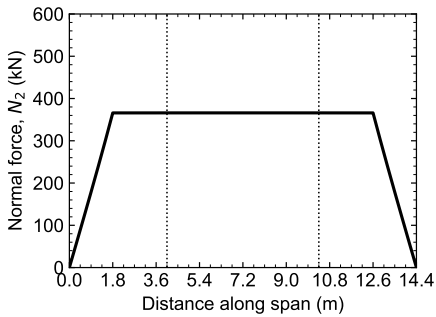
(e) Normal force.
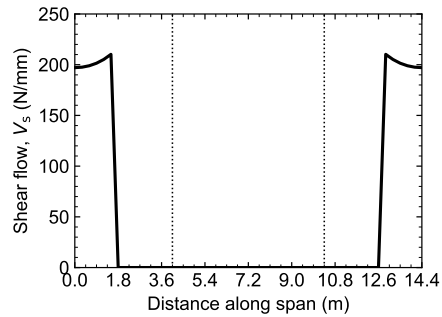
(f) Shear force flow.

Figure I.6 | Analytical results for shear connector arrangement C-6 (see subfigure b) for concentrated forces $F = 100$ kN applied at the locations indicated by vertical dashed lines.

J

DERIVATION OF WAGNER TORSIONAL RIGIDITY β_y

The Wagner torsional rigidity β_y is derived by assuming that the end of infinitesimal segment $\mathrm{d}x$ of a monosymmetrical cross-section is subject to a rotation $\mathrm{d}\varphi$ with respect to its other end, see Figure J.1. This causes a differential displacement of cross-sectional elements at infinitesimal distance $\mathrm{d}x$. Using the small angle approximation, the displacement of each cross-sectional element perpendicular to the line connecting the centroid of the cross-sectional element and the twist centre (TC), is given by

$$\delta = a \cdot \mathrm{d}\varphi = \sqrt{(z - z_\mathrm{s})^2 + \left(y - y_\mathrm{s}\right)^2} \cdot \mathrm{d}\varphi \tag{J.1}$$

The inclination δ' between the cross-sectional elements at both ends of the infinitesimal segment $\mathrm{d}x$ equals

$$\delta' = a \frac{\mathrm{d}\varphi}{\mathrm{d}x} \tag{J.2}$$

Consequently, the normal stresses $\sigma_\parallel$ (parallel to the beam axis) due to bending generate a stress component $\sigma_\perp$ perpendicular to the line connecting the centroid of the cross-sectional element and the twist centre, see Figure J.2. The magnitude of this stress component is

$$\sigma_\perp = \sigma_\parallel a \frac{\mathrm{d}\varphi}{\mathrm{d}x} \tag{J.3}$$

Such a stress component generates a bending moment around the twist centre with a magnitude

$$\mathrm{d}M = \sigma_\perp a \mathrm{d}A = \sigma_\parallel a^2 \frac{\mathrm{d}\varphi}{\mathrm{d}x} \mathrm{d}A \tag{J.4}$$

The resulting torque around the twist centre generated by all cross-sectional elements is then given by
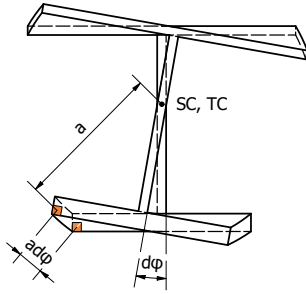
Figure J.1 | Torsion of a monosymmetrical cross-section leading to a rotation $\mathrm{d}\varphi$ around the shear centre and a displacement $a\mathrm{d}\varphi$ of the cross-sectional elements.
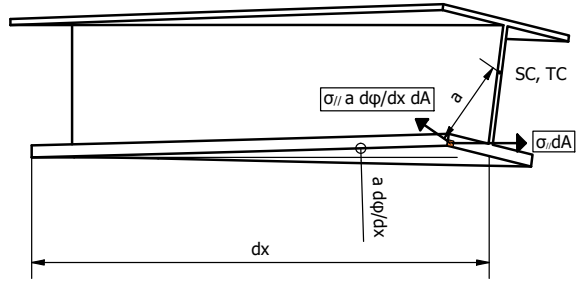

Figure J.2 | The relative inclination of the flanges causes the longitudinal stresses $\sigma_\parallel$ to generate a stress component perpendicular to the line connecting the centroid of the cross-sectional element and the twist centre.

$$T = \int \mathrm{d}M = \frac{\mathrm{d}\varphi}{\mathrm{d}x}\int_A \sigma_\parallel a^2 \mathrm{d}A = \beta_y \frac{\mathrm{d}\varphi}{\mathrm{d}x} \tag{J.5}$$

which stiffens the response if positive. In the previous equation, $\beta_y = \int_A \sigma_\parallel a^2 \mathrm{d}A$ is introduced as the Wagner torsional rigidity. For monosymmetrical beams subject to bending solely around the strong y-axis, β_y can be more conveniently expressed by

$$\beta_y = \frac{M_y}{I_y}\left(\int_A y^2 z\,\mathrm{d}A + \int_A z^3\,\mathrm{d}A\right) + 2z_\mathrm{s} \tag{J.6}$$

The previous equation demonstrates that the Wagner torsional rigidity is positive ($\beta_y > 0$) if the tension flange (positive z-direction) is further from the shear centre than the compression flange. Similarly the Wagner torsional rigidity is negative if the compression flange is further from the shear centre compared to the tensile flange. For bisymmetrical cross-sections it follows that $\beta_y = 0$.

J

ACKNOWLEDGEMENTS

CURRICULUM VITÆ

Martin Paul NIJGH

02-12-1992   Born in Vlaardingen, The Netherlands.

EDUCATION

2005–2011   Pre-University education
             Het College Vos, Vlaardingen

2012–2015   Bachelor of Science in Civil Engineering
             Delft University of Technology
             Thesis: Dubbele buiging in betonnen kolommen

2015–2017   Master of Science in of Civil Engineering
             Delft University of Technology
             Thesis: New materials for injected bolted connections

2017–2021   PhD. in Steel & Composite Structures
             Delft University of Technology
             Thesis: A multi-scale approach towards reusable steel-
                            concrete composite floor systems
             Promotors: Prof. dr. M. Veljkovic, Prof. dr. ir. L.J. Sluijs, dr. M.
                            Pavlovic

LIST OF PUBLICATIONS

JOURNAL PAPERS

J.1. **M.P. Nijgh**, and M. Veljkovic, *An optimisation strategy for the (in- and out-of-plane) resistance of steel beams in demountable composite floor systems*, Structures **24**, 880 (2020).

J.2. **M.P. Nijgh**, and M. Veljkovic, *Requirements for oversized holes for reusable steel-concrete composite floor systems*, Structures **24**, 489 (2020).

J.3. **M.P. Nijgh**, and M. Veljkovic, *A static and free vibration analysis method for non-prismatic composite beams with a non-uniform flexible shear connection*, International Journal of Mechanical Sciences **159**, 398 (2019).

J.4. **M.P. Nijgh**, I.A. Gîrbacea, and M. Veljkovic, *Elastic behaviour of a tapered steel-concrete composite beam optimized for reuse*, Engineering Structures **183**, 366 (2019).

J.5. A. Kozma, C. Odenbreit, M.V. Braun, M. Veljkovic, and **M.P. Nijgh**, *Push-out tests on demountable shear connectors of steel-concrete composite structures*, Structures **21**, 45 (2019).

J.6. H. Xin, **M.P. Nijgh**, and M. Veljkovic, *Computational homogenization simulation on steel reinforced resin used in the injected bolted connections*, Composite Structures **210**, 942 (2018).

J.7. **M.P. Nijgh**, H. Xin, and M. Veljkovic, *Non-linear hybrid homogenization method for steel-reinforced resin*, Construction and Building Materials **182**, 324 (2018).

CONFERENCE PAPERS

C.1. I.A. Gîrbacea, **M.P. Nijgh**, and M. Veljkovic, *Economic viability of demountable steel-concrete composite beams*, Proceedings of Nordic Steel 2019, 427 (2019).

C.2. I.A. Gîrbacea, **M.P. Nijgh**, and M. Veljkovic, *Proof of concept of a demountable steel-concrete flooring system*, Proceedings of Nordic Steel 2019, 571 (2019).

C.3. A. Gritsenko, **M.P. Nijgh**, and M. Veljkovic, *Towards a demountable composite slab floor system*, Proceedings of Nordic Steel 2019, 243 (2019).

C.4. **M.P. Nijgh**, H. Xin, and M. Veljkovic, *Mechanical properties of (steel-reinforced) resins used in injected bolted connections*, Proceedings of the 22nd International Conference on Composite Materials, (2019).

C.5. **M.P. Nijgh**, and M. Veljkovic, *Design of composite flooring systems for reuse*, IOP Conference Series: Earth and Environmental Science **225**, (2019).

C.6. **M.P. Nijgh**, I.A. Gîrbacea, and M. Veljkovic, *Optimization of a composite (steel-concrete) floor system for fast execution and easy demolition*, Proceedings of the Scientific Conference on Planning, Design, Construction and Building Renewal (iNDiS 2018), 45 (2018).

C.7. H. Xin, **M.P. Nijgh**, and M. Veljkovic, *Computational homogenisation simulation on steel rein-forced resin used in the injected bolted connections*, Proceedings of the 13th World Congress on Computational Mechanics, (2018).

C.8. A. Kozma, C. Odenbreit, M.V. Braun, M. Veljkovic, and **M.P. Nijgh**, *Push-out tests on demount-able shear connectors of steel-concrete composite structures*, Proceedings of the 12th interna-tional conference on Advances in Steel-Concrete Composite Structures, 549 (2018).

C.9. **M.P. Nijgh**, M. Pavlovic, and M. Veljkovic, *Flexible shear connectors in a tapered composite beam optimized for reuse*, Proceedings of the 6th Annual International Conference on Architecture and Civil Engineering, 32 (2018).

C.10. **M.P. Nijgh**, M. von Arnim, M. Pavlovic, and M. Veljkovic, *Preliminary assessment of a composite flooring system for reuse*, Proceedings of the 8th International Conference on Composite Con-struction in Steel and Concrete, 2017.

TRADE JOURNAL PAPERS FOR PRACTISING ENGINEERS

T.1. **M.P. Nijgh** and M. Veljkovic, *Demontabele verbinding met injectiebouten*, Bouwen met Staal **270**, 44 (2019).

PATENT

P.1. **M.P. Nijgh**, *New material for injected bolted connection*, World Intellectual Property Organisa-tion, **WO 2018/190705 A1**, (2018).

CONTRIBUTIONS TO EU-PROJECT REDUCE[1] DELIVERABLES

R.1. REDUCE Deliverable D5.2: Beam tests, pp. 1-27, 2019.

R.2. REDUCE Deliverable D5.4: Feasibility and structural testing of a demountable and reusable composite beam, pp. 1-43, 2019.

R.3. REDUCE Deliverable D6.1: Design and visualisation of a demountable multi-storey car park building, pp. 1-52, 2019.

R.4. REDUCE Deliverable D6.2: Technical and economic feasibility of a demountable and reusable multi-storey car park building, pp. 1-29, 2019.

R.5. REDUCE Deliverable D7.1: Guidance on demountable composite construction systems, pp. 30-40 & 90-99, (2019).

---

[1]The project deliverables are part of the research project "Reuse and Demountability using Steel Structures and the Circular Economy" REDUCE supported by the European Commission through the Research Fund for Coal and Steel.